Prevention and detection of bacterial pathogens on medical device materials

James Hall

A thesis submitted in partial fulfilment of the requirements of Nottingham Trent University for the degree of Doctor of Philosophy

Friday, 20 December 2024

Declaration

This work is the intellectual property of the author. You may copy up to 5% of this work for private study, or personal, non-commercial research. Any re-use of the information contained within this document should be fully referenced, quoting the author, title, university, degree level and pagination. Queries or requests for any other use, or if a more substantial copy is required, should be directed to the owner(s) of the Intellectual Property Rights.

Acknowledgements

Firstly, thank you to Samantha McLean, Gareth Cave and Rob Morris for their unwavering support and guidance during this project. I have learned so much in three different scientific fields during my PhD.

Secondly, I would like to thank all my friends, Adam Varney, Nicasio Geraldi, Subbareddy Mekapothula, Elvina Chrysanthou, Becky Coxhill, Dominic Craske, Macsen Fryer, Brad Sprouse and many others, the list is endless. Without you listening to me moan about failed experiments or setbacks, I would have gone crazy.

"However high we climb in the pursuit of knowledge we shall still see heights above us, and the more we extend our view, the more conscious we shall be of the immensity that lies beyond"

– William Armstrong 1863

LIST OF FIGURES

List of Tables

Abbreviations

MDR - Multidrug Resistance

ESKAPE pathogens - *Enterococcus faecium, Staphylococcus aureus, Klebsiella pneumoniae, Acinetobacter baumannii, Pseudomonas aeruginosa,* and *Enterobacter species*

ICU - Intensive Care Unit

WHO - World Health Organisation

DNA - Deoxyribonucleic Acid

MRSA – Methicillin Resistant *Staphylococcus aureus*

FDA – Food and Drug Administration

UTI's – Urinary Tract Infections

HGT – Horizontal Gene Transfer

EPS – Extracellular Polysaccharide

HCAI – Healthcare Associated Infection

VAP – Ventilator Associated Pneumonia

ET – Endotracheal tube

PVC – Polyvinylchloride

MPTMS – 3-Mercaptopropyltrimethoxysilane

CuO – Copper oxide

NP's – Nanoparticles

Glu-CuO nanoparticles – Glutamic acid coated copper oxide nanoparticles

CFU – Colony Forming Unit

TEM – Transmission Electron Microscope

SEM – Scanning Electron Microscope

EDS – Xray Energy Dispersion Spectroscopy

MRI – Magnetic Resonance Imaging

NMR – Nuclear Magnetic Resonance

PD – Proton Density

DLS – Dynamic Light Scattering

ICP-MS – Inductively Coupled Plasma – Mass Spectrometry

TGA – Thermogravimetric Analysis

UV – Ultraviolet

ASM – Artificial Saliva Media

MHB - Mueller Hinton Broth

TSB – Tryptic Soy Broth

MHA - Mueller Hinton Agar

TSA - Tryptic Soy Agar

RPM – Revolutions Per Minute

OD – Optical Density

PBS – Phosphate Buffer Saline

DMEM – Dulbecco's Modified Eagle Medium

MIC – Minimum Inhibitory Concentration

MBC – Minimum Bactericidal Concentration

MBEC – Minimum Biofilm Eradication Concentration

List of publications presentations and proceedings

Publications

Nanomaterials special edition 2024: Antipathogenic applications of copper nanoparticles in air filtration systems

Nanomaterials 2024: Bio-compatible antimicrobial coatings for medical devices (In preparation)

Conference presentations and talks

Microbiology society annual conference 2022: Poster

Institute of Physics: East midlands 2022 Three-minute wonder: Flash presentation and talk

Science and technology annual research conference (STAR conference) 2022: Poster

Table of Contents

Abstract

With a predicted ten million deaths per year estimated by the year 2050, alternative strategies in combating microbial infection are required. Current techniques to combat these infections rely on the heavy use of antibiotics, however, an increase in antimicrobial resistance has led to these predicted numbers. The leading cause of antimicrobial resistance is the biofilm various bacteria produce to increase their survivability, however, this production of a natural polysaccharide barrier only occurs when bacterial cells adhere to a surface, such as medical devices. By preventing this adhesion, it may be possible to slow down the rate of antimicrobial resistance and ensure this prediction is never realised.

The work presented in this thesis covers three aspects in preventing and detecting bacterial pathogens on medical devices. Firstly, copper oxide nanoparticles were synthesised and characterised both uncoated and coated in glutamic acid. These glutamic acid-coated nanoparticles (Glu-CuO NPs) were coated onto various medical materials, using 3-mercaptopropyltrimethoxysilane (MPTMS) to create an antimicrobial coating. The coating was applied using a dip coating and spray coating on various medical-grade materials. Leaching of the coatings was evaluated and found $(8 \pm 35$ mg $L^{-1})$ and $(2.7 \pm 1.1$ mg $L^{-1})$ for dip coating and spray coatings respectively. The coating materials were also tested against HaCaT epithelial cells to determine the toxicity of MPTMS (>0.1 mol L^{-1}) and the Glu-CuO NPs (325 mg L^{-1}).

Various pathogens, including ESKAPE pathogens, had their phenotypic and genotypic antibiotic resistance profiles evaluated and compared with slight concordance (53.7 %). The Glu-CuO NPs were tested on these species finding the minimum bactericidal concentration depending on species (325 mg L^{-1}). The nanoparticle coating was evaluated using a modified Minimum Biofilm Eradication Concentration (MBEC) assay and the reduction in viable counts was measured at both the MBC concentration and at 20 times MIC concentration (1-2 log reduction and 3-4 log reduction respectively), with the same results seen using a CDC bioreactor.

Finally, non-invasive measurements and imaging of different bacterial species were made using NMR and MRI to determine when a biofilm infection has occurred. T_1 and

T_2 relaxation values were measured using a 1.5 T Siemens Avanto scanner, between 2863 ms for T_1 measurements and 1100 ms for T_2^{eff}). Additional measurements of the apparent diffusion coefficient (ADC) and self-diffusion coefficient (SDC) were taken, with changes in ADC and SDC could be observed by the decrease in diffusion coefficient, during the first two days, then an increase afterwards. This indicated property changes of the media and could be used to evaluate contamination indirectly. T_1 and T_2 measurements of the porcine tracheal wall were taken to ensure enough contrast was observable. The measured values between the tracheal wall and biofilm were significantly different, such that both T1-weighted and T_2^{eff} weighted imaging sequences could be used, to visualise the biofilm on the silicone tube.

These results showed that copper oxide nanoparticles functionalised with an amino acid can be used as an antimicrobial coating when adhered at non-toxic concentrations to human epithelial cells. The coating can be applied to different medical materials and by different coating techniques allowing for reapplication of an antimicrobial coating on *ad-hoc* modified medical devices prior to surgery and offering an alternative to submerging a device in antibiotics. Finally, MRI can be used to non-invasively detect biofilm formation in an intubated porcine pluck, where a week-old biofilm is visible on silicone tube. This offers an alternative to invasive techniques and should be adopted to reduce the use of invasive techniques when determining biofilm infection, whilst also enabling earlier detect biofilms earlier. Collectively, this work shows new methods for preventing and detecting biofilm formation on medical devices, with a particular focus on endotracheal tubes.

Chapter 1. Introduction

1.1 A description of bacteria

1.1.1 The classification of bacteria

Bacteria are microorganisms that are found in almost every environment, ranging from soil and dirt to hospitals and the international space station[1,2]. These organisms compete for similar food sources and evolve to gain advantages over other bacterial species[3]. Taxonomically, all living organisms can be separated into three domains, the bacterial and archaeal domains, both comprise microorganisms that are categorised as prokaryotes. They are morphologically similar and were once classified as a single domain. However, there are distinct differences between the domains, which saw their reclassification into distinct domains due to differences in biochemistry and evolutionary history. Eukarya differs significantly from both bacteria and archaea, having a cellular nucleus and other membrane-bound organelles[4]. Below (Figure 1.1), a phylogenetic tree shows the evolution and distinction between the three domains that all life on earth can be categorised under[4]. These cells all originate from a common ancestor cell coined the Last Universal Common Ancestor (LUCA)[5].
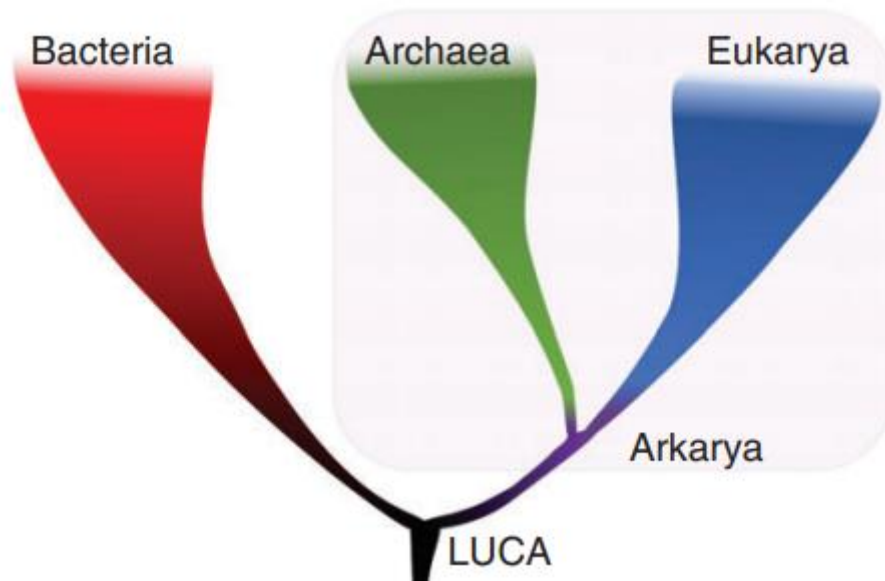
Figure 1.1 *The phylogenetic tree that separates all three domains that are used to categorise life. A phylogenetic tree that all life can be categorised as, with a common ancestor cell type termed LUCA[5]. Permission to use the image acquired from Nature publishing group*

There is debate in the literature as to how life should be subdivided at the Kingdom level, however for bacteria, classification at the level of phylum is more clearly defined. Bacterial phyla describe the largest delineations from LUCA in the bacteria domain, and even the definition at this level is debated, however, a popular definition is that at this level bacteria share 75% or less of the 16s rRNA genes sequence identity[6]. Further classifications are made at the levels of Class, Order, Family, Genus and Species[7]. Commonly bacteria are referred to by their genus and species, an example of this would be *Staphylococcus aureus*, where *Staphylococcus* describes the genus and *aureus* describes the species. Bacterial can finally be categorised based on their strain, where a single gene change can separate out two strains of the same species.

1.1.2 Morphology and structure of bacteria

There are different ways to characterize bacteria based on cellular morphology. The different morphologies of the bacteria are varied and are determined by both evolutionary factors as well as environmental pressures[8]. These morphologies show how diverse bacteria can be (Figure 1.2)[8]. Most bacteria fall under the cocci or bacilli

morphology, with examples of these species being *Staphylococcus epidermidis* for cocci, and *Escherichia coli* for bacilli[9].
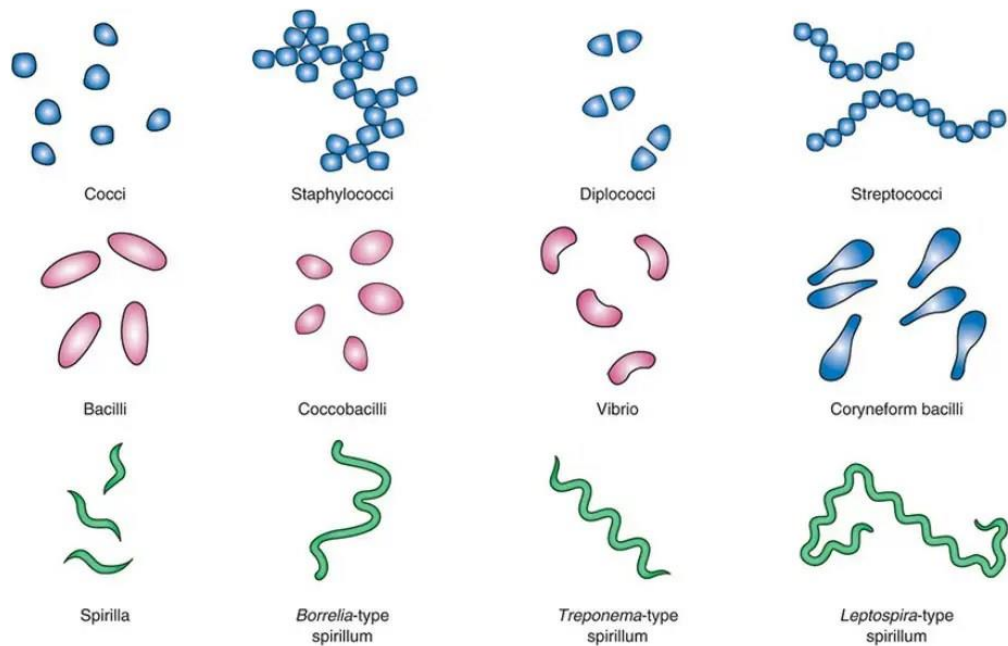
Figure 1.2 *The morphological shapes that bacteria may possess. Some of the different morphologies that bacteria can possess include the staphylococci shape for S. epidermidis and bacilli shape for E. coli [10]. Permission to use image acquired from the author of the blog.*

Under certain conditions, bacteria may adapt their shape from their typical norms due to different environmental pressures such as different food sources or pH levels in their local environment. Another morphological difference that can be used to classify different bacterial species is based on the cell envelope. These cell envelopes can be differentiated according to whether they contain an inner and outer membrane, encasing a thin well wall (Gram negative), or whether they contain a single cellular membrane surrounded by a thick cell wall (Gram positive). These differences can be identified by staining and microscopy and species categorised accordingly (Figure 1.3)[11].
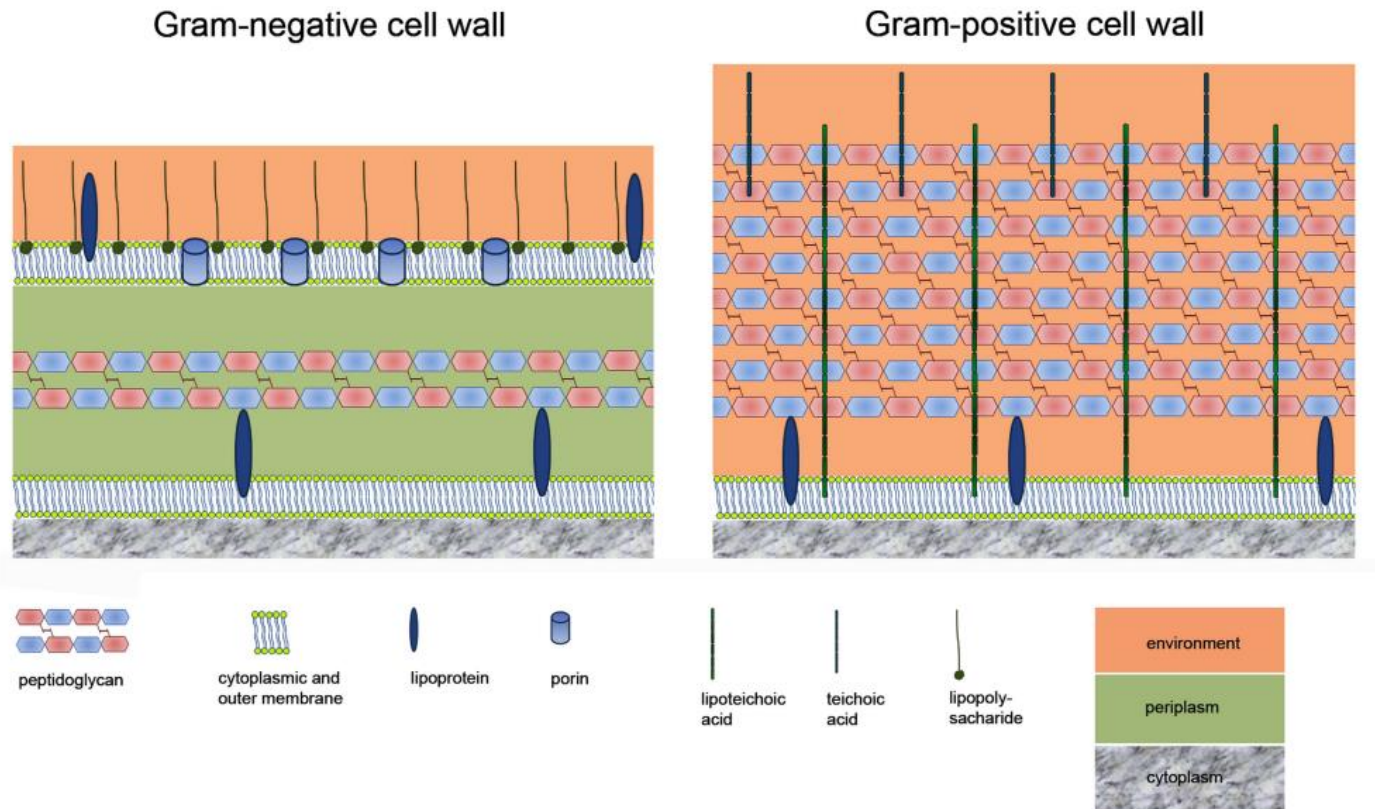
Figure 1.3 *A comparison of Gram negative and Gram positive species. The difference between Gram positive and Gram negative cell envelopes, demonstrating that Gram negative species have an additional cell membrane whereas Gram positive have a singular membrane and a thick peptidoglycan-based cell wall[12]. Permission to use image acquired from the American Society for Microbiology*

1.1.3 Characteristics of pathogenic bacteria

Bacteria are all around us, living on almost all surfaces including on and in our bodies. This includes on our skin and inside our gut[13]. Consequentially, we find ourselves both dependant on these bacteria, with some species in our gut aiding in digestion and producing important vitamins, whilst a small percentage of species can cause infectious diseases such as sepsis or pneumonia[14]. Pathogenic bacteria cause infections by colonizing tissues, adhering to various organ cells, and delivering toxins to disrupt host cells, destroying cell membranes and interrupting host defences[15]. In the presence of bacterial pathogens, the host immune system mobilises the immune response. The innate immune response is the first line of defence against such pathogens; however exposure causes a memory response, which is specific to the pathogen to more efficiently to combat the infection[16]. However, certain bacterial virulence factors have evolved to evade or otherwise survive these immune responses, with one such virulence factor being biofilm formation, whereby the microbial population encases itself in a self-producing extracellular polysaccharide matrix to protect the cells within[17].

1.2 Treatment of bacterial infections

With bacterial infections being a major health problem, the discovery of antibiotics by Sir Alexander Fleming in 1928 is still one of the most important medical discoveries in human history. His discovery came from observing mould contamination on an agar plate that prevented *Staphylococcus* cells from growing near the contaminant[18]. This observation famously led to the discovery of penicillin; an antibiotic produced by the mould as a mechanism for colonising environments by killing competitor organisms such as bacteria[18]. Many more antibiotics have since been identified or synthesised and have been used to treat bacterial infections since the 1940's, with a 'golden age' of antibiotic discovery in the mid-20th century[19]. However, this golden age of antibiotic discovery has ended, and the discovery of new antibiotics is few and far between, with lipopeptide discovery in 1987 heralding the start of an antibiotic discovery void and only one new class being discovered since (teixobactin)[20]. With increasing antibiotic resistance and a lack of new antibiotics, the mortality caused by pathogenic species will inevitably increase.

Different antibiotics have varying mechanisms of action; they can act by inhibiting cell growth (bacteriostatic) or by killing bacterial cells (bactericidal)[21]. These different bacteriostatic and bactericidal mechanisms can be seen below (Figure 1.4), with the main mechanisms of action being: inhibition of cell wall or membrane synthesis, inhibition of proteins synthesis and inhibition of nucleic acid synthesis or interference with DNA[22].
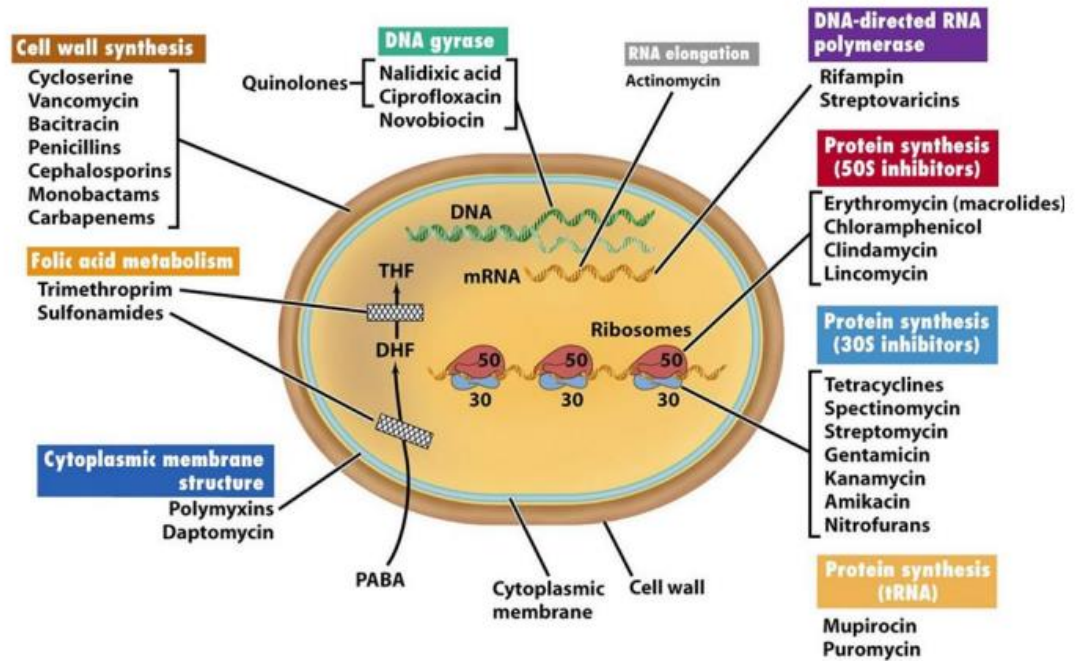
Figure 1.4 *Various antibiotics causing cell death to Gram positive and Gram negative bacteria. Three different types of cell death caused by different antibiotics against Gram positive and Gram negative bacteria[22]. Permission to use image acquired from the Wiley publishing group*

Bacterial species have also evolved mechanisms of intrinsic resistance, sometimes also called "non-susceptibility" as the trait did not evolve to combat antibiotic activity, instead it is a natural phenotype of the organism that happens to also confer resistance to specific antibiotics. For example, *Pseudomonas aeruginosa,* a Gram negative species, is intrinsically resistant to quaternary ammonium compounds, due to its outer membrane[23]. Similarly, vancomycin used to treat many Gram positive infections via targeting the peptidoglycan-containing cell wall, cannot penetrate the Gram negative outer membrane due to its size, thereby preventing access to the Gram negative cell wall[24].

1.2.1 The mechanisms of action by different antibiotics

As summarised in Figure 1.4, different antibiotics have different mechanisms of action, targeting different bacterial sites[25]. These mechanisms broadly include inhibition of cell wall synthesis, inhibition of nucleic acid synthesis or disruption of DNA and prevention of protein synthesis[26].

1.2.2 Inhibition of cell wall synthesis

Inhibition of cell wall synthesis covers multiple mechanisms of action, this includes inhibiting cell wall synthesis and causing damage to the existing cell wall, leading to lysis. For example, β-lactams and glycopeptides are antibiotics that interfere with cell wall synthesis leading to structural damage to the cell[26, 27]. B-lactams such as penicillin's, cephalosporins, carbapenems and monobactams do this by specifically targeting the penicillin binding proteins (PBP's) that are responsible for maintaining and repairing the cell wall[28]. The prevention of repairing damaged peptidoglycan strands and preventing cross linking of these strands causes cell deformation, ultimately leading to cell death usually due to osmotic stress[26]. However, some cell wall inhibitors are only effective against certain types of bacteria, for example, vancomycin effects the maturation of peptidoglycan, but can only do so in Gram positive species due to glycopeptides having generally lower membrane permeability compared to β-lactams due to their size[27]. Meanwhile, other cell wall inhibitors can pass through the outer membrane and bind to their target site, evading β-lactamase, an enzyme produced by bacteria to inhibit β-lactams (Figure 1.5)[29].
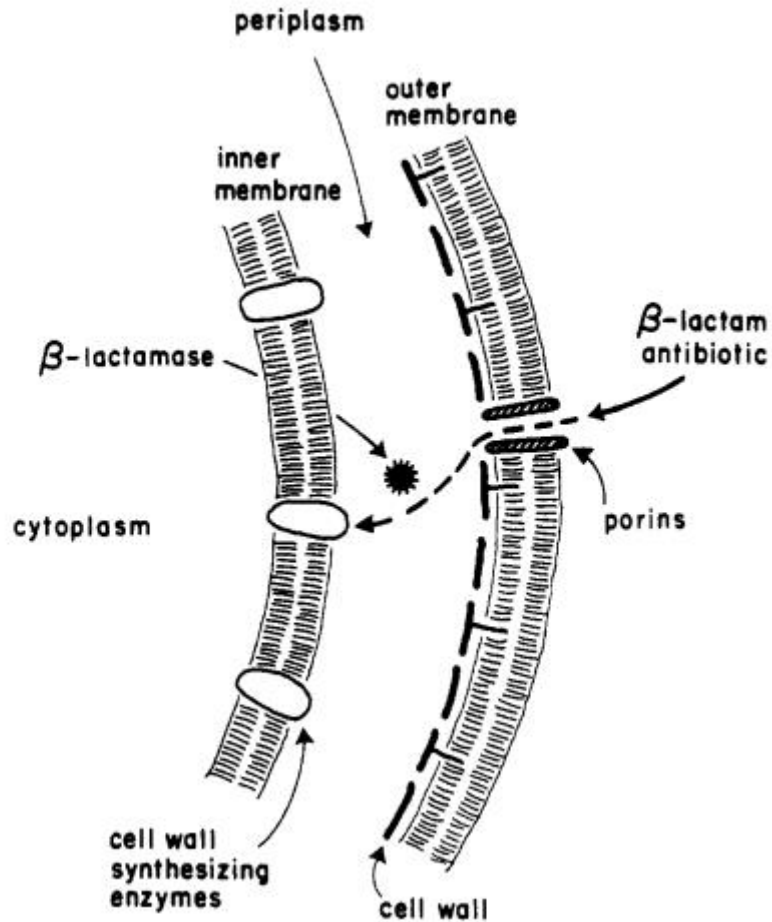
Figure 1.5 *An example of how a β-lactam class antibiotic enters a Gram negative cell membrane to target the cell wall synthesizing enzymes. The β-lactam antibiotic penetrates a Gram negative cell membrane via the porins used to transfer nutrients into the cell from the environment. The antibiotic passes into the periplasm where it can be intercepted by a β-lactamase, and become neutralised, or it can evade the β-lactamase and interact with the penicillin binding proteins, leading to cell death[29]. Permission to use image acquired from creative commons licences*

1.2.3 Inhibition of nucleic acid synthesis

Different antibiotics target different nucleic acids within bacterial cells, with some targeting DNA and others targeting RNA[30, 31]. An example of DNA targeting antibiotics are fluoroquinolones, including ciprofloxacin and levofloxacin. Fluoroquinolones are DNA targeting antibiotics that prevent bacteria from repairing damaged DNA, preventing the formation of new DNA, leading to the prevention of cell division[32]. They do this by targeting DNA gyrase, an enzyme that allows DNA to form helix coils that are cut, recombined, and wound, or relaxed, referred to as supercoiling[33]. Two different

9

types of supercoiling exist, firstly, positive supercoiling, an overwinding of the helix that puts pressure onto the DNA strands, or negative supercoiling, underwinding of the helix with considerably lower pressure[34]. By inhibiting the DNA gyrase, which preferentially causes negative supercoiling, the strain on the DNA double helix increases causing strand breakage, which is lethal to the bacterial cell[35].

1.2.4 Prevention of protein synthesis

Other antibiotics target protein synthesis[36]. Drugs such as the aminoglycosides and tetracyclines target the ribosomal RNA (rRNA) by attaching to sites on the RNA and preventing protein synthesis. Figure 1.6 highlights some of the RNA sites that are targeted by antibiotics in two different classes[37]. Once these antibiotics have bound to the RNA site, they prevent the translation of RNA, inhibiting protein synthesis within the bacterial cell[38]. This inhibition prevents the bacteria from producing key proteins, leading to structural damage of membranes and other essential structures within the bacterial cell leading to growth inhibition and cell death[38].
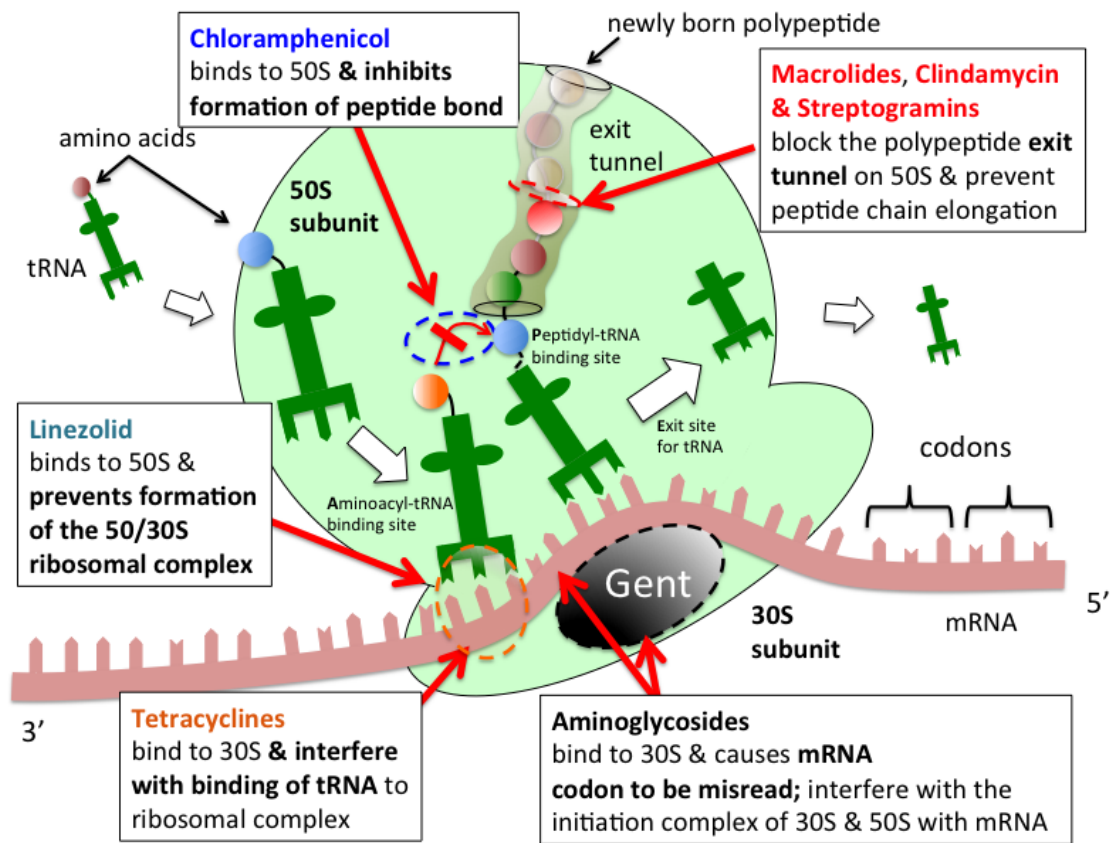
Figure 1.6 *The target sites of the antibiotics with the highlighted region being targeted by the corresponding antibiotic. Various antibiotics in the tetracycline and aminoglycoside classes targeting RNA sites highlighted in the corresponding colour[37].*

1.3 Bacteria can evolve resistance to antibiotics

Bacteria have evolved significant resistance to antibiotics, which can lead to persistent infections[39,40]. Bacteria can acquire antibiotic resistances through various mechanisms, including mutation and uptake of external genetic material[41].

1.3.1 Mutation of bacteria

During the growth of a bacterial population, bactericidal agents may encounter this population and initially prevent growth into this nutrient rich environment[42]. An example of this can be seen below (Figure 1.7), where *E. coli* grows in a rich agar medium, but is prevented from spreading into the second column of medium due to the presence of antibiotic at three-times the minimum inhibition concentration (MIC) for this strain. However, after 88 hours, random mutation allows the *E. coli* to grow in the presence of this level of antibiotic and progress into the new area, before being inhibited

by a higher concentration of antibiotic in the third column (30-times the MIC). Along the length of the agar medium the antibiotic concentration increased in a stepwise manner to 3,000-times the initial MIC of antibiotic. However, by 264 hours, the *E. coli* has evolved to be able to grow in this significantly increased concentration of antibiotic[43]. This evolution is driven by the random mutations that occur in bacteria as they grow and divide, initially starting with single cells that develop resistance to the antibiotic and spread, then rapidly increasing their resistance levels to grow on the higher concentrations of antibiotic. Eventually, this process repeats again for each increased concentration of antibiotic until the *E. coli* strain can grow in the full spectrum of antibiotic concentrations[43].
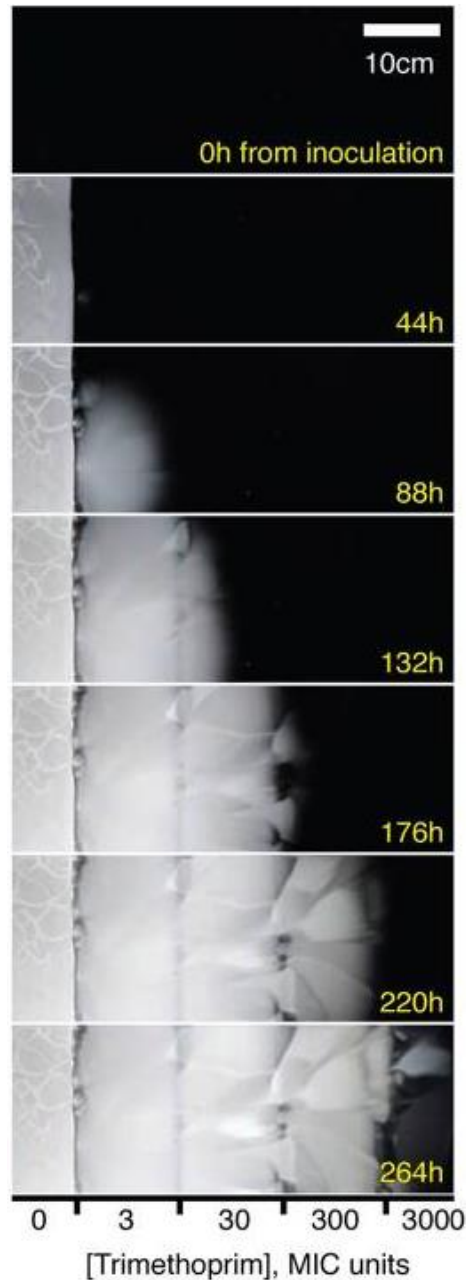
Figure 1.7 *A large agar plate with increasing concentrations of the antibiotic trimethoprim added to the agar at increasing concentrations to inhibit E. coli growth. A stepwise concentration gradient of the antibiotic trimethoprim is incorporated into the agar medium. Bacteria seeded into the medium are initially only able to grow on the agar with no antibiotic but after 88 hours, the strain is seen to have mutated and become resistant to three times the MIC concentration of the antibiotic. After 132 hours the strain has become resistant to 30-times higher concentrations of the antibiotic with resistance further increasing to 300-times at 176 hours and 3,000-times at 264 hours respectively[43]. Permission to use image acquired from the American Association for the advancement of science.*

1.3.1.1 Antimicrobial stewardship

Because of our use of antibiotics for the last 100 years, we have accelerated the rate at which bacteria have developed antibiotic resistance. There are many factors that have caused this acceleration in both developing countries and developed countries. In developing countries, it is common for antibiotics to be purchased over the counter without prescription and the vendor will be profit driven with little or no medical qualification[44]. In developed countries, over-subscription of antibiotics leads to excess tablets being disposed of inadequately and are found in water and in close proximity to waterborne pathogens, often driving antibiotic resistance, much like the *E. coli* seen in Figure 1.8[45, 46]. Antibiotics can also be found in waterways after passage through the body and into the wastewater treatment process, which does not remove these drugs from treated waters. Similarly, many antibiotics are used in agriculture to ensure that animals are healthy and can be used for human consumption[47,48]. Consequentially, more and more antibiotic resistant pathogens are evolving in animals, including to last-line antibiotics such as colistin, due to their overuse in the agricultural industries that should be avoided[49]. Indeed, use of last-line antibiotics is banned in many countries, but not in all, which continues to drive resistance. This excessive use causes traces of antibiotics to be found in animal waste, which passes into the soil and species found in soil then encounter trace amounts of the antibiotic and develop resistance also[50].

1.3.2 Horizontal gene transfer

Horizontal gene transfer (HGT) is the process where one bacterial cell transfers genetic material to another bacterial cell, this can occur between two different cells of the same species or between different species[51]. This process occurs by four main mechanisms: transformation, outer membrane vesicles, transduction, and conjugation. Below (Figure 1.8) the four main mechanisms of horizontal gene transfer are shown[52].
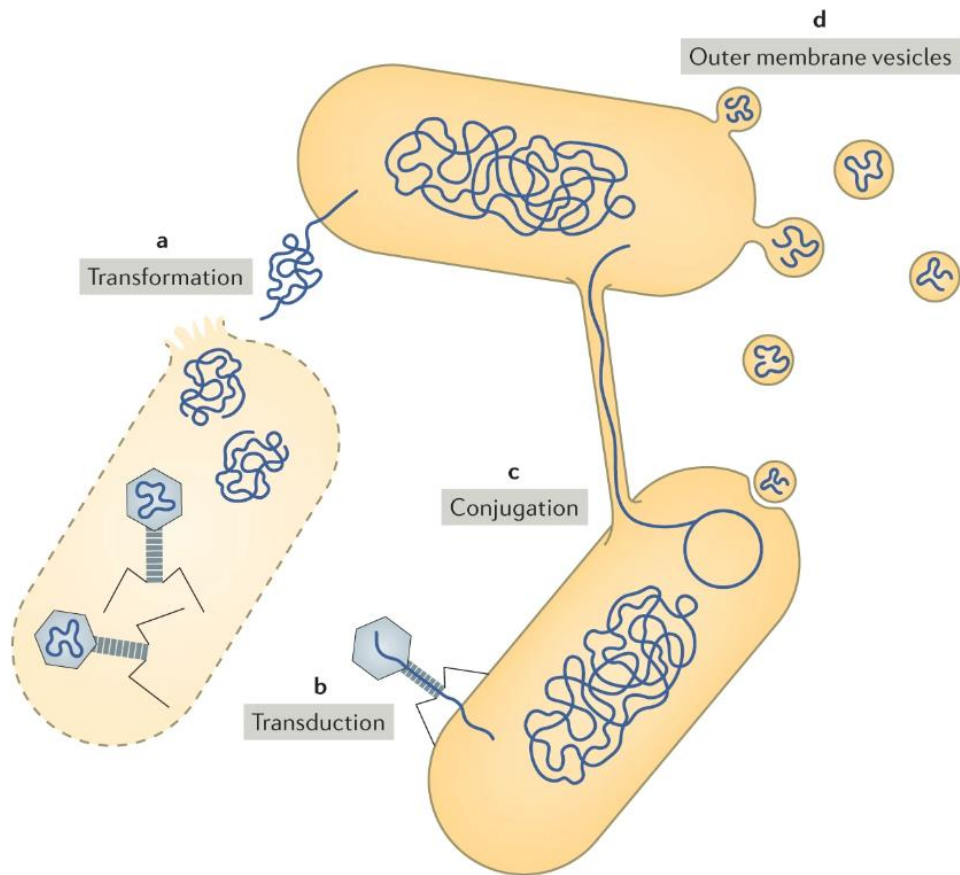
Figure 1.8 *The four methods of horizontal gene transfer between bacterial species. The main techniques in which bacteria can share genetic material between cells. A: transformation, genetic material that has left a cell and been taken up by another cell. B: outer membrane vesicles, small sacks of membrane carrying genetic material that is shared between cells. C: conjugation, physical contact made between two different cells via a pilus sharing genetic material. D: transduction, the transference of genetic material through a virus, known as a bacteriophage, during viral infection[51]. Permission to use image acquired from the Nature research publication group.*

1.3.2.1 Transformation

Transformation occurs when bacteria accept DNA from the environment around them and incorporate that into their own genetic material[53]. When bacterial cells die, they often lyse and the nucleic acid inside the cell is released into the local environment[54]. Similarly, healthy growing cells may excrete additional nucleic acid that they no longer require. Local cells can then take up this genetic material and if the recipient bacteria can integrate it into their cellular DNA through recombination, it can be expressed in the recipient cell, thus changing the phenotype of that cell. Below (Figure 1.9), the uptake

of genetic material through transformation can be seen, with the pathways of that material through successful recombination or circulation, leading to expression, or to degradation for the component parts to be used as a resource by the cell. If the host cell successfully recombines the new DNA with its own, the cell can acquire new resistances and become resistant to new antibiotics.
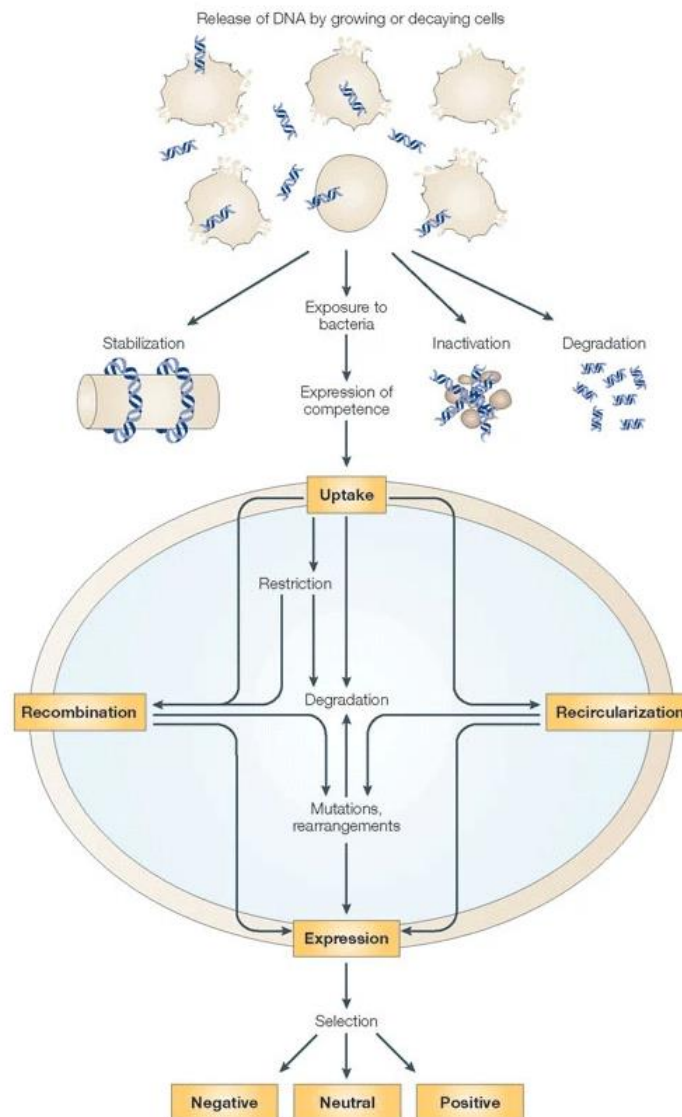
Figure 1.9 The cycle of transformation of genetic material released by a growing or dying cell into a new cell. The material expressed is released from a growing or dying cell and up taken into a new cell, in the new cell the DNA can be recombined with the current cell's DNA, degradation of the DNA can occur, or recirculation of the DNA can happen. Depending on the outcome of the DNA this can lead to the new cell expressing what is encoded to the up taken DNA.[53] Permission to use image acquired from the Nature research publication group.

1.3.2.2 Outer membrane vesicles

Outer membrane vesicles (OMVs) are small sacks grown on Gram negative bacteria during all stages of bacterial growth and are grown all over the membrane of the cell[55]. Within these sacks, genetic material is stored and once the vesicle has grown to a sufficient size, the fission of the vesicle from the cell membrane without damaging the cell membrane structure can occur[56]. The vesicle can transfer a variety of different compounds, including toxins, misfolded proteins, and antibiotic resistance genes via this mechanism[56]. Figure 1.10 shows a vesicle encountering a bacterial cell, transferring an antibiotic resistance gene that the host cell then takes up. This in turn causes the host cell to produce an antibiotic resistance protein that is transported in a new vesicle that can encounter an antibiotic and cause the antibiotic to be broken down, thereby reducing susceptibility to that antibiotic[57].
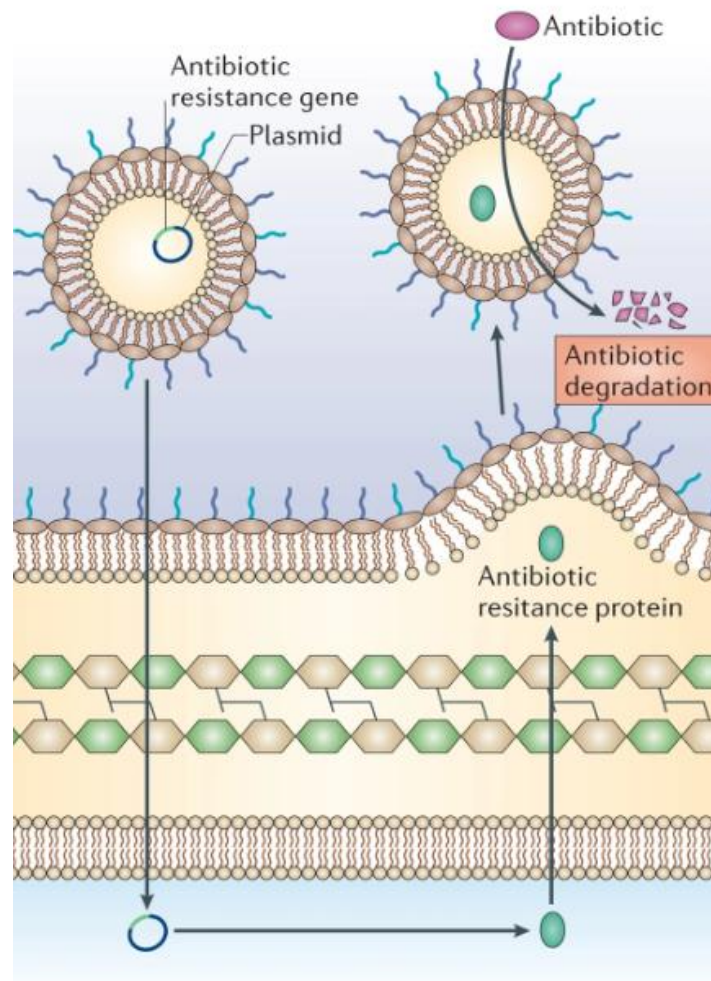
Figure 1.10 *two vesicles around a Gram negative bacterial cell, one coming into a cell and one leaving. An outer membrane vesicle transporting an antibiotic resistance gene on a plasmid encountering another bacterial cell. The cell will uptake the antibiotic gene and start producing the antibiotic resistance protein, causing further ventricles to be capable of carrying this protein and causing incoming antibiotics to be intercepted and broken down[5657]. Permission to use image acquired from the Nature research publication group.*

1.3.2.3 Conjugation

Conjugation occurs between two cells in proximity that make physical contact with each other and share genetic material[52]. Two close cells share a connection via a pilus, a needle-like appendage that is thrust into another cell through either one or both of its membranes[58]. With this connection, the cell can drive a conjugative plasmid between the host cell and the recipient cell, allowing transfer of antimicrobial resistance, or other genetic traits between the two cells. Figure 1.11 shows a pilus connecting two *E. coli* cells imaged using atomic force microscopy (AFM) as an example of conjugation[59].
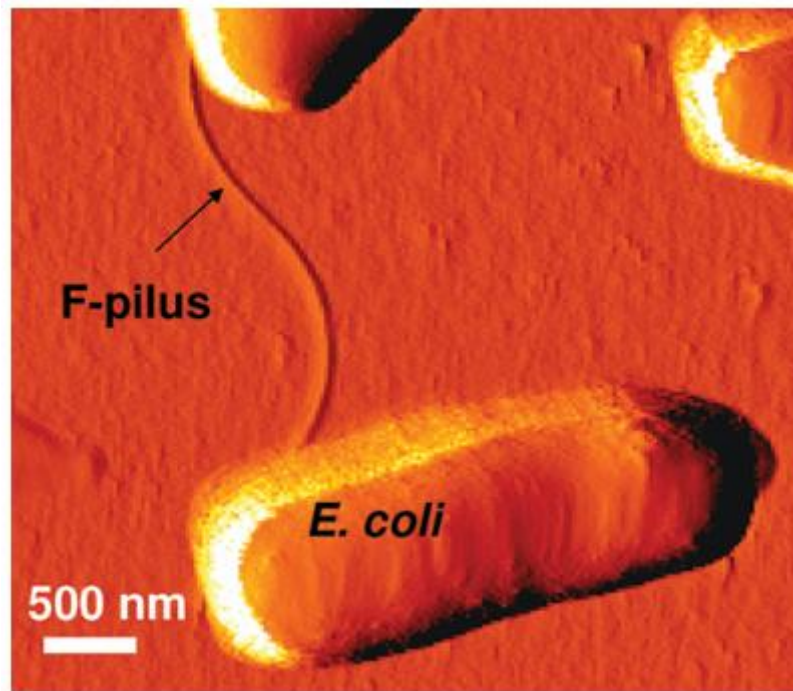
Figure 1.11 *an example of cell conjugation between two E. coli cells. The pilus of an E. coli cell can be seen extending from one cell towards another, allowing the transfer of genetic material to pass between two different cells[5959]. Permission to use the image acquired from creative commons licences.*

1.3.2.4 Transduction

The last type of gene transfer between cells comes from transduction, the transfer of genetic material through bacteriophages, [60]. These bacteriophages, or phages, are viruses that carry genetic material between bacterial cells [61]. During the growth of the phage, a small particle is formed that usually contains packaged phage DNA, however, occasionally the phage can accidentally package bacterial host DNA instead of its own, creating a transducing particle, capable of infecting other bacterial cells but no longer able to replicate. As the transducing particle infects another bacterial cell, this particle injects bacterial DNA into the infected cell, transferring the genetic material[61]. Once the genetic material is injected, the cell can then either assimilate the DNA, potentially creating a new phenotype, or use the DNA component parts as a resource during replication of its own DNA[62]. Should the receiving cell take up the genetic material, it can then be incorporated it into its own DNA and replicate it through the natural bacterial cellular replication process[62].

1.3.3 Biofilm formation

Biofilms are a community of bacteria, sometimes of one species but most frequently of multiple species, that excrete a glue-like substance, called extracellular polymeric substances (EPS). These substances consist of clusters of cells, excreted proteins, excreted lipids, humic substances, and polysaccharides[63]. Biofilm formation occurs in four distinct stages. Firstly, planktonic cells travel freely in an environment where they can encounter surfaces and subsequently attach to a surface, during this stage, the planktonic cells can be removed from the surface, this stage is known as reversible attachment. Secondly, the bacteria will begin to cluster and produce EPS and will no longer leave the surface of the material, known as irreversible attachment. The third stage of biofilm formation is where the cells cluster tightly into structures within the EPS and grow, during this time some cells will have a reduced metabolic rate and become dormant whilst others will be metabolically active. Finally, in the last stage of the biofilm's lifecycle, areas of the mature biofilm will rupture allowing planktonic cells to spread out into the environment, likely settling to create a new biofilm elsewhere, repeating the process (Figure 1.12)[25].

Figure 1.12 The lifecycle of a bacterial biofilm, starting at reversible attachment of planktonic cells to the maturation and release of new planktonic cells. The lifecycle of a bacterial biofilm starting as planktonic cells attaching to a surface, eventually becoming irreversibly attached, forming a microcolony and excreting a polysaccharide matrix. Finally, this matured colony then releases new planktonic cells to repeat the biofilm lifecycle[64]. Permission to use image acquired from the Nature research publication group.

Biofilms are extremely difficult to completely remove from a surface that they have adhered too. As a result, they cause persistent regrowth and long-term infection[65]. As part of biofilm formation, resistance to decontamination of various antimicrobials increases up to 1,000-fold compared to planktonic cells[65,66]. This increase in resistance comes from multiple different mechanisms within the biofilm. Firstly, the extracellular polysaccharide matrix acts as a physical barrier that reduces antibiotic permeability and therefore, reduces exposure to the antibiotic[67]. This prevents many antibiotics from successfully reaching bacterial cells in sufficient concentrations to cause harm. Inside the biofilm, the local environment has reduced nutrient flow causing cells to reduce their metabolism[68]. This reduced metabolism means that the bacterial cell imports and excretes nutrients and toxins at a slower rate, meaning the cell does not take in antibiotics, and when it does it has longer to neutralise them before toxic build-up occurs[69]. Additionally, due to this reduction in metabolic activity, many antibiotics become ineffective as they require metabolic activity for the mechanism of action to be effective. For example, β-lactam antibiotics require actively growing cells to disrupt cell wall synthesis [65].

1.3.5 Mechanisms of antibiotic resistance

Bacteria have a variety of ways to prevent antibiotic activity and these mechanisms vary from altering the drug target, to inactivating the antibiotic, physically removing the antibiotic from within the cell membrane and preventing the antibiotic from reaching its target[70].

1.3.5.1 Modification of the target drug

The modification of drug target sites, so antibiotics are no longer able to bind to bacteria is an important mechanism of resistance. One example of this type of resistance can be observed in the evolution of resistance to β-lactam antibiotics. This occurred by bacteria altering the structure of penicillin-binding proteins (PBP's), preventing β-lactam antibiotics from binding to them, lower resistance[71]. Penicillin-binding proteins include

peptidases, capable of cleaving peptides and allowing the peptidoglycan to cross link, which is essential for proper cell wall formation and bacterial structural integrity. Prevention of peptidoglycan cross linking leads to cell lysis and death[72]. An example of modification of the target is the evolution or acquisition of PBP2a in MRSA, which is structurally different to other PBP enzymes and, therefore, not recognised by the β-lactam antibiotics, rendering the cell resistant to methicillin and other β-lactam antibiotics [71]. Figure 1.13 shows the mechanism of β-lactam resistance in MRSA[73].
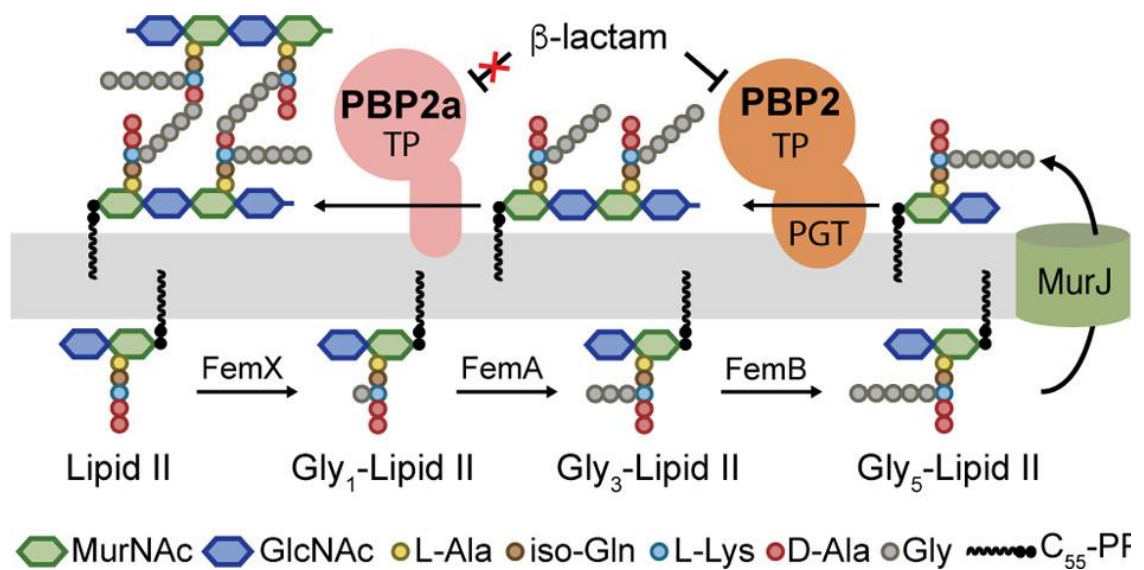
Figure 1.13 *A comparison between PBP2 and PBP2a binding to **β**-lactam. A comparison between PBP2 and PBP2a binding sites, in the case of PBP2, the antibiotic can freely bind to the site and prevent cross linking of the peptidoglycan, which will ultimately lead to cell lysis and death. Meanwhile the PBP2a site does not allow the β-lactam antibiotic to bind to it, meaning the peptidoglycan can freely cross link, repairing any damage and keeping the cells structural integrity[73]. Permission to use the image acquired from creative commons licences.*

Another technique that the bacteria can employ to prevent the binding of an antibiotic is target site modification, where bacteria can develop mutations and reduce the binding potential of the antibiotic[74].

1.3.5.2 Drug modification

Bacteria can prevent antibiotics from causing harm to the cell by modifying the antibiotic before it reaches its target site. This can be achieved via a variety of mechanisms

including, hydrolytic cleavage, acetylation, and phosphorylation, which alters the structure of the drug to prevent the antibiotic from binding its target[75].

A notorious example of drug modification is the overproduction of enzymes, causing hydrolytic cleavage of β-lactam antibiotics[76]. These antibiotics are disrupted by the expression of β-lactamase enzymes, which attach to the β-lactam ring of the drug and cause hydrolytic cleavage, inactivating the drug[77]. Figure 1.14 shows a β-lactamase enzyme cleaving a β-lactam antibiotic[78].
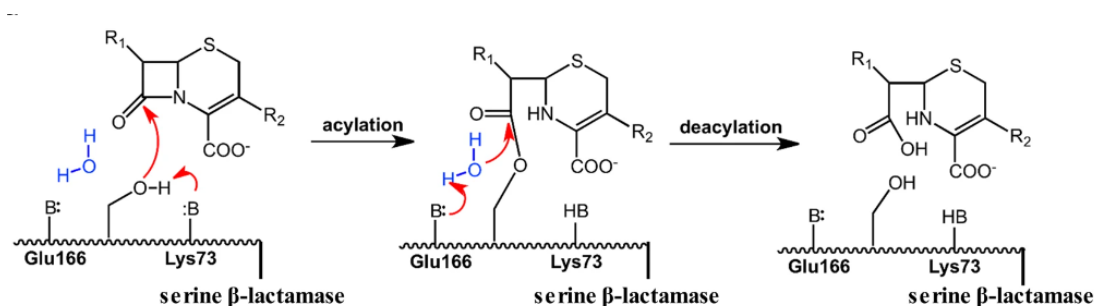
Figure 1.14 *Hydrolytic cleavage of the **β**-lactam ring by a β-lactamase enzyme. The hydrolytic cleavage of a serine β-lactamase casing acylation, the process of attaching a functional group through acyl linkages, and diacylation of the modified target drug. The enzyme produced by a bacterium facilitates this change in chemical structure, rendering the antibiotic ineffective[78]. Permission to use image acquired from the Nature research publication group.*

Macrolides are also subject to hydrolytic cleavage, by the reduction of the lactone ring caused by interaction with esterase enzymes[79]. These enzymes attach to the lactone ring and inhibit the active bonding agent on the ring, preventing attachment to protein synthesising sites[80].

1.3.5.3 Efflux systems

Another avenue of resistance can be conferred by an over expression of efflux systems, which expel toxic compounds from the bacterial cell[81]. There are five major families of efflux system present within bacteria: ATP binding cassette (ABC) family, which efflux metal ions and antimicrobial agents from the periplasm past the outer membrane,

driven by ATP hydrolysis. Resistance, nodulation, cell division (RND) family, which expel local toxic substances from the periplasm through the outer membrane of the cell using sodium or hydrogen ion antiporter systems. The small multidrug resistance (SMR) family, like the RND family, uses the ion transporter system but brings toxins through the inner membrane. Multidrug and toxic compounds efflux (MATE) transporters, like the SMR family bring toxins from the cell through the inner membrane. These efflux systems use an electrochemical gradient to transport the cations across the gradient, in the same method as the RND and SMR family. Finally, the major facilitator superfamily (MFS), brings toxins form the cell through the inner membrane into the periplasm using the antiporter system[82].

1.3.5.4 Metabolic bypass

Bacterial cells can bypass antibiotic activity via the expression of alternate metabolic pathways that achieve the same cellular function but bypass the action of the drug. For example, resistance to the sulphonamides can occur via the mechanism of metabolic bypass, whereby bacterial cells acquire via horizontal gene transfer an isozyme of the sulphonamide target; dihydropteroate synthase that performs the same metabolic function as the native enzyme but has a reduced affinity for the antibiotic causing resistance [83].

1.3.5.5 Membrane permeability

Finally, the membrane that bacterial cells possess can inhibit an antibiotics' ability to permeate through the membrane and access the drug target site[84]. Gram negative bacterial species have the additional outer membrane that prevents many antibiotics from permeating the membrane by consisting of a higher hydrophobic surface than the meshed peptidoglycan cell wall of Gram positives[84]. The specific structure that increases the outer membranes hydrophobicity is the lipopolysaccharide layer, that in addition to increasing the hydrophobicity, also prevents the passive diffusion of antibiotics and other antimicrobials[85]. Figure 1.15 shows the lipopolysaccharide layer in an *E. coli*

strain's outer membrane that contributes to the hydrophobicity and prevents diffusion of antibiotics and other antimicrobials[86].
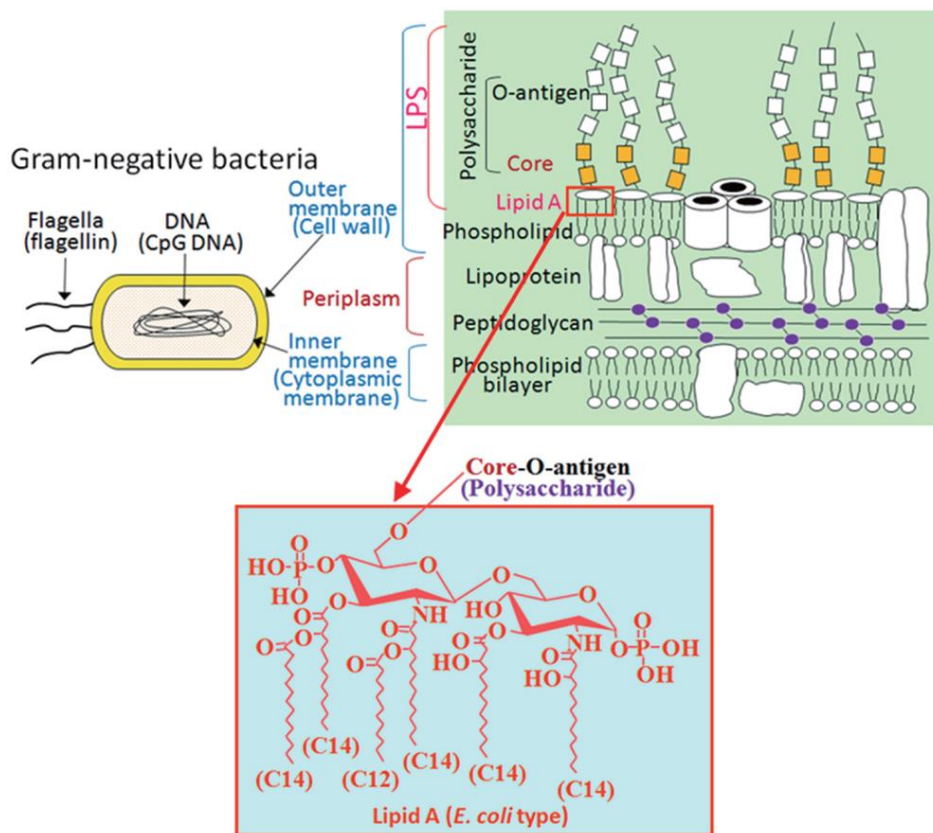
Figure 1.15 *The lipopolysaccharide layer in the outer membrane of an E. coli that contributes to antibiotic resistance. The lipopolysaccharide layer that forms part of the outer membrane, increasing the hydrophobicity of the outer membrane and preventing passive diffusion across the membrane[86]. Permission to use image acquired from the Nature research publication group.*

1.3.6 The global impact of antimicrobial resistance

The impact of antimicrobial resistance has become a global concern due to the massive impact it has on human life both directly and indirectly. In 2014 a report by Lord Jim O'Neil stated that 700,000 people die each year due to antibiotic resistant bacterial infection, this figure is set to grow to ten million per year by 2050[87]. This growth is also predicted to lead to global deficit in production of up to 100 trillion USD by 2050[87]. However, this report has been superseded by further evidence suggesting that the ten million deaths per year quoted, is a conservative estimate, with a study commissioned by the World Health Organisation (WHO) finding that the following pathogens,

Escherichia coli, Staphylococcus aureus, Klebsiella pneumoniae, Staphylococcus pneumoniae, Acinetobacter baumannii and *Pseudomonas aeruginosa* contributed to 4.95 million deaths globally in 2019[88]. Similarly, the 100 trillion USD by 2050 loss in production globally, is also underestimated, as the current predictions indicate a 3 trillion USD loss in the current American economy and not including European or Asian markets[88].

Some of these bacterial species are categorised as the ESKAPE pathogens by the WHO, a collective that includes *Enterococcus faecium, Staphylococcus aureus Klebsiella pneumoniae, Acinetobacter baumannii, Pseudomonas aeruginosa* and *Enterobacter spp.* that are deemed to pose the greatest threat to human health[89]. Whilst antibiotics are seen as the gold standard of treatment against bacterial infection including ESKAPE pathogens, the overuse and misuse of antibiotics has caused these strains to acquire antibiotic resistance, turning them into multidrug resistant (MDR) species. This has led to the ESKAPE pathogens becoming critical and high priority pathogens, requiring new research and antibiotic development[90]. Some of these pathogens are so prolific at acquiring antibiotic resistant genes that they have become extensively drug resistant and are resistant to last line antibiotics such as carbapenem and colistin[91].

1.4 Classifying the species used in this study

A selection of bacterial species were used within this project to ensure a broad range of species, both Gram positive and Gram negative, including ESKAPE species and other clinically relevant species were represented and that results obtained are relevant to a wide range of infection types. The isolates used within this thesis were either clinical or well examined species to ensure a broad diversity of test criteria.

1.4.1 *Escherichia coli*

Escherichia coli is a Gram negative species of bacteria first described in 1885 by Theodor Escherich in his lecture 'The intestinal bacteria of the neonate and infant'[92]. *E. coli* has become one of the most important species of bacteria, widely used to develop new

techniques in microbiology as well as being one of the most well studied of the pathogens[93]. *E. coli* can be found in the human gut microbiome and can be beneficial to human health, however, when an individual is immunocompromised even non-pathogenic strains can develop into an infection and can become problematic[94]. Many pathovars of *E. coli* are pathogenic and are found commonly in infections with many pathogenic strains having become multidrug resistant[95]. *E. coli* is not an ESKAPE pathogen, however it is described as a critical pathogen by the WHO, with particular focus on species that are cephalosporin-resistant[96].

E. coli 0157:H7 is a strain of *E. coli* that has been studies extensively due to its prevalence in northern America and the European continent[97]. This strain causes the host to experience symptoms such as diarrhoea and is commonly found on cattle farms[98]. This strain is also found in abattoirs and in the various minced beef products that come from these sources, transitioning to human infections[98,99,100]. This strain has acquired many drug-resistant genes, creating multidrug resistant capability[101]. Because of this strain being found in agricultural sources, excessive use of antibiotics in this industry can be attributed to this strain developing broad spectrum antibiotic resistance, including cephalosporin resistance[102].

1.4.2 *Staphylococcus aureus*

Staphylococcus aureus are Gram positive cocci that are often found on the skin and in the upper respiratory tract. *S. aureus* was first discovered in 1880 by Alexander Ogston, who described the organism as a 'bunch of grapes'[103]. In 1884, this was further differentiated by Friedrich Julius Rosenbach who described the colour of the bacteria as *aurum*, the Latin word for gold[104]. *S. aureus* is one of the most well-known bacterial species for being resistant to antibiotics, with many strains becoming *methicillin resistant* (MRSA) and being advertised as one of the main 'super bugs' of the late 20th and early 21st century[105]. MRSA refers to strains that are resistant to the β-lactam antibiotic, methicillin. More recently MRSA strains have evolved significant additional resistances, making many of them extensively drug resistant. MRSA is an ESKAPE

pathogen and is high on the WHO's list of pathogens for research, with focus on vancomycin indeterminate or resistant species[90].

S. aureus can be found on the human skin and possess a huge risk to infection due to this, particularly post operative wound infections[106]. Consequentially, *S. aureus* and MRSA strains can frequently be found in hospitals and other long term health care facilities[107]. Symptoms of an MRSA infection can include diarrhoea and vomiting, toxic shock syndrome and scalded skin syndrome, with the infection propagating through the blood stream[108]. As vancomycin is becoming increasingly less effective at treating these infections due to multiple resistance mechanisms emerging, new antibiotics such as linezolid are being used to treat MRSA strains[109].

1.4.3 *Pseudomonas aeruginosa*

Pseudomonas aeruginosa is a Gram negative, rod-shaped bacterium and is one of the most common bacterial species in healthcare associated infections. It is an opportunistic pathogen that has a high infection rate in patients with immunocompromised systems, particularly those with cystic fibrosis or cancer and can often be found causing pneumonia in those patients, as well as those using ventilators[110]. Some *P. aeruginosa* species produce a polysaccharide matrix around the cells contributing to enhanced drug resistance, in part contributing to many multidrug resistant strains[110]. This polysaccharide matrix is a biofilm that is extensively associated with *P. aeruginosa* respiratory infections, particularly in individuals with cystic fibrosis[111]. As *P. aeruginosa* is opportunistic, if is often found in nosocomial backgrounds and strains with carbapenem resistance are listed as critical on the WHO ESKAPE pathogen list[90].

1.4.4 *Klebsiella pneumoniae*

Klebsiella pneumoniae is a Gram negative rod-shaped bacterium that is non-motile and facultative anaerobic species. Discovered in 1882 by Carl Friedlander after isolation from the lungs of patients who had died with cases of pneumonia[112]. The species belongs to the larger *Enterobacteriaceae* family which includes *E. coli* and *Salmonella enterica*. *K.*

pneumoniae infections are often associated with pneumonia and have become one of the leading causes of respiratory infections in China since 2017[113]. Like *P. aeruginosa*, *K. pneumoniae* is a prolific biofilm former and is also frequently found in respiratory related cases but can also be found in urinary tract infections[114].

K. pneumoniae is part of the ESKAPE pathogen list under the carbapenem resistant, extended spectrum β-lactamase producing *Enterobacteriaceae*[90]. Furthermore, *K. pneumoniae* is an avid biofilm former and studies have found that multi drug resistance and extensively drug resistant species are typically biofilm formers compared to species susceptible to antibiotics[115].

1.4.5 *Salmonella enterica*

Salmonella enterica is a Gram negative rod-shaped bacterium with flagella that is often the cause of many food poisoning cases with many countries combatting cases of salmonellosis[116]. First identified by Theobald Smith in 1855, the species has expanded to be a wider collection of subspecies with the subspecies *S. enterica subsp. enterica* denoting the general subspecies and the serovar, or distinct variation of the subspecies, denoted after, with examples including Enteritidis and Typhimurium. Accounting for 99% of cases of *Salmonella* infections in humans and warm-blooded animals[117]. Prevention of infection by this species often includes practicing good hygiene and food safety, through thorough handwashing, avoiding cross contamination and ensuring proper cooking temperatures are met.

S. enterica is not part of the WHO's critical pathogen list, but it still has high prevalence for human infection due to its association in the poultry industry[118]. Because of the high incidence rate, and the environment in which these strains can be acquired, pre-emptive screening of the species is regularly performed in the agricultural industry, with particular concern as multidrug resistant strains are emerging within health care systems globally[119]. This species is also capable of producing biofilms, however, while it appears to be less prolific than other species, the biofilm production itself still contributes significantly to the resistance profile of the strains that can form biofilm. The severity of the species can vary between strains, however, children, the elderly and

those with compromised immune systems can suffer severe symptoms such as gastroenteritis[119].

1.4.6 *Staphylococcus epidermidis*

Staphylococcus epidermidis is Gram positive coccus that is facultatively anaerobic and like *S. aureus* is found on the skin. Originally called *Staphylococcus albus* by Friedrich Rosenbach for its white colour, *albus* being the Latin word for white, to differentiate it from *S. aureus*[103]. Later it was renamed as *S. epidermidis* due to its prevalence on the human skin. Typically, infections that occur due to *S. epidermidis* are from invasive treatments such as catheterisation or insertion of pulmonary devices[120]. *S. epidermidis* is not considered a pathogenic species and is seen as a commensal species, it can cause infection in the right conditions, due to its prevalence on the human skin[121].

Like *S. enterica*, *S. epidermidis* is not a part of the WHO's critical pathogen list[90]. However, the prevalence of *S. epidermidis* in medical device infections and urinary tract infections is a growing trend, in an environment with immunocompromised patients[122, 123]. This species can also grow substantial biofilms, which contribute significantly to the antimicrobial resistance profile of the *S. epidermidis* pathogen.

1.4.7 The emergence of the *Acinetobacter* genus

The genus *Acinetobacter* defines species that are Gram negative, semi rod shaped species that include *Acinetobacter pittii* and *Acinetobacter baumannii.* It is a significant genus due to its prevalence and pathogenicity compared to other genera and is difficult to differentiate between different species within the genus[124]. Figure 1.16 is taken from a study in 2012 of the *Acinetobacter* genus based upon the average nucleotide difference from 16S rRNA sequencing, and shows the close nature of the different species within the *Acinetobacter* complex before the recent additions of *A. seifertii* and *A. dijkshoorniae*[125]
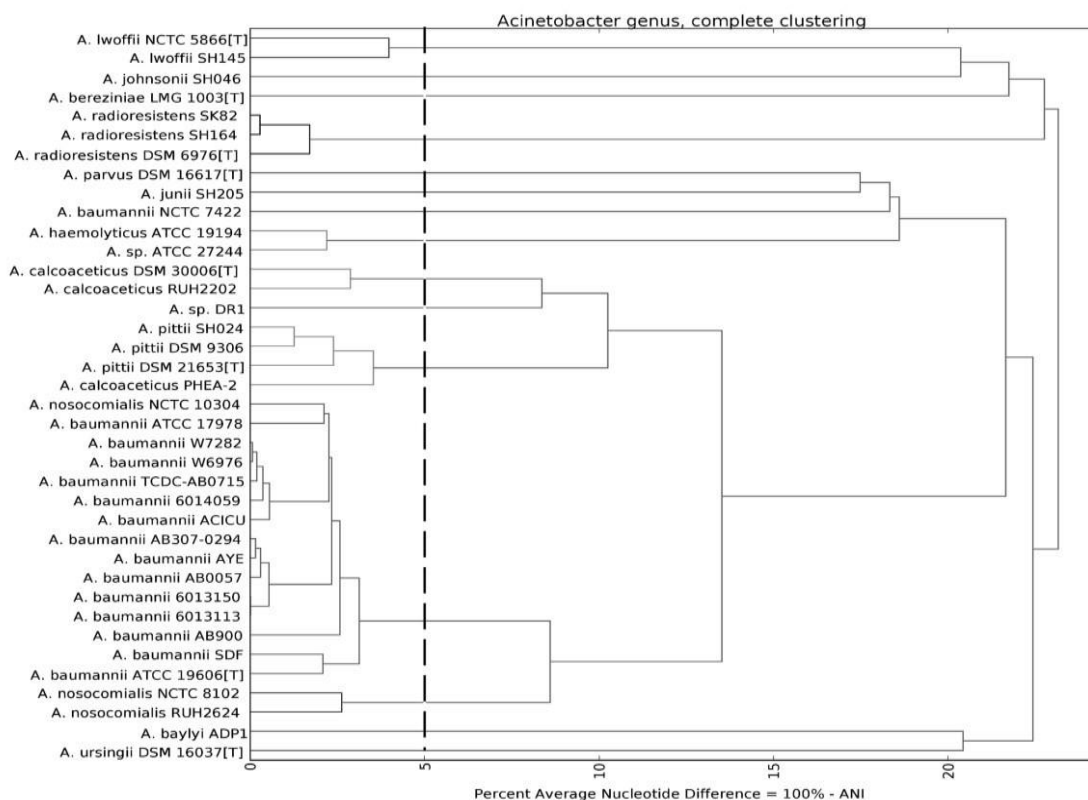
Figure 1.16 *16S rRNA sequencing performed in a study on 38 different strains belonging to the Acinetobacter genus. The Average Nucleotide Identity difference between species, the dashed line represents a five percent difference between two species, with any splitting branches on the left of the dotted line representing a different strain or species[125]. Permission to use image acquired from the Nature research publication group.*

Within this genus, the two species investigated in this work, are *Acinetobacter baumannii* and *Acinetobacter pittii;* one species that is part of the WHO's critical pathogen list, and *A. pittii*, which is often mistaken for *A. baumannii* due to them sharing very similar biochemical and phenotypic properties[126].

1.4.8 *Acinetobacter baumannii*

Acinetobacter baumannii is a Gram negative aerobic nonmotile non-fastidious and non-fermenting bacterial species with a complex history of identification. In 1911, Willem Beijerinck isolated an organism called *Micrococcus calco-aceticus* from soil in a calcium acetate containing medium. Over the course of the following decades at least 15 other species from different genera were described which included, *Diplococcus mucosus,*

alcaligenes haemolysans, Mima polymorpha, Moraxella iwoffi, Herellea vaginicola, Bacterium anitartum, Moraxella iwoffi var *glucidolytica, Neisseria winogradskyi, Achromobacter anitratus and Achromobactin mucosus.* In 1954 the genus designation *Acinetobacter* was proposed by Brisou and Prevot to separate the nonmotile species from the motile species of the *Achromobacter* genus[127]. It was not until 1968, however, that this designation became widely accepted when Baumann published a comprehensive survey where all the described species belonged to the same genus[127]. In 1971, the subcommittee of the taxonomy of *Moraxella* and allied bacteria officially acknowledged the *Acinetobacter* genus. In 1974 *Acinetobacter anitratum* was placed into the *Acinetobacter* genus[128]. In 1986 Bouvet and Grimont used DNA hybridization to identify 12 genospecies of *Acinetobacter,* before this only *A. anitratum* and *A. lwoffii* had been identified as belonging to the same genus however these had been placed in the *Achromobactereae* genus[129]. Alongside *A. baumannii* three other species, *A. pittii, A. calcoeticus* and *A. nosocomialis* make up the *Acinetobacter baumannii-calcoeticus* (ABC) complex, but recently two additional species, *A. seifertii* and *A. dijkshoorniae* have recently been added taking the complex to six species in total[130]. This complex of species is difficult to differentiate at the species level as the different species display similar phenotypic and biochemical properties[130].

It is described by the Infectious Diseases Society of America as one of the six most important multidrug resistant (MDR) microorganisms in hospitals worldwide[131]. *A. baumannii* is an ESKAPE pathogen, one of six pathogens that have evolved multidrug resistance and are at forefront of a major crisis to human health[26,132]. *A. baumannii* is an opportunistic pathogen and infections typically occur in patients in intensive care units (ICU) and surgical wards. It is highly adaptive, with some strains having persisted for up to five months on inanimate surfaces, it is well known for its ability to adapt to environmental conditions, being able to resist dry conditions, a range of pH's both acidic and alkaline and temperature ranges between 20 to 44 °C, making it excellent at surviving in human hosts[133,128] The multidrug capabilities (MDR) of *A. baumannii* as well as its prevalence to remain in hospital environments, cause this species to be a concern, particularly its resistance to carbapenems, which has also caused it to be categorised by

the WHO into a critical group of priority pathogens for research and new antibiotic development.

Typically, multidrug resistant bacteria are defined as strains resistant to one antibiotic in at least three categories and extensively drug resistant bacteria are defined as strains resistant to at least one antibiotic agent in all classes except two categories of antibiotics[134]. *A. baumannii* is particularly resistant to antibiotics and when referring to *A. baumannii* multidrug resistant (MDR) species are resistant to carbapenems and resistant to three or more classes of antibiotics[135]. This definition is slightly different to the one proposed by Magiorakos *et al.* as it includes carbapenems explicitly, but this work will progress with the Magiorakos definition as all species and strains should adhere to the same criteria to be called MDR[134]. With *A. baumannii* becoming increasingly prevalent in clinical settings as well as in agricultural settings, the species and strains are being studied extensively. With studies showing that up to 70% of *A. baumannii* isolates collected in clinical settings were MDR which included resistances to carbapenems with some strains also acquiring resistance to the last line antibiotic, colistin[126,135].

Found naturally in soil and standing water, *A. baumannii* is often called "iraqibacter" due to its emergence in US and British soldiers returning from the war in Iraq[126]. Over the last 30 years, *A. baumannii* has emerged as one of the most clinically significant pathogens due to its ability to upregulate resistance determinants, increasing the rate at which antibiotics become ineffective against strains of this species. The overuse of antibiotics, both in humans and the agricultural industry has caused some *A. baumannii* strains to become resistant to all known antibiotics available, highlighting the need for decisive action within the health care community as well as the food production industry[136].

1.4.9 *Acinetobacter pittii*

Acinetobacter pittii is a Gram negative species that is part of the *calcoaceticus-baumannii* complex. The species is less prevalent than *A. baumannii* but due to the difficulty in identification, misidentification is likely caused by geographical location and

the availability of technology[137]. This species, like *A. baumannii,* is prevalent in health care-associated environments but has also been found in environments such as the International Space Station (ISS), showing a similar level of adaptability and survivability to that of *A. baumannii*[138]. *A. pittii* also shows multidrug resistance, expressing the same genes as *A. baumannii* and the subsequent enzymes and proteins that confer resistance to whole drug classes such as carbapenems[139].

Acinetobacter pittii, similarly to *Acinetobacter baumannii*, is a prolific biofilm former and can survive on surfaces for up to six weeks whilst remaining viable[140]. This also contributes to its drug resistance capabilities.

1.5 Metal-based antimicrobials and metal resistance

Considering the extensive evolution of antibiotic resistance in bacteria, alternative therapeutics are required to treat these drug resistant infections. Metal antimicrobials have been used for millennia, in both conventional medical applications, the Ancient Greeks using silver to treat headaches and wounds, and in consumable sterilisation, the ancient Egyptians using copper to sterilize drinking water[141]. Early examples of the modern use of metals predate the discovery of penicillin as silver was used by doctors to treat burns, ulceration, wounds, and infections in the 1800's[141]. The mechanisms behind the antimicrobial activity of silver were unknown at this time, but it was described as having oligodynamic action, referring to the toxic effect metal ions have on microorganisms[142].

The use of metals as antimicrobials has developed since, in the 19th century, arsenic was used to treat acne, pellagra and malaria[143]. Arsenic was used as the mainstay treatment for syphilis until the discovery of penicillin[143]. Gold cyanide was used to treat tuberculosis in the late 19th and early 20th century and was championed by Robert Koch, a German bacteriologist who discovered the bacteriostatic properties of gold cyanide against *tubercle bacillus* [143][144].All these previous applications of metal antimicrobials were used as ingestible, injectable, or topical therapies.

Metal antimicrobials are not only found as compounds within medicine. Surface applications of metals are receiving more attention due to the need to offer a stable

permanent performance for a variety of applications[144]. Crucially, metallic surfaces that exhibit antimicrobial properties allow for the prevention of biofilm formation by causing cell death to the initial planktonic cells that attempt to adhere to the surface. In 2008, a hospital trial was undertaken to understand the effect of replacing contact surfaces with a copper alloy surface. The results found that there was a significant reduction in viable cells recovered from the copper alloy door handles compared to the viable cells recovered from the control surface[145].

Due to the increasing amount of multidrug resistant strains and species, studies have been conducted to discover which of the heavy metals are susceptible to antimicrobial resistance[146]. This study also investigates the extent to which metal compounds are active and non-toxic, offering 246 active compounds against tested organisms[146]. The findings indicate that more work needs to be undertaken into the discovery and development of these metallic antimicrobial compounds as there are new novel candidates that may have pharmaceutical or biomaterial application.

1.5.1 Metal based antimicrobials

Various metals can be used as an antimicrobial and have had their properties approved by the Food Drug Authority, including gold, silver, and copper[147]. These metal-based antimicrobials are entering clinical trials, with some having already passed clinical trial and being used for other medical applications such as cancer treatment[147]. These studies show that a variety of metals have therapeutic applications when investigated in various states such as salts and nanoparticles, and that these metals need to be investigated thoroughly as their own class of antimicrobials[148].

1.5.1.1 Silver as an antimicrobial

Silver is a soft, white lustrous metal with excellent conductive properties and has a face centred cubic crystal structure. It has a melting point of 1,234 Kelvin and is non-toxic, however, silver salts are poisonous. Silver has been used as an antimicrobial since the ancient Greeks and while the mechanisms for silvers antimicrobial activity was unknown

then, they are better understood now[149]. Currently, according to the FDA, only certain silver compounds are antimicrobial and unless supported by scientific research and approval, products are unable to claim biocidal capabilities[150]. Silver is only biologically active when it is in its ionic state (Ag^+) in an aqueous environment[146]. Silver acts on microbes in three ways, firstly silver cations can penetrate and puncture cell walls. Secondly, the silver ions can enter the bacterial cell, inhibit cellular respiration, and disrupt cellular metabolic processes. Finally, silver can disrupt the replication cycle of the cell[151].

Silver is the most well understood antimicrobial metal and was once the most important antimicrobial compound before the discovery of antibiotics[152]. This has meant that silver is actively investigated in many studies, in many different forms ranging from nanoparticles to silver salts and other complexes[153]. Due to the level of investigation, there are a wide range of silver-based antimicrobials, but because of this, there has also been an over subscription of these antimicrobials and consequentially, reports are emerging of silver resistant species of bacteria[154].

1.5.1.2 Copper as an antimicrobial

Copper is a soft ductile material with excellent thermal and electrical conductivity. It has an orange-red colour with a melting point of 1,357 Kelvin. Copper is essential for life as it improves energy production via blood oxygen transport. It is a highly abundant heavy metal that can be purposely alloyed with other metals, such as tin or zinc to create bronze or brass respectively[155]. In 2008, the United States Environmental Protection Agency (EPA) recognized copper and copper alloys as antimicrobial metals and allowed its use as an antimicrobial under specific conditions[156]. A study in Southampton showed that the viability of MRSA on a copper coating showed almost complete eradication after 75 minutes, confirming the EPA's understanding of copper surfaces bactericidal properties[156]. There are multiple reports of copper resistance in different species of bacteria, highlighting the natural development of antimicrobial sources in bacteria[157,158].

The use of copper as an antimicrobial has led to a lot of research into its mechanisms of action and, as such, are also understood[159]. There are three main mechanisms that cause

cell death, and these require the copper ion to cause damage. Firstly, as copper ions accumulate in the cell membrane, they cause cell membrane integrity to degrade, leading to cell lysis[160]. Secondly, ionic copper atoms can penetrate the cell membrane and bind to both DNA and RNA causing structural deformation of these nucleic acids, leading to the production of oxygenated free radicals within the cell, leading to the production of carcinogens at concentrations that only effect bacteria, inducing cell mutation, and other toxic compounds that will ultimately kill the cell[160, 161]. Finally, ionic copper can inhibit protein functions and prevent important protein functions taking place, causing cell degradation and ultimately cell lysis[162, 160].

1.5.2 Copper oxide as an antimicrobial

Copper oxide predominantly comes in two forms, copper (I) oxide (CuO) or cupric oxide, and copper (II) oxide (Cu_2O) sometimes known as cuprous oxide. These oxides can form at room temperature but can also be created under high temperatures, pressures and humidity[163]. Copper oxides also exhibit an antimicrobial effect and are shown to have a bactericidal effect against different strains of bacteria[164]. Both copper oxide species exhibit antimicrobial properties and this is caused by the same bactericidal processes as copper (Cu). These processes include the production of Reactive oxygen species (ROS) or by binding to cell membranes, leading to cell wall damage[165].

1.5.3 Metal antibiotic mechanisms of action

The three main mechanisms of metal antimicrobial action are the inhibition of proteins, cell membrane damage and causing the creation of reactive oxygen species within the cell[160]. Each mechanism inhibits cellular activity or cell function in a variety of different ways, with certain mechanisms of action having a greater impact on causing cell death, depending on the metal used[166]. There are five ways to interfere with cellular processes, these processes include protein dysfunction through various means, the production of reactive oxygen species (ROS) impairing membrane functionality, interfering with nutrient uptake and finally genotoxicity[166]. These mechanisms can involve the creation of these ROS or can use the metal itself to interfere with the cellular processes which

can be seen below (Figure 1.17) where the five main processes of interference are described[166].
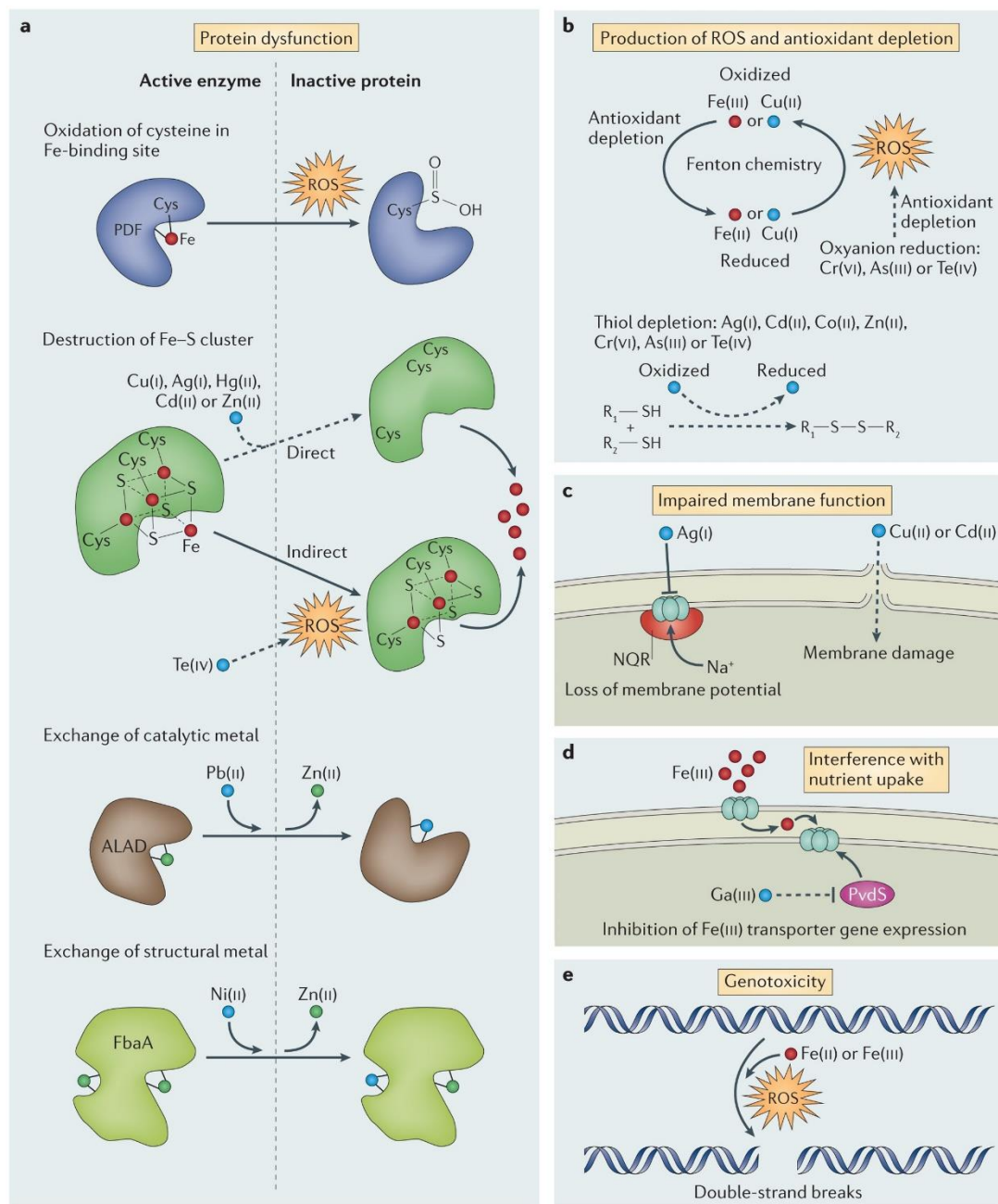
Figure 1.17 *The five different techniques metal interferes with cellular processes within bacterial cells. a. Different methods of protein dysfunction caused by different metals and possible reactive oxygen species. b. The explicit production of reactive oxygen species causing antioxidant depletion. c. Impaired membrane function caused by copper, silver, and cadmium. d. Iron interfering with nutrient uptake and Iron transporter expression. e. genotoxicity caused by radical oxygen species causing DNA strand breakages[166]. Permission to use image acquired from the Nature research publication group.*

1.5.3.1 Cell membrane damage caused by copper and copper oxides

Copper is essential for life as it helps in the function of proteins within living organisms, including bacteria, however, it is an active redox metal and so is heavily regulated within cellular activity[167]. Copper and copper oxides are taken in from the external environment and transferred to the periplasm via porins, upon excessive copper intake, regulation is performed by efflux systems that can detect the excessive intake of copper from the external environment and eject them from within the bacterial cell. Below (Figure 1.18), the copper intake through either a porin, or absorbed by proteins PcoB and OmpB, used for various functions within the cell, and excessive copper is exported out of the cell via the CusA-C efflux system[168]. The accumulation of copper within the periplasm causes a loss of cell membrane integrity by adhering to amino acids essential for producing proteins that are crucial to the membrane[169].
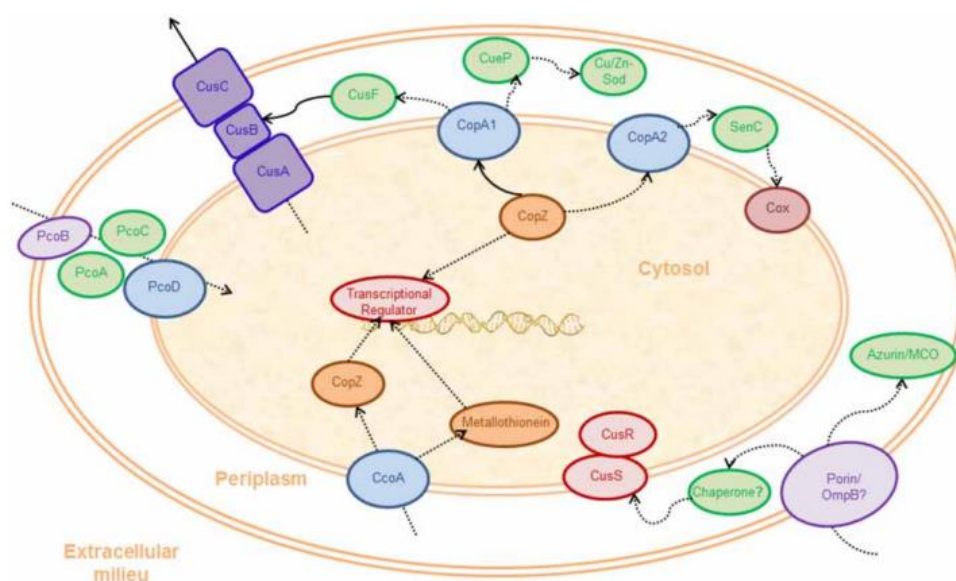
Figure 1.18 *The homeostatic process in which copper is absorbed or removed by a cell. Copper intake can be seen through a porin, or absorbed by proteins PcoB and OmpB, used for various functions within the cell, whilst excessive copper is exported out of the cell via the CusA-C efflux system[168]. Permission to use the image acquired from creative commons licences*

1.5.3.2 Protein dysfunction

Metal antimicrobial ions are readily attachable to amino acids within the bacterial cell, catalysing them and preventing the formation of new proteins[169]. This occurs due to metal oxides having a high affinity to amino acid side chains, the atoms connected to the primary carbon of the molecule[170]. This leads to a loss of activity in the enzymes caused by the metal ions, or an increase in detoxification enzyme production, caused by an increased number of reactive oxygen species[171]. The proteins that metal oxides bind to require specific metal ions to function properly and fold correctly, but this process is interrupted by metal ions such as copper and silver that will displace the required metal[172]. Above (Figure 1.17) shows how both metal ions, and reactive oxygen species interact with enzymes and proteins to deactivate them[166].

1.5.3.3 Genotoxicity caused by reactive oxygen species

As reactive oxygen species enter the intracellular environment antioxidant enzymes are produced to modulate the total concentration of ROS and prevent them from reaching lethal levels[173]. As these enzymes require time to produce and require certain excesses of nutrients, a progressively increasing level in ROS can lead to extreme effects on the bacterial cell, such as causing damage directly to the DNA of the bacterial cell[173]. The damage is caused by the ROS inducing single strand and double strand breakage and leading to a rapid increase in mutagenesis, which can lead to destructive mutations and cell death[174, 175] (Figure 1.19).
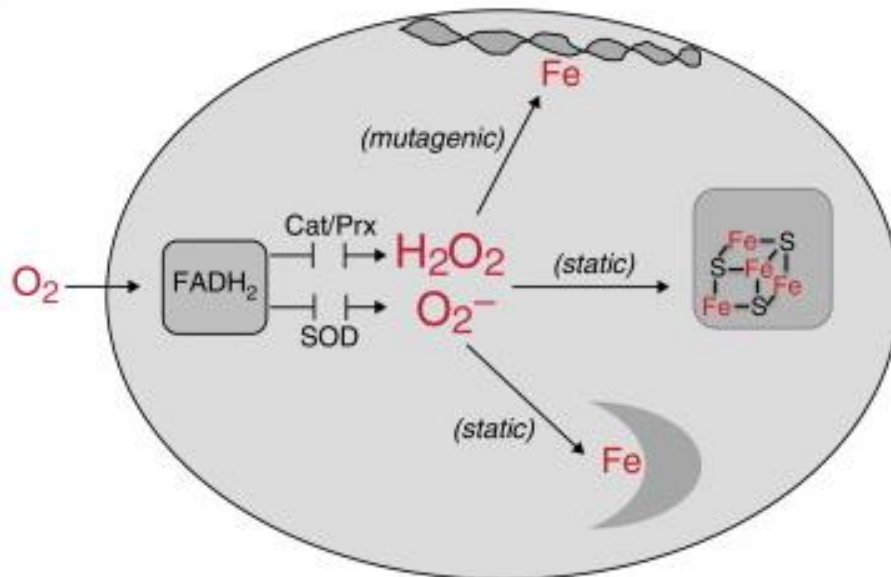
Figure 1.19 *the production of reactive oxygen species within a cell, that can lead to mutagenic responses. The bacterial cell responds to reactive oxygen species within a bacterial cell. The response can lead to DNA bond damage, leading to mutagenesis of the DNA, whilst the other responses are bacteriostatic, the removal of the ROS into enzymes or the use of ROS to produce other beneficial enzymes[173, 175]. Permission to use the image acquired from creative commons licences*

1.5.3.4 Interference with nutrient uptake

Within the cell, responses to depleted metabolite pools cause the cell to actively uptake metabolites that are depleted to perform the functions required[3]. However, in the process of taking up new metabolites, metal antimicrobials can interfere with this process by inducing a metabolic sparing response, preventing the signalling for cells to take up that metabolite, which then can lead to cellular depletion of a nutrient crucial to cell homeostasis[176]. An example of this is chromium preventing the uptake of sulphur in yeast by inducing sulphur sparing responses and due to a lack of production of enzymes that require sulphur, leads to cell death[176]. Similarly, gallium can be used as an antimicrobial as it mimics the effect of iron, which bacteria cannot differentiate between[177]. Iron is critical for bacteria as it facilitates many metabolic, reproductive and growth processes, so by absorbing gallium through the same pathways instead of iron, cell death becomes inevitable[177].

1.5.4 Metal antimicrobial resistance

Metals are being used in novel applications of antimicrobial treatments, due to increasing resistance of pathogens to antibiotics[149]. A wide variety of metals are currently being utilised as antimicrobials and the mechanism for their antimicrobial properties varies between these metals. For example, silver contact can cause membrane damage, which can then lead to fragmentation of the cell prematurely and hence lead to cell death[178]. Copper behaves differently and can penetrate the bacterial cell membrane, damaging enzymes and leading to cell death[179]. The different mechanisms for cell death are also dependent on the category of bacteria, differentiating between Gram negative and Gram positive species as the negatively charged lipopolysaccharide molecules of the Gram negative outer membrane decreases free ion penetration, causing intracellular damage[179]. Application of these antimicrobials can be limited due to the high toxicity some metals exhibit on cellular structures and are therefore not used[180]. Nanoparticles, for example, have a larger specific surface area compared to macromolecules of the same element, increasing the reactivity of the particle and culminating in greater cell death[180].

Firstly, Gram negative species have a greater intrinsic resistance to metal antimicrobials due to their additional cell membrane, this reduces the permeability of the metal into the cell[181]. Gram positive cell envelopes only possess an inner membrane with an outer peptidoglycan cell wall, which is dense enough to prevent the diffusion of small molecules[182]. Within this cell envelope, there are additional efflux systems produced by bacteria to further reduce the ability of copper to accumulate within the cell[183]. Many of these efflux systems also cause resistance to classical antibiotics in a process called co-selection[183]. One such efflux system, the TetA(L) system, confers resistance to both tetracycline antibiotics and cobalt[183]. These efflux systems function in the same manner described in 1.3.5.3, however as some heavy metals such as copper and iron are essential to cellular function, they only pump out excess levels of metals[184]. One of the most well-known examples of an efflux pump being used to remove heavy metals is the Cus system, which removes additional copper and silver that is not required in normal cellular function[182].

Like antibiotic resistance mechanisms, bacteria can target metals by producing proteins that actively bind to metals preventing them from interacting with their target sites[185]. These secretions can bind to a full metal ion, preventing any interaction of the ion with crucial metabolic functions and they are also capable of detoxification of the ion by binding the ionic metal to a protein[186]. These secretions are controlled by sensory systems that selectively close and open the release of metal-acquiring enzymes or by closing and producing the required structures for the bacterial cell[187]. Figure 1.20 shows the metal-sensing regulators processing the response of the bacterial cell, signalling the acquisition of metal ions before closing again to process the acquired ions. Figure 1.20 shows the various sensing regulators that aid in the production of important enzymes and proteins within the cell that require metal ions from external sources[187].
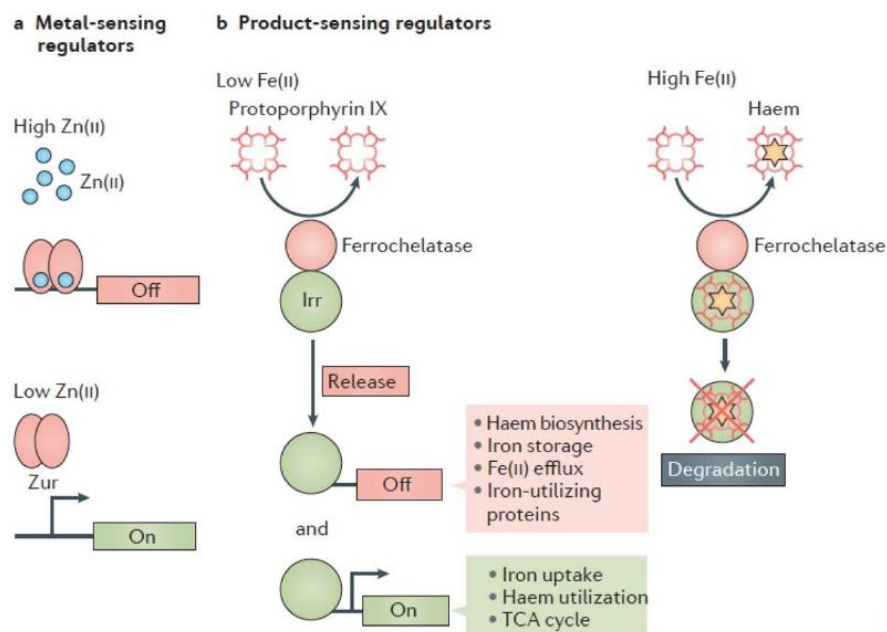
Figure 1.20 Metal sensing regulators that signal the acquisition of metals, until sufficient quantities have been acquired to produce various products the bacterial cell requires. a. Metal sensing regulators that facilitate the acquisition or rejection of metals based upon the bacterial cells need. b. Product sensing regulators that turn the metal storage in a cell on or off, facilitating the production of required products within the cell [187]. Permission to use the image acquired from creative commons licences

Finally, biofilm formation is an important mechanism for the prevention of antimicrobial metal activity, to prevent the antimicrobial metals from interacting with the cells in the first instance[188]. As described previously in 1.3.3, a biofilm is the formation of an

extracellular polysaccharide matrix consisting of proteins bacterial cells and lipids, forming a physical barrier preventing interaction with cells[189, 190, 115]. As part of biofilm formation, cells become metabolically inactive, further reducing the effect of any metal antibiotic[191].

1.6 Development of metal nanoparticle technologies

Nanotechnology is defined as the understanding and control of matter between 1 nm and 100 nm where unique phenomena enable novel applications[192]. Nanotechnology was proposed by Richard Feynman in 1959, during a lecture titled, "There's plenty of room at the bottom", where he desried the concept of manipulating matter at the atomic level[193]. Between 1959 and 2000 research into nanotechnology developed from being a theory of possibility to having application in the medical, agricultural, processing and manufacturing industries[194].

Nanoparticles have been used since the turn of the century for medical application, with particular focus on their application in magnetic therapies, due to their high magnetic susceptibility and drug delivery therapies[195]. These technologies explore some of the medical applications of nanoparticles, but it was not until the late 2000's that nanoparticles were being used explicitly as antimicrobials[196]. Nanoparticles offer excellent applications in the fight to prevent microbial infection. As the name implies, nanoparticles are on the nanoscale and have a size of 10^{-9} m. Particles of this size have fewer atoms that are unexposed to outside materials, and this means that there is a greater area for exposure. This can be proven by calculating the surface to volume ratio which is calculated by the following equations:

$$Area\ of\ sphere = 4\pi r^2 \tag{1}$$

$$Volume\ of\ sphere = \frac{4}{3}\pi r^3 \tag{2}$$

$$\frac{Area}{volume} = \frac{4\pi r^2}{\frac{4}{3}\pi r^3} = \frac{3}{r} \tag{3}$$

As the measurement of a nanoparticle is determined by its diameter, a 20 nm sized particle offers a surface to volume ratio of 1.5×10^{10}. Comparing to a 100 nm sized particle, which has a surface to volume ratio of 3×10^8, therefore, smaller-sized nanoparticles offer incredible potential contact surface.

1.6.1 Nanoparticle synthesis

Nanoparticles can be synthesized in a variety of different techniques with varied benefits, including scale-up costs, size distribution and yield of the nanoparticles. These methods include chemical precipitation, electrochemical synthesis, microemulsion methods, template assisted synthesis and vapor phase deposition and are sometimes referred to as top-down, nanoparticles made from larger sized material, or bottom up, synthesis starting as single atoms or molecules, synthesis[197,198].

Chemical precipitation is the most common type of nanoparticle formation due to its simplicity and straight forward method. The method typically consists of mixing an inorganic salt precursor and a chemical base, allowing nanoparticle aggregates to form a seed crystal that is prevented from growing beyond the nanometre scale. The size and shape of the nanoparticles can be dictated by other aspects of the reaction, including the temperature, concentration, pressure, and reaction times, as well as mass trasfer[199].

Electrochemical synthesis creates nanoparticles by using an electrical current to drive the shape and size of nanoparticles that are formed on an electrode. The electrical current is driven through a bath of a metal ion solution that acts as the precursor. After the current is applied, the positively charged metal ions aggregate on the cathode where nucleation begins and nanoparticles form. Controlling the size of the nanoparticles is performed by controlling the voltage and current applied to the ion bath, as well as the temperature of the bath during the reaction[200].

Deep eutectic solvents (DES) can be used to produce inorganic nanoparticles from green alternatives[201]. DES are formed by mixing two solid materials, a hydrogen bond donor such as choline chloride, and a hydrogen bond acceptor such as copper (II) chloride and mixing at temperatures around 60 to 80 °C, forming a liquid environment. These DES aid in the formation of a nanoparticle by being a substitute eutectic environment, an

environment that has a lower melting point than its two constituent components, whilst enabling C-C coupling reactions to take place[202]. DES also possess a highly biocompatible, environmentally safe and non-toxic environment for nanoparticle synthesis, which can be adjusted by controlling the ratio of the two donor molecules, such as urea and choline chloride, allowing the production of various sizes and shapes of nanoparticles[202].

Microemulsion synthesis uses a colloidal system to create a confined reaction environment that allows determination of the size and shape of the nanoparticles. The reaction occurs when a suitable reagent or condition is supplied creating a chemical reaction that causes nanoparticles to form from droplets within the microemulsion[203].

Template-assisted synthesis requires a suitable scaffold to allow the desired nanoparticle size and shape to form. The scaffold can be biological in form, for example virus capsid, or synthetic such as an organic polymer material[204]. Nanoparticles are then grown onto the surface of the template using one of the other synthesis techniques described. Once the desired nanoparticle shape and size has nucleated, the template can be removed using a dissolution or thermal treatment.

Inorganic nanoparticles are typically characterised using X-ray Diffraction (XRD), Transmission Electron Microscopy (TEM), Dynamic Light Scattering (DLS), Zeta potential, Thermogravimetric Analysis (TGA), FTIR and UV-vis spectroscopy [205].

1.6.1.1 Creating copper oxide nanoparticles and the conditions effecting shape and size

Creating copper oxide nanoparticles is possible using the techniques mentioned in 1.6.1.1, and different techniques have advantages and disadvantaged based upon the desired characteristics of the nanoparticle such as size and shape[206]. Chemical methods are the most conventional methods as creating copper oxide nanoparticles can be accomplished by using a copper precursor, such as copper chloride or copper acetate and added to a base solvent such as sodium hydroxide[207]. In a study performed by Siddiqui *et al*, by simply changing the copper salt precursor, between copper (II) nitrate trihydrate and copper (II) chloride dihydrate, the nanoparticles produced resulted in an orthorhombic structure for the copper nitrate and a monoclinic structure for copper chloride[207]. The concentration of the precursor can also affect

the produced nanoparticles, changing which species of copper oxide nanoparticles are produced. Alam *et al* produced nanoparticles using varying concentrations of copper sulfate pentahydrate between 0.03 M and 0.12 M[208].

During the copper oxide nanoparticle synthesis, the temperature of the reaction can alter the size and shape of the nanoparticle as seen in a study by Sagadevan *et al*[209]. During their study, copper oxide nanoparticles were produced using copper acetate pentahydrate and capped by ascorbic acid through a combustion technique at 100 °C and 300 °C and using SEM to image the difference between the nanoparticles produced. Comparing the two sizes of the nanoparticles, it was found that using the combustion technique at the higher temperature, smaller copper oxide nanoparticles were produced[209]. Similarly, in synthesis techniques which include a rotational influence, such as a spinning disc reactor or co-precipitation technique using a magnetic flea, the rotational speed influences the synthesised nanoparticle size[210]. Chang *et al* showed that by changing the rotational speed of a spinning disk reactor, from 500 RPM to 4000 RPM, the average nanoparticle size decreased from 79.3 nm to 58.3 nm[210]. The combination of both the rotational speed and temperature of the reaction can be used to achieve a desired size of nanoparticles, with both higher rotational speed and higher temperature resulting in smaller nanoparticles produced.

Other techniques can be used to produce copper oxide nanoparticles such as laser ablation or an electrochemical method. During laser ablation, a focused laser is pulsed onto a copper target, where copper and copper oxide nanoparticles are ejected from the target and can be directly deposited onto a target surface[211] This study performed by Fernandez-Arias *et al* showed that both copper, cuprous oxide and cupric oxide nanoparticles can be produced using this technique by ablating the copper target under different conditions such as whether its open air or under a constant flow of argon[211]. During electrochemical synthesis, copper electrodes are placed into an electrolyte solution and a current is applied. This causes copper ions to dissolve into the electrolyte solution where they react with hydroxides in the solution, forming copper oxide nanoparticles[212]. During this process, the choice of electrolyte is considered the most significant factor in producing copper oxide nanoparticles, as different electrolytes can produce different shapes and sizes of nanoparticles. For example, a solution of sodium nitrate mixed in with an ethanol-water solution at a 1:1 weight-by-weight ratio produced nano spindles with a size of 100 nm in diameter with a length of 300 nm. However, when the electrolyte solution was just a water-ethanol mixture, nanorods of 50 nm in diameter and 200 nm in length were created[213].

1.6.2 Nanoparticle creation characterisation

During the creation of nanoparticles, controlling size and shape can be achieved through various means as such as changing temperature and mass transfer during the synthesis[214, 215]. Higher temperatures commonly lead to a larger nanoparticle size, and this is caused by increased rates of reaction and subsequent aggregation of nanoparticle crystallites. Increasing the temperature further can result in the formation of non-spherical nanoparticles[214]. Furthermore, the various techniques of nanoparticle synthesis also factor into the size and morphology of the nanoparticles[197,198,200].To analyse the shape and morphology of the nanoparticle synthesised, various imaging and spectral techniques are used, as well as other characteristics such as the zeta potential, hydrodynamic size, and crystal orientation[216,217, 218].

1.6.2.1 Scanning electron microscopy

Scanning electron microscopy, or SEM, is a technique that uses electrons to image the surface of a material at higher magnifications than classical optical microscopy[219]. A scanning electron microscope operates by focusing an electron beam using electromagnetic lenses onto the surface of a conductive sample[220]. The focused electron beam scans in a raster pattern across the surface of the sample causing low-energy electrons to deflect, or high-energy electrons to backscatter from the sample, referred to as secondary electrons., backscattered electrons as well as X-rays. Secondary electrons, or the low-level electrons, provide a topological signal from the sample, allowing for surface level imaging[221]. Back scattered electrons come from below the surface of the sample, and provide information about the composition of the sample, albeit at lower resolution as the number of electrons received by a detector is also lower when compared to secondary electrons[222]. Finally, at sufficiently high electron beam levels, X-rays are produced from interactions with the sample. These X-rays provide elemental analysis of the sample as the X-rays produced have discrete energy levels that correspond to the alpha, beta, or gamma lines[223]. These X-rays are required to perform energy dispersive spectroscopy (EDS), which can be used to image the elements of the sample[223].

Materials and material coatings, such as nanoparticles, are excellent samples for SEM analysis as a combination of topological imaging, with elemental analysis, allowing the measurement of sizes and defects[224]. SEM is also an exceptional technique for investigating biofilm formation as it provides sufficiently high magnification whilst also allowing for contrast between different elements of the biofilm, such as a bacterial cell, or the EPS the cells produce[225,226]. One downside to imaging biological samples such as biofilms, is that they are not conductive inherently and must be coated in a conductive layer to allow topological coating[227]. Figure 1.21 shows a dispersion of copper nanoparticles under a scanning electron microscope, with an average size of 50 nm[228].
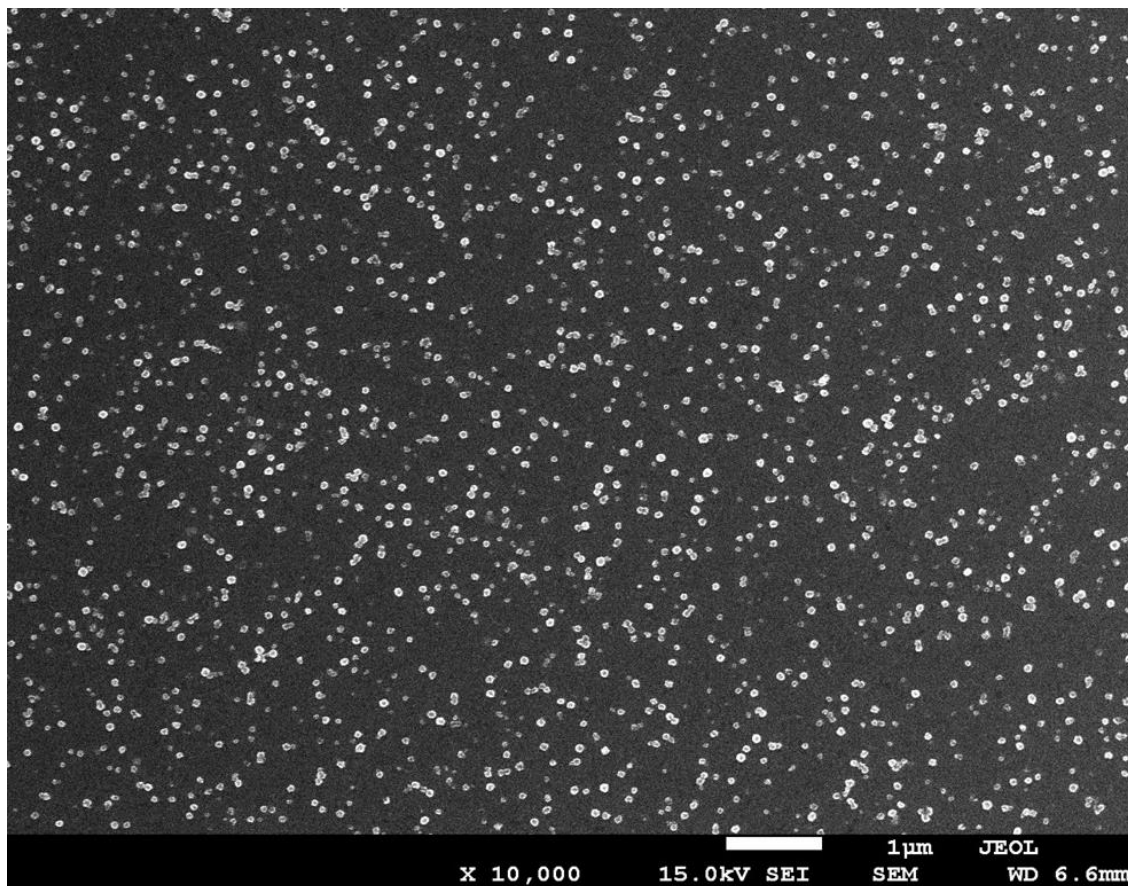
Figure 1.21 *A collection of copper nanoparticles imaged using SEM. Copper oxide imaged under SEM showing SEMs ability to resolve nanoparticles with sufficient dispersion [228]. Permission to use the image acquired from Elsevier publishing group.*

1.6.2.2 Transmission electron microscopy

Transmission electron microscopy, or TEM, like SEM uses a focused electron beam to investigate the properties of thin samples, however, unlike SEM, TEM focuses on thin material slices as the electrons penetrate through the sample[229]. As the electrons pass through the thin sample, they will either transmit through the sample carrying information about crystalline structure, or they will cause some form of scattering whether by an elastic electron ejection, X-ray emission, either by Bremsstrahlung radiation or characteristic radiation[229]. TEM is particularly powerful as it allows higher resolution imaging compared to SEM, but also allows crystalline structure to be visible[230].

Due to its high resolution and ability to perform EDS as well as resolve crystalline structure, TEM is used as a primary imaging technique to resolve nanoparticles and measure their size[231]. Biological samples are also possible to image using TEM, however, due to the high accelerating voltage that the electron beam possess, this is often a destructive technique for biological samples[232]. Below (Figure 1.22) a TEM is being used to measure atomic lattice sizes and the orientation of the atomic lattice of copper nanoparticles coated in graphene[233]. These atomic lattices are a repeating structure of atoms that form the material's physical properties such as strength and conductivity.
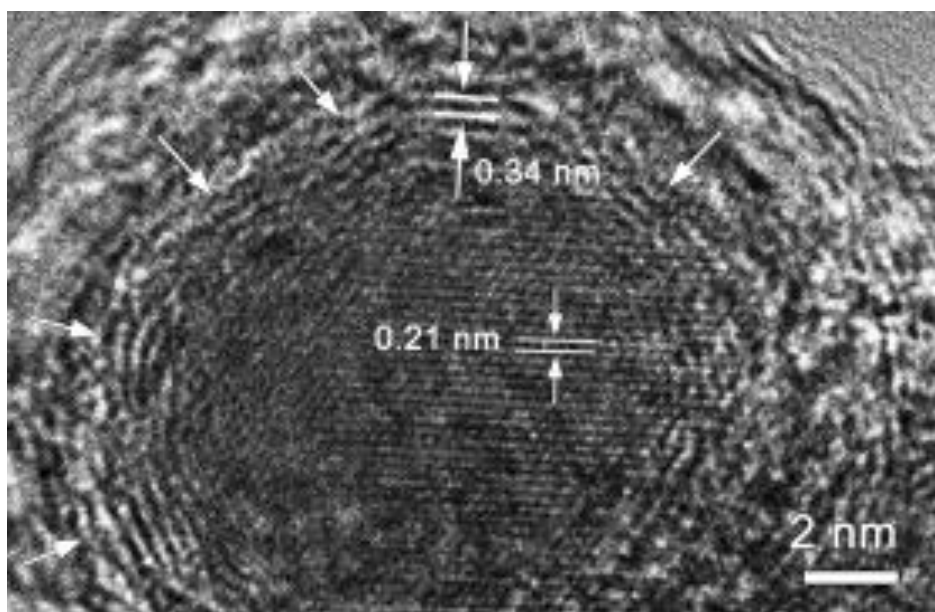
Figure 1.22 *TEM image of a copper nanoparticle coated in graphene. The atomic lattice structure of the copper core can be seen in the middle, with an atomic spacing of 0.21 nm while the carbon outer layer can be seen to have a spacing of 0.34nm [233]. Permission to use the image acquired from Elsevier publishing group.*

1.6.2.3 Thermogravimetric analysis

Thermogravimetric analysis or TGA, is used as a technique to measure the changes in mass of a material as a function of temperature or as a function of time and is useful at measuring a material coating[234]. As nanoparticles are often coated to improve their functionality, measurement of the composition of a nanoparticle coated in organic materials such as amino acids, TGA can measure the coating weight of the amino acid[235, 236]. TGA can also be used to analyse the weight of a coating on a surface, by increasing the temperature over time, if the coatings boiling point is lower than that of the coated substrate, the weight of the coating can be measured[237]. This technique can be paired with other analytical techniques such as mass spectroscopy and can be used to analyse the evaporated gas that is boiled away from the nanoparticles or the coated substrate[238]. Figure 1.23 shows copper oxide nanoparticles undergoing TGA after being coated with various amino acids and losing mass based the amino acid[239].
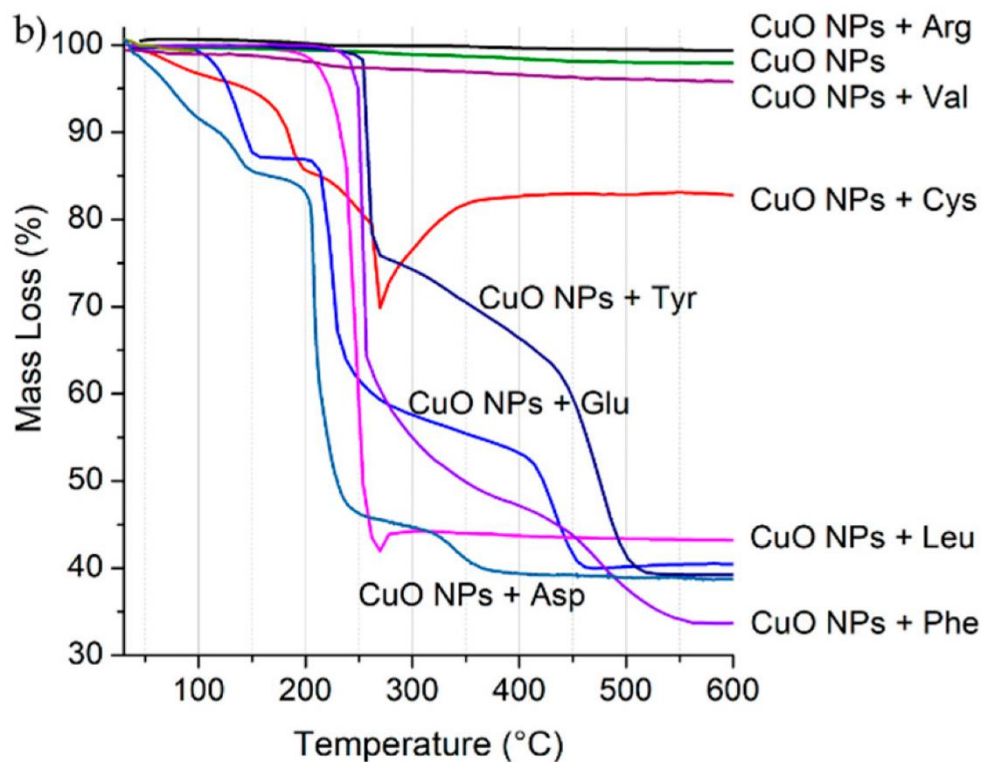
Figure 1.23 *The loss of mass of various amino acid coated copper oxide nanoparticles. Various amino acids are used to coat copper oxide nanoparticles to improve their functionality and colloidal stability. Performing TGA shows how much mass the amino acid contributes to the total mass of the coated nanoparticle* [239]. *Permission to use the image acquired from creative commons licences*

1.6.2.4 Dynamic light scattering

Dynamic light scattering (DLS) is a technique that uses the scattering of a laser light focused through a sample with small particles to measure the hydrodynamic size of the particles or to understand the Brownian motion of these particles in a fluid[240]. The measure of the hydrodynamic size of the nanoparticles is determined by the scattering of the light incident on the particle, with larger nanoparticles scattering light in a forward direction as opposed to a back scattering direction[241]. By measuring the intensity of the scattering, the dispersity of the particles within the sample can be observed[242]. However, as light is scattered from nanoparticles that are often oxidized, the light becomes scattered from a distance further away than the core of the nanoparticle[243].

A function within DLS is the measurement of a nanoparticle's zeta potential, a measurement of the electric potential moving under an electrical field, i.e. how a

charged particle moves in an electric field[244]. The zeta potential measurement can also be used to determine the colloidal stability of a nanoparticle in a liquid or other medium, where values of zeta potential between ±0 - 20 mV are considered unstable, values between ± 20 − 30 mV are considered moderately stable, and values > ±30 mV are considered highly stable[244].

1.6.3 Copper oxide nanoparticles as an antimicrobial

While it is known that copper oxide has antimicrobial properties, Copper oxide nanoparticles, specifically Cupric oxide (CuO) nanoparticles, are rapidly expanding as a new antimicrobial[245]. The creation of these nanoparticles can be performed via simple techniques such as the precipitation as described previously, enabling high throughput production. Techniques such as using a spinning disc reactor, allow the precipitation method to be upscaled to produce large quantities of nanoparticles while remaining monodispersed[246]. These copper oxide nanoparticles can be further functionalised using a coating; to improve biocompatibility and this allows the nanoparticle's antimicrobial properties to be enhanced[247]. The effect of copper oxide nanoparticles on different bacterial species are currently being studied with many of the ESKAPE pathogens being inhibited by CuO nanoparticles at sizes ranging from 200 nm, down to 12 nm[248][249]. These CuO nanoparticles have a few mechanisms to give them their antimicrobial properties, including metal ion toxicity, the generation of reactive oxygen species (ROS), the interference with cellular processes and the disruption of cell membranes[250-252]. These mechanisms change based upon various factors, including the nanoparticles size, the ion species and the type of bacterial species the nanoparticle interacts with.

1.6.3.1 Metal Ion toxicity of copper oxide nanoparticles

Two different states of copper oxide exist, firstly cupric oxide, or CuO and Cuprous oxide, or Cu_2O. Both nanoparticle species can release Cu^+ ions during interaction within the cell, and an excess of ions will interfere with other essential metals during their use in DNA production[253]. This interference was shown by Chatterjee *et al* where copper oxide nanoparticles were compared to copper chloride, and the effect of ions released by the

nanoparticle and the nanoparticle precursor was determined to be the predominant factor in DNA damage[253]. Furthermore, it showed that the ions released by the copper oxide nanoparticles had a greater effect overall in the damage of the DNA compared to the ions released by copper chloride. Cu_2O also releases Cu^+ ions as seen by a study performed by Behzadinasab *et al* where the Cu_2O was chelated by bicinchoninic acid disodium salt hydrate (BCCA), preventing the release of ions[254]. This prevention of ion release in Cu_2O showed a significant reduction in bactericidal properties of a coating compared to the unchelated variant[254]. CuO possesses a greater release of these ions compared to Cu_2O as seen in these studies and shows greater promise at killing cells using this technique.

1.6.3.2 Copper oxide nanoparticles generating reactive oxygen species

Both CuO and Cu_2O nanoparticles can produce reactive oxygen species within bacterial cells, by interacting with water molecules within the cell[252]. Within the bacterial cell, these copper oxide species undergo a redox cycle with hydrogen peroxide, exchanging an electron and causing negatively charged OH to interact adversely with the production of various growth processes within the cell[255]. During a study performed by Meghana *et al*, both CuO and Cu_2O were evaluated in their production of reactive oxygen species and found that CuO produced higher concentrations of OH^- compared to Cu_2O in an *E. coli* species[252]. The CuO species introduced was found to directly cause the production of free radicals in the Cu-Zn superoxide dismutase, an enzyme that removes these reactive oxygen species, indicating it could produce super oxides (O_2^-) that Cu_2O could not[256, 252]. This showed that CuO has a greater antimicrobial effect than Cu_2O, even at lower concentrations because of its ability to produce these super oxides.

1.6.3.3 Copper oxide nanoparticles interrupting regular cellular functions

As both CuO and Cu_2O nanoparticles can enter a cell through porins or by protein absorption, they can interact with elements within the cell and disrupting cell homeostasis[257]. The reactive oxygen species mentioned previously can directly interact with amino acid synthesis and is one such technique in which the nanoparticle can

interact with cell homeostasis. However, a study performed by Macomber *Et al* showed that it was possible to examine copper replacing iron in an iron-sulfur cluster in isopropyl malate isomerase under aerobic conditions, causing a reduction in two copper regulatory genes and reducing the viability of an *E. coli* species[258]. While this mechanism does very little to directly cause cell death, it does aid other mechanisms by increasing the total copper nanoparticle concentration within the cell, leading to higher concentrations of reactive oxygen species and extensive ion accumulation within the cell.

1.6.3.4 Cell membrane damage caused by copper oxide nanoparticles

Finally, as these nanoparticles can penetrate a cell, they are both capable of interacting with the cells membrane leading to cell lysis[252]. As bacterial cells move and interact with copper oxide nanoparticles, electrostatic interaction will cause the nanoparticles to attach and interfere with bacterial cell membranes[259]. A study performed by Bezza *et al* showed that Cu_2O nanoparticles could destroy the integrity of the cell membrane using a TEM and comparing treated and untreated cells[260]. However, other studies have found that Cu_2O has a greater effect in causing membrane damage than CuO[252].

1.6.4 Nanoparticle coatings

Functionalising a nanoparticle with a coating is one way to improve the properties of a nanoparticle, without changing the material of a nanoparticle[261]. These coatings can be applied during or after synthesis and can aid in improving the monodispersity of a nanoparticle synthesis, or by improving the particle's physical properties such as zeta potential[262, 263]. While these modifications do not directly increase the antimicrobial efficacy of the nanoparticle, it will improve the particle's ability to interact with a bacterial cell in two forms. Firstly, improved monodispersity of an antimicrobial nanoparticle, with a smaller size will improve the efficiency of the production process, resulting in larger volumes of small nanoparticles. This is caused by a correlation between nanoparticle size and bacterial survival rates, where smaller nanoparticles exhibit a greater killing effect on a bacterial species[264]. Secondly, by altering the zeta

potential of a nanoparticle by coating it with an amino acid such as glutamic acid, the nanoparticle can be suspended in a solution. This causes the now-coated nanoparticle to stay in suspension and interact with a greater volume of mobile bacterial cells, where if uncoated, may precipitate from solution and not interact with the mobile bacterial cells[265].

1.6.4.1 Coating materials with copper oxide nanoparticles

Copper oxide nanoparticles are used as a coating material for a variety of different materials and substrates. These coatings are often used for their anti-viral, anti-fungal and antibacterial properties and can be coated on various materials including textile materials, stainless steel and incorporated into paints[266, 267, 252]. Coating 100% cotton fabric with copper oxide nanoparticles was performed by Anita *et al* where fabric was exhausted in a bath of copper oxide nanoparticle solution at 50 degrees for 30 minutes, squeezed to remove excess then dried and finally cured at temperatures of 80 degrees and 150 degrees Celsius respectively[267]. This coating process was then evaluated using a washing test using AATCC standard 61(1A)-2001 and the results showed a decrease in the zone of inhibition in both a *Staphylococcus aureus* and *E. coli* species, showing that the treatment method was capable of degredation. However, the coating was tested and showed that the antimicrobial properties that the coated fabric had acquired, because of the copper oxide nanoparticles, was still present after washing. This process clearly shows the capability of coating fabrics in copper oxide nanoparticles, furthermore, the tested nanoparticles were coated in a 3% sodium alginate solution via ionic gelation to improve the stability of the coating and improve adherence to the cotton fabric. Similarly, the 316L stainless steel that was coated in copper oxide nanoparticles encapsulated in a matcha tea / polyethylene glycol solution, performed by Bezza *et al*, showed that it is possible to coat metals[260]. This coating was performed by an airbrush spray technique and was tested against *Staphylococcus aureus* and *E. coli* where both species exhibited a zone of inhibition around the copper oxide coated stainless steel, compared to uncoated stainless steel which showed no zone of inhibition[266].

Both of these coatings showed that copper oxide nanoparticles can be capped in a biocompatible material whilst retaining there antimicrobial properties and that they can be coated onto various materials using different techniques. The antiviral properties of CuO nanoparticles are also seen on a coating in a study performed by Merkl *et al*. In their study, CuO nanoparticles were produced using a flap spray pyrolysis method and were deposited onto a

glass substrate and annealed to ensure adequate coating[268]. Similarly, the antifungal properties of copper oxide nanoparticles were tested, by embedding them into polyvinyl chloride, polyvinyl methyl ketone and polyvinylidenefluoride and then subsequently spin coating these materials[269]. These materials were then tested against *Saccharomyces cerevisiae*, where a reduction was seen across all materials, with an increased reduction in viable as the copper oxide nanoparticle concentration increased[269].

These studies show that different coating techniques are suitable for different materials as a high force may not be suitable to coat a porous material such as cotton fibre, but simply spraying and allowing the material to dry would not be suitable for a hard nonporous material. The coating of the copper oxide nanoparticles in various biocompatible materials also showed that coating a copper oxide nanoparticle does not always prevent the mechanisms by which they are antimicrobial, as each of the various coatings showed antimicrobial effects after both a capping agent was applied to the nanoparticles and the various materials were coated[267-269].

1.6.5 Glutamic acid coated nanoparticles

Glutamic acid is an essential amino acid that many bacterial species cannot synthesize and is required for balanced cell homeostasis[270]. This amino acid can be taken into a bacterial cell via transporter systems, such as the GltS and AlsT systems in *Staphylococcus Aureus* and be used during bacterial cell growth[271]. These systems encourage the uptake of glutamic acid and offer a novel avenue to introduce an antimicrobial, such as copper oxide nanoparticles, into bacterial cells. This increased uptake in an antimicrobial caused by the presence of glutamic acid has been previously explored by Zhao *et al* who discovered that by providing a glutamic acid rich environment, *E coli* had a lower tolerance for drug resistance in all but macrolides[271].

1.7 Biofilm formation and colonisation of medical devices

Biofilm formation is one of the key factors in antibiotic tolerance and resistance, by creating a barrier between the environment and active cells, biofilms physically prevent

antibiotics reaching their targets[272]. Biofilms also increase the adherence of bacterial cells to a surface, by forming a barrier to local shear forces, allowing localised cells to remain in one place under low shear stress during early biofilm life cycles, and later high shear stress during its final stage[273]. Additionally, during a biofilms lifecycle, cells that initiate the lifecycle will have limited nutrition, slowing their metabolic rates, causing the cells to become dormant, this also improves the tolerance of bacterial cells to antibiotics due to the changed metabolic rates[274]. These factors underpin why biofilm infections are significantly more difficult to remove compared to other infections[275]. Biofilm related infections often refer to infections that are caused by biofilms contaminating medical devices and are often referred to as healthcare associated infections (HCAI). These HCAI's are a massive factor in the cost of healthcare with estimates of these infections, costing the US healthcare system, between 8.3 to 11.5 billion US dollars[276]. With the value of care to HCAI's being substantial, it is important to understand how biofilms form, perpetually exist and subsequently avoid treatment, to tackle costs.

1.7.1 Medical device colonisation and subsequent infection

Within hospital settings, medical devices are crucial to patient survival, particularly those in intensive care units (ICU). These devices offer another surface for bacterial colonisation, biofilm formation and subsequent infection and *A. baumannii* is a dominant cause for these infected devices[277]. Devices include urinary catheters, endotracheal tubes, and ventilators to name a few. Health care associated infections (HCAI) were reported to have a prevalence of 6.4% in 1,000,000 cases reported each year and include events such as catheter-associated urinary tract infection (CAUTI), ventilator-associated pneumonia (VAP) and surgical site infections (SSI)[278]. There are a few common factors when considering the colonization of any medical device. Contamination before insertion is a common cause of medical device colonization, one study indicated that only 40-50% of surfaces that should be sterilized are sufficiently cleaned, providing opportunity of cross contamination[278]. Infection can also occur at the site of insertion, bacteria on the skin can contaminate the invasive device at the site of insertion and enter the blood stream or oesophageal tract. One study examined the

contamination that occurred in patients who required central venous catheters (CVC) and found that 91% of 213 patients had coagulase negative staphylococci on their skin at the sight of insertion[279]. This study highlights the requirement of site sterilisation, this study looked at CVC tip colonisation which found that 13.7% of cases were contaminated, this study does not examine every tip as 25% were left in post hospital visitation or were not sent for testing[279]. Another source of contamination occurs from water sources which can spread directly to the host or indirectly through contaminated food and drink preparation through poor hygiene, airborne contamination, or contamination in the water supply[277].

Infection of these medical devices and the severity of the infection depends on multiple factors associated with the needs of the patient. Firstly, patients who require central venous catheters for over 30 days are at a greater risk of infection from luminal colonization compared to those who are not[279]. Comparably, patients who require urinary catheters have a risk of infection which increases by 10% per day the catheter is in place, with the main strategy for reduction being replacement of the catheter, which can cause further complications[279]. Endotracheal tube infection is well documented and is often a precursor to ventilator associated pneumonia[280]. This is due to bypassing the hosts immune system in the oesophageal tract, allowing for foreign bacteria to directly access the airways. Infection of these ET's is often luminal however presence of biofilm is found on its outer surface[280]. VAP is defined as pneumonia occurring in a patient after 48 hours of mechanical ventilation via an endotracheal or tracheostomy tube and can be early onset (occurring within 96 hours of intubation) or late onset (post 96-hour intubation)[280]. Resistance of bacteria in VAP cases is also well documented, where studies have shown that endotracheal tubes are a significant site of infection. In one study where suspected *A. baumannii* infections were isolated and identified 47% of the species were resistant to imipenem, part of the carbapenem class of antibiotics, which are often prescribed after other antibiotics have failed[281]. One study found that multidrug resistant ESKAPE pathogens were present on endotracheal tubes, in the form of biofilms in 70% of patients and that these pathogens were also found within the lungs of these patients, suggesting that biofilms represent a significant source of persistent pathogenic bacteria[282]. The opportunistic properties of *A. baumannii* can be observed in

the rising number of cases identified in a short period of time. In December of 2005, a medical centre in Arizona reported five cases of *A. baumannii* infection in two weeks versus 11 cases in the previous six months, all the patients recorded in December were all receiving mechanical ventilation[283]. Medical devices are a key site for microbial infection; with the increasing number of cases, the high rate of resistance through the development of biofilm and other resistant mechanisms, preventing these infections is a high priority[281,283].

1.8 Medical materials

Medical devices are made from a variety of materials and combinations of materials to achieve the desired flexibility, durability, hardness, and biocompatibility. These attributes must be considered when developing medical devices as insufficient flexibility will inhibit the use of the material for application. For example, an endotracheal tube needs to be sufficiently flexible to pass through the oesophageal tract but needs to have a certain hardness to forcefully keep the airways open if required[284]. Some of the materials used include polyvinyl chloride (PVC), expanded polytetrafluoroethylene (ePTFE), silicone, polyethylene (PE), and polyethylene terephthalate[285].

1.8.1 Endotracheal tubes

Endotracheal tubes are used to help keep the airways open during respiratory issues or oesophageal tract collapse by creating a physical barrier pushing against the collapsing trachea and supplying air, either mechanically or passively, into the lungs of the patient. They serve as an additional layer of protection during severe injury, by protecting the lungs from gastric contents and blood by separating the airways from the gastric system[286]. Endotracheal tubes (ETs) are often made with PVC, a flexible, durable polymer that is soft but can be made suitably stiff for intubation[286]. Other materials used in ET's include silicone, rubbers, and metals and are suitable for different applications. The positioning of an endotracheal tube is significant, too far into the throat and the

endotracheal tube may perforate softer tissues, whilst not far enough and sufficient support for the airways is not provided and the patient cannot breathe adequately[287, 288,289].

While the endotracheal tube is capable of keeping a patient alive by allowing air to flow in and out of the airways, it also opens an opportunistic pathway for respiratory pathogens[290]. Bacterial infection and biofilm formation are significantly likely to occur during intubation, as the airways are ideal locations for respiratory based pathogens like *P. aeruginosa* and *S. epidermidis* causing pneumonia[291]. Current techniques in keeping endotracheal tubes clean during intubation include covering the tube in antiseptics, or by nebulising antibiotic down the ET during initial intubation, techniques that are temporary and do not prevent infection later during patient recovery[292, 293]. These temporary measures do not prevent infection during long term intubation and after initial intubation, patients either become symptomatic, or another invasive technique such as optical coherent tomography, are required to determine whether a biofilm has adhered to the ET[294].

1.8.2 Catheters

Catheters come in a variety of forms and types with different purposes. The different types of catheters include urinary tract catheters, which can lead to catheter associated urinary tract infections (CAUTI)'s, central venous catheters, and haemodialysis catheters, used in dialysis often in conjunction with vascular access grafts. Catheters are often made from different materials, which include silicone, polyurethane, PVC or latex and are suitably chosen for the location within a body[295]. Catheters are crucial for patients in critical care where an indwelling urinary catheter is used as well as those going through routine procedures requiring intravenous catheters for saline drips[296].

Due to the wide diversity of catheter use, there is a high association with catheter usage and bacterial infection[297]. When the catheter is placed within a patient for an extended period, there is a significant increase in the likelihood of bacterial infection[298]. Due to the variety of catheters involved, there is no one specific species of infection for all catheters. Species most involved with urinary tract infections include *E. coli* and *K.*

pneumoniae, whilst *S. epidermidis, S. aureus* and *P. aeruginosa* are amongst the most common for intravenous catheters[299, 300]. Biofilms are incredibly common during infections caused by surgical procedures and the insertion of the various catheters[301]. Catheters are one of the most well studied medical devices and as such there are many studies that investigate various methods in preventing bacterial infection and biofilm formation on these devices. Some of these studies include coating the material in antibiotics prior to insertion and impregnating the device with antimicrobial compounds such as silver nanoparticles[302, 303].

1.8.3 Metal pins and plates

Metal pins and plates are used in orthopaedic procedures to treat bone fractures and injuries by fixing them in position and allowing bone tissue to reform[304]. Metal pins, also known as intramedullary rods, are often used for fractures in the radius and ulna, or in the fibula and tibia[305]. Plates on the other hand are used for rigid fixation and are usually used for total fractures of bones where more permanent fixing is required[306]. These pins and plates are often made with stainless steel or titanium, which are durable materials and will improve the strength of the local area and aid in preventing further stress related injuries post healing[306]. These are not the only metals used for orthopaedic procedures, for example, the hook used for anterior cruciate ligament injuries are made from cobalt chromium molybdenum alloys, which are particularly good for rotating and moving[307].

As implantation requires surgery, it is common for infection to occur during the surgical procedure and subsequent implantation of the metal device[308]. Consequentially, strategies are used to prevent infection, including surface modification of a medical device using nanopatterning to increase hydrophobicity, dipping the implant in a bath of antibiotic agents such as iodine or conventional antibiotics and more recently, incorporating antimicrobial metals onto the surface[309]. Some implant alloys have antimicrobial metals incorporated into them, particularly nickel, is used for the anticorrosion properties the metal induces on alloys[310]. Even with these strategies in

place, infection is still common and can be attributed intraoperative surface modification of the implant[311].

251252253254255256257257258258258258258259259259260261262260262

1.9 Material coatings

A coating is a material deposited onto the surface of another material, either as a liquid or a powder to enhance the properties of the material underneath. Coatings can have a range of properties that serve to enhance a material, paint or lacquers serve as a decorative coating as well as protecting the surface of the material underneath. Other coatings such as an anodizing layer have more functional applications such as corrosion resistance and prevent stress cracking[312]. Coatings can also be applied in a variety of different ways that have their own unique benefits and drawbacks and should also be considered. For example, spray coating allows a material to be coated uniformly but will only coat the outer surface of any material, whilst a dipcoat will coat the entirety of a material but may be prone to an uneven coating if the removal speed is not constant.

1.9.1 Spray coating

Spray coating applies a thin layer of material onto the surface of another material to enhance its properties. Application of any material in a controlled manor can be difficult but with spray coatings, the thickness can easily be manipulated by adjusting the nozzle or pressure of the coating material[313]. There are four major techniques to spray coating; air spray uses compressed air to atomize a coating and propel it onto the surface of a material, airless spray uses a high pressure pump to force a coating material through a nozzle and spray fine droplets, electrostatic spray uses a charged coating material and sprays it across the surface of a grounded or oppositely charged material and finally powder coating which uses a dry powder that is heated adhering to a substrate[314]. Below (Figure 1.24) a wire arc spray coater that uses relatively low temperatures to coat materials in aluminium and zinc[315].
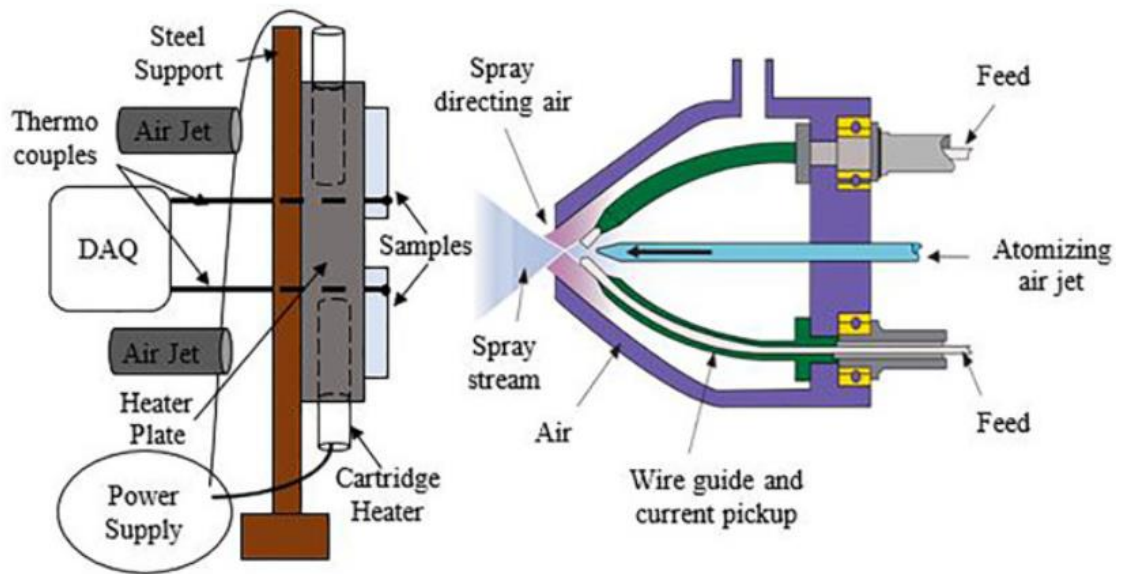
Figure 1.24 *A low temperature wire arc spray technique used to coat various materials. An example of a spraying technique that involves an atomized air jet to spray coat a sample at relatively low temperatures[315]. Permission to use the image acquired from Elsivier publishing group*

1.9.2 Dip coating

Dip coating is another technique of material coating that allows the adherence of a thin coating to a substrate by submerging the substrate into a bath of coating solution and then slowly removing the substrate from the bath[316]. The thickness of the coating can be changed through different means, for example, changing the submersion time of the substrate will increase or decrease the thickness respectively. Similarly, the rate of removal from the bath will alter the thickness of the coating[316].

1.9.3 Plasticizers

During the coating process, some materials will crack due to sheer stress at imperfections during the curing stage and can propagate into large canals exposing the substrate[317]. Plasticisers are materials that reduce the forces on polymer chains, increasing the materials pliability and making the material softer and include agents such as glycerol, polysorbate, polyethylene glycol. Glycerol is used in a variety of

different industries, including food, pharmaceutical and cosmetic industries, due to it being non-toxic[318].

1.9.4 Material testing

Various analytical techniques exist that can be used to test a material coating and its robustness against use applications. A leaching test can determine how well the coating will stay adhered to the applied material and can be measured through inductively coupled plasma mass spectrometry (ICP-MS). To do this, a sample will have some fluid or gas passed across the sample's surface, to create a sheer force and intentionally try to separate the coating from a material. This is then collected in a solution such as water and is digested in a suitable medium such as nitric acid. The digested sample is then diluted, typically into parts per billion, or by a factor of nine, so that the sample can be ionised in a plasma. The ionised sample is then accelerated towards a mass spectrometer where an ions mass-to-charge ratio is determined, matching the ion to an element[319].

1.9.5 ISO standards for medical device testing

The international organization for standardisation, produces ISO standards that are an internationally recognized set of standards with a wide range of applications designed to keep protocols and procedures standardised for every lab who may wish to test the protocol or procedure[320]. These standards can be used for, but are not limited to, testing, and developing new materials, techniques to test materials and performing other experiments. ISO's are used by many companies and research institutions, with examples including ISO 20776-1:2006, which is the ISO that describes MIC and MBC testing used by EUCAST to determine antibiotic susceptibility[321]. Other ISO standards include ISO 20743, which allows for the testing of antimicrobial fabrics[322].

1.10 Nuclear magnetic resonance

Nuclear magnetic resonance (NMR) is the precession of a nuclei with non-zero spin, with all nuclei having either an integer or half integer spin. Nuclei, such as hydrogen (H^1),

in a magnetic field can be interacted with if a radio frequency is applied, causing the nuclei to precess and have a time sensitive, changing magnetic field, causing a measurable voltage to be induced. At rest, nuclei outside of a magnetic field have no net magnetization, however, when exposed to a static magnetic field, nuclei precess at the Larmor frequency, which is given by equation 1.

$$\omega = -\gamma B_0 \hspace{6cm} 1$$

Where ω is the precessional frequency or Larmor frequency, γ is the gyromagnetic ratio and B_0 is the strength of the static magnetic field.

However, the application of the magnetic field also causes a splitting in energy levels, where the high energy protons are aligned to the magnetic field and the number of nuclei that align is proportionally to the strength of a magnetic field applied. This is given by the Zeeman interaction, describing the Zeeman energy, or the energy differential between the high and low energy state nuclei, given by equation 2.

$$\Delta E = \gamma h B_0 \hspace{6cm} 2$$

Where ΔE is the Zeeman energy, h is Planck's constant, γ is the gyromagnetic ratio and B_0 is the strength of the static magnetic field.

This differential between nuclei in the magnetic field determine the net magnetisation of the system and is proportional to the number of nuclei in a higher energy state, given by equation 3.

$$M \propto \frac{N_{high} - N_{low}}{N_{high} + N_{low}} \hspace{5cm} 3$$

Furthermore, the number of nuclei that are in the higher energy state is also inversely proportional to the temperature given by equation 4.

$$\frac{N_{up}}{N_{down}} = e^{\left(\frac{\gamma h B_0}{kT}\right)} \hspace{5cm} 4$$

Where $\frac{N_{up}}{N_{down}}$ is the ratio of nuclei in low energy or high energy spins, $\hbar$ is the reduced Planck's constant, γ is the gyromagnetic ratio and B_0 is the strength of the static magnetic field, k is the Boltzmann constant and T is temperature.

After the magnetic field is applied, the net magnetisation is small. Considering a magnetic field strength of 1.5T and a temperature of 20 degrees Celsius, the ratio between the the two proton energy states) is 1 in 100,000 protons, which contribute to the signal received[323].

323

Alternatively, additional fields can be applied, like the radio frequency field (B_1) to further alter the direction of the net magnetisation, leading to a measurable electrical signal. By varying the time that the B_1 field is applied, the net magnetisation of the nuclei within the system can be altered and is given by the flip angle and seen in equation 5.

$$\alpha = \gamma B_1 T \qquad\qquad\qquad\qquad\qquad 5$$

Where α is the flip angle, γ is the gyromagnetic ratio and B_1 is the strength of the static magnetic field and T is the time that the radiofrequency field is applied for.

This, however, is the simple case and is complicated by inhomogeneous fields and different radiofrequency pulse shapes, causing the nuclei system to have a non-uniform flip angle across the received signal. After the radiofrequency field has pulsed, the excited nuclei will begin to return to equilibrium, its lowest energy state within the B_0 field by processing at the Larmor frequency in parallel to the magnetic field. This change in net magnetisation caused by the relaxation of the nuclei, referred to as longitudinal relaxation or T_1, can be measured by a coil placed perpendicular to the B_0 field. This change in net magnetisation causes an induced voltage in the coil, allowing measurable properties, such as T_1, to be investigated.

1.10.1 T$_1$ or Spin-lattice relaxation

T$_1$ relaxation or spin-lattice relaxation, is the relaxation of magnetic moment in the plane parallel to the B$_0$ magnetic field, where the net magnetization is measured through receiving coils. The T$_1$ value of a proton nuclei is different in each individual material and is dependent on temperature and other chemical characteristics the protons are found in and around[324]. The T$_1$ value of a proton is the time taken for longitudinal recovery to occur and is equal to $1 - 1/e$ or ~ 63% of the net magnetization (M$_0$). Using techniques like T$_1$ inversion recovery, estimations of the T$_1$ value of a substance using NMR can be achieved. This inversion recovery is performed by applying an initial inversion pulse and then measuring the signal after an inversion time. By altering the inversion time, the signal measured will vary, which can be plotted and fit to equation 6.

$$S = K * [H] * \left(1 - 2e^{-\frac{T_i}{T_1}} + e^{-\frac{TR}{T_1}}\right) * e^{-\frac{T_e}{T_2}} \qquad\qquad 6$$

Where S is the signal intensity which can be negative or positive, K is a scaling factor, [H] is the spin density, T$_i$ is the time elapsed after a pulse is applied, T_1 is the time required for longitudinal relaxation TR is repetition time, Te is the echo time and T_2 is the transverse relaxation time.

1.10.2 T$_2$ or Spin-Spin relaxation

T$_2$ relaxation or spin-spin relaxation, is the precession of a proton perpendicular to the B_0 static magnetic field. In a homogenous field a single nucleus will precess about the magnetic field in the transverse plane. By including additional nuclei into the system, the precession of these nuclei induces a magnetic field causing localised magnetic fields to interact with neighbouring protons, leading to dephasing of adjacent protons. Over time these protons will rephase, leading to a local net magnetisation causing a 'relaxation' of the magnetic moments. By considering the simple case, a single nucleus with no adjacent nuclei in a homogenous field, there would be no change in the net magnetisation. However, during the application of a radiofrequency field, the net

magnetisation aligns with the main magnetic field and decays back to the transverse plane. This change in signal is given by equation 7.

$$M_{x,y}(t) = M_0\, e^{-t/T2} \qquad\qquad\qquad 7$$

Where $M_{x,y}$ is the net magnetic moment in the *x,y* plane, t is the time elapsed after a radiofrequency pulse has been applied and T_2 is the time for transversal relaxation to decay to 37%

However, by adding additional nuclei, or by considering inhomogeneities in the magnetic field, the dephasing and rephasing occurs at an accelerated rate. This more realistic scenario causes T_2 to be referred to as T_2^* which is measured in a sample with the difference seen below (Figure 1.25)
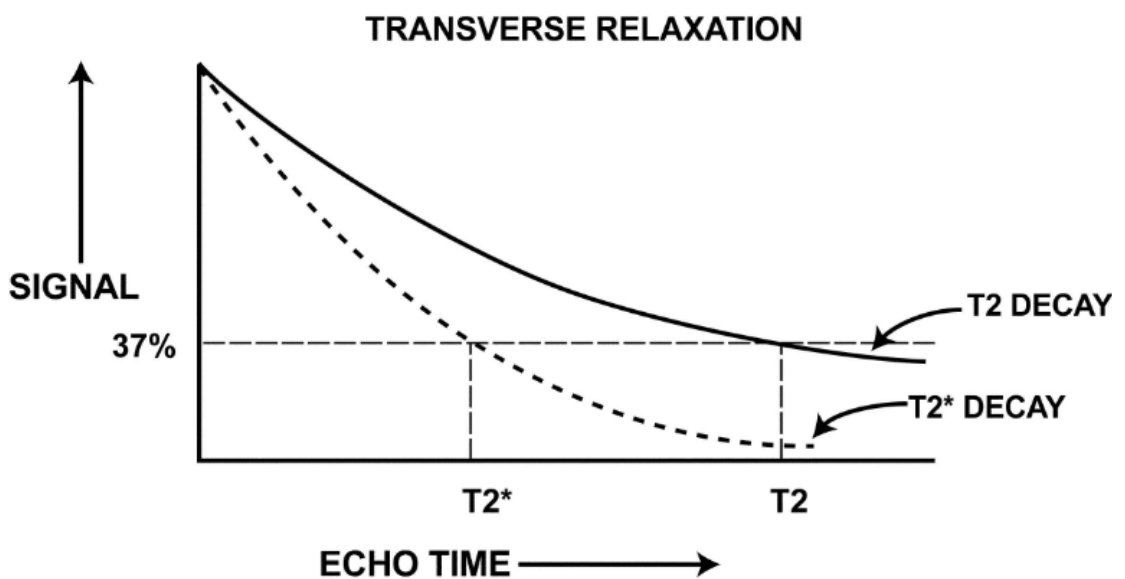
Figure 1.25 *The difference between T_2 and T_2^* decay. The difference between the two transverse decays, where T_2 is the real transverse signal decay that cannot be measured due to inhomogeneous fields and T_2^* the measurable decay that happens at an accelerated rate[325] . Permission to use the image acquired from creative commons licences*

1.10.3 Various NMR sequences to investigate relaxation

Making measurements with NMR requires altering the nuclei and tipping them out of alignment from a B_0 field, to measure the relaxation in the longitudinal plane and the decay in the transverse plane.

The Free Induction Decay (FID) method is the simplest method for measuring nuclei spin changes. In this method, a single pulse of radiofrequency is applied in the transverse plane, causing the nuclei within the sample to begin the dephasing and rephasing cycle, until they are realigned with the B_0 field. This signal decay can be measured using a receiver coil, where a simple sample might show a monoexponential decay, whilst a complex system may display a polyexponential decay. This FID method does not work in homogenous fields due to accelerated decay, nor can it investigate T_1 relaxation.

An alternative method to measuring the decay of spin-spin relaxation is by using a spin echo sequence. This sequence is caused by applying an initial 90° pulse to the system, causing nuclei to precess about the longitudinal axis. After a short time, a second radiofrequency pulse is applied at 180° to the system, causing these nuclei precess in the negative direction, causing rephasing to happen. This will cause a measurable signal to reappear before decaying again. This reappeared signal will also not be as intense as the initial signal, and this is caused by the self-diffusion of the system. By plotting the decay of this maximum magnetization, we can achieve another time constant, known as T_2^{eff}.

1.10.4 Magnetic resonance imaging

Magnetic resonance imaging (MRI) is a powerful medical imaging modality that relies heavily on nucleus alignment in the presence of large magnetic fields. The most common nuclei to be imaged is the hydrogen nucleus, which is a singular proton and is the most abundant nuclei in human tissue, where MRI is most used. This imaging modality relies upon the T_1 and T_2 properties of the nuclei within different tissue, providing different contrasts based upon those properties and allowing contrast in images to be observed[326]. Below (Figure 1.26) a comparison between T_1 weighted, T_2 weighted, STIR

(Short tau inversion recovery) and proton density imaging of a normal brain, showing the different contrast between white and grey brain matter when imaging is performed with different MR sequences[327].
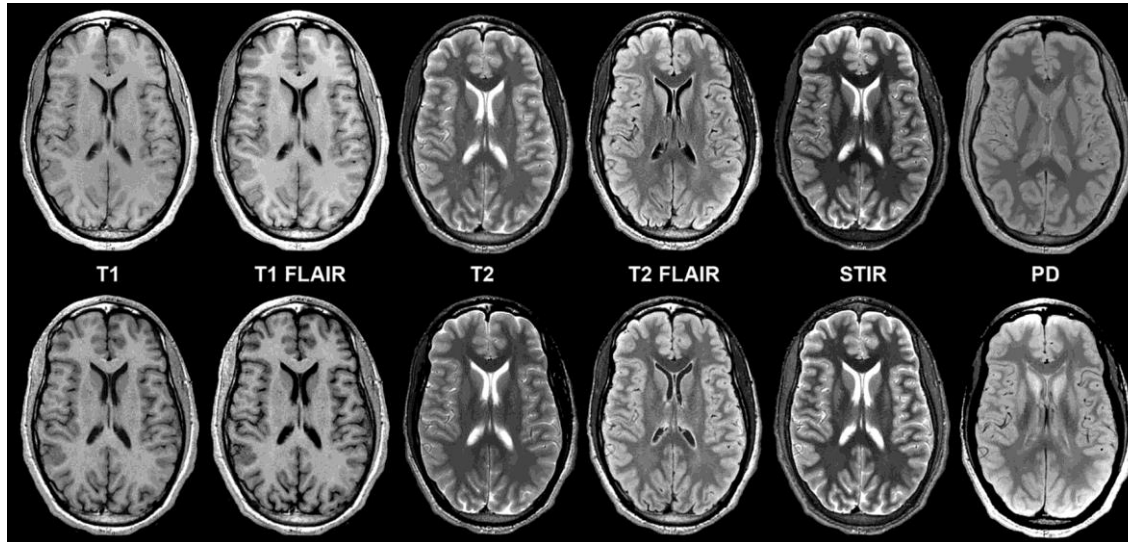
Figure 1.26 *Various MRI sequences used to image a healthy human brain. Various MRI sequences used on a healthy human brain showing contrast between white and grey brain matter. The sequences include with T_1 weighted imaging, T_1 fluid attenuated inversion recovery, T_2 weighted imaging, T_2 fluid attenuated inversion recovery, short tau inversion recovery and proton density imaging[327]. Permission to use the image acquired from Radiological society of North America.*

The technique was first performed in 1973 by Paul Lauterbur who published the first image of two capillary tubes using magnetic field gradients corresponding to a B_o and B_1 [328].

Gradients are formed by altering the main static field slightly, so that the centre of the field remains the same, while the net magnetic strength of the field increases or decreases towards either end of the field. By applying a gradient, the Larmor frequency of the nuclei along the magnetic field is now altered based on the net magnetic field strength and is given by equation 8.

$$\omega = \gamma(B_0 + B_{2,x,y,z}) \hspace{4cm} 8$$

Where $B_{2,x,y,z}$ is the gradient applied in the x, y, or z axis.

Two different encoding techniques can then be used to achieve imaging, firstly, frequency encoding, which is the shifting of the Larmor frequency with the gradient field. Secondly, phase encoding, caused by the application of the gradient field. Phase encoding can be considered as the result of acceleration of the precession a proton. If the precession is thought as the position along a sinusoidal wave and one rotation is the wavelength between two peaks the wave, then the application of a gradient can accelerate the position of the proton and when the gradient is removed, the speed at which the proton travels along the wave continues. The change between this accelerated proton compared to a reference proton is the phase shift and is remembered by the proton which can be seen in figure 1.27.
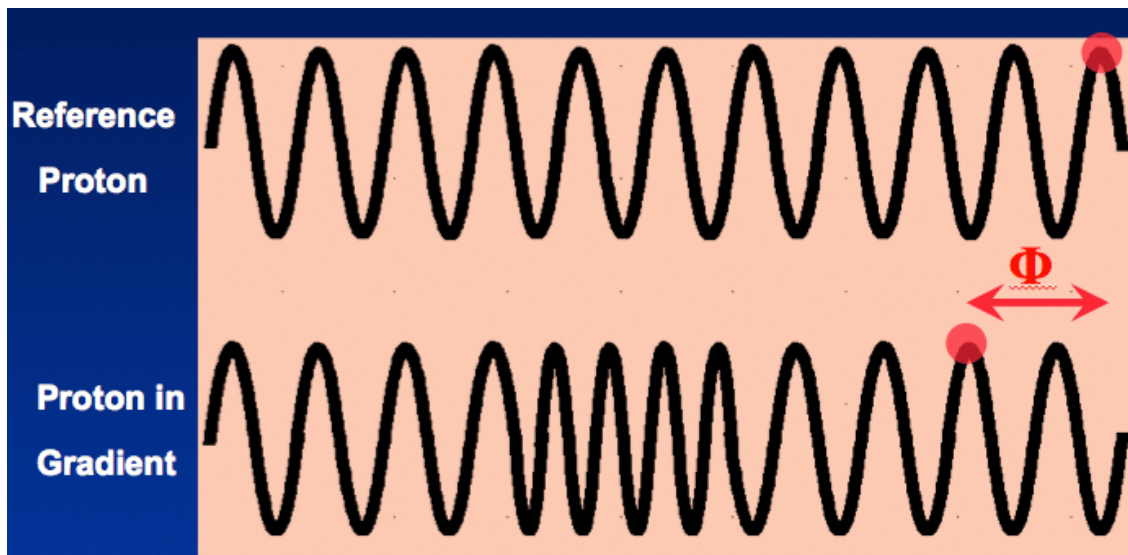
Figure 1.27 *Two proton phase change compared to a reference proton. The phase change between a reference proton and a proton that has had a gradient field applied to it for some length of time. Permission to use the image acquired from creative commons licences*

The technique was then further expanded upon by Peter Mansfield who concluded that with the use of a magnetic field gradient, slices of material could be imaged[329]. However, this imaging took substantial computing power and time to gather the required signal that could not be used for practical imaging of large samples or human patients. It wasn't until later that Mansfield, Garroway and Granell used a new method of collecting rapid

images and coined it, Echo Planar Imaging (EPI). This new technique now forms the basis for many clinical imaging sequences used in MRI.[330].

1.10.5 T_1 weighted imaging

T_1 weighted imaging is an MRI technique that provides tissue contrast based on the relaxation properties of the different tissues and is suitable for investigating structural changes in the human body. T_1 weighted imaging is used to highlight the difference between T_1 relaxation times in different tissues, examples of this include fat appearing bright due to the short T_1 value of fat[331]. Whilst T_1 weighted imaging is often used for clinical human studies, it is not limited to just humans as other living beings and inanimate objects are both imaged regularly[332].

1.10.6 T_2 weighted imaging

T_2 weighted imaging is a technique that provides contrast based on the dephasing of the spin-spin relaxation and allows for fine detail between similar soft tissues[333]. T_2 weighted imaging is used for imaging finer details in structures such as ligaments and tendons in muscle regions, but is also useful for imaging inflammations, fluid accumulation in oedemas, and infections[334]. The benefit of using T_2 weighted imaging allows the user to examine inflammation associated with infections due to its sensitivity to water[335].

1.10.7 Proton density imaging

Proton density (PD) imaging, as the name suggests, is a technique using MRI that focuses on imaging the density of nuclei in the slice selected. One of the benefits of using PD imaging is that you can visualise small structural changes, or small tissue changes but lose information in similar tissues due to lower contrast[336].

1.10.8 Diffusion imaging using Magnetic Resonance Imaging

MRI sequences have been developed to investigate the diffusion of water or other fluid through a permeable barrier. An example of this is examining the diffusion of blood in the brain to examine potential injuries[337]. Using MRI, diffusion through biofilms has been performed to investigate the detachment of biomass and further biofilm growth. Diffusion can be performed using spin echo sequencing and is given by the following equation, also known as the Stejskal-Tanner equation 9[338].

$$S_{(T)} = S_0 e^{\frac{2D\gamma^2 G^2 T_e^2}{3}} \qquad\qquad 9$$

Where $S_{(t)}$ is the signal at received at echo time T_e, S_0 is the signal at echo time = 0, D is the diffusion coefficient, G is the gradient of the magnetic field and T_e is the echo time.

Measurements of a sample are taken at different echo times T_e and the change in signal allows the measurement of diffusion (D) to be possible. This technique is used when the magnetic field is inhomogeneous and is not adjustable, for example, when a Halbach array is used and is the original pulsed field gradient sequences used.

As new sequences have developed, so have new diffusion imaging sequences leading to Diffusion Weighted Imaging (DWI) sequences[339]. These sequences can be performed using an MRI scanner and the diffusion can be measured by the following equation 10.

$$S_T = S_0 e^{-bD} \qquad\qquad 10$$

Where b is the b value assigned to the Diffusion weighted imaging sequence.

This again provides a measurement of the Apparent Diffusion Coefficient (ADC) the value of b is estimated using the equation 11.

$$b = \gamma^2 G^2 \delta^2 (\Delta - \frac{\delta}{3}) \qquad\qquad 11$$

Where γ is the gyromagnetic ratio of the proton, G is the gradient amplitude, δ is the time of applied gradient and Δ is the time between two pulses.

Using DWI sequences, we achieve the same result as the Stesjkal-Tanner equation, using a variable gradient system, with the benefit of a substantially shorter acquisition time.

These sequences are known as Pulsed Gradient Spin Echo (PGSE) sequences where two pulses, an initial 90° pulse is followed by a 180° pulse after some time τ and provide insight into the diffusion occurring within the system.

1.10.9 Imaging biofilms using magnetic resonance imaging

MRI has been used to image biofilms and water diffusion through biofilms to understand biofilm growth, structure, diffusivity, and immobilisation of heavy metals[340]. The focus of these studies is on wastewater streams to understand how we can better treat our water[340]. The resolution of MRI means that structural imaging and diffusion imaging are the most common techniques for biofilm imaging and provide significant detail in both the structure and flow through the various densities of biofilms[341]. These details can help understand how biofilms transport nutrients through bulk media using Pulsed Gradient Spin Echo sequences and measuring the diffusion by using the Stesjkal-Tanner equation. It can do this to aid in determining how a biofilm immobilises external components, such as nutrients in a media, aiding in its antibiotic resistance mechanism[342]. Below (Figure 1.28), a NMRI of biofilms compared to an optical image of the same biofilm with an 81% agreement and a net error of 12%[343].
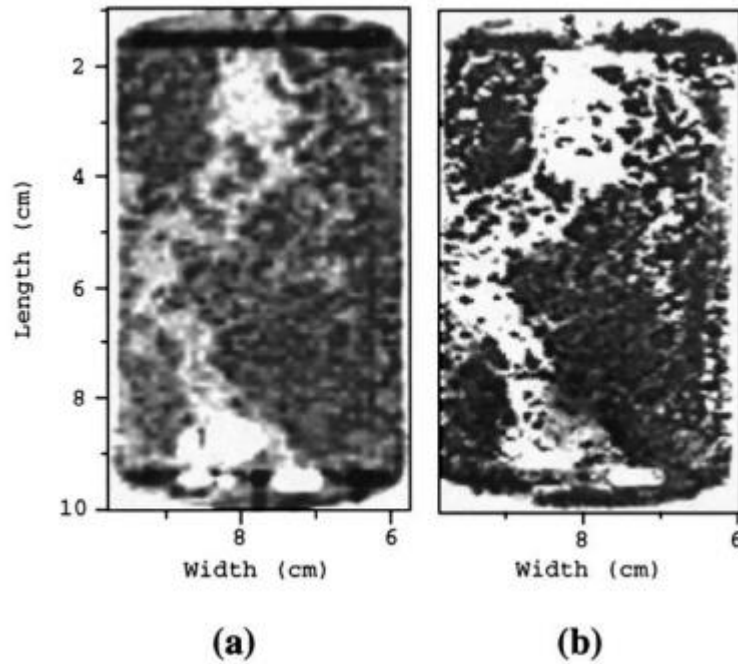
Figure 1.28 *A comparison between an NMRI image and an optical image. a. an NMRI image taken of a biofilm parallel plate reactor, of an Escherichia coli biofilm on the surface of the parallel plate. b. The optical equivalent of the biofilm grown in the parallel plate reactor[343]. Permission to use the image acquired from Elsevier publishing group.*

Using MRI to image biofilms is not always performed on parallel plate reactors, as there are many types of biological reactors including a packed bed bioreactor, a stirred-tank bioreactor, a bubble column bioreactor and a fluidised bed bioreactor[344-347]. Many studies that use MRI to investigate biofilms use packed bed bioreactors to understand how biofilms disturb the diffusion of water or nutrients[348]. MRI is used for these reactors as requires no contrast unlike other imaging modalities, and can evaluate growth over time, as seen in research performed by Nott *et al*, who measured the flow of water in a *Serratia sp.* Biofilm and the precipitation of lanthanum phosphate[349]. In this study, a gradient echo sequence was used to measure water flow, evaluate the blockage fraction caused by the biofilm, and describe the flow of water in the reactor.

Current research investigates the use of MRI as an imaging modality to investigate contaminated implanted medical devices. This research investigates the use of metal artifact suppression (MARS) sequences, to examine implanted knee replacements where infection has occurred[350]. Li *et al* found that using MRI, it was possible to

determine differences in synovitis, infections and non specific synovitis in patients with total knee arthoplasty[350]

1.10.10 Imaging biofilms using other imaging modalities

While MRI has been covered as an imaging modality used to visualise biofilms, it is not the only technique to do so. Optical coherence tomography (OCT) is frequently used to detect biofilms on indwelling medical devices such as catheters and endotracheal tubes[351]. OCT emits light onto a biofilm and onto a detector, where the biofilm reflects light back towards the detector, creating an interference pattern that can be processed into a cross-sectional image. Typically, these images are taken at the end of a probe that can be used to image matter with a thickness of a few millimetres[352]. As OCT exploits light photons, there is no ionising radiation, leading to a non-destructive technique for biofilm imaging that can be exploited as a non-invasive technique externally to a patient, or invasive when appropriate[353]. Using OCT, Rasmussen *et al* found it possible to actively image anti-biofilm effects of 1% chlorhexidine gluconate on a complex multispecies biofilm model[354].

Another prominent technique in biofilm imaging is fluorescent microscopy. During bacterial homeostasis, fluorescently labelled antibiotics can be introduced in a biofilm rich environment, and diffuse across the outer layers of a biofilm, leaving the fluorescent tag and imaged either live, or after diffusion has fully saturated the biofilm[355]. The fluorescent dye used may bind to certain aspects of a biofilm, such as its extracellular DNA (eDNA), allowing investigations into the role that eDNA may play[356]. These dyes are often found to be toxic to bacterial cells, making their use on implanted medical devices unsuitable and alternative imaging techniques are required[357].

Finally, micro Computed Tomography (µCT) can be used to image biofilm formation on medical devices[358]. Once a contaminated medical device is removed, it can be stained with a contrast agent such as potassium iodide, enhancing the contrast between cells and extracellular polysaccharide, and the device[359]. This technique provides a three-dimensional image of the biofilm, providing overall morphology, density and thickness, while being non-destructive to the biofilm. However, a clear drawback to µCT is the ionising radiation the technique employs. This might be a suitable technique for *ex vivo* imaging, but due to equipment limitations, is not ideal for *In vivo* quantification. The alternative solution would be to consider classical CT, which is

routinely used for medical diagnosis of a wide range of issues, including septic participants[360, 361]. However, contrast agents used are often non-targeting unless directly applied to the region imaged, requiring an injection to achieve the required contrast[362].

1.11 Aims and objectives of this thesis

The aims of this thesis and the work that is entailed are listed below in order of appearance in the results of the thesis. Firstly, the assessment of synthesised copper oxide nanoparticles using a precipitation technique and transmission electron microscopy quantifying the nanoparticle coating, using classical analytical techniques including inductively coupled plasma mass spectrometry and thermogravimetric analysis. Secondly, using these nanoparticles as a coating on a variety of materials to ascertain whether copper oxide nanoparticles can be used as an medical device coating, as well as determining the toxicity of the nanoparticles and the chemical used to create a material coating.

The third aim of this project was to categorise all the bacterial species that were to be tested with the copper oxide nanoparticles and the coatings. To determine the degree of effect of Glu-CuO nanoparticles for preventing biofilm formation. The next objective looked at using the copper oxide nanoparticle coatings to reduce the microbial load both in viable cell count and biofilm formation in relevant biofilm models including a modified Minimum Biofilm Eradication Concentration (MBEC) assay as well as the Centre for Disease and Control (CDC) reactor.

Finally, as an alternative to prevention, the ability to detect biofilm maturation, non-invasively was performed using MRI. Current *in vivo* techniques rely on optical coherence tomography (OCT) which is an invasive technique[363]. To determine the correct MRI sequence that best informs clinical decisions, the T_1 and T_2^{eff} values of bulk biofilms in different systems to determine whether they are sensitive enough to detect a biofilm forming. Subsequent analysis of these bulk measurements was then used to

optimize imaging sequencing in a porcine pluck to appropriately image biofilm formation on an intubated silicone tube, mimicking an endotracheal tube.

Chapter 2. Synthesis of glutamic acid coated copper oxide nanoparticles and coating medical grade materials

2.1 Introduction

With antibiotics becoming less effective against the most prevalent health care associated bacterial pathogens, other alternative treatment methods are required. A major factor in resistance to antibiotic efficacy is the prevalence of biofilm forming pathogens. During the life cycle of a biofilm forming pathogen, planktonic cells travel through different human tracts such as the oesophageal tract and adhere to surfaces, where they begin to reproduce and form biofilms. When a mature biofilm is formed bacterial cells are most resistant to antibiotics, being up to 1,000-fold more resistant than during planktonic growth, this is due to multiple mechanisms. Two of the main mechanisms that lead to this resistance are, firstly, that microbes in biofilms are encased in a matrix of polysaccharides, proteins, lipids, and extracellular DNA acting as a physical barrier to many antibiotics. Secondly, microbial cells within this matrix alter their metabolism, which reduces the effectiveness of many antibiotics that can penetrate the polysaccharide matrix and rely on bacterial metabolic processes for their activity. Additionally, once a mature biofilm is formed, some microbial cells periodically detach and travel to other sites to establish new biofilms. In humans, this can lead to additional infection sites and further complicate treatment options.

Consequently, microbes within mature biofilms, protected by the extracellular matrix, are extremely difficult to treat. Therefore, strategies aimed at preventing biofilm formation show significant potential as one of the main resistance mechanisms becomes significantly less effective. Material coatings that prevent the adhesion of planktonic cells and thus the initial stages of biofilm formation hold promise as alternate and pre-emptive treatment options. Copper and its alloys present a clear opportunity in development of anti-biofilm surfaces as their touch killing and long-term bactericidal effects are well documented, but the toxicity of copper is also well studied[141]. Due to their considerably smaller size copper oxide nanoparticles offer an alternative to a dense

copper coating whilst also allowing the coated substrate to keep many of its own properties. Copper oxide nanoparticles have antimicrobial properties as they have two different mechanisms that cause bacterial cell death. Firstly, nanoparticles can penetrate the cell membrane and create extremely toxic free radicals within the cell causing oxidative stress and damaging proteins and DNA within the cell. Secondly, as copper oxide is positively charged it will adhere to negatively charged bacterial cell membranes, causing them to become damaged and leading to cell lysis[364]. Therefore, by coating a material in copper oxide nanoparticles, the coating will aid in preventing an infection occurring in the first place, reducing the dependency on last line antibiotics, and reducing the drive of antimicrobial resistance in many pathogens.

One potential solution to prevent infection caused by biofilms is via the use of copper as a coating on medical devices. However, in high concentrations, copper is cytotoxic and cannot be used as a solid coating, nanoparticles on the other hand offer the same antimicrobial properties but do not need to be in high concentration to have these properties. Copper oxide nanoparticles have been synthesised using various techniques such as precipitation microemulsion and electrochemical processes for different applications, each with their own advantages and disadvantages that allow for different nanoparticle morphologies and sizes[197,197,198].

This chapter firstly aimed to synthesise copper oxide nanoparticles, characterise them and evaluate the technique used in their synthesis. Secondly, the copper oxide nanoparticles were tested using minimum inhibitory concentration and minimum bactericidal concentration assays, to quantify the concentration required for antimicrobial activity against numerous clinically isolated bacterial pathogens, with toxicity tests also performed against a human cell line to understand whether therapeutic concentrations might be non-toxic to the host and to determine the potential therapeutic window. Finally, silicone tubing was coated and characterised, to understand the uniformity of the coating, how much copper leached from the material and how much of the coated material was made up of the copper oxide nanoparticles.

In this chapter, the production and evaluation of copper oxide nanoparticles using a simple precipitation technique is explored. These nanoparticles are then reevaluated after they have been functionalised with glutamic acid using mechanochemistry, a

technique used to induce a chemical reaction through heat and pressure, to cause a phase change in the glutamic acid, coating the nanoparticles in the process. These nanoparticles are evaluated using various techniques, including transmission electron microscopy (TEM), scanning electron microscopy (SEM) and thermogravimetric analysis (TGA). These nanoparticles are coated onto different materials, with the Glu-CuO nanoparticles ultimately coating titanium, stainless steel, silicone and polyvinyl chloride, using 3-mercaptopropyltrimethoxysilane (MPTMS) as the bonding agent. This coating is further enhanced by the inclusion of plasticizers, with both polysorbate 80 and glycerol investigated, improving its robustness. The toxicity of the Glu-CuO nanoparticles is investigated against Human keratinocyte cells, and the MPTMS is evaluated in both a liquid and cured form. These coatings are then tested using leaching tests where the resultant leached material was analysed using inductively coupled plasma mass spectrometry. Finally, the Glu-CuO nanoparticles and MPTMS are investigated in a rapid spray coating for mobile applications.

2.2 Methods

2.2.1 Nanoparticle synthesis and coating

Copper oxide nanoparticles were synthesized using aqueous precipitation, following a modified literature procedure using a spinning disc reactor[365]. Copper (II) chloride (100 mL, 0.1 M, 97% purity, Sigma Aldrich) was added with sodium hydroxide (100 mL, 0.2 M, 97% purity, Sigma Aldrich) *via* a peristaltic pump onto the centre of a rotating concave disc, (10.5 cm diameter, 18 3x3 mm stepped ridges, 1000 RPM) at 60°C, yielding copper oxide nanoparticles (6.42 g, 80.9 %). The resultant solution was filtered and washed with deionized water, then centrifuged to remove the surfactant before drying and storing the dried nanoparticles. This step was repeated until the water was clear, indicating the nanoparticles where clean. The copper oxide nanoparticles that were synthesized were mixed at a 1:1 weight by weight ratio with glutamic acid in a mortar and pestle. This mixture was then ground together, causing the glutamic acid (≥99% purity, Sigma Aldrich) to electrostatically coat the copper oxide nanoparticles from a eutectic melt.

2.2.2 Dip coating endotracheal tubes, vascular access grafts and catheter tubing

Coating preformed tubing materials was undertaken *via* a dip coating method in two stages and depended on the tube length undergoing treatment. Two treatment solutions were required for all coatings, firstly, a 0.1 M concentration of mercaptopropyltrimethoxysilane (MPTMS) (95% purity, Sigma Aldrich) was created. Secondly, the desired concentration of nanoparticles was developed. Tubing that was adhered to twenty-four well plates to create modified, Minimum Biofilm Eradication Concentration (MBEC), assays, which are described further in section 3.2.18, required two additional well plates that were used for the dip coating process[366].

A third solution glycerol plasticiser was created at concentrations 0.1%, 1%, 2%, 5%, 10% and 100%, mixing glycerol into 100 mL of 18 MΩ water that was acquired from an Ultra Clear RO 30 (Avadity Science, USA). Four concentrations of polysorbate 80 were also

tested at concentrations of 0.1%, 1%, 2% and 5% but were later discarded because of the effects of the plasticiser not being adequate. The solutions were poured into 2 mL aliquot into each well of a twenty four well plate.For the twenty-four well plates, an additional plate was prepared with 2 mL of MPTMS solution in all but three wells, which were used as controls. Another plate was prepared with 2 mL of nanoparticle solution at the desired concentrations. The twenty-four well plate lid with adhered tubing was placed onto the plate with MPTMS in the wells for one minute with gentle oscillation. After MPTMS treatment, the lid was then placed into a 24 well plate of the plasticiser aliquots for 10 seconds. Finally, the lid was then placed onto the nanoparticle plate for one minute and given another gentle oscillation. After treatment, the lids were dried for 24 hours at room temperature (20°C), to ensure the MPTMS and nanoparticle coating were fully adhered.

2.2.3 Spray coating endotracheal tubes and Centre for Disease and Control reactor coupon surfaces

Two 50 mL spray bottles were prepared in advance of spray coating materials, one with the desired 0.1 M MPTMS and the other with the desired 325.5 mg L^{-1} concentration of nanoparticles. The samples were placed in petri dishes, on top of an absorbent blue roll in a fume hood and were sprayed 30 cm away to ensure even spreading, this was performed at room temperature (20°C). The MPTMS spray was employed three times to ensure complete coverage and the Glu-CuO nanoparticle suspensions were sprayed three times at 1.2 mL per stroke, as per manufacturing specifications. The samples were then cured in a UV box, using 254 nm wavelength, for 30 minutes before analysis using SEM and leaching experiments, as described in section 2.3.1, to examine the properties of the UV curing.

2.2.4 Imaging and inspection of the coatings

Visually inspecting the coating applied from the dip coating technique was performed using scanning electron microscopy using a JEOL JSM-7100F SEM. This involved cutting 5 mm lengths of coated material and adhering it to stainless steel cylindrical mounts

using conductive carbon tape. They were then coated in a 5 nm layer of gold using a plasma deposition (Quorum Q150R ES) to ensure there was good conductivity across the sample. Further analysis of the coating was performed using Energy Dispersive X-ray Spectroscopy (EDS) to determine where the coating is and to determine where cracks or defects form on the coating.

2.2.5 Leaching analysis of the coated materials

Leaching was investigated by pushing media through a 10 cm coated tube and using Inductively Coupled Plasma Mass Spectrometry (ICP-MS) on the resultant media o The leaching on the tube was performed using a peristaltic pump to pass at a rate of 0.75 mL min^{-1} for 22 hours to completely pass through one litre of artificial saliva medium. Coated CDC coupons were placed into 24 well plates with 2 mL of plasma-like media and oscillated for 24 hours at 100 RPM and at room temperature (20°C), before being taken for ICP-MS.

2.2.6 Evaluation of copper oxide nanoparticle size

Evaluation of the size of any nanoparticles was performed using transmission electron microscopy to image the nanoparticles and then ImageJ to evaluate and count the size of the nanoparticles[367]. A 10 µL suspension of the nanoparticles was placed onto a TEM imaging grid and allowed to dry, ensuring no fluid was present on the grid when put into the loading arm. After imaging, ImageJ was loaded, and the inbuilt particle size function was used (as described in section 2.2.14)[367]. A mask filter was applied to this function to ensure the function was accurately measuring the particle size.

2.2.7 Thermogravimetric analysis of the coated nanoparticles and coated materials

Thermogravimetric analysis was performed using a PerkinElmer TGA 4000 (PerkinElmer, USA) by loading a ceramic weigh boat with copper oxide nanoparticles or silicone tube coated with glutamic acid coated copper oxide nanoparticles and measuring the change in weight of the material. Both tests were performed by holding at room temperature

for one minute, then gradually increasing the temperature in increments of five degrees per minute, until the temperature peaked at 900 °C when it was then held for a further minute. The graph generated by the equipment shows the decrease in mass as the temperature increases, reaching and exceeding the boiling point of water, removing moisture from the mass, and then exceeding the boiling point of MPTMS and glutamic acid, leaving only silicone tubing and copper oxide nanoparticles.

2.2.8 Dynamic light scattering of the copper oxide nanoparticles

Dynamic light scattering was performed using a Zetasizer nano series (Malvern, UK) to evaluate the hydrodynamic size of the nanoparticles. This was performed by pipetting 1 mL of suspended copper oxide nanoparticles in water, into a cuvette and loading the sample into the Zetasizer. Single runs were performed until the quality report provided by the software indicated adequate concentration, as too concentrated or too dilute could have provided error in the measurements. These experiments were run at room temperature (20°C). The software was run for 100 repetitions and repeated in triplicate for each sample to accurately measure the size of the nanoparticles.

2.2.9 Zeta potential measurements of the copper oxide nanoparticles

The zeta potential of the copper oxide nanoparticles both coated and uncoated was performed using a Zetasizer nano series, (Malvern, UK) to evaluate the nanoparticle's ability to stay in suspension. The potential was measured by filling a surface zeta potential cell with the copper oxide nanoparticle suspension ensuring no bubbles were in the track. Each measurement was taken at room temperature (20°C). The vessel was then wiped down, including the gold contacts to prevent burning of the contacts caused by excess moisture or spillage, this was repeated in triplicate to correctly measure the zeta potential of the nanoparticles before and after coating in glutamic acid.

2.2.10 Inductively coupled plasma mass spectrometry

Inductively coupled plasma mass spectroscopy (ICP-MS) was performed using a PerkinElmer Nexion1000 (PerkinElmer, USA) to measure the presence of copper in leached samples. Experiments were performed by firstly producing a calibration curve, using known copper standards prepared in nitric acid. The standards were prepared by diluting the standard concentrate into 1, 50, 100, 250, 500, 750 and 1000 ppb in 2 % nitric acid (70% purity, Sigma Aldrich). This calibration curve was used to calculate the counts measured at known concentrations, allowing unknown samples to be measured. Samples of leached medium, control medium and sterile filtered water were taken and digested in 70 % nitric acid for two hours at a 1 in 10 dilution. The digested sampled were then diluted down in 2% nitric acid at a 1 in 100 dilution until a dilution of 10^{-9} was achieved. These sampled were then measured and analysed to determine any copper present in the leached material.

2.2.11 Electron microscopy imaging and ImageJ analysis

A variety of different imaging techniques were employed to evaluate various aspects of the project. SEM was used to examine the cells within a biofilm matrix as well as material coatings with nanoparticles and other composite materials. SEM-EDS was used to evaluate the coverage of individual components of coatings applied. TEM was used to evaluate individual nanoparticles before and after the glutamic acid coating to confirm size of the particles. Analysis was performed in ImageJ to measure sizes or to evaluate coverage of a material[367].

2.2.12 Scanning electron microscopy

A JEOL JSM-7100F Scanning Electron Microscope (SEM) was used as part of the surface analysis of the copper oxide nanoparticle coatings on various materials. The SEM equipment is maintained at a room temperature of (21°C) SEM analysis was performed by loading either 1 mm ring cuttings from coated samples or 5 by 5 mm area cut out from the ring cuttings onto the stubs via double-sided copper conductive tape. These samples were then coated in a 5 nm gold coating to ensure the samples were

conductive. Once the samples were placed onto the loading stand, they were placed into the loading window of the SEM to allow for the vacuum to come down to the correct pressure. After the correct pressure was achieved, the electron beam was turned on to allow for rastering across the sample and image acquisition. To obtain the highest resolution, focusing, wobble and stigmata correction was performed to account for the electron beams imperfections, and this was performed every time a new region of a sample was selected. Images taken were using the High Definition (HD) function on the SEM, providing 4096 x 4096 resolution (4k) and allowing the sizes of 100 nm to be imaged. Alternative sample preparation was performed by cutting samples smaller than the 12.5 mm diameter sample holder and adhering them via the double-sided copper conductive tape.

Each sample required unique settings to ensure optimal imaging, silicone tubing coated in copper oxide nanoparticles required a 15 KeV beam current, alongside a small spot size of less than four to ensure high resolution. These settings were too destructive for fabric samples and so only 5 KeV were used to analyse the fabric materials.

2.3.1.1 Energy dispersive X-ray spectroscopy

Energy dispersive X-ray spectroscopy, or EDS, was performed to confirm the presence of copper oxide nanoparticles, to examine the isotropy of the copper oxide nanoparticle coatings and to measure the percentage coverage in an inspected area. EDS requires high voltage electrons interacting with ground state atoms to eject the electrons of the atoms inner shell, this ejected electron has a discrete energy, or quantized energy, based on where the electron is ejected from. Referencing these energy levels, electrons will eject with a K (inner most shell), L (Second inner most shell) or M (Third inner most shell) X-ray known as the characteristic X-ray.

The presence of copper is detected using its Kα line at 8.04 KeV, the Kβ line at 8.91 KeV or the Lα at 0.93 KeV. Analysis of the images is dominated at the Kα and Kβ wavelengths as they provide the largest distinct peaks in the spectrum whilst the Lα line is difficult to resolve against the large spectrum peak of oxygen found at its Kα emission of 0.525 KeV. Examination of the sample's using EDS was performed using the JEOL JSM-7100F at 10

KeV or greater, ensuring the energy of the incident electrons was greater than the required ejected energy of the Kβ KeV. The resulting spectra were examined confirming or rejecting the presence of copper oxide nanoparticles. Mapping was also performed, allowing for a topological mapping of copper oxide nanoparticles across the sample surface. This resulting topological map was processed in ImageJ to threshold the colour from the image, determining total pixel coverage and subsequent coverage of the imaged region.

2.2.13 Transmission electron microscopy

A JEOL JEM-2100Plus (Japan) Transmission Electron Microscope (TEM) was used to analyse each batch of nanoparticles made. 5 µL of nanoparticle solution was pipetted onto the TEM sample grid and dried for 20 minutes in a fume hood. Samples were then loaded into the TEM sample holder and slowly placed into the TEM vacuum chamber, allowing 30 minutes for the vacuum to come down to pressure. With the sample fully inserted, adjustment of the electromagnetic lenses was performed to increase focus and reduce chromatic aberrations allowing for resolutions of up to 1 nm to be achieved and crystal lattice structure to be observed.

2.2.14 ImageJ analysis

After the images were gathered, analysis using ImageJ was performed[367]. Firstly, the images were processed through a threshold filter to convert the image to black and white. This causes the image to reduce in data size, allowing a clear definition of what is considered a particle or what is considered empty space. Next the 20 nm scale in the image was used to set the scale of the pixels, resulting in a 32.8 pixels per nm length. This helped to determine the size of the nanoparticles when they were measured. As background noise was observed, a rolling ball average with radius of 40 pixels was applied to remove the noise.

2.2.15 Reviving cells from frozen culture

Frozen cells were recovered by warming up the cells to 37°C and adding them to an additional 1 mL of Dulbecco's modified eagle medium (DMEM) (Sigma Aldrich). The 2 mL of inoculum was then centrifuged at 300 g for 6 minutes to recover any cells from the bottom of the 10 mL falcon tube, The supernatant was separated, and the pellet was resuspended in 1 mL of DMEM. The suspended cells were added to a TC25 flask along with an additional 5 mL of DMEM to recover and grow the cells for future experiments. Cells within the TC25 flask were stored in a static incubator at 37°C and were checked every day for contamination. The medium in the TC25 flask was replaced every day to ensure a constant supply of nutrients to the cells ensuring optimal growth. Revived cells came from either the initial starting culture or from passage five and all future cell stocks were frozen at passage five to ensure all experiments were performed at the same passage number.

2.2.16 Splitting cells

Once a TC75 tissue culture bottle has reached confluence the culture was split. The Dulbecco's eagle medium was removed from the TC75 bottle slowly and the sides of the bottle coated in cells was washed with Dulbecco's PBS (Sigma Aldrich) to remove any remaining medium. The PBS was removed from the bottle and a thin layer of trypsin (Sigma Aldrich) was added to unbind the adhered cells of the coated surface of the TC75 bottle. The trypsin and cell mixtures were incubated for up to 30 minutes depending on the resistance of the adhered cells, until cells were no longer adhered to the TC75 bottle. Then, DMEM was added to the trypsin to neutralise it and the trypsin/cell/medium mix was pipetted into a sterile centrifuge tube. The mixture was centrifuged 300 rpm for 5 minutes until a large pellet was formed. The surfactant was removed carefully as to not lose the pellet and was resuspended in 5 mL of fresh media to count the cells for future assays. Generation of additional cell flasks by adding a portion of the resuspended cells to a fresh flask. Cells within the TC75 flask were stored in a static incubator at 37°C and were checked daily for contamination.

2.2.17 MTT assay

Each MTT (98% purity, Sigma Aldrich) solution was prepared to a concentration of 5 mg mL^{-1} in Dulbecco's Phosphate Buffer Saline (PBS) (Sigma Aldrich) and stored in a fridge to protect the MTT solution from from light. All MTT assays were performed with HaCaT cells that had been passaged to passage 7. Cells grown in 96 well plates were grown overnight and prepared by washing the remaining media with PBS, removing any potential cytotoxic compounds that may alter the effect of the MTT solution. After adding 100 μL of PBS in each well and adding 10 μL of MTT solution to each well, the plate was incubated for between 30 minutes to 1 hour, depending on identification of formazan production at 37°C. After crystals were formed, 100 μL of DMSO (99% purity, Sigma Aldrich) was added and given minor agitation to the plate to ensure the formazan crystals were dissolved. These 96 well plates were then measured at OD$_{570}$, with more viable cells having a greater optical density.

An additional MTT assay was required following, the biological evaluation of medical devices, ISO 10993-5:2009, where 3 mm x 3 mm silicone tube cuttings were coated in MPTMS (Sigma Aldrich) with concentrations ranging from 1 Molar to 0.01 Molar. Similarly, a control with no sample and a negative control with just sterile silicone tube was included to observe effects caused by the mass of silicone added to the cells.

2.3 Results

Copper oxide nanoparticles can be synthesised using various techniques that include seeding, chemical reduction, coprecipitation, and microemulsion techniques[200]. Different techniques have various requirements and benefits, for example, hydrothermal techniques require high pressures and temperatures but commonly result in nanoparticles with non-dispersible properties. Herein, copper nanoparticles were synthesised using a co-precipitation method described in 2.2.1 and were characterised using transmission electron microscopy (TEM), dynamic light scattering (DLS), as well as spectroscopic analysis using UV-visible light spectroscopy.

2.3.1 Evaluation of copper oxide nanoparticle synthesis and particle size

Each batch of nanoparticles was evaluated using TEM to confirm their size and shape. These images were processed using ImageJ to measure the number and size of the copper oxide nanoparticles in the samples[367]. Figure 2.1 represents a typical TEM image of the synthesised nanoparticles that were used to evaluate the size and dispersion.
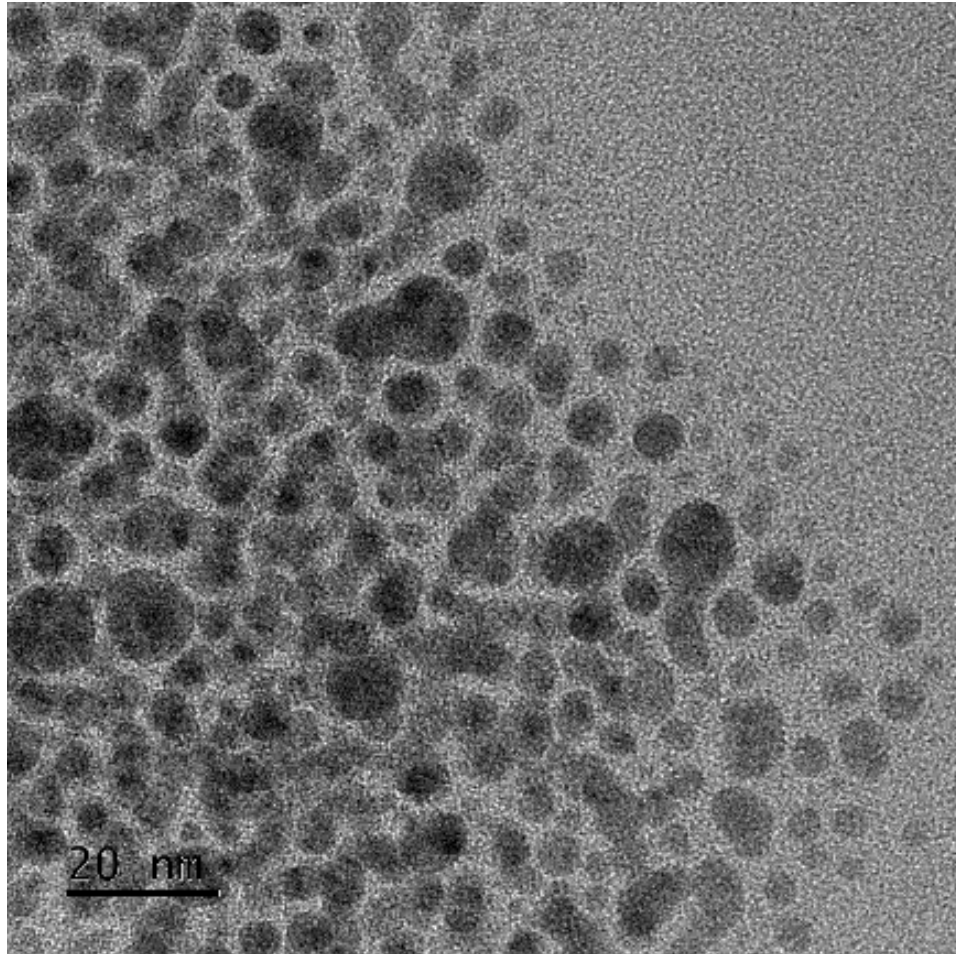
Figure 2.1 *Transmission electron microscopy of copper oxide nanoparticles that have undergone ImageJ image transformation and particle detection. TEM image of a CuO nanoparticles synthesised using the precipitation technique. ImageJ was used to pass the SEM image through a threshold turning the image black and white.*

After the images were gathered and processed, the distribution of the nanoparticles was determined (Figure 2.2). The average size of the nanoparticles was measured across three separate batches. Three images were taken from each batch and were processed using this technique resulting in 50 total nanoparticles measured and analysed, resulting in an average size of 5.8 ± 1.8 nm.
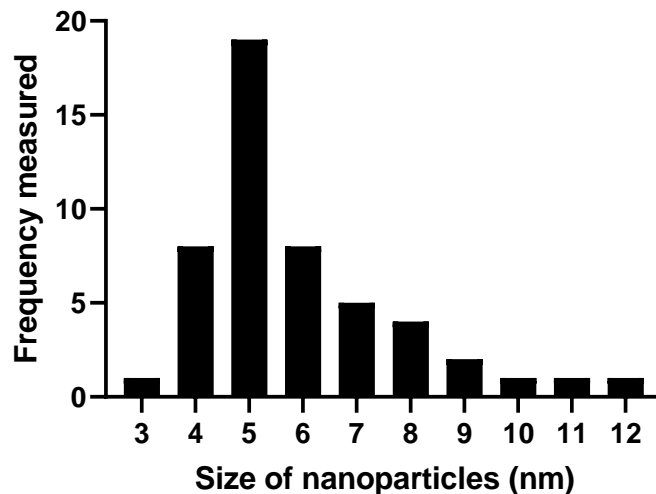
Figure 2.2 *Histogram plot of the nanoparticles measured across three separate syntheses. Histogram plot of nanoparticle size measured from three separate syntheses where at least three separate TEM images were taken, processed. The measured average nanoparticle diameter was 5.8 nm ± 1.8 nm, N = 50.*

2.3.2 Dynamic light scattering of copper oxide nanoparticles

DLS was performed to evaluate the hydrodynamic size and the dispersity of the CuO nanoparticles. Hydrodynamic size is the measurement of a sphere that would behave as a particulate moving through a fluid. Therefore, measured hydrodynamic size of nanoparticles is always larger than that of the particle when measured using other techniques such as TEM. Three different synthesised nanoparticle processes were taken, and the average is displayed below (Figure 2.3)
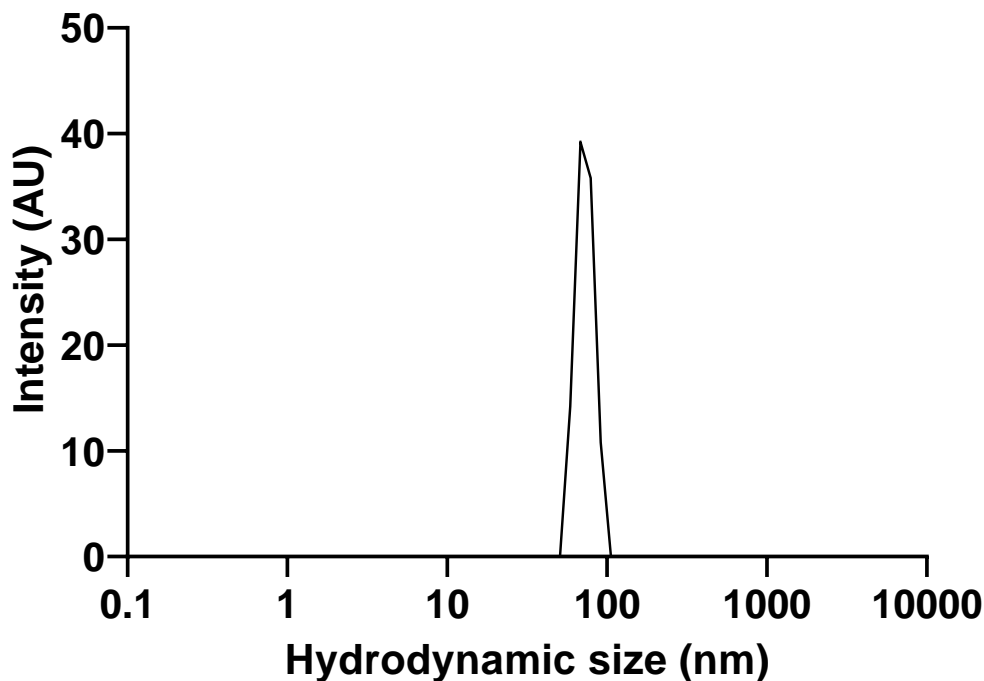
Figure 2.3 *The measured hydrodynamic diameter of the copper oxide nanoparticles. The hydrodynamic size of the CuO nanoparticles was measured using dynamic light scattering. The peak occurs at 74.93 ± 5.170 nm with a polydispersity index of 0.35, N = 3.*

2.3.3 Measuring the zeta potential to determine stability in solution

The stability of nanoparticles is the measurement of the surface charge of a nanoparticle, and it can vary by coating and in different solutions. This measurement of the electrical charge in the slipping plane of the particle indicates whether there is a high degree of electrostatic propulsion. For nanoparticles, a high zeta potential indicates a high degree of electrostatic propulsion that commonly resists aggregation, which is the main attribute for precipitated material. Typically, for a nanoparticle, a value of ± 40 mV indicates a stable nanoparticle that will resist aggregation and remain in suspension within the solution it is added to. During initial MIC testing it was noticed that the copper oxide nanoparticles precipitated out of suspension in purified water within minutes after sonication. This precipitation prevented initial antimicrobial activity testing as MIC and MBC assays require nanoparticles to remain dispersed in solution in an incubator for 18 hours with no agitation. Therefore, the zeta potential of nanoparticles was evaluated using the Zetasizer nano-series (as described in section 2.2.9). The measured

value of the uncoated copper oxide nanoparticles was determined to be -0.4 ± 6.2 mV indicating that the nanoparticles would not be stable in aqueous solution and would rapidly agglomerate within minutes if not agitated, which agreed with the visual observations of aggregation in solution reported. This analysis was performed on three separate synthesised nanoparticle processes to determine the average and standard deviation in the measured zeta potential.

2.3.4 Coating nanoparticles to improve stability and aqueous dispersion

Different materials can be used to coat nanoparticles to improve their characteristics including zeta potential (and therefore ability to remain in solution), such as amino acids polymers or proteins[194261261]. Glutamic acid was used to coat the nanoparticles because it is an amino acid commonly used by bacteria as a nutrient for growth, whilst also being anionic, meaning it is negatively charged[368]. To coat the copper oxide nanoparticles, mechanochemistry was performed by grinding glutamic acid and the nanoparticles together, causing the powdered amino acid to electrostatically adhere around the nanoparticles, a phenomenon that occurs via eutectic melt that later resolidifies. The glutamic acid coated CuO nanoparticles were then imaged using TEM to determine how the size and morphology of the coated nanoparticle changed. The resulting coated nanoparticles (as shown in Figure 2.4) can be seen, as black crystalline structures highlighting the nanoparticle whilst the grey areas indicate remaining glutamic acid that was not used in coating the nanoparticle.
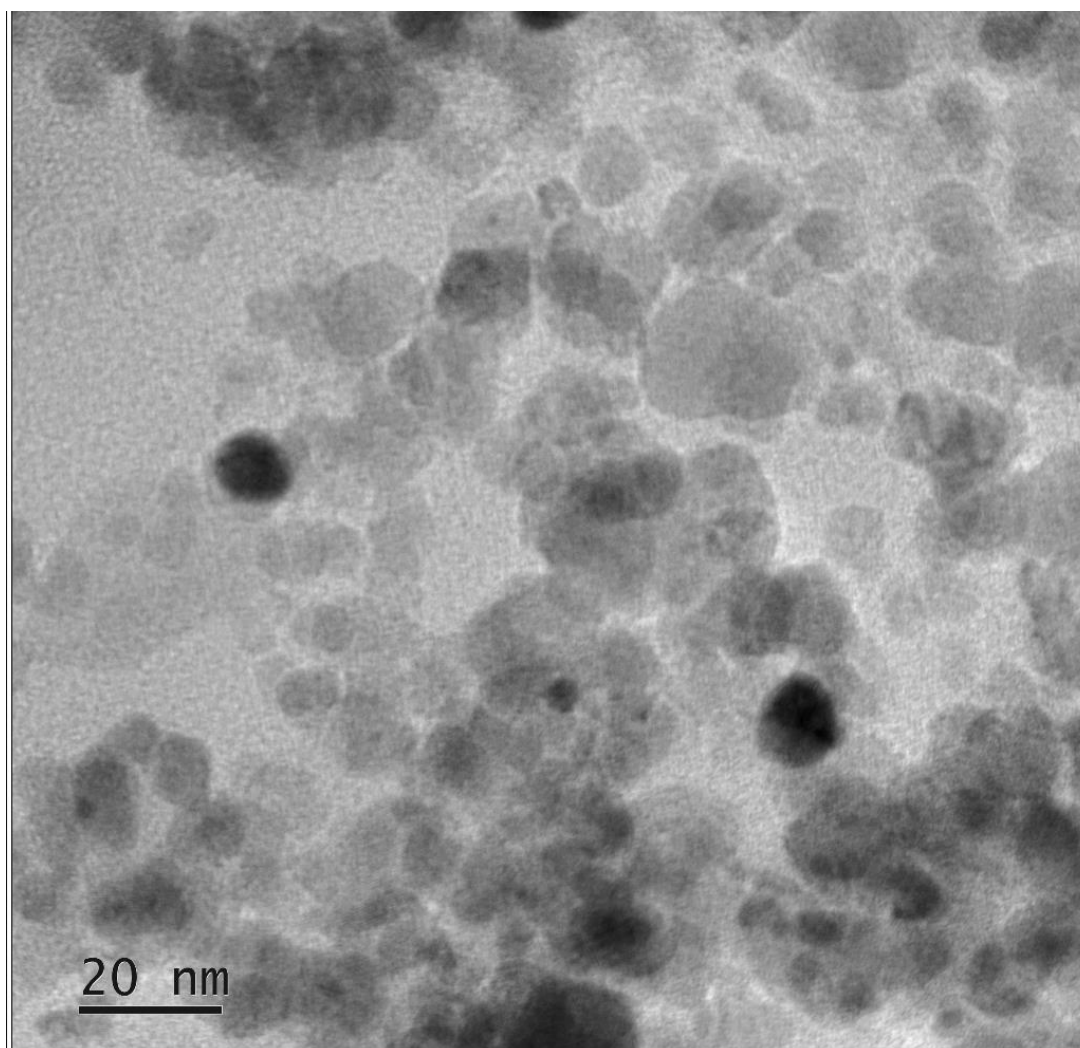
Figure 2.4 *Transmission electron microscope images of the copper oxide nanoparticles coated in glutamic acid. Crystalline structure is seen within the darker regions of the glutamic acid coated CuO nanoparticles whilst the lighter grey regions are the organic glutamic acid that has not been coated on the nanoparticles.*

After coating the nanoparticles and imaging *via* TEM, the new glutamic acid coated CuO nanoparticles were measured using the same process as 3.2.1, using ImageJ and masking to determine the size of the particle across multiple images. The glutamic acid coated copper oxide nanoparticles were measured as 21 ± 6 nm, which can be seen in the histogram below (Figure 3.5).
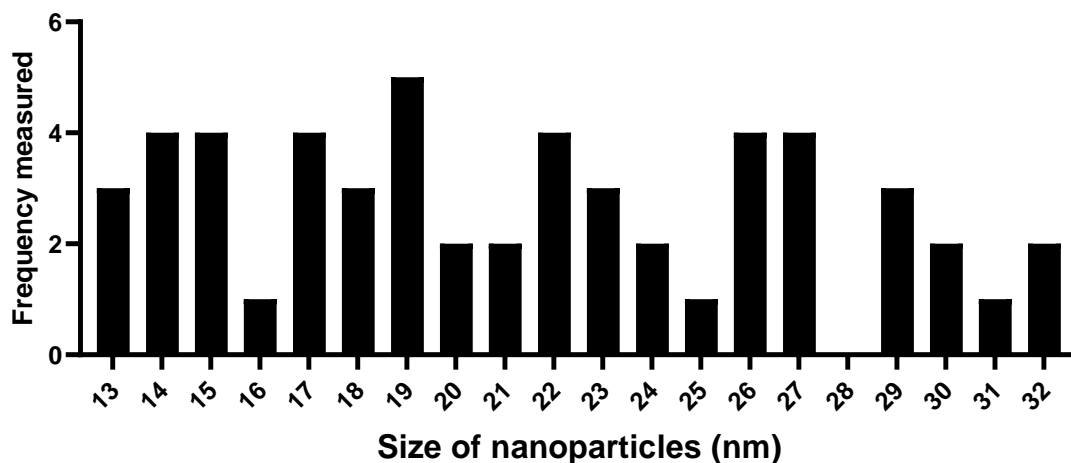
Figure 2.5 *Histogram of the size of glutamic acid coated copper oxide nanoparticles that were measured using TEM imaging. Average size of the glutamic acid coated copper oxide nanoparticles was measured to be 21.3 ± 5.5 nm, N = 50*

The hydrodynamic size and zeta potential of glutamic acid coated CuO nanoparticles were also measured to examine how this had changed because of the coating. By suspending the coated CuO nanoparticles in ultra-pure water, the hydrodynamic size was measured to be 123± 12 nm (Figure 2.6). The zeta potential of these coated nanoparticles was also measured and determined to be -42.0 ± 3.21 mV.
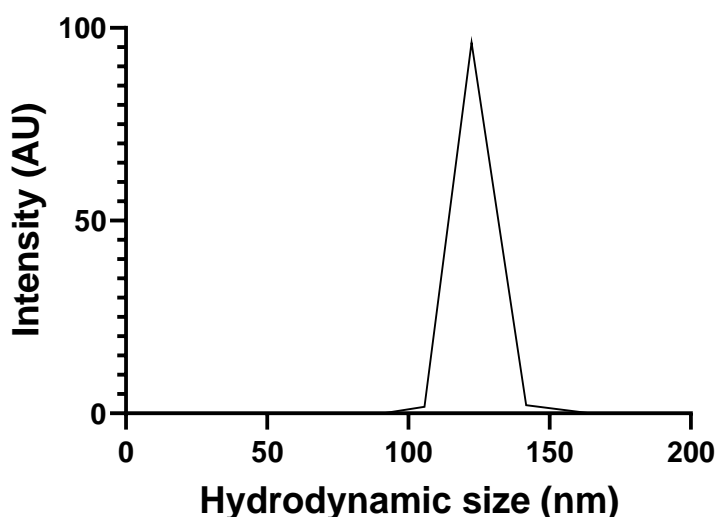
Figure 2.6 *DLS graph showing the hydrodynamic size of the Glu-CuO nanoparticles. The hydrodynamic size of glutamic acid-coated copper oxide nanoparticles was measured to be 123.1 ± 12.77 nm.*

A comparison between the measured size, hydrodynamic size, and the zeta potential of the uncoated and coated CuO nanoparticles can be seen below (Table 2.1).

CuO nanoparticle	Uncoated	Coated in glutamic acid
Measured size (nm)	5.8 ± 1.8	21 ± 6
Hydrodynamic size (nm)	75.0 ± 5.2	123.0 ± 12.7
Zeta potential (mV)	-0.4 ± 6.2	-42.0 ± 3.21

Table 2.1 *A summary table of the change in measurements between uncoated and glutamic acid coated copper oxide nanoparticles. The size of Glu-CuO nanoparticles increased compared to the uncoated, as well as the hydrodynamic size of the coated nanoparticles. However, due to the anionic state of glutamic acid, the zeta potential decreased, leading to higher stability within different solvent media.*

2.3.5 Thermogravimetric analysis of the glutamic acid coated copper oxide nanoparticles to determine amino acid coating load

To confirm the results of the mechanochemistry coating of the copper oxide nanoparticles in glutamic acid, thermogravimetric analysis was used. The initial mixture was a 1:1 w/w ratio between glutamic acid and copper oxide nanoparticles, which underwent mechanochemical grinding to coat prior to analysis. Thermogravimetric analysis showed the final ratio of water, glutamic acid and copper oxide nanoparticles was 0.0297:1.19:1 (1.34 ± 0.02%, 53.60 ± 0.02%, 45.06 ± 0.02%) respectively as seen below (Figure 2.7). This meant that for one gram of Glu-CuO nanoparticles, 0.457 grams would be copper oxide, and 0.543 grams would be glutamic acid.
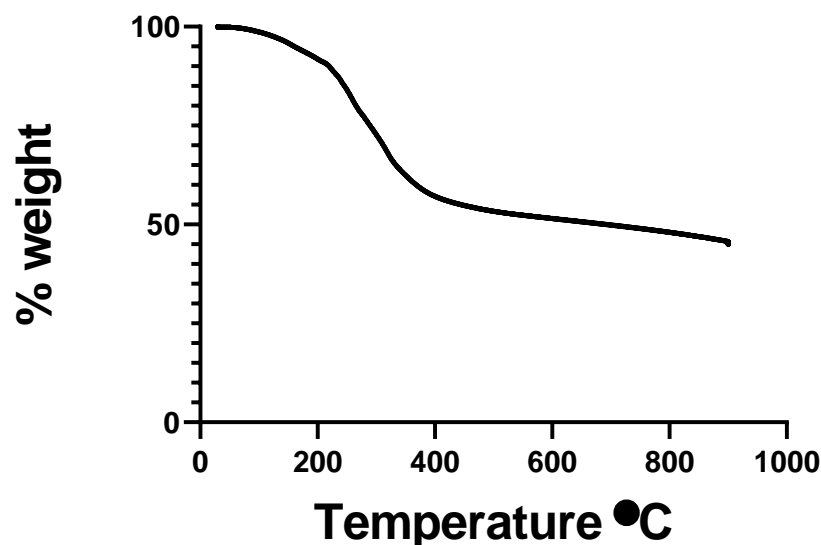
Figure 2.7 *The glutamic acid coated copper oxide nanoparticles, thermogravimetric analysis showing the change in mass of the glutamic acid coated copper oxide nanoparticles. Thermogravimetric analysis of the Glu-CuO nanoparticles to determine the weight of copper oxide nanoparticles to glutamic acid coating (1:1.19 w/w). N = 3 The error is absorbed by the symbol size.*

2.3.6 Bonding copper oxide nanoparticles to medical grade silicone tubing

With copper being well studied as an antimicrobial, a surface coating of copper should also be antimicrobial. To understand whether glutamic acid coated copper oxide nanoparticles can be adhered to medical grade materials, different coating techniques were investigated. Binding Glu-CuO nanoparticles to silicone tubing was performed using a three-step dip coating technique. Firstly, silicone tubing was submerged in a 0.1 M mercaptopropyltrimethoxysilane (MPTMS) solution for one minute. MPTMS is an organosilicon compound, defined by a silicon atom directly bonded to a carbon atom, which is used in various industrial processes as an adhesive agent, by increasing the number of reactive thiol groups on the surface of glass[369]. MPTMS when cured is also hydrophobic, which should reduce the bacterial cell's ability to adhere to the medical material. The silicone tube was next submerged into a Glu-CuO nanoparticle solution. The concentration of the copper oxide nanoparticle solution was determined by MBC assays at a concentration of 325.5 mg L^{-1}. These steps were analysed using a JEOL JSM-7100F SEM to examine the bonding after each step. As seen below (Figure 2.8) agglomerated nanoparticles can be seen adhered to the surface of silicone tubing.
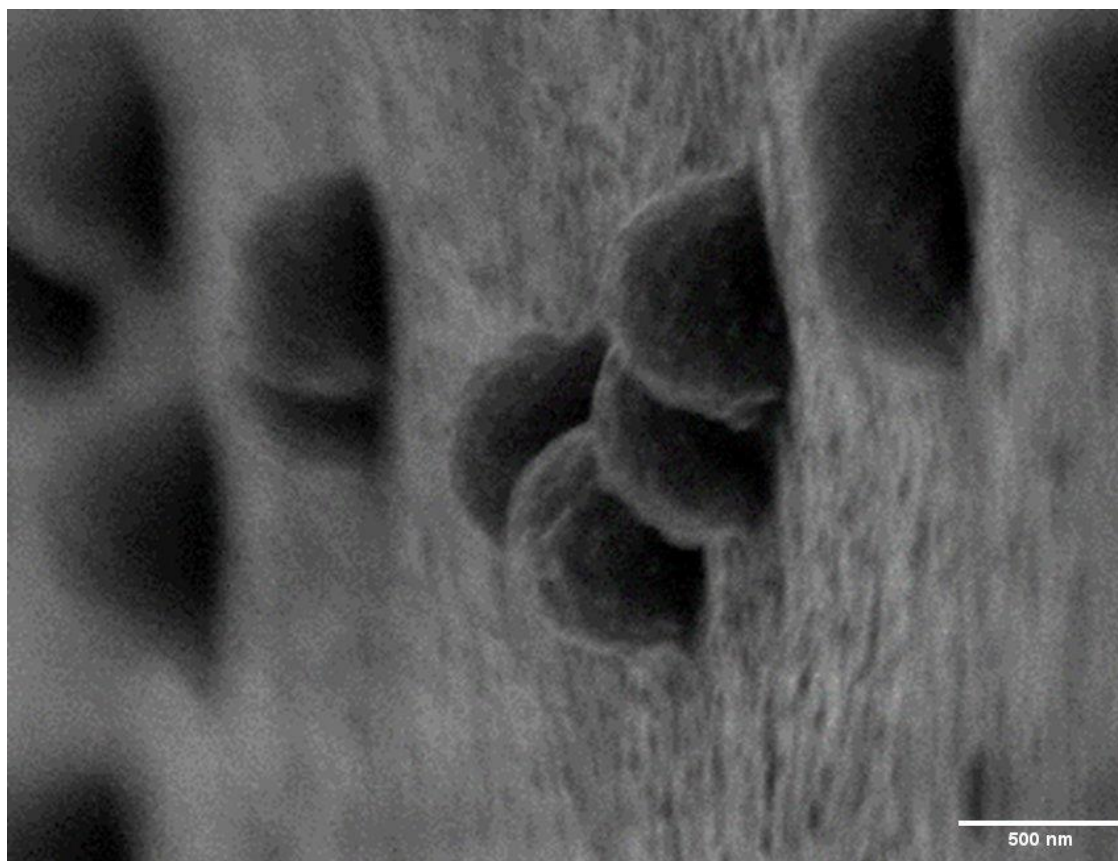
Figure 2.8 Scanning electron microscope images of Glu-CuO nanoparticles adhered to the surface of silicone tube. Clusters of Glu-CuO nanoparticles adhered to the surface of a silicone tube using MPTMS as a bonding agent between the silicone and the Glu-CuO nanoparticles

2.3.7 Evaluating the coating after initial dip coating and curing

During the evaluation of the two-step dip coating process, EDS was used to investigate the coverage the coating provided, and it was noticed that cracking occurred (Figure 2.9). This is due to the MPTMS drying too quickly during the curing phase of coating resulting in cracking and exposing the silicone tube underneath the nanoparticle coating. This cracking can be seen in Figure 2.9, using EDS that shows backscattering electrons (BSE) that detect the silicone tubing underneath as well as the elements detected from the coating materials with carbon and oxygen ignored from the spectral analysis due to their presence in most organic and inorganic materials.
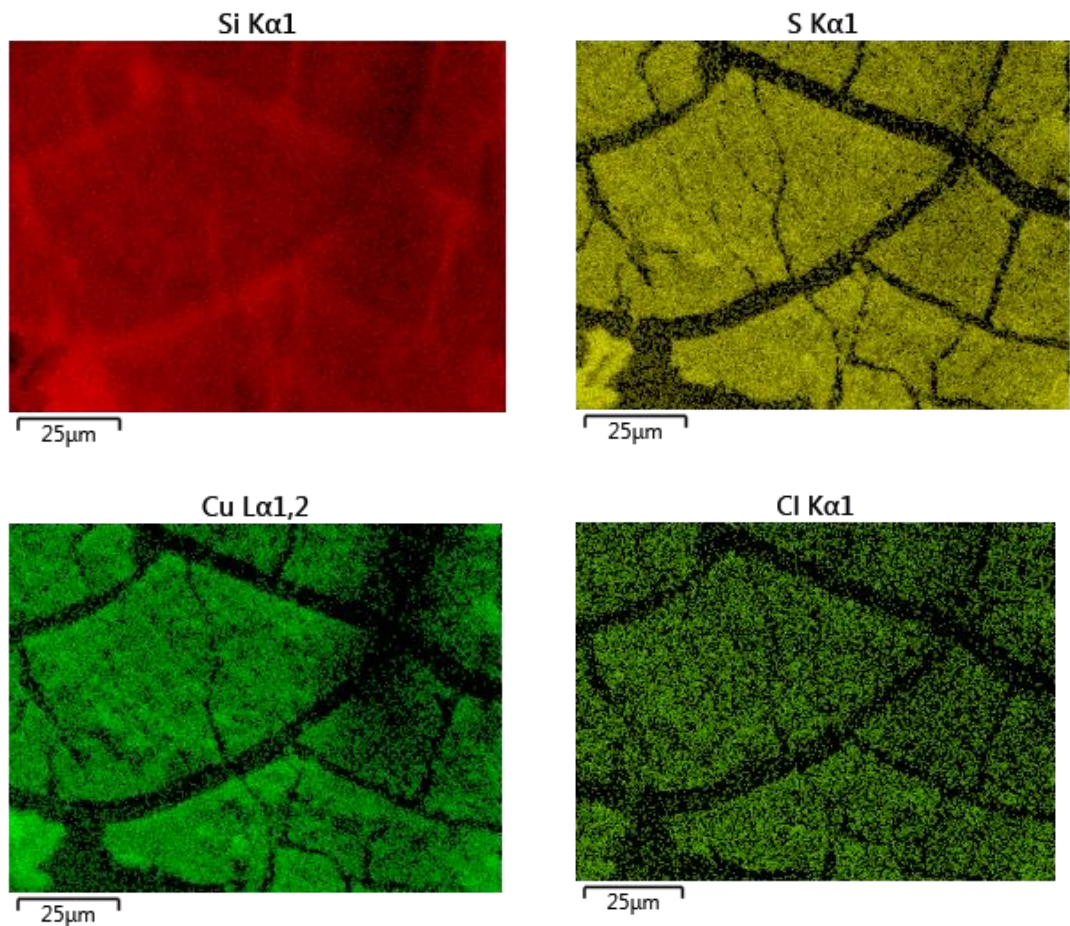
Figure 2.9 *EDS analysis performed on glutamic acid coated copper oxide nanoparticle coating, highlighting different elements in different colours. SEM-EDS of the Glu-CuO nanoparticle silicone coating. The EDS analysis of the coating showed that cracking occurred frequently. The coating was roughly one µm in thickness as incident electrons from silicone were present in the measurements.*

2.3.8 Introducing an undercoating and plasticiser to the coating to prevent surface fracture

Cracking of the antimicrobial coating could lead to bacterial binding to the silicone tubing inside the fissures, leading to the establishment of a biofilm and possible failure of the antimicrobial coating. It was therefore necessary to develop a coating process that reduced cracking and exposure of the uncoated silicone tubing as described in 2.2.2. Two different plasticisers were tested as possible solutions to prevent cracking and future degradation of the material coating. The two tested plasticisers were glycerol and polysorbate 80 as they are used in both the pharmaceutical and food industries for human consumption. The results in Figures 2.10-2.12 show that at all glycerol

102

concentrations, cracking was prevented, but in the polysorbate analysis, cracking still occurred. All future coatings tested were performed using a 0.1% glycerol solution as this reduced the quantity of the plasticiser and therefore its cost to include in the coating process, whilst also having more consistent results than the polysorbate 80.
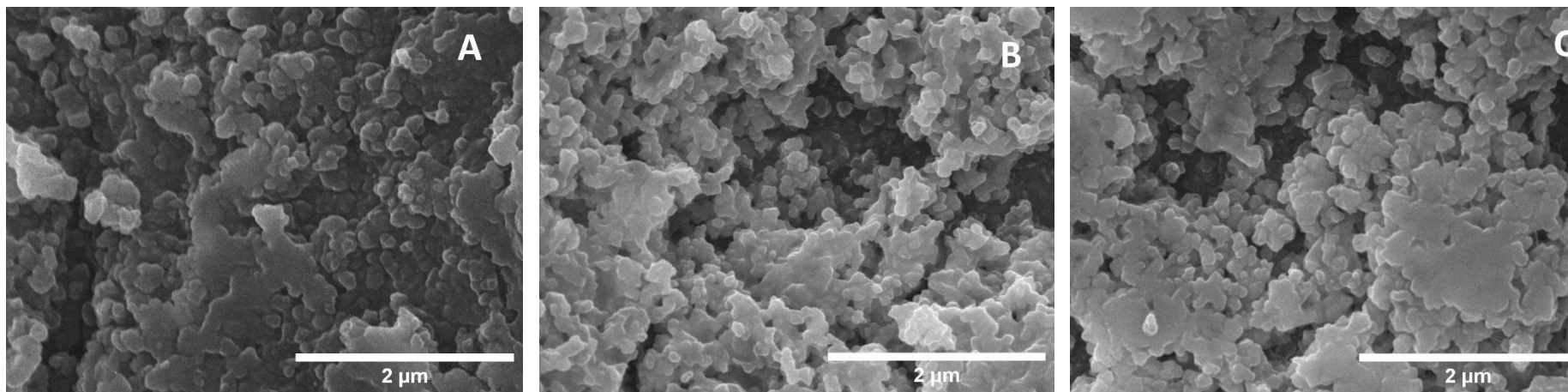
Figure 2.10 SEM imaging of increasing concentrations of glycerol as an additional step to reduce cracking in the material coating. During the coating process, concentrations of glycerol were added after the MPTMS coating step. A variety of concentrations were applied A) 0.1%, B) 1%, C) 2%. Coating steps were completed in triplicate and as all steps showed a clear reduction in cracking, 0.1% glycerol was used to reduce material use and keep the cost of the coating to a minimum.
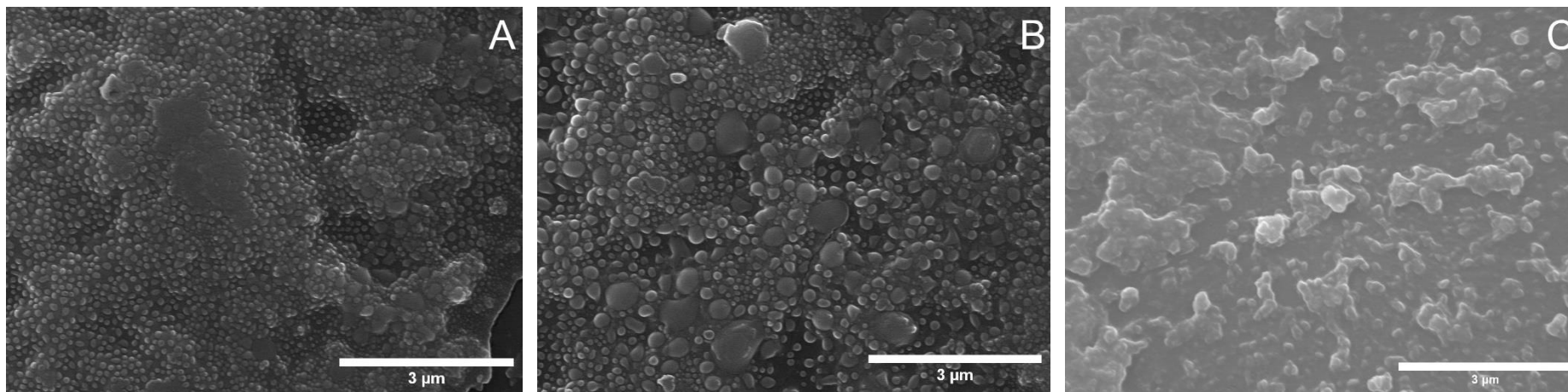
Figure 2.11 *SEM imaging of increasing concentrations of glycerol as an additional step to reduce cracking in the material coating. During the coating process, concentrations of glycerol were added after the MPTMS coating step. A variety of concentrations were applied: A) 5%, B) 10%, C) 100%. Coating steps were performed in triplicate and as all steps showed a clear reduction in cracking, 0.1% glycerol was used to reduce material use and keep the cost of the coating to a minimum.*
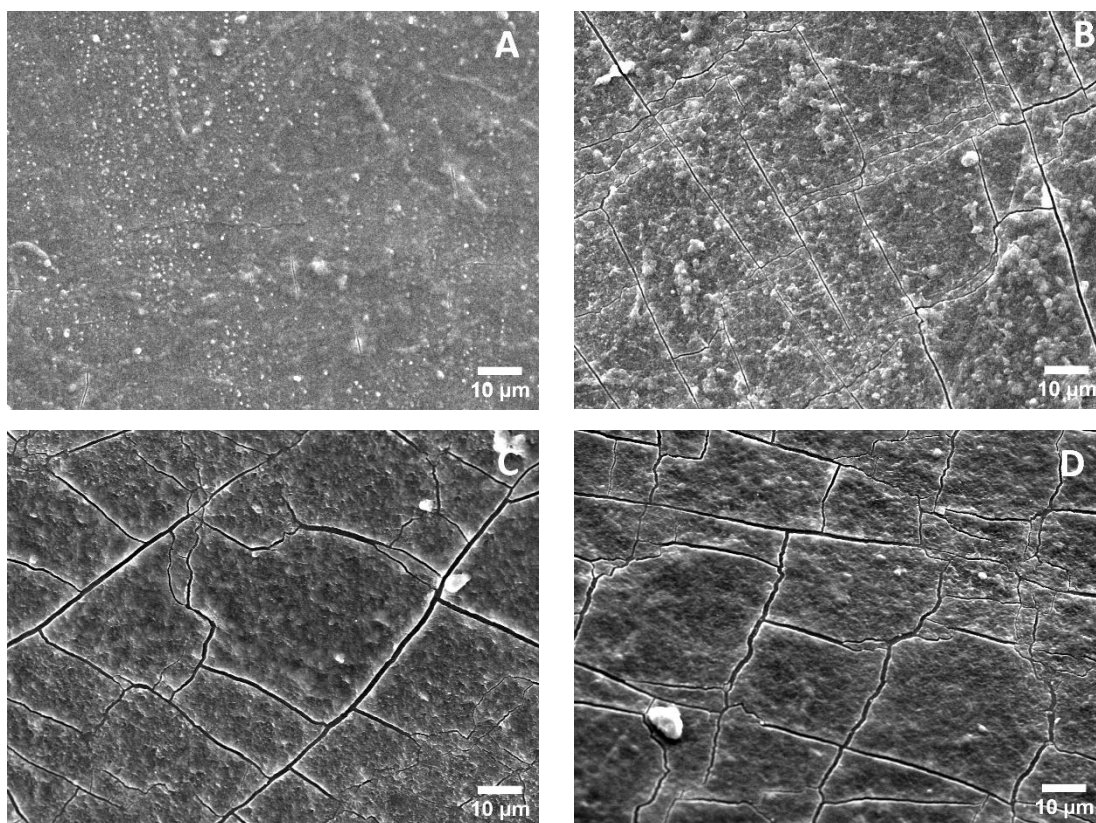
Figure 2.12 *SEM images of polysorbate 80, mixed into the Glu-CuO nanoparticle coating, ranging from 0.1% w/w to 5% w/w concentration showing that it is not a suitable plasticiser for this coating as cracking is still present at all concentrations. Concentrations of Polysorbate 80 were added during the coating stage prior to adding the mercaptopropyltrimethoxysilane. Concentrations higher than 5% were not used as the viscosity of the polysorbate was not appropriate for coating. A) 0.1%, B) 1%, C) 2%, D) 5%. All the coatings with polysorbate 80 showed cracking.*

2.3.9 Leaching of the dip coated material

Following the optimised coating methodology for tubular medical materials, analysis of the adhered coatings properties were performed. This was to establish whether the coating was robust and would not easily be removed during handling. Material leaching was tested to confirm whether any of the Glu-CuO nanoparticles would separate from the silicone tubing under local sheer forces from artificial saliva medium during test conditions to simulate what might happen in a patient upon exposure to saliva if the coated tubing was utilised as an endotracheal tube. This was performed by flowing artificial saliva medium, through coated material and performing ICP-MS on passed medium to determine the leached Glu-CuO nanoparticle content. The ICP-MS results

show that 800 ± 35,000 parts per billion, or 8 ± 35 mg L^{-1} was sheered from the material (Table 2.2).

Sample	Total Cu (ppb)	Cu (mg L^{-1})
Water used to create media	65000 ± 29000	65 ± 29
Artificial saliva medium	65000 ± 29000	65 ± 29
Leached artificial saliva media	73000 ± 6000	73 ± 6
Total leached copper	800 ± 35000	8 ± 35

Table 2.2 *Measured leaching from the glutamic acid coated copper oxide nanoparticle coating adhered to silicone tubing. The measured concentration determined by the resultant leached medium. The water used to create the media was measured separately to measure the background copper concentration. The artificial saliva media post creation was measured separately to determine any additional copper from the salts and other components. 73 mg L^{-1} was measured in the leached medium, indicating 8 mg L^{-1} had leached from coated silicone tubing after considering the background water and salt content.*

2.3.10 Thermogravimetric analysis of the silicone tube coated with glutamic acid coated copper oxide nanoparticles

Thermogravimetric analysis was performed on Glu-CuO nanoparticle coated silicone tubing to determine how much copper was loaded onto the silicone tubing and determine how much copper was deposited (Figure 2.13a). Uncoated silicone tube, coated silicone tube and coated copper oxide nanoparticles were evaluated side by side to compare the change in water content, the evaporation of the organic glutamic acid, and the oxysilane, mercaptopropyltrimethoxysilane. Each evaporating compound can be seen in the change of mass of both the coated nanoparticles and the nanoparticle coated silicone tube. The resultant weight of the copper oxide nanoparticle coating was determined to be 0.62% ± 0.007% (Figure 2.13b). The resulting copper loading on 1 metre of silicone tubing would be 1.276 grams of Glu-CuO nanoparticles.
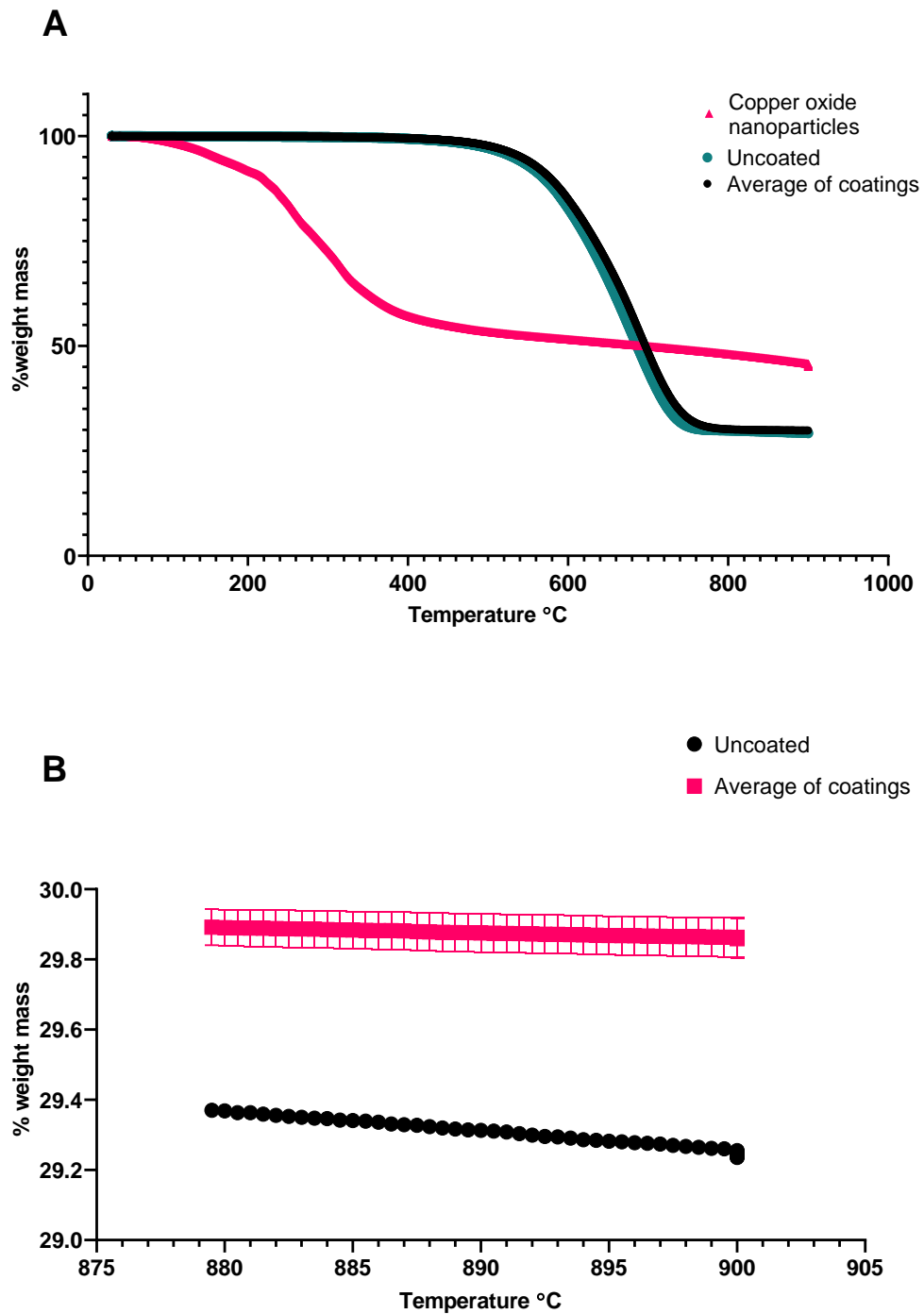
Figure 2.13 *Thermogravimetric analysis of the Glu-CuO nanoparticle coating on silicon tube. A. The full analysis of the Glu-CuO nanoparticle coating on silicone tube performed showing the changing weight over time as temperature increases. B. The final hundred data points measuring the uncoated and coated material after any organic matter had been sublimated.*

2.3.11 Measuring the potential cytotoxicity of glutamic acid coated copper oxide nanoparticles and MPTMS

To better understand whether the coating would be suitable for medical use in patients, testing the constituent parts of the coating using standard techniques such as an MTT assay to understand potential toxicity to human cells is required. If any component of the material is toxic, then the coating should not be used, and alternatives should be investigated. Analysis of the cytotoxic effect of copper oxide nanoparticles was investigated using the MTT assay, examining increasing concentrations of copper oxide nanoparticles and increasing molar concentrations of MPTMS. A HaCaT cell line was used as they are an immortal human skin cell line which is used extensively as model system for infection models and testing cytotoxicity of compounds. The toxicity of Glu-CuO nanoparticles depends on size and on concentration, with reports of smaller nanoparticles having higher cytotoxic effects[370]. The reported toxicity value of uncoated copper oxide nanoparticles at 23.5 nm in size was measured to have an LD_{50} of 413 mg kg^{-1} [371]. After performing the MTT assay, the measured significant level of toxicity was determined to be 350 mg L^{-1} seen below (Figure 2.14).
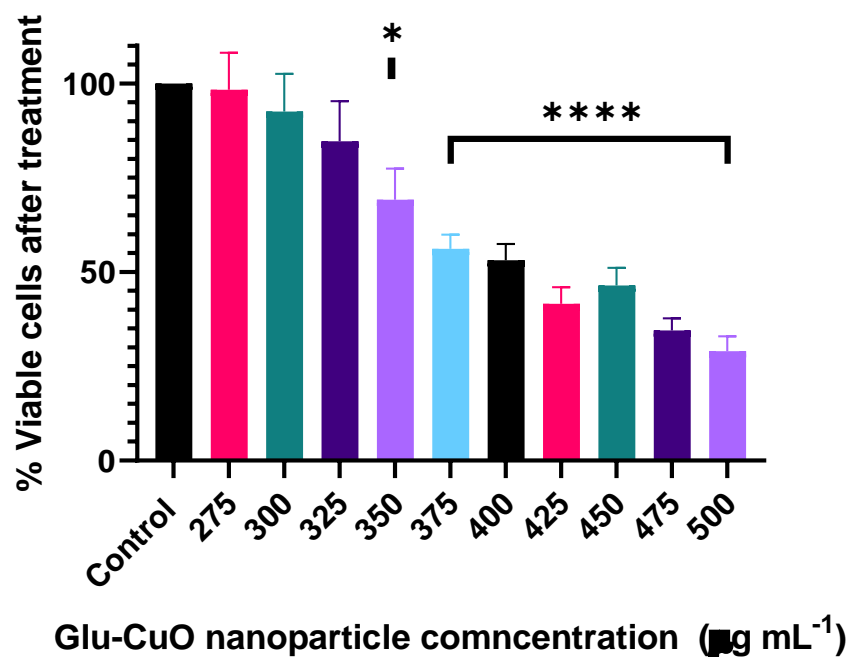
Figure 2.14 *Viable HaCaT cell percentage after treatment with copper oxide nanoparticles. The change in viable cells after 24 h treatment with an increasing concentration of copper oxide nanoparticles determined by an MTT assay. The viable cells recovered decreased with an increased concentration in nanoparticles. Statistical significance was performed where P* > 0.05 P**** >0.001 N = 9 using one-way ANOVA test.*

The toxicity of the MPTMS was also measured (Figure 3.15) and even at 0.05 Molar concentrations, MPTMS is toxic and human cells should not be exposed to this compound in liquid form due to its significant toxicity even at very low concentration.
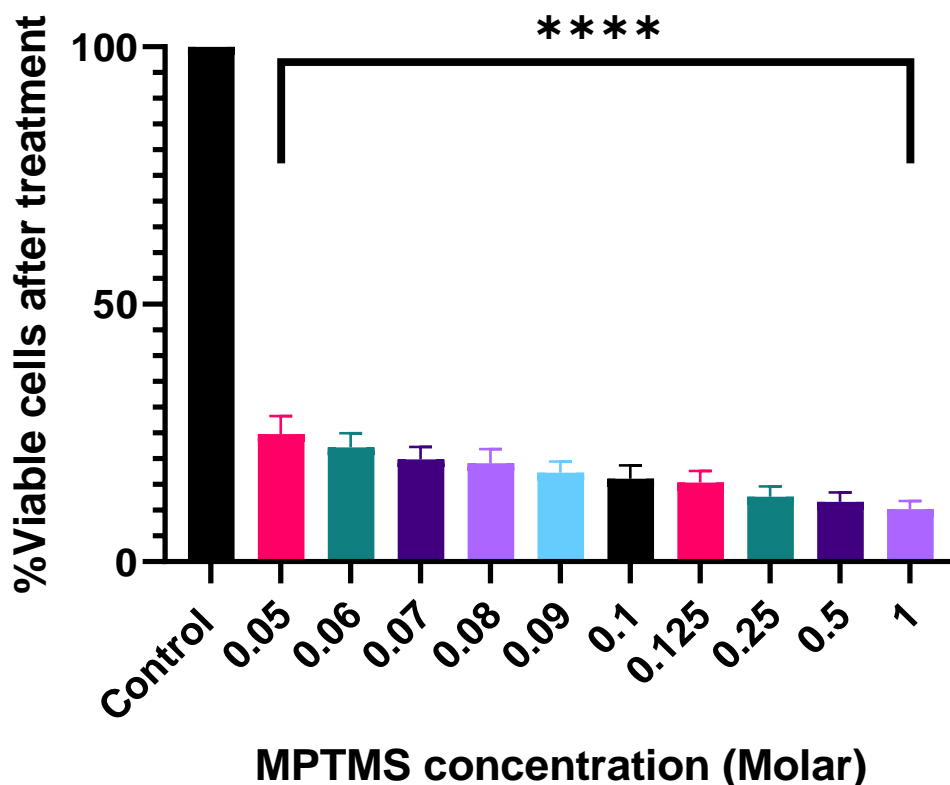
Figure 2.15 *The percentage of viable HaCaT cells after 24 hours exposure to MPTMS. The indirect measurement of viable cells recovered after 24 hours of exposure to liquid MPTMS. Statistical significance was performed where P > 0.001 N = 9 using a one-way ANOVA test*

Due to the measured toxicity of the MPTMS (Figure 3.16), further evaluation of MPTMS was performed using ISO 10993-5:2009 the international standards organisation for testing cytotoxicity in materials, where 3 mm by 3 mm slices of silicone tubing were used as a surface for coating at various concentrations of MPTMS[372]. This ISO standard tests the cytotoxic effect of a compound on a material, which in the case of MPTMS, allowed testing of the cured bonding reagent rather than leaving the bonding agent in liquid form. The tests showed vastly different cytotoxic effects, with toxicity only presenting at 0.25 Molar concentration, however the toxic effects may be present at lower concentration, just above the last insignificant toxic effect of 0.1 Molar concentration, as seen below (Figure 2.16). All materials were coated with a 0.1 Molar concentration, ensuring that the total exposure to MPTMS was below measurable toxic levels whilst reducing the total cost of the coating.
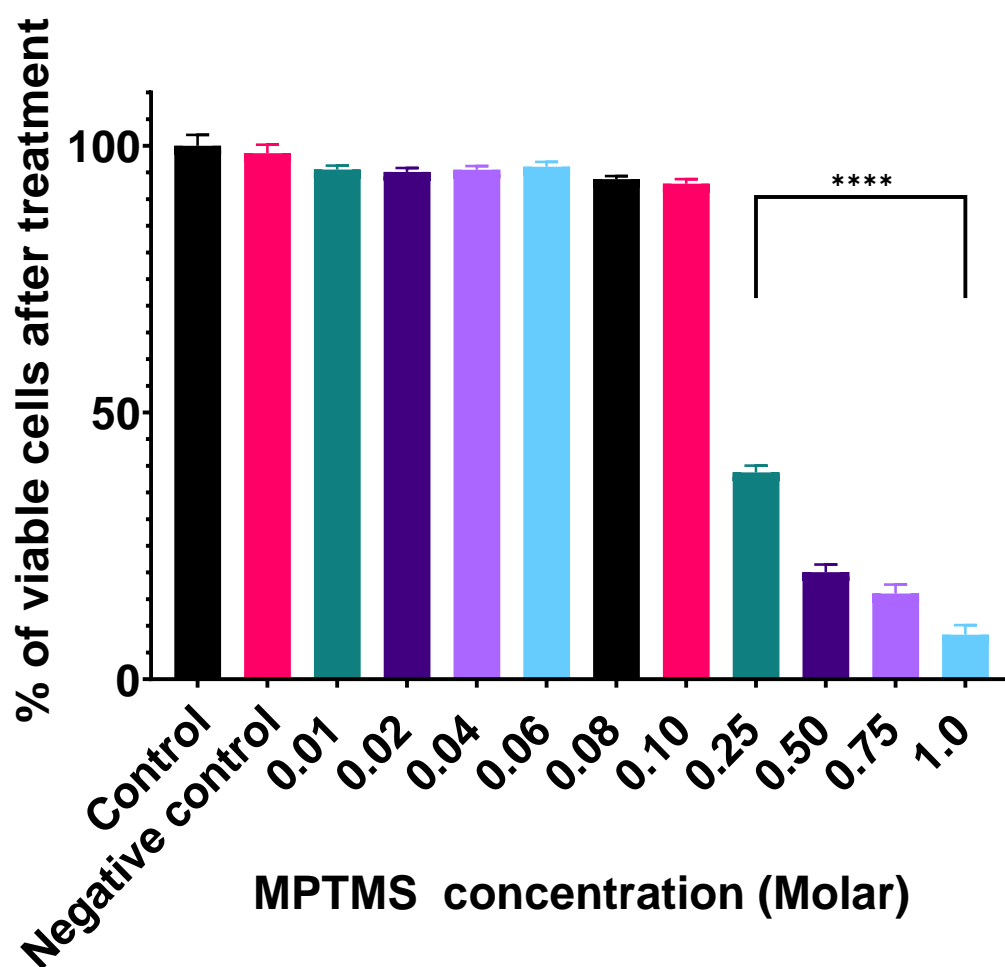
Figure 2.16 *The cured MPTMS results following ISO 10993-5:2009. When the MPTMS was cured onto silicone tubing and placed into the 96-well plate, the resulting toxicity was considerably lower than that of the liquid MPTMS. Statistical significance was performed where P > 0.005, N = 9 using a one-way ANOVA test*

2.3.12 Spray coating for rapid mobile adhesion of an antimicrobial coating

MPTMS can be cured by using Ultraviolet (UV) light for 30 minutes to cure the Glu-CuO nanoparticle coating for rapid mobile coating through adhesion. Using MPTMS in this way would allow the curing process to be conducted in any environment with safe UV curing. An example of this may be in an operating theatre, where medical implants, often made with stainless steel or titanium are sterile, but may require ad hoc modification prior to implantation, which is common practice in maxillofacial surgery. To reduce the likelihood of infection after implantation of modified materials, these materials are often then dipped into a liquid antibiotic such as gentamycin, which has

significant implications for the spread of antimicrobial resistance and should be avoided where possible. By using a sprayable, rapidly cured coating, the surface could be coated in an antimicrobial material such as the Glu-CuO nanoparticle coatings described herein that does not drive antibiotic resistance but would reduce the incidence of infection.

To test whether medical materials can be successfully coated using this rapid spray coating and curing technique, small 1.27 cm, diameter coupons of stainless steel were spray coated with 0.1 M MPTMS, followed by Glu-CuO nanoparticles at MIC concentration, 325.5 µg L^{-1}, three times. This MPTMS bonded Glu-CuO nanoparticle coating was examined using SEM-EDS to evaluate the coating (Figure 2.17) where the coverage was measured using ImageJ to be 70.69 ± 1.49 % of the total area[367].
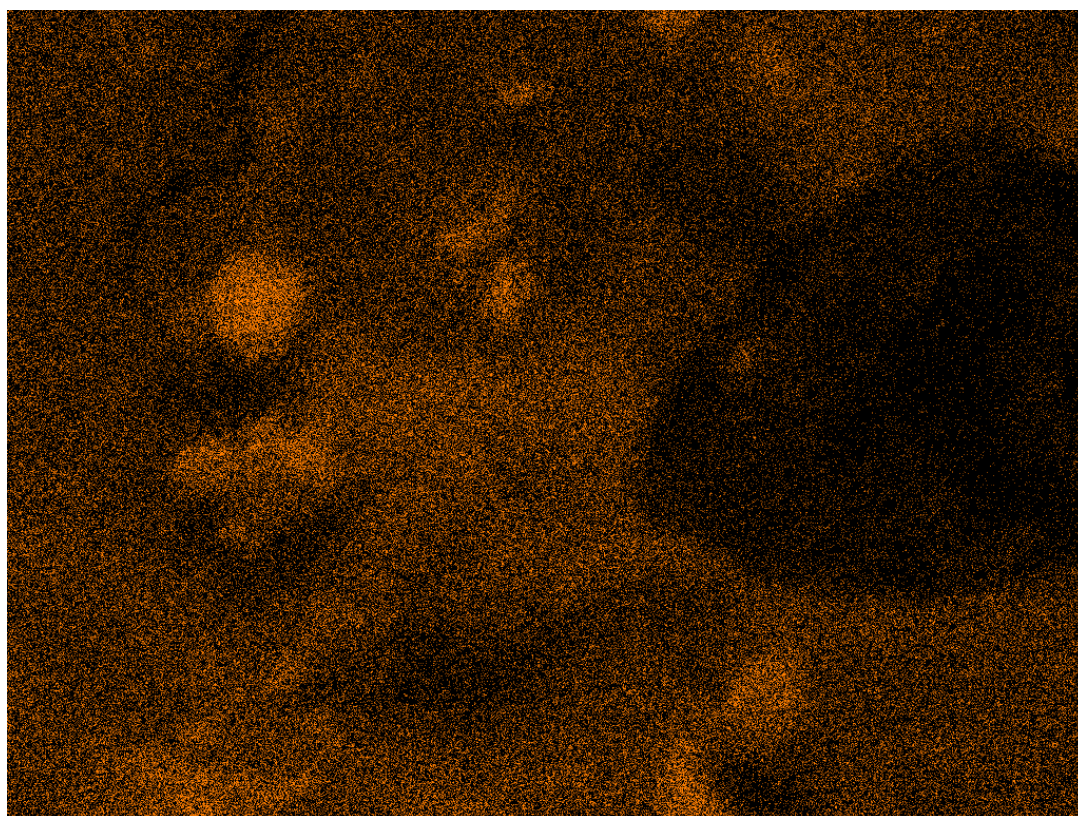
Figure 2.17 EDS spectral image showing copper electron scattering. The SEM-EDS image of a stainless-steel coupon, showing the scattered copper electrons in orange pixel regions. The coverage of this coating was calculated to be 70.69 ± 1.49% of the total area. N = 3 across three different coated images.

2.3.13 Leaching of the mobile coating on stainless steel CDC coupons

Leaching assays were performed on Glu-CuO nanoparticle coated stainless-steel coupons in a 24 well plate. The coupons were coated 45 minutes prior to submersion in a plasma like medium, 15 minutes after the 30-minute cure time. The plate was shaken at 150 RPM for 24 hours to recover any material that may leach in the following 24 hours. The results can be seen below (Table 2.3), where 2.73 mg L^{-1} of copper was seen to leach from the material.

Sample	Total Cu (ppb)	Cu (mg L^{-1})
Water used to create plasma like medium	65000 ± 250	65 ± 0.25
Plasma like medium	67000 ± 520	67 ± 0.52
Leached media	67000 ± 1100	67 ± 1.1
Total	2700 ± 1100	2.7 ± 1.1

Table 2.3 *The ICP-MS data acquired from testing leached materials after spray coatings with copper oxide nanoparticles. No leaching was observed from the tested material as any material detected is below the level of copper in the water and control media that was also detected using ICP-ms. N= 30*

2.4 Discussion

After each batch of nanoparticles were created, TEM images like that seen in Figure 2.1A were gathered and used to confirm the size of the nanoparticles. ImageJ was used to threshold, mask and analyse the size of the nanoparticles seen in Figure 2.1, where 50 nanoparticles were measured, and the size was determined to be 5.8 nm ± 1.8 nm from the distribution seen in Figure 2.2. These nanoparticles were made in abundance and met the criteria of a nanoparticle as defined by the European commission, whilst also being easy to synthesise using the spinning disc reactor[373]. Using TEM along with ImageJ and scripts to measure the nanoparticles, was an efficient and repeatable method, with the ability to mask the measured area, allowing easy verification of the size of the nanoparticles. DLS was used to measure the hydrodynamic size of the copper oxide nanoparticles, and the uncoated nanoparticles were measured to be 74.93 ± 5.170 nm as seen in Figure 2.3, larger than the measured value from TEM and ImageJ. However, true comparison between the size measured using TEM and the size measured using DLS is not appropriate due to the difference in measurements made. Hydrodynamic size is not equivalent to the size of a nanoparticle, and this is due to the electrostatic forces being larger at the surface of nanoparticles causing light to scatter before interaction with the nanoparticle. This measurement is the behaviour of the nanoparticle, as if it were a large solid sphere and is given by the Stokes-Einstein equation[374]. However, it can be used to determine the polydispersity of the coated copper oxide nanoparticles and shows that they have a limited polydispersity index value of 0.35 indicating a low level of variance between different nanoparticle sizes which is also seen in the variance of the measured nanoparticles described by TEM and ImageJ.

These uncoated nanoparticles were held in aqueous suspension for later testing of their antibacterial properties in inhibitory and bactericidal testing, however, it was observed that they precipitated and subsequently were not appropriate for use in these tests. The zeta potential, a measurement of the electrostatic repulsion or attraction of the nanoparticle to the suspension solution, was taken and measured to be -0.4 ± 6.2 mV indicating that the nanoparticles would not remain in suspension. The solution to this was coating the copper oxide nanoparticles in an amino acid via mechanochemical grinding, a typical solution to improving the solubility of nanoparticles whilst retaining their properties[247]. Nanoparticles are routinely coated in amino acids to improve their

biocompatibility and reduce their toxic potential, with amino acids such as Lysine being routinely used[375,376] . Glutamic acid is used to coat nanoparticles, although these nanoparticles are predominantly paramagnetic nanoparticles, such as magnetite or super paramagnetic iron oxide nanoparticles[377,378]. Furthermore, glutamic acid is an essential amino acid that not all bacteria produce, so exploring the use of glutamic acid to hide the bacterial toxic nanoparticle was undertaken in this chapter. The nanoparticles that were recovered from the mechanochemical grinding were all added to water and allowed to settle for 24 hours. The settled solution showed both precipitant nanoparticles, nanoparticles that were not coated in the glutamic acid, and a blue supernatant. The supernatant contained the coated copper oxide nanoparticles and copper(II) ions complexed to the amino acid indicated by its colour and was removed from the precipitant carefully. The coating changed the size of the nanoparticles seen in Figure 2.4, both measured by TEM, 21 ± 6 nm and DLS, 123.1 ± 12.77 nm, the zeta potential after coating in glutamic acid was measured to be -42.0 ± 3.21 mV, which showed that the coated nanoparticles were stable in solution due to their higher electrostatic potential, causing them to be repulsive to water molecules. This allowed the conventional microbiology experimentation such as minimum inhibitory concentration and minimum bactericidal concentration (MIC and MBC) assays to be performed. The mass of the coated nanoparticles was then measured at 900°C to determine the resulting mass of glutamic acid that was sublimed off the copper oxide nanoparticles. Again, this measurement was taken past the boiling point of glutamic acid to minimise the effect any remaining glutamic acid had on the weight measured. The measured weight of glutamic acid was 53.60 ± 0.02% and the copper oxide nanoparticles were measured to be 45.06 ± 0.02% weight, indicating the 1.19:1 w/w ratio between the glutamic acid and the copper oxide nanoparticles as seen in figure 2.7 and 2.13. This ratio is larger than the 1:1 mass ratio that was mixed initially, indicating some of the nanoparticles were not coated and confirming the previous decision to remove the supernatant from the precipitant before making measurements of the coated nanoparticle solutions.

This precipitation technique in conjunction with the spinning disc reactor, produced nanoparticles that were smaller than those produced by precipitation techniques alone[379, 380]. The addition of the spinning disc reactor reduced the dispersity of the nanoparticles significantly compared to those produced in the literature[381, 382]. These smaller nanoparticles were then coated using glutamic acid, *via* mechanochemistry to improve stability in solution and improve biocompatibility compared to unfunctionalized copper oxide nanoparticles agreeing with literature, where previous work showed that the functionalised nanoparticles possessed greater antimicrobial effects than unfunctionalized nanoparticles[247]. Further analysis of these nanoparticles showed that coating these nanoparticles *via* mechanochemistry in glutamic acid increases the size of the nanoparticles by a factor of four, indicating that this is a viable alternative compared to other coating techniques[383].

These coated nanoparticles were then adhered to various medical-grade materials using 3-mercaptopropyltrimethoxysilane (MPTMS). MPTMS is used in various industries for a variety of different applications such as water treatment and biosensor applications[384, 385]. Developing this coating technique, which applied a homogenous and isotropic coating to medical devices was essential for testing the functionalised nanoparticles as an antimicrobial coating. For tube based medical devices, a dip coating was decided upon as it offered the ability to coat both the inner and outer diameter of the tube and is a standard coating technique used for a variety of different applications[316,386, 387].

Testing of the coating included EDS to analyse the surface profile of the coating, examining whether dip coating was homogenous and isotropic. Initial imaging using EDS showed that single coating caused cracking and different techniques were tested to determine whether this could be reduced or prevented entirely. Firstly, a double coating was applied where a first coating was applied and allowed to cure for 24 hours, then a secondary coating was applied and allowed to cure before EDS was performed, the results of which are seen in Figure 2.9. These EDS images show that cracking still occurs on the outer layer, but due to the inner coating, there is still full coverage of copper oxide nanoparticles. However, this double coating significantly increased the production time and increased the number of nanoparticles used in each coating, which is undesirable for industrial application. Another way to prevent the cracking was to add

plasticisers, with glycerol and polysorbate 80 being the two chosen, as they are safe for consumption. A range of concentrations from 0.1% to 100% glycerol mixed with water w/w % was added as a step between the MPTMS dip coat and the copper oxide nanoparticle coating and allowed to cure. Glycerol showed that at all concentrations it aided in preventing the MPTMS Glu-CuO nanoparticle coating from cracking. Meanwhile the polysorbate 80 was ineffective at any concentration tested. A triple coating was decided upon to move forward with, as the change in curing time between coatings that included the plasticiser and those without was negligible. This curing process required multiple wait steps that slowed down the coating process, culminating in a 24 hour wait step. Thermogravimetric analysis was also used to examine the additional weight the coating had on the silicone tube. By comparing uncoated silicone tubing to coated silicone tubing, the weight difference of the additional layer of copper oxide nanoparticles, not including the MPTMS and glutamic acid was determined to be $0.62 \pm 0.007\%$ of the total weight of tubing which can be seen in Figure 2.13 showing a negligible weight increase of the total tube weight.

Adherence of nanoparticles to various materials using oxysilanes is a developing field in medical research[388]. Whilst the application of oxysilanes and the process of salinization is well studied, the potential to use this process for medical applications is not well studied. The work performed herein, showed that it is possible to adhere Glu-CuO nanoparticles to medical grade silicone using a simple coating technique. After initial testing and observing the cracking caused by rapid curing on a malleable surface, glycerol, a food safe and widely used plasticizer was added at a low concentration of 0.1 w/w volume, to improve the robustness of the coating[318]. This robust coating allowed an active antimicrobial material to readily adhere to medical devices such as endotracheal tubes, which are a major source of health care associated infections[280].

Investigation of the leaching was performed by drawing artificial saliva medium (ASM) through coated tubes for 24 hours and measuring the resultant leached copper in the ASM. Leaching is typically performed in water or a saline media, such as Phosphate Buffer Saline (PBS), which is an inert medium and not representative of the conditions the material will be subjected to in the real world[389]. Evaluating this leaching was important as it is determined the concentration where copper oxide nanoparticles

present a cytotoxic effect on human cells at sufficient concentration and whether this tubing could be used safely in a medical application in contact with humans[390, 152]. Evaluation of the tube coated with copper oxide nanoparticles, and accounting for the copper found in the components of the leaching medium showed 8 mg L^{-1} was leached from the material.

Toxicity of the coating was measured in two steps, firstly the Glu-CuO nanoparticles were measured against HaCaT epithelial cells in an MTT assay at concentrations ranging from 275 mg L^{-1} to 500 mg L^{-1} with significance determined to be 350 mg L^{-1}. Then the MPTMS was measured to calculate the maximum concentration that can be applied before a toxic effect is observed. Firstly, this was performed with the MPTMS in liquid form, however, from the results, illustrated in Figure 2.15, in liquid form MPTMS is toxic against HaCaT cells at all tested concentrations. However, MPTMS can be used to remove heavy metals from water and would not be used if it was potentially toxic to ingest[391, 392]. This changed the way MPTMS was tested and as such another MTT assay was performed, however, it was evaluated by following ISO 10993-5:2009, where 3 mm by 3 mm silicone tube cuttings were treated and added to cells, with both a negative control and a blank control to determine the effect of contacting the silicone tube directly onto the cells[372]. No significant negative effect was measured when placing the silicone tube onto the cells, and toxicity caused by MPTMS was only observed at greater than 0.10 Molar concentrations as seen in Figure 2.16, however, the next concentration tested was 0.25 Molar, a significant jump.

The leaching of the Glu-CuO coating was found to be minor compared to the concentration of the loaded coating, however, excessive copper intake is known to be toxic[393, 394]. To evaluate whether the leached concentrations were toxic, tissue culture techniques, using HaCaT cells, an immortal epithelial cell line, were performed to evaluate the toxicity of the copper oxide nanoparticles and compare it to other studies. The measured toxicity of the Glu-CuO nanoparticles was measured to be 350 mg L^{-1}, which is lower than literature values of 413 mg kg^{-1}, assuming a conversion of 1 litre to 1 kilogram[371]. The toxicity of copper oxide nanoparticles is dependent on size and as the toxicity measured by Chen *et al*, have an average size of 23.5 nm and the nanoparticles coated in glutamic acid, produced in this work, have a size averaging 21 nm[180]. This

indicates that either the increase in size significantly increases toxicity, or the enhanced bioavailability of the copper coated in the amino acid increases uptake, causing toxic effect due to a lower concentration[180]. MPTMS was evaluated as it is reported to be toxic in the safety data sheet of the chemical with values of its lethal dose occurring at 730 μL kg^{-1} in rats[395]. This high toxicity was observed when tested against HaCaT cells, as all measured concentrations were significantly toxic, however, due to the application of MPTMS in various industries, including wastewater management, it was remeasured after the MPTMS had cured on silicone tubes[372,396]. Toxicity of the cured MPTMS was measured between 0.1 molar and 0.25 molar concentration, with 0.1 molar being the highest measured concentration with no toxic effect, showing that it can be used as an adhesive in a material coating and that this material coating should be considered safe.

To determine whether the spray coating technique was sufficient, EDS analysis of spray coated CDC reactor coupons were imaged (as seen in Figure 2.17). After spraying, these coupons were cured for 30 minutes using UV at 254 nm and to test this curing, leaching was performed straight after curing to determine how well the MPTMS coating had cured. The results in Table 2.3 show that a small amount of Glu-CuO nanoparticles leached from the material coating on the stainless-steel coupons. The rapid spray coating and curing of the coupons means that *ad hoc* modification of the surface material can be recoated with an antimicrobial coating without the need for antibiotics. This is a novel rapid coating of an antimicrobial material on the surface of medical grade materials that builds from modern coating techniques.

As MPTMS can be cured quickly with UV irradiation, the final investigations of the coating were performed[397]. Medical materials are sometimes modified *ad hoc* during surgical procedures to adequately fit the patient requiring them and conform to the structure of the patient's skeletal structure, in the case of orthopaedic implants[398, 399]. A spray coating was applied to stainless steel coupons to show the adhesive MPTMS still adhered Glu-CuO nanoparticles to another medical grade material. This novel adherence technique could be cured within 30 minutes using UV irradiation confirming literature results and showed that minimal Glu-CuO nanoparticles leached from the material and that this was at concentrations below toxic effects were present. These coating techniques allow a known antimicrobial to be coated to various medical grade

materials, whilst being below a toxic limit to HaCaT epithelial cells, the microbiological evaluation and efficacy of the coating against bacteria will be determined in the next thesis chapter.

In this chapter, the novel coating of the glutamic acid coated copper oxide nanoparticles using 3-mercaptopropyltrimethixysilane was explored. The precipitation technique was employed, which has extensively been used in literature, to create copper oxide nanoparticles, with a new spinning disc reactor technique used to mass produce quantities of nanoparticles and offers a scalable production of these nanoparticles. Exploration of coating these nanoparticles in glutamic acid, an essential amino acid that not many bacteria can produce, showed that whilst they increased the size of the particles, they also increased the stability of the nanoparticle, which allowed them to be tested in conventional antimicrobial assays. These coatings could be cured by both a dip coating and spray coating, offering their own unique benefits, with both a tubular and topological surface being coat able. Finally, the ability to rapidly coat and cure using UV irradiation allows novel *ad hoc* application of antimicrobial coating. This offers a novel alternative to dipping orthopaedic implants in antibiotics after intraoperative modification but prior to implantation.

Chapter 3. Antimicrobial testing of glutamic acid coated copper oxide nanoparticles on medical materials

3.1 Introduction

Establishing new antimicrobials is critical to prevent the economic and social loss that will arise if antimicrobial resistance continues to spread[400]. With the number of new antibiotics coming to market reducing yearly, alternative antimicrobials are required[401]. Currently, predicted estimates suggest that by 2050, ten million people will die per year due to antibiotic resistant pathogens[400]. These pathogens include the ESKAPE species, *Enterococcus faecium, Staphylococcus aureus, Klebsiella pneumoniae, Acinetobacter baumannii, Pseudomonas aeruginosa* and *Enterobacter* species[133]. These species are all designated by the World Health Organisation (WHO) as critical or high priority pathogens crucial for research and development of new antibiotics, showing that the currently available antibiotics available are failing[90]. However, there are other bacterial species, which are not listed as critical or high priority such as *Salmonella enterica* and *Staphylococcus epidermidis* that are also developing strains, which are antibiotic resistant[122].

 A well-known alternative to antibiotics are antimicrobial metals, such as silver and copper, which have been used for this purpose both knowingly and unknowingly at different stages of human history[153]. Due to the oversubscription of antibiotics and the subsequent evolution of antibiotic resistance seen in many species, metals are being revisited with the aim of producing new antimicrobials[47,48149]. Copper alloys, such as brass, are currently employed in hospitals on common touch surfaces as there are measurable touch killing effects[141]. These metals can be made into nanoparticles using various techniques such as the precipitation method used in Chapter 2, allowing them to exist with excellent surface to volume ratio, whilst maintaining their antimicrobial properties[195]. Furthermore, it has been established in Chapter 2, that these nanoparticles can be adhered to different medical grade material surfaces using 3-mercaptopropyltrimethoxysilane. Whilst metals have been known as antimicrobial for thousands of years, nanoparticles are a modern material that is becoming increasingly important in the modern age, and further research in their therapeutic potential is

critical[402] The antimicrobial properties of these metals occur in two different techniques, firstly, copper oxide nanoparticles are ionic. This state causes free electrons to enter the bacterial cell, creating reactive oxygen species that lead to cell death[156] Secondly, the ionic state of the nanoparticles leads to adhesion to cell membranes, which will ultimately cause cell lysis[145]. This modern advancement of turning metals into nanomaterials coupled with novel research into different a new adhesive technique targeting nanoparticles, allows conventional and new techniques into antimicrobial testing in this nano form. Standardised testing such as minimum inhibition concentration and minimum bactericidal concentration assays can be performed to determine the antimicrobial activity level of the particles, as well as evaluating various coatings using industry standard techniques such as the MBEC assay[366]. Assays such as this allow for reproduceable biofilm examination, and alongside the MBC's can be used to determine antibiotic material coatings. Biofilms form one of the major mechanisms of tolerance and resistance to antibiotics and other antimicrobials and consequentially are a major area of research, with the aim to prevent and reduced biofilm formation[189]. These biofilms are often found on medical devices such as endotracheal tubes and orthopaedic implants, so new material coatings such as the Glu-CuO coating, created in Chapter 3 offer therapeutic windows to treat these biofilms and subsequent biofilm contamination.

The coating of nanoparticles can be applied in various ways, by both dip coating and by spray coating allowing for diverse application across multiple surfaces and materials (Chapter 3). Adhesion of the CuO nanoparticles using either technique will lead to a meaningful way to measure the difference in biofilm formation and viable cell count between treated and untreated surfaces and determine how the adhered nanoparticles behave on different bacterial species. Evaluating the efficacy of this coating on medical grade silicone tubing is the first step to reducing the burden of usage of antibiotics by preventing infection in the first place. Furthermore, if a sufficiently appropriate coating can be applied to implanted devices, the practice of washing these materials in antibiotics when they are *ad hoc* modified prior to implementation, can be reduced thus reducing the rate of antibiotic resistance[403].

This chapter evaluates various species of the ESKAPE pathogens, evaluating 7 species and determining their phenotypic and genotypic resistances. Each species is investigated, to determine which phages are present and which virulence factors each species possesses. An appropriate model is selected with a modification to a classical minimum biofilm eradication concentration assay with a defined artificial saliva media is used to evaluate the effectiveness of the Glu-CuO nanoparticles that were synthesised as part of the previous chapter. Furthermore, the chapter investigates the Glu-CuO nanoparticle coating that is adhered with 3-mercaptopropyltrimethoxysilane using this model and media. Finally, Lysine coated copper oxide (Lys-CuO) nanoparticles, produced by Pharm2Farm, a Nottingham Trent University spin-out pharmaceutical company, bringing nanoparticles to the agricultural industry, are evaluated for their antibacterial properties in both a touch-killing and long-term capacity. This is evaluated in a polypropylene face mask material and a polyethylene air filtration material that has the potential for commercial application.

3.2 Methods

All experiments conducted within the biosafety level two laboratory were performed using an aseptic technique. Experiments with flammable solutions were performed in a biosafety level two (BSL2) flow cabinet when sterility was required. Experiments conducted with materials or equipment taken out of the BSL2 laboratory were sterilised before removal, either by autoclave sterilisation or Ultra-Violet (UV) exposure and use of disinfectant where appropriate (5% Biocleanse solution or equivalent).

3.2.1. Artificial saliva medium

Artificial saliva medium as defined by Wong *et al* was made in one-litre volumes[404]. 979 ml of 18 MΩ water was acquired from an Ultra Clear RO 30 (Avadity Science, USA) and Magnesium chloride hexahydrate (99% purity, Sigma Aldrich), Calcium chloride (93% purity, Sigma Aldrich), Sodium Bicarbonate (99% purity, Sigma Aldrich), Monopotassium phosphate (99% purity, Sigma Aldrich), Potassium phosphate dibasic (98% purity, Sigma Aldrich), Sodium chloride (99% purity, Sigma Aldrich) and Potassium chloride (99% purity, Sigma Aldrich) and Type III Porcine mucin (Sigma Aldrich). Final concentrations of each chemical were added to deionised water to produce this media which can be seen in (table 2.1). Some of these chemicals could not be autoclaved and were added after the remaining ingredients were autoclaved by filter sterilisation. The following ingredients were added after autoclaving and cooling down to room temperature (20°C) 1 mL of one molar potassium thiocyanate (99% purity, Sigma aldritch), 1 mL of one molar ammonium chloride (99.5% purity, Sigma Aldrich) and 1 mL of one molar urea (99% purity, Sigma Aldrich) .

Material	Mass/volume per litre
$MgCl_2 \cdot 6H_2O$	0.04 g
$CaCl_2 \cdot H_2O$	0.13 g
$NaHCO_3$	0.42 g
0.2 M KH_2PO_4	7.70 mL
0.2 M K_2HPO_4	12.30 mL
NH_4Cl	0.11 g
KSCN	0.19 g
$(NH_2)2CO$	0.12 g
NaCl	0.88 g
KCl	1.04 g
Mucin	3.00 g
DMEM	1.00 mL

Table 3.1 Table of materials added to water to create 1 litre of artificial saliva media. A full list of the chemical materials used in one litre of Artificial saliva media (ASM). These materials were added at different times to prevent degradation of certain components such as ammonium or urea

3.2.2 Mueller Hinton broth

Mueller Hinton broth (Sigma Aldrich, Millipore) was created in either 500 mL or one litre volumes, where 10.5g per 500 mL of dehydrated powder was added to deionised water. These volumes were then autoclaved for 15 minutes at 121 °C and allowed to cool to room temperature before use and were stored at room temperature. The broth was examined before use and 100 µL was streaked onto an agar plate to ensure sterility.

3.2.3 Mueller Hinton agar

Mueller Hinton Agar (Sigma Aldrich, Millipore) was created in volumes of 500ml or one litre at a time with 19g per 500 mL, where the dehydrated powder was added to deionised water (18 MΩ, retrieved from an Avidity science, UltraClear RO 30) and mixed thoroughly. The media was then autoclaved for 15 minutes at 121 °C and allowed to cool to room temperature for long term storage or, storing temporarily in a 55 °C oven if the media was required immediately. The agar was poured evenly into 90 mm petri dishes

and allowed to cool to room temperature with the lids on or under blue flame for faster cooling.

3.2.4 Tryptic Soy agar

Tryptic Soy Agar (TSA) (Sigma aldritch, millipore) was made in volumes of 500 mL or one litre, with 20g of dehydrated powder per 500 mL of deionised water, which was then thoroughly mixed. The mixed media was autoclaved for 15 minutes at 121 °C and allowed to cool to for long term storage or, storing temporarily in a 55 °C oven if the media was required immediately. The agar was poured evenly into 90 mm petri dishes and allowed to cool to room temperature with the lids on or under blue flame for faster cooling.

3.2.5 Tryptic Soy broth

Tryptic Soy Broth (TSB) (Sigma Aldrich, Millipore) was created in either 500 mL or one litre volumes, where 15g per 500 mL of dehydrated powder was added to deionised water. These volumes were then autoclaved for 15 minutes at 121 °C and allowed to cool to room temperature before use and were stored at room temperature. The broth was examined before use and 100 μL was streaked onto an agar plate to ensure sterility.

3.2.6 Plasma like medium

Plasma like medium was prepared by adapting the recipe for this medium from Voorde *et al* and Ackermann *et al*[405, 406]. This medium was adapted by Vanina Garcia-Altamirano for preparation in various bacterial work to mimic human plasma. Plasma like medium used was prepared by Becky Coxhill for use with the CDC reactor described in 3.2.19.

3.2.7 25% medium-glycerol stock solution

Mix One part glycerol (≥ 99% purity, Sigma Aldrich) was mixed with three parts broth in the required quantity, which was typically 5 mL of glycerol to 15 mL of broth. After

thorough mixing, the solution was left to settle to have as few bubbles as possible and was filter sterilised into a new universal tube using aseptic technique. This was then stored at room temperature (20°C) but was used shortly after creation to reduce the chance of contamination.

3.2.8 Bacterial strains used

A variety of strains were used to determine whether the antimicrobials were effective and to make sure the antimicrobials were adequately tested. These species were used during all experiments alongside a variety of control strains where appropriate, in experiments such as Minimum Inhibitory Concentration (MIC) and Minimum Bactericidal Concentration (MBC) assays. These strains can be seen in table 3.2.

Bacterial species	Strain collection number	Strain origin
Escherichia coli	SMC 005	0157:H7
Staphylococcus aureus	SMC 007	USA300 LAC JE2
Pseudomonas aeruginosa	SMC 009	Clinical isolate, neonate sepsis
Klebsiella pneumonia	SMC 010	Clinical isolate, neonate enterocolitis
Salmonella enterica	SMC 011	Human clinical isolate
Staphylococcus epidermidis	SMC 034	ATC 12228 JCT collection
Acinetobacter pittii	SMC 042	Clinical isolate, bronchial lavage (PS_acine7)
Acinetobacter baumannii	SMC 042	Clinical isolate, Wound (PS_acine9)

Table 3.2 *The list of strains used during this project. The main bacterial species used during this work as well as the local strain collection and the origin location of the strain.*

3.2.9 Making glycerol stocks of bacterial strains

A fresh plate of agar was poured and each bacterial species that was stocked was streaked onto the plate. An overnight culture of each species was created by adding a few colonies from the agar plate to 5 mL of Mueller Hinton Broth (Sigma Aldrich) in a sterile universal tube. These overnight cultures were placed into a shaking incubator at 37°C at 150 RPM for 18 hours. On the next day 1 mL of the overnight culture was taken and put it into a sterile microcentrifuge tube, centrifuging it for two minutes at 3k rpm to form a pellet at the bottom of the tube. The supernatant was removed and a further 1 mL of overnight culture was added, repeating the centrifuge step, and removing the supernatant. The large pellet was added to 1 mL of the glycerol (99% purity, Sigma Aldrich) broth stock mix ensuring the pellet was fully resuspended. This inoculated glycerol broth stock was transferred to a correct cryotube and was stored in a -80 or -20 freezer depending on the use of the stock.

3.2.10 Reviving glycerol stocks

A fresh agar plate was prepared for streaking from the glycerol stock and the glycerol stock was recovered from the freezer and placed into a freezer block during the process. Using aseptic technique, a sterile loop was used to recover some of the stock from the freezer block and was gently spread across the surface of the agar plate. This was then further streaked using a quadrant streak technique so that when incubated, single colonies would form on the surface of the agar in the later quadrants. The streaked plate was then Incubated at 37°C for 18 hours in a static incubator.

3.2.11 Growth curve

Overnight cultures were prepared in triplicate of 5 mL of inoculated broth growing at 37°C for 18 hours at 200 rpm. Three 250 mL Erlenmeyer flasks were sealed with cotton wool and aluminium foil and autoclaved for sterility. 20 mL of sterile medium was placed into each flask and was inoculated with 200 μL, or 1 % of the overnight culture. The flask was placed into an incubator at 37°C for 24 hours at 200 rpm to allow the inoculum to grow. One mL was taken every hour and at inoculation to measure the optical density

at 600 nm using a spectrophotometer. Measurements were taken until the stationary phase had been reached and four measurements were taken after this point to ensure that growth had plateaued.

3.2.12 Comparison of culture turbidity and viability

Overnight cultures were prepared in triplicate for each species used and were grown at 37 °C for 18 hours at 150 rpm. Once grown, the overnight cultured were centrifuged in 1 mL centrifuge tubes at 3k rpm for two minutes. After centrifuging the cultures, the supernatant was removed and another 1 mL of overnight culture was added, recentrifuged and the supernatant removed again. The large pellet was resuspended in Phosphate Buffer Saline (PBS) (Sigma Aldrich) and diluted down to get the turbidity of the suspension to 1.0 OD_{600}. In a 96-well plate each well had an appropriate amount of sterile PBS added to create dilutions equivalent to 1.0, 0.8 0.6 0.4 0.3 0.2 and 0.1 OD_{600}. The last column was left as pure PBS to check for sterility when plating.

Each dilution was spotted onto a Mueller Hinton Agar plate, in 10 μL volumes and were allowed to dry so that no liquid was visible. Viable cell counts were high so serial dilution of 20 μL concentrations to 180 μL sterile PBS was performed up to eight times, again spotting on agar plates in 10 μL volumes. These plates were then incubated overnight at 37°C for 18 hours and were counted. Each spot of the dilution had between three and thirty individual colonies, was repeated five times and in biological triplicate for an average count with the dilution factor considered for each turbidity spotted.

3.2.13 Minimum inhibitory concentration assay

Overnight cultures were grown in Mueller Hinton Broth (Sigma Aldrich) in triplicate at 37°C. Separately, a 96 well plate was prepared with 100 μL of sterile MHB in each well. In the first column of the plate, an appropriate amount of antibiotic or antimicrobial solution was added to make 200 μL of starting antimicrobial media mix. Serial dilution was performed transferring 100 μL from the first well into the second well and mixing well. Subsequent dilutions were performed until column 10, leaving column 11 for

sterility control and column 12 for positive bacterial growth control. For nanoparticle solutions, serial dilution was not appropriate and so desired concentrations were made before adding to the well in microcentrifuge tubes.

The overnight cultures were diluted to an OD_{600} of 0.1 using PBS (Sigma Aldrich) and 10 µL of this diluted culture was added to each well excluding the sterility control column. All concentrations were tested in triplicate by both biological repeats and technical repeats. The inoculated plate was then incubated overnight for 18 hours at 37 °C and read in the morning after, recording wells which showed no sign of growth.

3.2.14 Minimum bactericidal concentration assay

After MIC's were performed 10 µL was spotted from the wells onto Mueller Hinton Agar (Sigma Aldrich) plates, taking from the wells that show no growth, additional wells at lower dilutions are also spotted to ensure the correct bactericidal concentration was determined. These agar plates were incubated for 18 hours at 37 °C and the minimum concentration is determined to be the lowest concentration of antimicrobial where no colonies grew on the agar plates.

3.2.15 Nanoparticle MIC and MBC

50 mg of nanoparticles was added to 10 mL of Mueller Hinton broth to obtain a concentration of 5 mg mL^{-1}. Three 96 well plates were prepared with two species, one in the first three rows and the second in the final three rows, leaving two empty rows in the middle of the plate. These wells were tested inoculating wells with a concentration of 10^5 viable cells in 100 µL of medium. Two wells were left for nanoparticle sterility and medium sterility controls respectively. Using microcentrifuge tubes, create dilutions of nanoparticles starting at 1 mg mL^{-1} decreasing to 100 µg mL^{-1} and add 100 µL of each nanoparticle concentration into the 96 wells. After Incubating the plate for 18 hours at 37 °C, the wells where no bacterial growth was observed was recorded as the MIC, although this was difficult due to the nanoparticles changing the colour of the media. To

account for this, when performing the MBC additional wells were spotted to count the number of cells.

3.2.16 Biofilm formation assay

Overnight cultures of bacterial strains were grown in Mueller Hinton Broth (MHB) and grown at 37 °C. Overnight cultures were diluted to an OD_{600} value of 0.5, in Phosphate Buffered Saline (PBS) (Sigma Aldrich). In a twenty-four well plate, 1 mL of sterile MHB was added to each well and 100 µL of each OD_{600} inoculum was added in triplicate, providing both biological and technical repeats. Three wells were left with sterile medium to assure that there was no contamination. The plate was then left to incubate overnight for 18 hours at 37 °C to grow the biofilm.

After incubation, the twenty-four well plate was slowly tipped to remove the medium and the planktonic cells whilst not disturbing the biofilm. The plate was blotted onto dry tissue to remove any droplets. The biofilm was then washed with 1 mL PBS in each well and shaken at 100 rpm for five minutes to remove any planktonic cells that remained. These steps were repeated to remove all unbound cells from the wells.

500 µL of crystal violet dye (90% purity, Sigma Aldrich) at 0.1 % weighted concentration was slowly added to each well to allow for biofilm staining, this was incubated at room temperature for one hour to allow the dye to stain the biofilm. Excess crystal violet was tipped away slowly to not disturb the biofilm. 1 mL of PBS was slowly poured into each well to remove any remaining dye and planktonic cells and was repeated until the PBS crystal violet elute was clear, indicating the excess dye was removed. After one more blotting, 200 µL of ethanol was added into each well with shaking at 100 rpm for 2 minutes. 100 µL of ethanol solution from each well was transferred into a 96 well plate, the OD_{550} was read using a BioTek Cytation 3 (Agilent, USA) cell imaging multi-mode reader.

3.2.17 Antibiotic disc diffusion

Overnight cultures were prepared in triplicate, grown at 37 °C for 18 hours at 200 rpm. After growth, the cultures turbidity was measured at 600 nm, using PBS to dilute the turbidity until the culture was equivalent to the turbidity of a 0.5 McFarland standard. 100 µL of the diluted inoculum was pipetted onto Mueller Hinton agar (Sigma Aldrich) plates and was spread across using a sterile spreader using one of the triplicates per plate. After the plates are evenly spread, antibiotic discs were applied firmly to the agar plate, ensuring the disc was flat and adhered to the plate with good space between other discs. Each plate was labelled over the antibiotic disc, indicating which zone of inhibition was caused by which disc the plate with each antibiotic disc used. After each plate was labelled, they were incubated for 18 hours at 37 °C where the zones of inhibition will have appeared and can be measured. The EUCAST breakpoint tables from 2021 indicated what zones of inhibition determined the susceptibility and resistance breakpoint of the antibiotic[321].

3.2.18 Minimum biofilm eradication concentration assay

Three overnight cultures were prepared per bacterial strain tested for biological repeats ensuring that at least 2 mL per overnight culture was available for centrifuged into pellet form. Each overnight culture was grown in the same medium as the experiment to be performed to ensure the growth of biofilm was the same between empty wells and wells with adhered tubes in.

Each plate was prepared by adhering 24, one centimetre silicone tubes onto a twenty-four well plate lid using Loctite 401, (Henkel, Germany) adhesive. Once the tubes were in place, the plates were left for 24 hours to ensure the solvent-based adhesive was fully cured and would not affect the assay. The 24 well plate, with adhered silicone tube, was coated as described in 2.1.2 with an additional step to incorporate a plasticiser. Glycerol (99% purity, Sigma Aldrich) and Polysorbate 80 (Sigma Aldrich) were chosen as plasticisers due to their food-grade quality. The concentrations of glycerol and polysorbate 80 solutions tested, ranged from 0.1% to 100% weight by volume, which was achieved by diluting with water. Examining the plasticisers was performed with

nanoparticles and after 24 hours had passed to ensure the new coating had fully cured. The tubes were then coated as described in 2.2.2 and left for another 24 hours.

Each well had 1,800 µL of medium added and 200 µL of overnight inoculant, which was diluted with PBS (Sigma Aldrich) to 10^6 CFU mL^{-1}, was added to each well, except three wells which were used as a sterility control. The inoculated plate was incubated at 37 °C for 18 hours in a shaking incubator at 150 rpm.

After incubation there were three experiments run, a fourth column of the 24 well plate was designed to be left over for control analyse of an uncoated tube. The second of the experiments was the quantification of crystal violet dyed biofilm using the same method as described in the biofilm formation assay. The final experiment quantified the viable cells within the biofilm and was performed. After incubation, the tubes were removed from the lid and placed in individual sterile 7 mL tubes, where they were centrifuged in 2 mL of PBS. 100 µL of medium was taken from each tube for serial dilution. Each dilution was spotted in 10 µL spots, five times per tube, onto agar plates and counts were recorded.

3.2.19 Biofilm growth in the CDC reactor

A CDC reactor was used to evaluate the antimicrobial coating on different materials in a standardised way such that multiple materials could be tested at the same time. CDC reactor coupons were prepared by spray coating copper oxide nanoparticles onto the material and curing them with UV, also sterilising them in the process. The coupons were made from stainless steel 316, PVC, medical grade titanium and silicone rubber (BioSurface technologies, USA). The bioreactor was autoclaved in advance to ensure a sterile environment for the plasma like medium, of which 500 mL was added and inoculated with 1 mL at 10^8 CFU mL^{-1} of *S. aureus* USA300 LAC JE2. The reactor was then kept on a rotating stir plate using a magnetic flea at 125 rpm where it remained for 24 hours.

After the 24-hour reaction the coupon holders were aseptically removed from the vessel ensuring the biofilms formed on the coupons were not disturbed. The coupons that were used for viable counts were then removed from holders and removed such that

the treated side was unperturbed until it was time to scrape the surface of the coupon into 5 mL of PBS. The scraped surface was then scraped twice more ensuring all of the biofilm had been mechanically removed from the coupon. After scraping, the coupon's scraped surface was washed with 5 mL of PBS in 1 mL pipettes to ensure all of the biofilm was recovered, this wash was added to the 5 mL of PBS used for the initial scrape. As there were 12 coupons per material, three for biofilm measurements, three for viable count measurements, three for SEM imaging and three controls, two full bioreactor runs were required for the four different coupon materials The 10 mL of PBS (Sigma Aldrich) /biofilm culture was used for serial dilution and crystal violet staining to enumerate the viable cells. The coupons that were used for biofilm staining were taken and removed, but the side that was uncoated was scraped instead. The side with coating and any remaining biofilm formation was covered with 500 μL of crystal violet (Sigma Aldrich) and incubated at room temperature for one hour. This stained biofilm was then washed with 500 μL of ethanol to remove it from the coating and was placed into a 24 well plate for optical density reading at OD_{550}. These steps were also performed on the control coupons for appropriate quantification.

3.2.20 Bacterial fixation

To image the biofilms using SEM, the biofilms needed to be fixed to the material that was being imaged. This was done in a fume hood, with the material being placed into 4% paraformaldehyde (95% purity, Sigma Aldrich) for 30 minutes, then placed into a 50%, 60%, 70%, 80%, 90%, ethanol solution for 20 minutes each and then in a 100% ethanol solution for 40 minutes. After this the material is placed into a 1:2 ratio of Hexameythlydisalzane (99.9% purity, Sigma Aldrich) :100% ethanol (95% purity, Sigma Aldrich) solution for 20 minutes, then a 2:1 HDMS:100% ethanol solution for 20 minutes until finally placed in a 100% HMDS solution overnight at until the HMDS has evaporated. Each step was performed at room temperature (20°C) and in a fume hood for safely extracting HMDS vapors.

3.2.21 DNA extraction

DNA extraction was performed using a Sigma Aldrich extraction kit, with the instructions of the kit followed until DNA was successfully recovered. This DNA was tested by aliquoting 1µL of eluted DNA onto a UV-Vis spectrophotometer to determine the 260nm to 280 nm ratio and DNA concentration (ng µL^{-1}). With sufficient samples, the extracted DNA was sent to MicrobesNG for sequencing.

3.2.22 Sequence assembly and analysis

Sequence analysis was performed using online resources databases such as Galaxy Europe, The Comprehensive Antibiotic Resistance Database (CARD) or The Virulence Factor Database (VDFB) to analyse sequenced data and determine the genes which are expressed conferring resistance and virulence factors which contribute to the spread and growth of biofilms. Firstly, the data recovered from MicrobesNG was passed through FastQC, a quality control software that reports on the quality of the sequence data to determine whether the sequence data needs to be trimmed. All data provided by MicrobesNG did not require trimming.

Unicycler was then used to create assemblies of the forward and reverse sequence reads where the software was run to exclude contigs shorter than 200 bp in length. This provided two files, a complete final assembly of the genome and an assembly graph of the genome. The assembly graph was run through bandage to provide a visual representation of the genome, showing any plasmids as well as the full chromosome.

Statistical analysis was performed at this stage using Fasta statistics software, which allowed basic analysis of the largest and shortest contigs, as well as the total number of contigs and the total genome size. The next step was to confirm the species of the sequenced data and identify how closely related the species was to a reference sequence, ensuring that the sequence data was from the correct species that was extracted and sent to MicrobesNG. This was compared by downloading reference sequences from the National Library of Medicine (NLIM) of each species extracted from Genbank. Once reference sequences for the species tested were acquired, FastANI software was used to compare the Average Nucleotide Identity (ANI) to the reference

sequence, confirming whether the DNA extracted belonged to the same species of bacteria.

3.3 Results

3.3.1 Characterisation of bacterial species used in this study

Relevant bacterial species were chosen to establish whether the proposed methods of coating influenced the development of biofilm formation and the viable cell count. The species selected were of clinical / human origin and represented several of the ESKAPE pathogens and *S. epidermidis* that whilst not recognised as a true pathogen, is known to cause infection from implanted medical devices. The species used in this study were *A. baumannii*, *E. coli, S. aureus, S. epidermidis, K. pneumonia* and *P. aeruginosa*. To establish appropriate requirements for all starting inoculations of future experiments, viable cell counts were measured at varying optical density at 600 nm (OD_{600}) as seen below (Figure 3.1 and Figure 3.2).
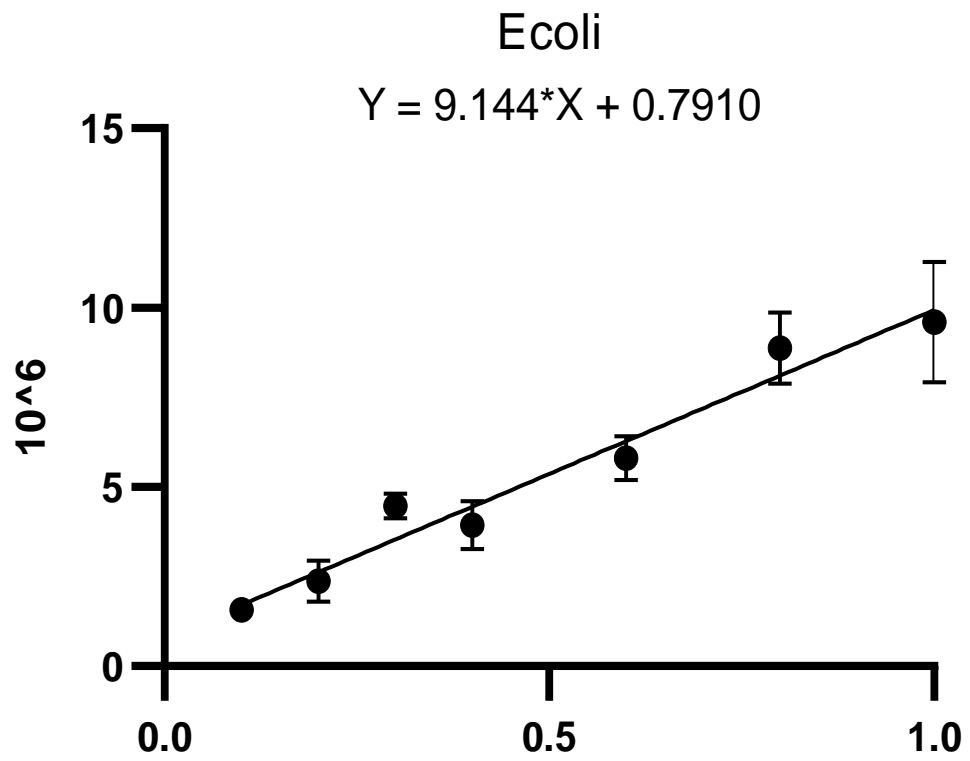
Figure 3.1 *A comparison of the viability vs turbidity of Escherichia coli, Staphylococcus aureus, Pseudomonas aeruginosa and Klebsiella pneumonia. Plots of four species measuring the viability of cultures at varying optical densities (OD$_{600}$). N = 3, ± SEM.*
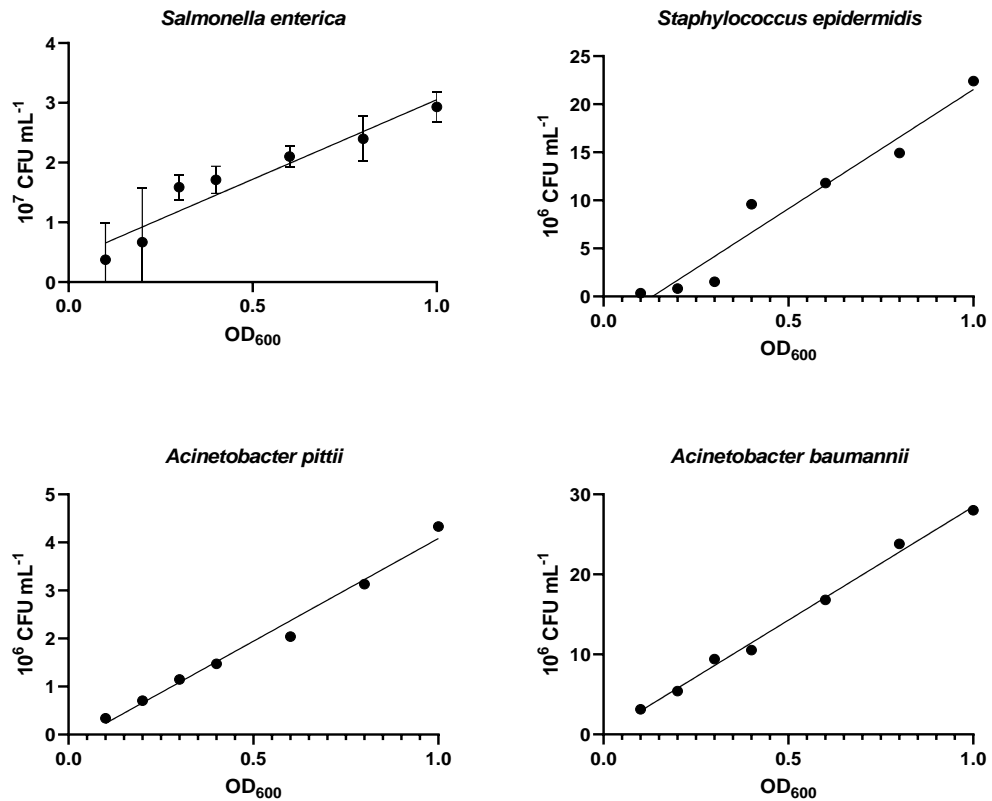
Figure 3.2 *A comparison of the viability vs turbidity of Salmonella enterica, Staphylococcus epidermidis, Acinetobacter pittii and Acinetobacter baumannii. Plots of the four species measuring the viability of cultures at varying optical densities. N = 3, ± SEM.*

These plots were used, to calculate the OD_{600} for each of the species at 10^6 CFU mL^{-1} as seen below (Table 4.1) as 10^6 CFU mL^{-1} is the required concentration of viable bacterial cells in many assays such as biofilm assays and other ISO standard experiments. Each optical density measurement made from the plots seen previously (Figure 4.1 & 4.2) and these results were used as the foundation for any experiment to create consistent viable cell inoculation.

Bacterial species	OD$_{600}$ at 10^6 CFU mL^{-1}	Linear equation
Escherichia coli	0.136	y = 24.81*X - 3.2732
Staphylococcus aureus	0.100	Y = 9.14*X + 0.791
Klebsiella pneumoniae	0.065	Y = 14.8*X – 0.0307
Pseudomonas aeruginosa	0.255	Y = 10.5*X - 2.58
Staphylococcus epidermidis	0.172	Y = 24.81*X - 3.273
Salmonella enterica	0.522	Y = 2.66*X + 0.3898
Acinetobacter pittii	0.279	Y = 4.277*X - 0.1957
Acinetobacter baumannii	0.0322	Y = 28.37*X + 0.0869

Table 3.3 *Comparison of the turbidity required to achieve 10^6 cfu mL^{-1} for different bacterial strains*

3.3.2 Phenotypic antimicrobial resistance profile of the bacterial strains

Evaluating the resistance profile of the species tested was important to determine how important the development of novel antimicrobial agents is. The antibiotic resistance levels observed in the strains used in this study would also highlight the efficacy of novel antimicrobial treatments against a variety of antibiotic resistances. Table 3.2 shows the resistance profile of all main bacterial species investigated as well as showing extensive resistance profiles of the two *Acinetobacter* strains. Colistin was measured using minimum inhibitory concentration (MIC) and minimum bactericidal concentration (MBC) assays, as disc diffusion assays are not a recognised method of measuring antibiotic susceptibility to this antibiotic by EUCAST[321]. The Acinetobacter strains showed significant antibiotic resistance across a range of antibiotic classes, whist resistance profiles of the other strains were more varied.

Antibiotic class	Strain	*Escherichia coli* 0157:H7	*Klebsiella pneumonia*	*Pseudomonas aeruginosa*	*Acinetobacter pittii*	*Acinetobacter baumannii*	*Staphylococcus aureus* USA 300	*Staphylococcus epidermidis* ATCC 12228	Interpretation of zone of inhibition compared to EUCAST 2022 breakpoint value
	Antibiotic	Zone diameter (mm)	Zone diameter (mm)	Zone diameter (mm)	Zone diameter (mm)	Zone diameter (mm)	Zone diameter (mm)	Zone diameter (mm)	Interpretation
Carbapenems	Doripenem	26.7	22	13.7	0	0	N/A	N/A	Susceptible
	Ertapenem	N/A	N/A	N/A	0	0	N/A	N/A	Resistant
	Meropenem	N/A	N/A	N/A	0	0	N/A	N/A	Susceptible, increased exposure
	Imipenem	N/A	N/A	N/A	0	0	N/A	N/A	
Aminoglycosides	Tobramycin	23.5	17.8	21.3	0	0	18	29.5	
	Amikacin	25.5	19.5	21.7	0	0	16.2	26.1	
	Gentamycin	24.6	18.7	N/A	0	0	18.7	30.2	
Fluoroquinolones	Levofloxacin	37.7	30.1	25.1	N/A	N/A			
	Ciprofloxacin	N/A	N/A	N/A	N/A	N/A	18	30.1	
Cephalosporin	Cefepime	25.3	18	21.3	0	0	N/A	N/A	
	Cefoxitin	N/A	N/A	N/A	N/A	N/A	13.8	30.2	
Monobactams	Aztreonam	N/A	N/A	N/A	0	0	N/A	N/A	
Diaminopyrimidines	Trimethoprim	N/A	N/A	N/A	N/A	N/A	14.3	22.2	
Polypeptide	Colistin	N/A	N/A	N/A	2*	2*	N/A	N/A	

Table 3.4 *The antibiotic resistance profile of the six tested bacterial species, as per the 2022 EUCAST breakpoint tables. The antibiotic resistance profile measured from disc diffusion assays performed using the EUCAST standard assay[321]. * Colistin was measured via dilution in MIC as it is not suitable for diffusion assays.*

3.3.3 Genotypic analysis of bacterial strains used in this study

To confirm the identity and fully understand the strains under study, genome sequencing was employed. This allowed a greater understanding of mechanisms behind the phenotypically derived antibiotic susceptibility profiles of the strains, as well as facilitating an understand of the virulence of these isolates. Genomic DNA was extracted from each of the bacterial strains tested phenotypically. DNA quality was checked using a NanoDrop microvolume spectrophotometer (ThermoFisher Scientific) and quantified using a Qubit 4 fluorometer (Invitrogen). Whole genome sequencing was performed on the Illumina HiSeq/NovaSeq platform by MicrobesNG (Birmingham, UK). Reads were assembled using SPAdes v3.15.5. A summary of draft genomes is provided below (Table 3.3). The coverage is the average amount of times each base pairs (bp) is sequenced, with a minimum of 30 being expected for short reads such as those seen below (Table 3.3). The number of contigs are the number of fragments read by the sequence, with higher contigs indicating more fragments in the readable data.

Strain origin	Designation	Species identification	Coverage (x)	GC (%)	Length (bp)	Contigs	N50 (bp)
O157:H7	SMC 005	*Escherichia coli*	70.44	50.33	5,438,363	155	194,103
USA300 - Lac JE2	SMC 007	*Staphylococcus aureus*	99.26	32.65	2,845,738	19	872,985
Neonatal sepsis	SMC 009	*Pseudomonas aeruginosa*	96.66	66.45	6,351,693	26	652,061
Neonatal enterocolitis	SMC 010	*Klebsiella pneumoniae*	77.94	57.17	5,454,993	87	294,974
ATCC 12228	SMC 034	*Staphylococcus epidermidis*	85.80	31.88	2,548,618	34	185,522
Human isolate - wound	SMC 042, PS_Acine7	*Acinetobacter pittii*	115.72	38.88	4,185,437	71	196,532
Human isolate - bronchial lavage	SMC 044, PS_Acine8	*Acinetobacter baumannii*	106.28	38.91	3,928,496	54	194,321

Table 3.5 Summary information for genomes generated from the clinical isolates described in this study. The data retrieved from MicrobesNG for each of the strains that had its DNA extracted and sent for sequencing. The E. coli strain had a large amount of contigs compared to the rest of the sequenced strains

3.3.4 Genotypic antibiotic resistance profile of the bacterial strains

To understand the genotypic basis for the phenotypic antibiotic resistance observed above (Table 3.3), genotypic resistance profiles were examined using The Comprehensive Antibiotic Resistance Database (CARD, v3.2.5). Each bacterial species showed different predicted genes responsible for antimicrobial resistance as summarised below (Table 3.4).

Bacterial strain	Number of predicted AMR genes	Antibiotic classes to which resistance is predicted
E. coli	53	Aminocoumarin, Aminoglycosides, Cephalosporins, Elfamycins, Flouroquinolones, Macrolides, nitroimidazoles, Nucleosides, Peptides, Phosponic acid, Tetracyclines
S. aureus	42	Diaminopyrimides, Fluoroquinolones, Tetracyclines, Penams, Aminocoumarins
P. aeuriginosa	59	Aminoglycoside, Carbapenem, Flouroquinolone, Macrolide, Monobactam, Peptide, Nitroimidazole,
K. pneumoniae	28	Aminoglycoside, Bicyclomycin, Carbapenem, Elfamycin, Flouroquinolone, Marcolide, Monobactam, Peptide, Phenicol
S. epidermidis	11	Sulfanomide, Aminglycoside, Elfamycin, Flouroquinoline, Macrolide, Monobactam, Tetracycline, Phenicol, Phosphonic acid, Sulfonamide
A. pittii	16	Macrolide, Aminoglycoside, Carbapenem, Cephalosporin, Glycopeptides
A. baumannii	29	Aminoglcoside, Carbapenem, Cephalosporin, Flouroquinolone, Glycylcyline, Macrolide, Tetracycline, Peptides, Sulfonamide

Table 3.6 *Summary of the number and class of antimicrobial genes predicted for each bacterial strain using CARD database. A table of the number of predicted antimicrobial resistance genes and antibiotic classes to which they confer resistance using the CARD database.*

Comparison of the phenotypic and genotypic data was further determined through measuring the concordance and discordance between the two data sets for each strain. Below (Figure 4.3) the concordance and discordance between the two data sets can be seen, with three of the seven species having greater discordance between the two data sets, whilst *S. epidermidis*, *E. coli* and *P. aeruginosa* data showed higher concordance. Varying levels of concordance were observed as the different bacterial species were only tested with certain antibiotic classes, leading to missing phenotypic data that may alter the concordance between strains.
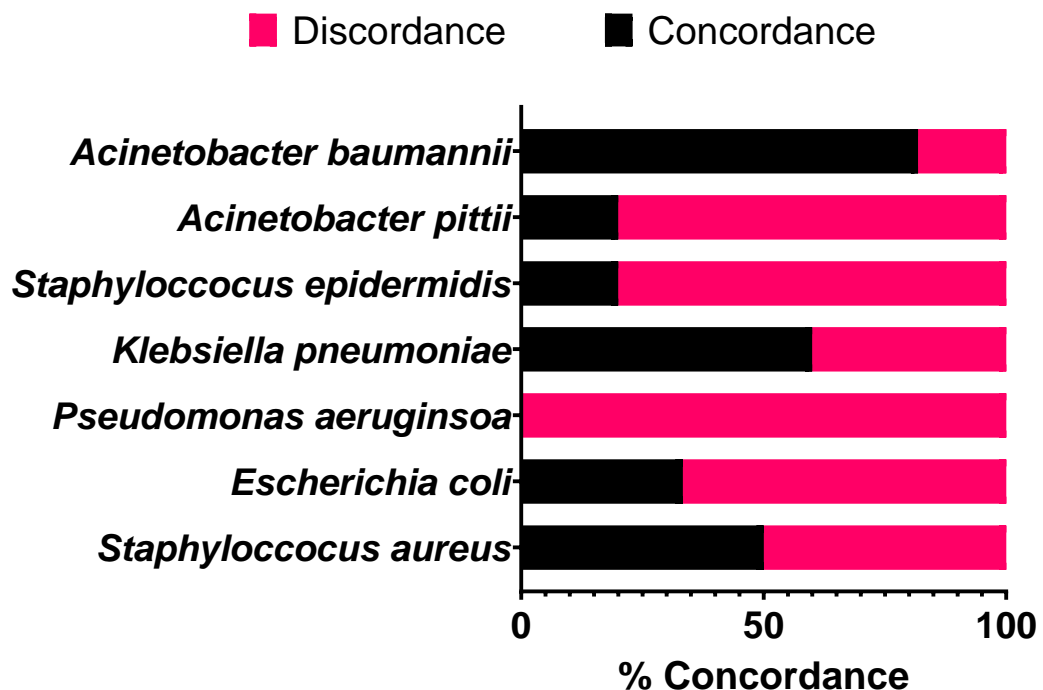
Figure 3.3 *The concordance and discordance between the antimicrobial genotypic data and the phenotypic data for seven bacterial strains. The concordance and discordance between genotypic and phenotypic data gathered from genome sequencing and the disc diffusion assay performed (Table 3.2).*

3.3.5 Bacteriophage present within the bacterial species

Bacteriophage can carry virulence and antimicrobial resistance genes and thus can play a major role in the phenotypic characteristics of bacterial strains. To understand whether the bacterial strains used in this study contained bacteriophage and whether any phage identified were intact or had lost phage related genes, draft bacterial

sequences were searched for the presence of bacteriophage. Draft genome sequences were interrogated using the Phage Search Tool Enhanced Release (PHASTER) server to extract predicted phage present within draft genomes, giving intact, questionable, and incomplete scores based upon the phage data provided. Below (Table 3.5) are the results of the phage data extracted from PHASTER, incomplete phage data was removed due to the unreliability of this data to correctly identify phage sequences. In the table below, each species shows the most likely phages present from the sequence data, with the table showing multiple intact phages in each species, except for *S. epidermidis* and *A. baumannii* as the quality of the predicted phages was too low to be reliably predicted.

Strain	Completeness	Score	Region length	GC%	Total proteins	Likely phage
Staphylococcus aureus	intact	150	53.4 kb	48.32%	50	PHAGE_Salmon_118970_sal3_NC_031940(23)
	questionable	70	20.8 kb	49.71%	24	PHAGE_Burkho_BcepMu_NC_005882(14)
	questionable	85	10.6 kb	49.55%	16	PHAGE_Entero_P4_NC_001609(8)
Escherichia coli	questionable	70	28 kb	47.92%	10	PHAGE_Stx2_c_Stx2a_F451_NC_049924(4)
	intact	107	14.2 kb	48.81%	18	PHAGE_Entero_P4_NC_001609(10)
	intact	130	35.7 kb	51.28%	31	PHAGE_Entero_fiAA91_ss_NC_022750(19)
	intact	150	17.8 kb	54.13%	22	PHAGE_Entero_SfV_NC_003444(21)
Pseudomonas aeruginosa	intact	110	39 kb	43.29%	45	PHAGE_Salmon_SSU5_NC_018843(20)
	questionable	80	20.1 kb	38.90%	31	PHAGE_Entero_fiAA91_ss_NC_022750(2)
	intact	140	18.6 kb	42.24%	24	PHAGE_Stx2_c_1717_NC_011357(4)
	questionable	70	9.8 kb	37.75%	10	PHAGE_Nodula_vB_NspS_kac65v151_NC_048756(4)
Klebsiella pneumoniae	intact	130	50.6 kb	52.68%	76	PHAGE_Escher_HK639_NC_016158(9)
	questionable	80	10.8 kb	55.39%	14	PHAGE_Escher_500465_1_NC_049342(11)
	questionable	90	34.2 kb	51.84%	44	PHAGE_Klebsi_phiKO2_NC_005857(36)
	intact	120	23.8 kb	50.33%	41	PHAGE_Entero_mEp235_NC_019708(10)
	questionable	70	10.7 kb	51.44%	18	PHAGE_Klebsi_phiKO2_NC_005857(9)
Staphylococcus epidermidis	No phage identified in the bacterial genome					
Acinetobacter pittii	intact	110	39 kb	43.29%	45	PHAGE_Salmon_SSU5_NC_018843(20)
	questionable	80	20.1 kb	38.90%	31	PHAGE_Entero_fiAA91_ss_NC_022750(2)
	intact	140	18.6 kb	42.24%	24	PHAGE_Stx2_c_1717_NC_011357(4)
	questionable	70	9.8 kb	37.75%	10	PHAGE_Nodula_vB_NspS_kac65v151_NC_048756(4)
Acinetobacter baumannii	Data incomplete, no phage's reported					

Table 3.7 *Phage data extracted from bacterial draft genome sequence data. The most likely phage predicted from the extracted genome sequence data provided by MicrobesNG. Only predicted phage with a score greater than 70 were recorded.*

3.3.6 Virulence factors possessed by the examined bacterial species

Virulence factors play a major role in the ability of bacterial strains to establish and maintain infections. Examples of virulence factors include biofilm formation proteins, adhesins and toxins. To understand the virulence of the strains used in this study, virulence genes for each bacterial species were identified from their draft genome sequences. Each species was examined and heatmaps of the virulence factors were generated. A condensed version of the results can be seen below (Figure 3.4-3.7). The *Acinetobacter* strains presented fewer virulence factors, but this may in part be due to the lack of widespread genome analysis of the *Acinetobacter* complex. Various virulence factors contribute to each of the species ability to produce biofilms, produce various efflux pumps that effect an antibiotics ability to interact with the cell. A copper exporter was noticed in the S*. aureus* isolate that may present higher resistance to the Glu-CuO nanoparticles produced in Chapter 2. This data also highlights the variety of different virulence factors that are present within different genera of bacteria, which can be utilised to understand whether any key virulence factors play a role in detoxification of novel antimicrobials.
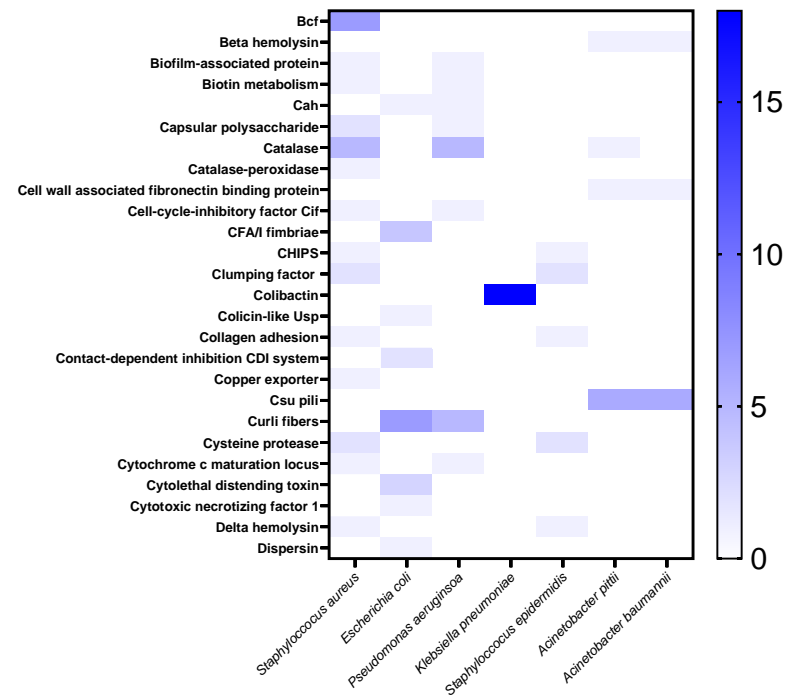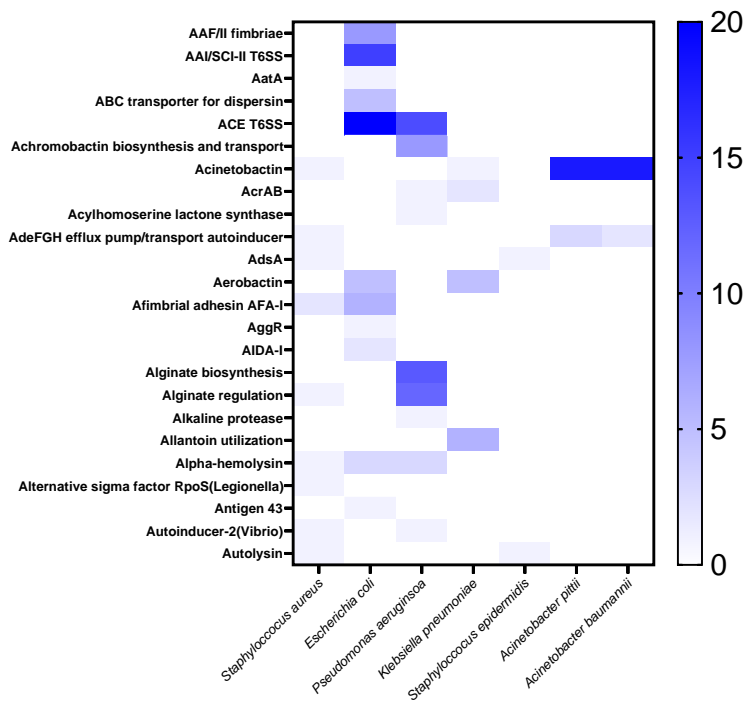
Figure 3.4 *Virulence factors of bacterial species used in this study in alphabetical order from A to D. All the virulence factors present in each species indicating different mechanisms the bacteria use to proliferate, protect itself from antibiotics and to cause damage to the host. Due to the diversity in species, virulence factors were expressed rather than the gene causing the factor to reduce the total number of entries from 1400 to 200. 50 different factors can be seen that contribute each species virulence.*
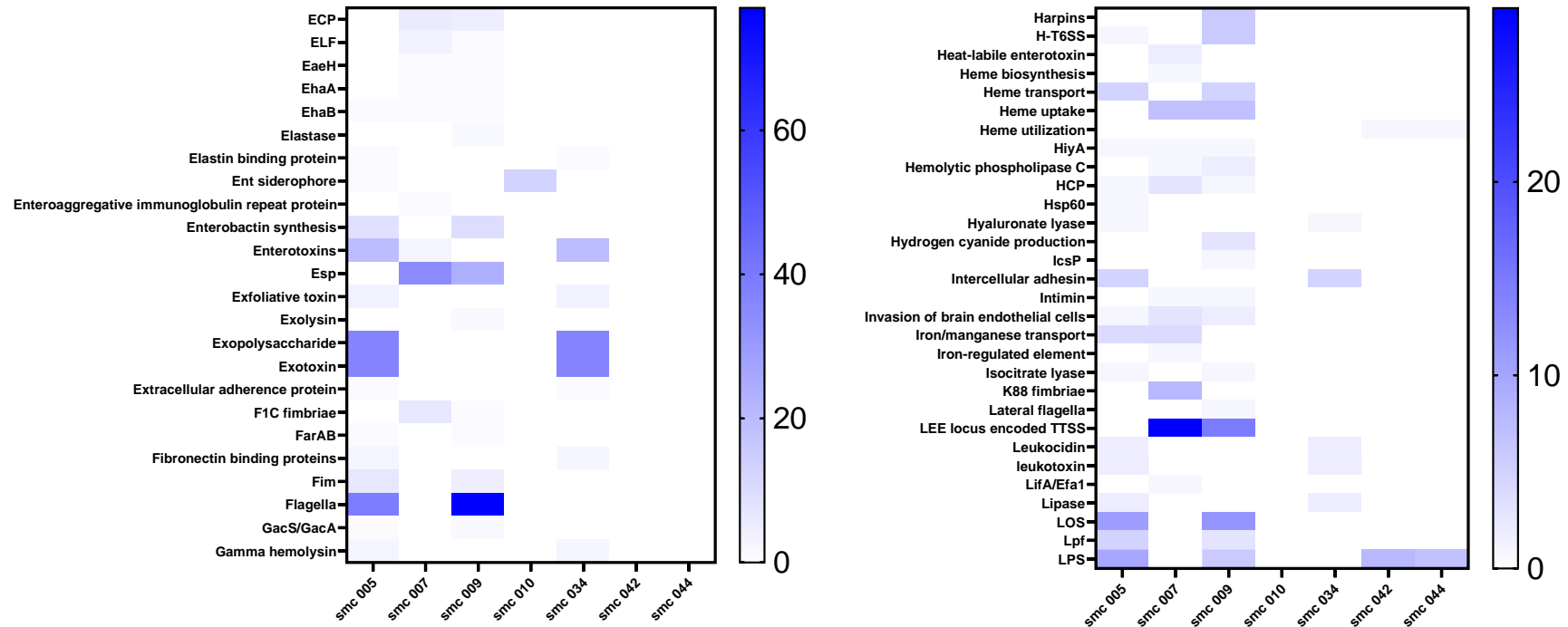
Figure 3.5 *Virulence factors of bacterial species used in this study in alphabetical order from E to L. All the virulence factors present in each species indicating different mechanisms the bacteria use to proliferate, protect itself from antibiotics and to cause damage to the host. Due to the diversity in species, virulence factors were expressed rather than the gene causing the factor to reduce the total number of entries from 1400 to 200. 54 of the virulence factors can be seen, contributing to each species virulence.*
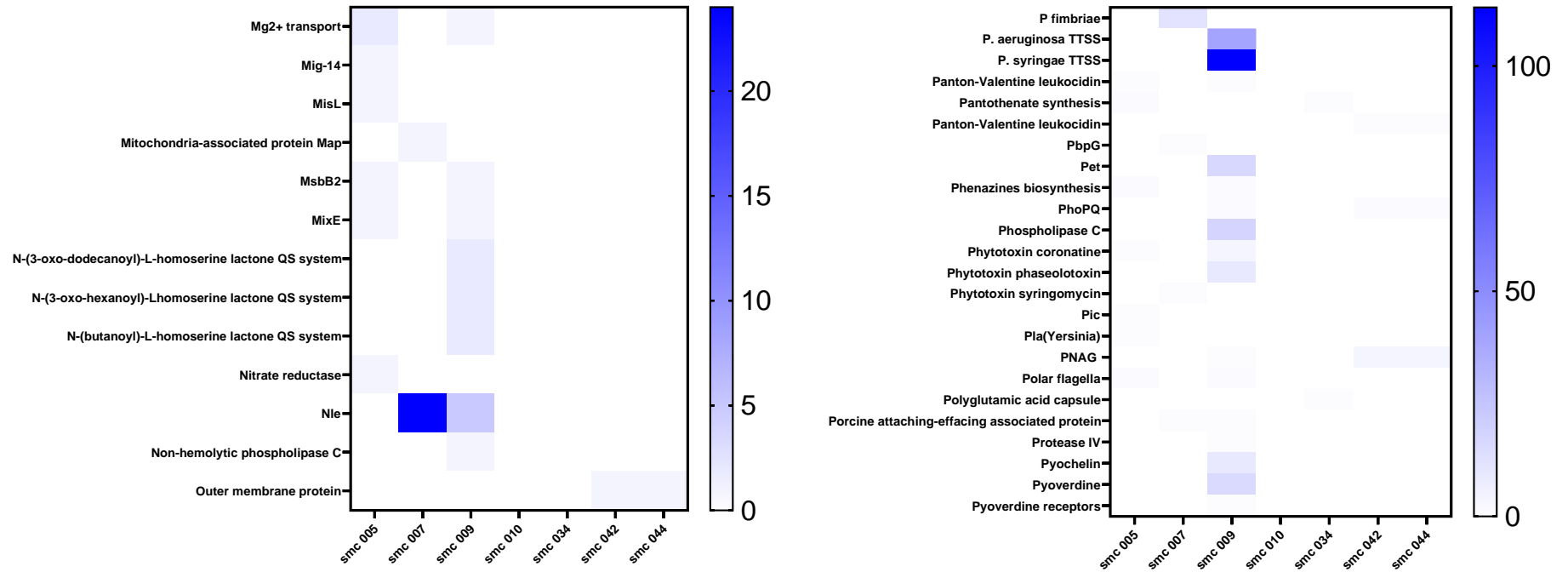
Figure 3.6 *Virulence factors of bacterial species used in this study in alphabetical order from M to P. All the virulence factors present in each species indicating different mechanisms the bacteria use to proliferate, protect itself from antibiotics and to cause damage to the host. Due to the diversity in species, virulence factors were expressed rather than the gene causing the factor to reduce the total number of entries from 1400 to 200. 37 different factors can be seen that contribute each species virulence.*
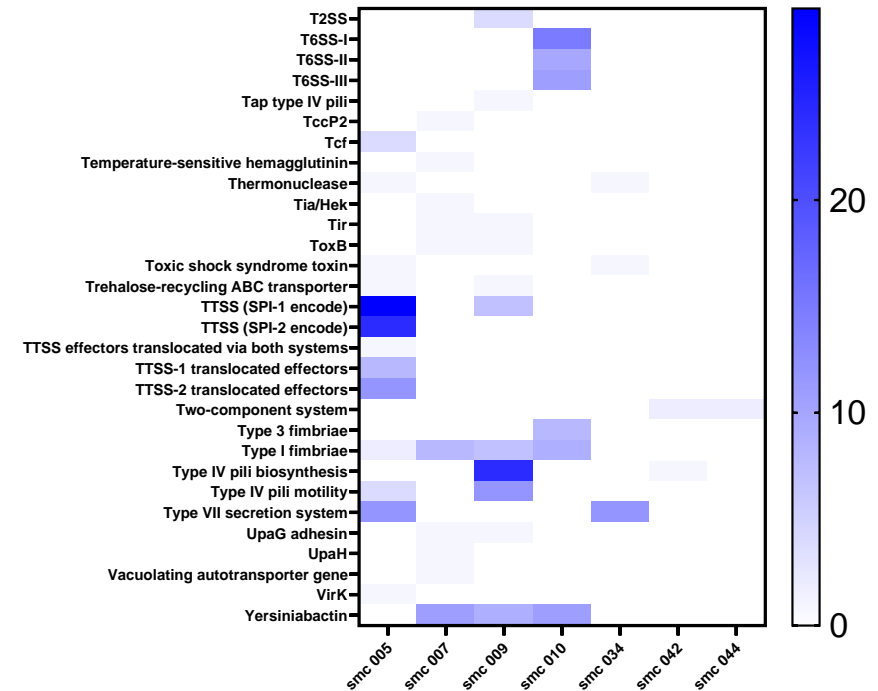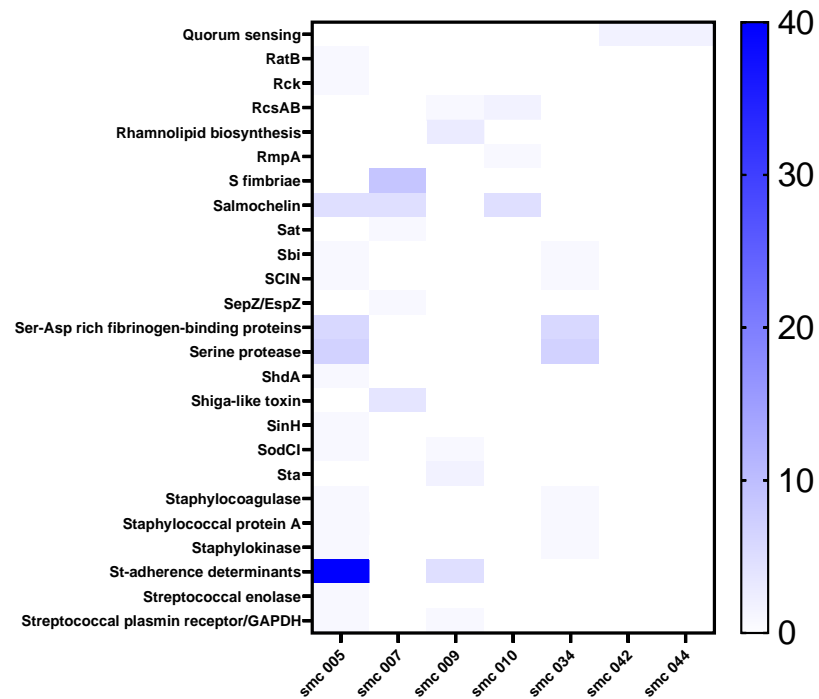
Figure 3.7 *Virulence factors of bacterial species used in this study in alphabetical order from Q to Y. All the virulence factors present in each species indicating different mechanisms the bacteria use to proliferate, protect itself from antibiotics and to cause damage to the host. Due to the diversity in species, virulence factors were expressed rather than the gene causing the factor to reduce the total number of entries from 1400 to 200. 55 different factors can be seen that contribute each species virulence.*

3.3.7 Media selection for antimicrobial testing should have physiological relevance

Selecting the relevant growth medium for testing antimicrobials under development is an important factor in determining whether any future antimicrobial material is effective. For example, to determine whether the antimicrobial coating developed in Chapter 2 could be appropriate for use in endotracheal tubes, a medium relevant to the oesophageal tract and mouth is a suitable option. Different media were investigated due to the different nutrient composition, whilst Mueller Hinton broth (MHB) may cause a bacterial species to grow prolifically, minimal defined medium may have the opposite effect and cause slow growth, each of which are likely to have an impact on the efficacy of antimicrobials. Investigation into different media led to using an artificial saliva medium (ASM), which has been used by virologists to examine contamination of facepiece respirators[404]. Physiological relevance represents an intensive care patients bacterial load on untreated endotracheal tubing and treated endotracheal tubing. Further experiments were performed using this artificial saliva medium alongside MHB to better understand the role that different media types play in understanding the efficacy of the antimicrobial coatings that were developed, with particular focus on biofilm formation and total viable cell counts as markers of real-world infection of endotracheal tubing.

3.3.8 The relevance of bacterial loading in antimicrobial assays

To determine the appropriate starting inoculum for biofilm assay and understand whether this was impacted by media type, I tested multiple concentrations of starting inoculum for *A. pittii* in a biofilm formation assay. The results in Figure 3.8, show that there was no statistically significant difference between starting inoculation and the resulting biofilm formation after 18 hours between MHB, TSB and ASM.
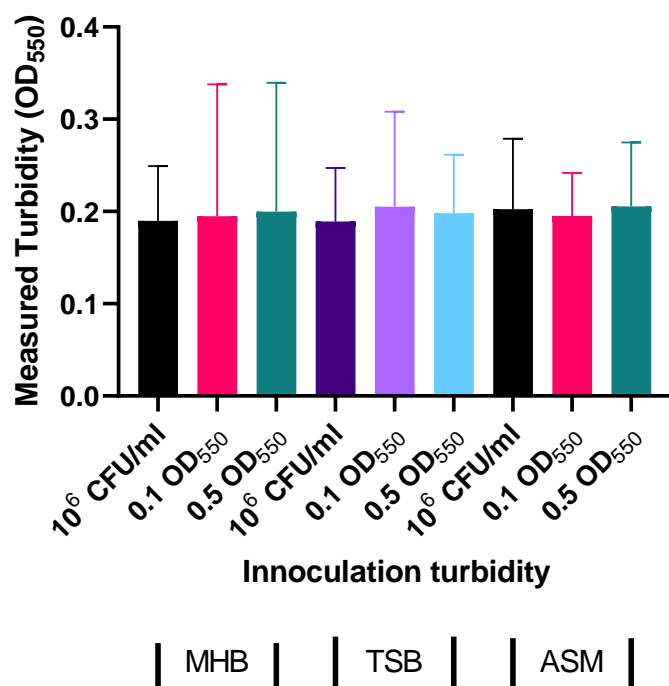
Figure 3.8 *The turbidity at OD$_{550}$ between different medias and different inoculation concentrations. The measured turbidity of A. pittii biofilms after 18 hours of incubation with a starting inoculation concentration of 10^6 CFU mL^{-1}, 0.1 OD$_{550}$ and 0.5 OD$_{550}$ respectively, in three different media. Biofilm was taken from the adhered tubing attached to a 24 well plate lids using the modified minimum biofilm eradication concentration assay described in 2.5.11. No significance was determined between starting inoculant concentration and medium used.*

3.3.9 Antimicrobial activity of copper oxide nanoparticles against a panel of bacterial pathogens

A variety of compounds exhibit antimicrobial properties; however, nanotechnology and nanoparticles are an emerging field of science with broad application. Knowing that copper oxide nanoparticles are an excellent antimicrobial agent, an applied coating of copper oxide nanoparticles would give medical devices such as endotracheal tubes, antimicrobial properties and reduce the number of infections recorded from these devices.

Glutamic acid coated copper oxide nanoparticles were synthesised using a precipitation method as described in 2.2.1 and were analysed using a JEOL JEM-2100Plus TEM. Both the size of nanoparticles and number of nanoparticles were measured in a 10 µL droplet as seen in 2.2.1. To determine the antibacterial properties of Glu-CuO, MIC and MBC

tests were performed. These tests confirmed the efficacy of copper oxide nanoparticles by evaluating a range of concentrations. Copper chloride, the precursor to the nanoparticles synthesised, was used as a control to highlight the improved antibacterial effects of Glu-CuO nanoparticles. The results of the MIC and MBC tests can be seen below (Table 3.6), which shows that copper chloride required concentrations ranging from five to ten times larger than that of their glutamic acid coated copper oxide nanoparticle equivalent to inhibit bacterial growth. Copper chloride salt was also ten to twenty times less effective at killing bacteria than copper oxide nanoparticles.

	MIC (mg L^{-1})		MBC (mg L^{-1})	
Bacterial species	Salt	Nanoparticle	Salt	Nanoparticle
E. coli	1562.3	258	3125	325
S. aureus	1562.3	258	6250	325
P. aeruginosa	3125	325	6250	325
K. pneumoniae	3125	325	6250	325
S. epidermidis	1562.3	258	6250	325
A. pittii	1562.3	258	3125	325
A. baumannii	1562.3	258	3125	325

Table 3.8 *Table of results showing the MIC and MBC values of copper chloride salt and Glutamic acid coated copper oxide nanoparticles made from the salt precursor. MIC and MBC table showing the copper chloride salt and copper oxide nanoparticle inhibitory concentrations and the bactericidal concentrations.*

Copper salt was used as a comparison to Glu-CuO nanoparticles during MIC and MBC assays and shows that there is a difference in weighted concentration between the salt and the Glu-Cuo nanoparticles.. Initial issues arose due to the solubility of uncoated copper oxide nanoparticles in Mueller Hinton broth to follow EUCAST guidelines. These issues were rectified using the glutamic acid nanoparticle coating, as described in 2.2.4 with measurements made to confirm the improved stability.

3.3.10 Modification of the minimum biofilm eradication concentration assay

Standard biofilm assays are performed by allowing bacterial cells to settle on the bottom of 24- or 96-well plates, however, this is not an accurate reflection of biofilm formation and results can be confused by sedimentation of organisms. The Minimum Biofilm Eradication Concentration (MBEC) assay was developed to combat that, with plastic pegs attached to the lid of 96-well plates, ensuring that biofilm formation on the pegs is a true reflection of biofilm formation. However, this still does not reflect the environment of medical device tubing. Therefore, I developed the Modification MBEC assay to better understand biofilm formation of both the inner and outer surfaces of endotracheal tubes. The new modified MBEC assay performed similarly to a typical MBEC assay, however, here biofilm formed on both the inner and outer surfaces of tubing rather than on a plastic peg, which is better suited to analysis of coatings developed for medical device tubing[366]. Meaning that the modified MBEC assay was closer to what would be expected in a clinical situation, where biofilm forms on both an inner and outer surfaces of the tubing. An example of the modified MBEC assay plate is shown below (Figure 3.9).

Figure 3.9 *Modified minimum biofilm eradication concentration assay showing the lengths of silicone tube used instead of the polystyrene plastic pegs. Silicone tube was cut and adhered to the lid of a 24 well plate, then sterilised by UV light exposure to create a modified MBEC assay plate.*

3.3.11 Comparison of biofilm formation in mMBEC assays in different media

Using the modified MBEC assay a comparison between coated and uncoated silicone tubing was performed at the minimal inhibitory concentration of each bacterial strain to determine whether the coated nanoparticles were effective in preventing biofilm formation by the pathogens selected. Using the modified assay described in 3.2.18, crystal violet optical density readings were performed on the treated and untreated coatings to determine total biofilm biomass. A significant reduction in the biofilm biomass was found against the *S. aureus, E. coli*, and *A. baumannii* strains. This experiment confirmed that the nanoparticle bonding process does not detrimentally affect their antimicrobial properties. Below (Figure 3.10), the change in biofilm formation on Glu-CuO nanoparticle coated silicone tubing compared to uncoated silicone tubing can be seen, where the coated mMBEC assays had a lower biomass adhered to the tubing, when compared to the same species on uncoated tubing.
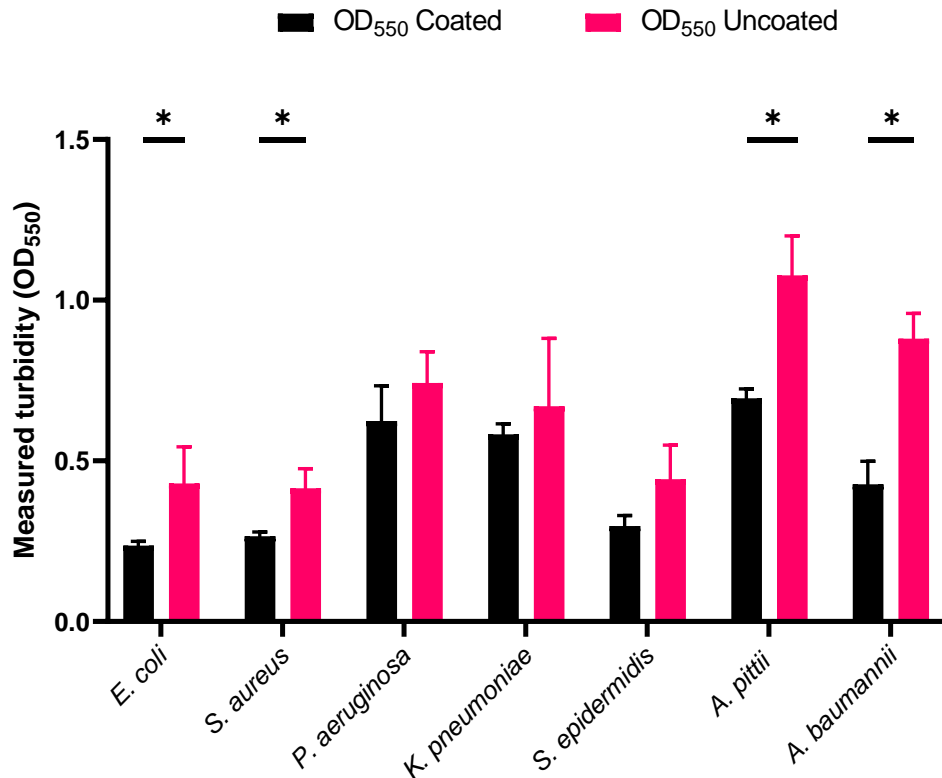
Figure 3.10 *Silicone tube coated in Glu-CuO nanoparticles compared to uncoated silicone tube suspended in MHB inoculated with different species at a concentration of 10^6 CFU mL^{-1}. MMBEC assays were prepared with silicone tubing coated in Glu-CuO nanoparticles and some assays were prepared without. Each assay was prepared initially with MHB and inoculated with each bacterial species. Both samples were incubated at 37 degrees for 18 hours. *P < 0.05, using t test.*

The experiment does show however that there is still significant biofilm formation, and that the coating does not completely inhibit binding and growth of the bacteria. This could be due to significant increase in size of the nanoparticles, due to the effective concentration of nanoparticles being lower, as some of them will not be free to penetrate adhered bacterial cells. Using a physiologically relevant medium decreased the proliferation of the bacteria and reduced the overall production of biofilm when compared to the rich medium, MHB. This decrease is seen below (Figure 3.11) where the significance can be seen between the *Acinetobacter spp.*, *P. aeruginosa, E. coli* and *S. epidermidis.* Performing the same experiment with Artificial Saliva Media (ASM) shows that there is still a significant reduction in the biofilm total biomass of the *A. baumannii* species, when comparing treated and non-treated silicone tubing. It was

seen that the significant reduction *in S. aureus* and *E. coli* was lost when using the Artificial Saliva Medium.
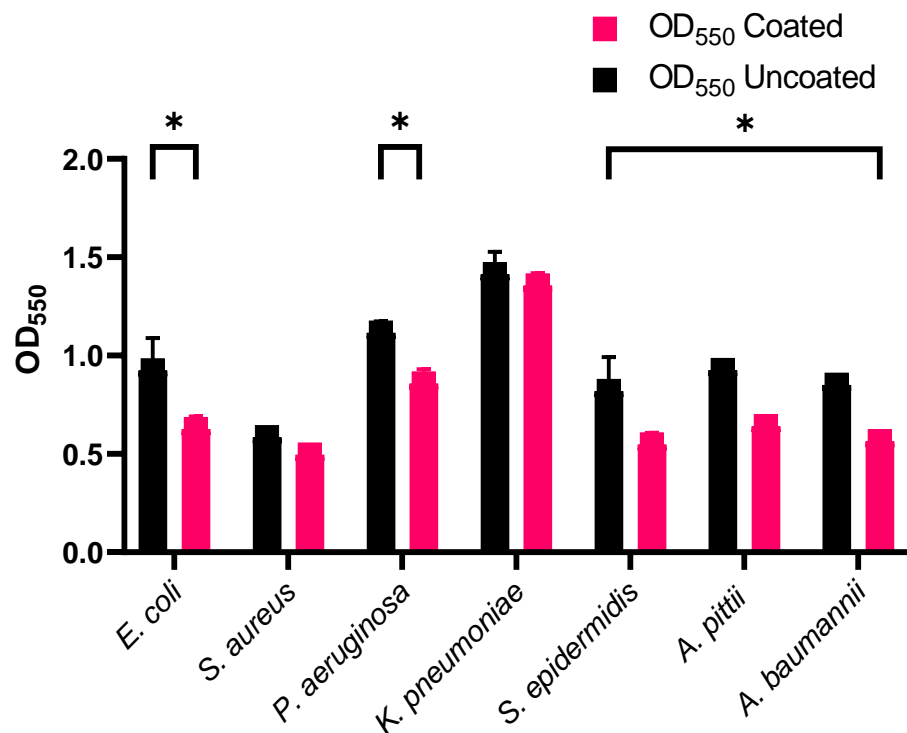
Figure 3.11 *Uncoated and coated silicone tubing in inoculated ASM of various bacterial species. Both uncoated and coated silicone tubing mMBEC assays were inoculated with each species to compare the biofilm formation on these devices after incubation 37 °C for 18 hours.*

3.3.12 Comparison of the viable cells recovered between Glu-CuO nanoparticle coated and uncoated mMBEC assays

After total biofilm biomass on the medical tubing was evaluated, the viable cell count was determined to compare the difference between viable cells within the biofilms and total biofilm biomass upon exposure to the antimicrobial coating. Below (Figure 3.12), the reduction in viable cells can be observed when the material was loaded with Glu-CuO nanoparticles at the minimum inhibitory concentration for each strain. Here, a significant reduction in viable cell count for the coated tubing was observed across all species, however, to be classified as significantly bactericidal, a minimum reduction in viable cell count of at least 2-log is required. This was observed for *E. coli* and *S. aureus*.
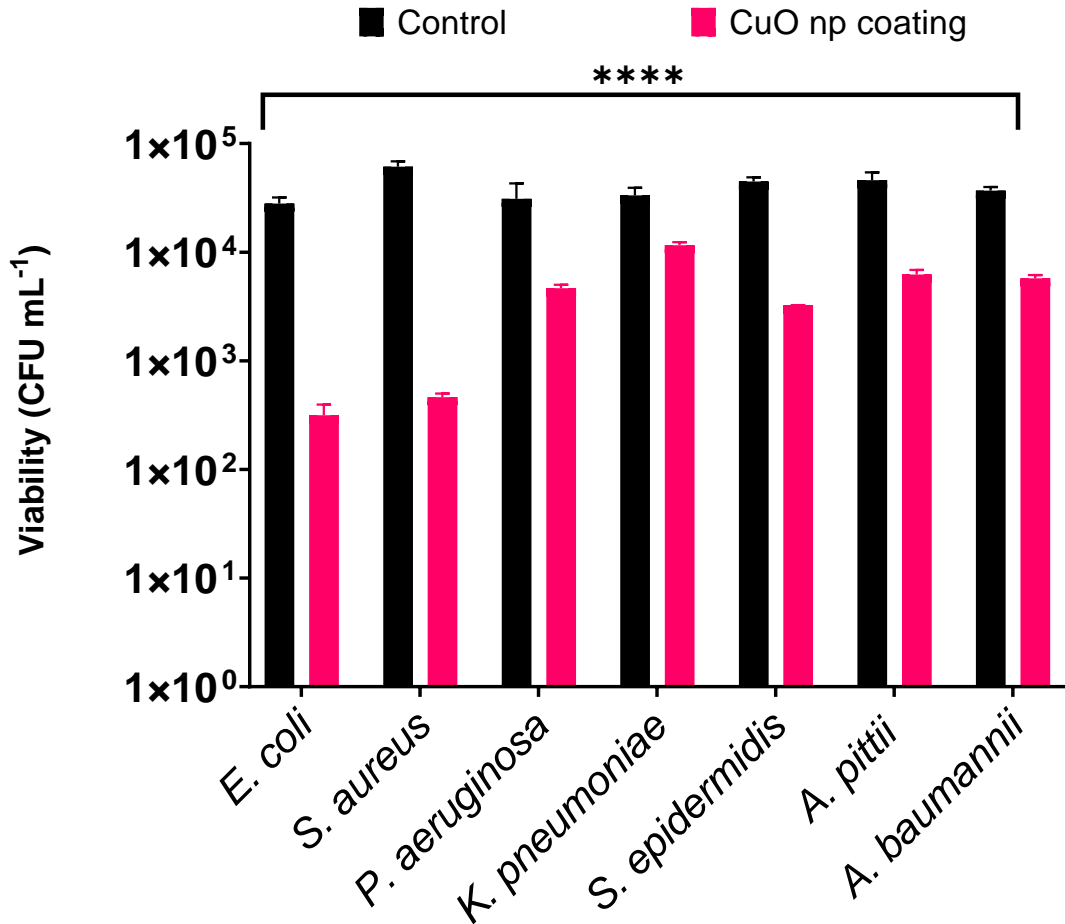
Figure 3.12 *Fewer viable bacterial cells were recovered from biofilms exposed to the antimicrobial coating for 18 hours, across all tested species of bacteria. A comparison between coated and uncoated viable cell counts, of each species using the mMBEC assay. Each tube was submerged in ASM which was inoculated with 10^6 CFU Ml^{-1} of each species and was incubated at 37 °C for 18 hours.*

3.3.13 Increasing the bactericidal coating to 20 times the bactericidal concentration

As the bacterial coating only shows a minor antimicrobial effect when coated at the minimum inhibitory concentration, the coating concentration was increased to 20 times the MBC value to determine whether the bactericidal effect of the coating could be improved. The concentration was increased based upon the leaching data acquired as seen in Chapter 2 (Table 2.2), assuming a linear increase in the amount of Glu-CuO nanoparticles leached, 20 times the MIC would equate to 160 mg L^{-1} of leached Glu-CuO

nanoparticles. This was still well below the measured toxic limit for Glu-CuO nanoparticles against HaCaT cells, whilst increasing the coating nanoparticle concentrations that might improve bactericidal effect. Below (Figure 3.13), the results of the increased concentration of Glu-CuO nanoparticles in the mMBEC assay, against the same species show that there was a greater reduction in biofilm formation on coated silicone tubing compared to uncoated silicone tubing. The change in biofilm biomass between coated and uncoated silicone tubing at 20x MBC concentration, was also greater with the increased coating concentration, when compared to the mMBEC assay performed with one time the MBC concentration.
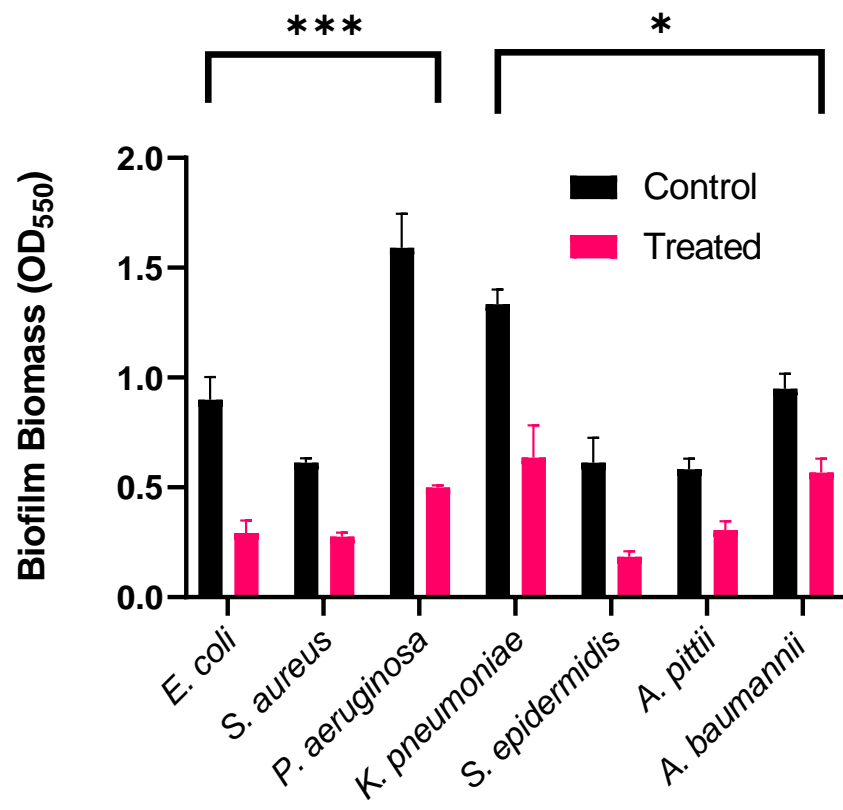
Figure 3.13 *The reduction in biofilm between control and treated modified MBEC plates at 20 times the MIC concentration. The reduction in biofilm biomass between Glu-CuO nanoparticle coated mMBEC assay compared to uncoated mMBEC assays. Each silicone tube was submerged in ASM and each species was inoculated at a concentration of 10^6 CFU Ml^{-1} and was incubated at 37 °C for 18 hours.*

The viable cell count was also measured at 20x the MBC, the nanoparticle coating reduced the viable cell counts to a greater extent than in the previous mMBEC assays

performed at 1x the MBC (Figure 3.11 and Figure 3.12). The results can be seen below (Figure 3.14) where there is once again a significant reduction in viable cells for all tested species, however the reduction observed here is log-2 to log-4 compared to the log-1 to log-2 reductions seen previously, establishing that the increased Glu-CuO nanoparticle concentration in the coating resulted in an increased bacterial killing effect.
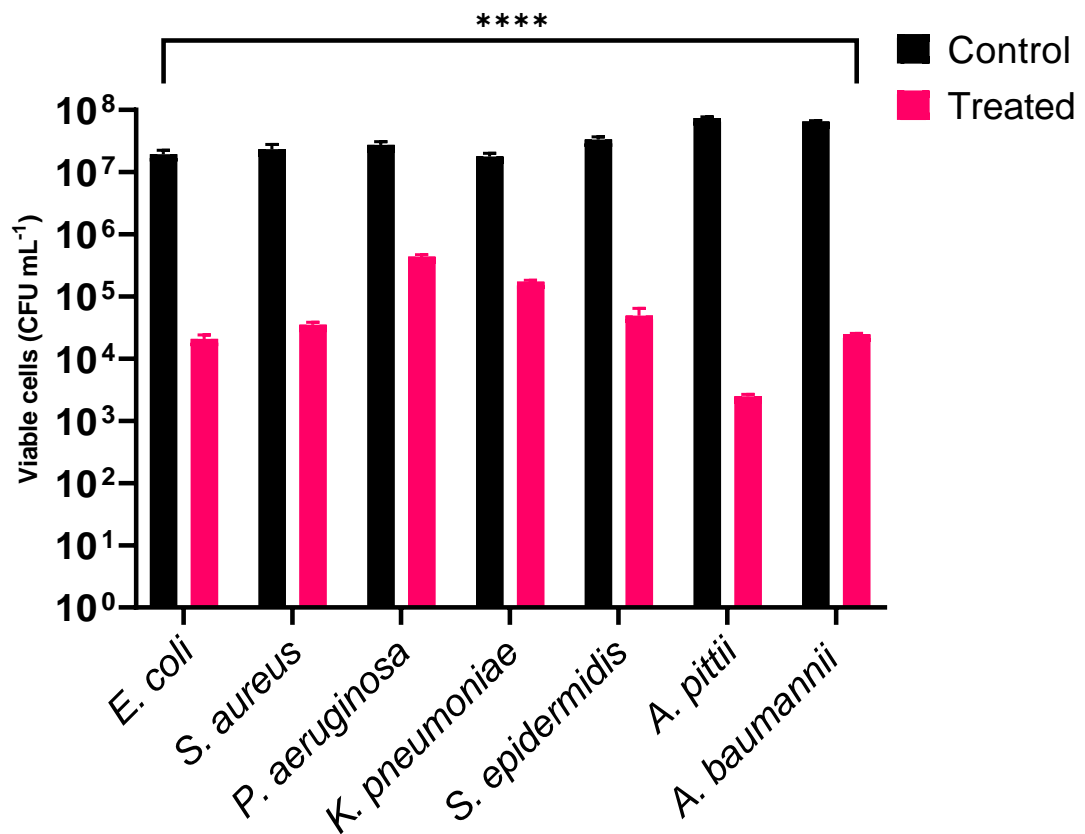
Figure 3.14 *The reduction in viable bacterial cells within biofilms at 20 times the MIC for Glu-CuO nanoparticles. The reduction in viable cells between Glu-CuO nanoparticle coated mMBEC assay compared to uncoated mMBEC assays. Each silicone tube was submerged in ASM and each species was inoculated at a concentration of 10^6 CFU Ml^{-1} and was incubated at 37 °C for 18 hours.*

3.3.14 Evaluating the rapid curing spray coating of Glu-CuO nanoparticles, using a Centre for Disease and Control reactor

Having established the efficacy of the antimicrobial coating of silicone tubing, I next evaluated the spray coating developed in Chapter 2, which presents a potential rapidly curable coating of the antimicrobial Glu-CuO nanoparticle coating for application in

medical devices that often require manipulation before implantation. For this coating to be relevant, and a potential novel coating for intraoperative, evaluation of the coatings antimicrobial effect was investigated.

Four different materials; stainless steel, titanium, polyvinyl chloride, and silicone rubber CDC coupons (12.7mm in diameter) were coated. The coating was applied to the CDC Reactor coupons as described in section 2.2.19 onto each of the four materials to better understand how the coating would affect different medical grade materials. Below (Figure 3.15) the biofilm formed on uncoated and Glu-CuO nanoparticle coated coupons after 24 hours incubation in a CDC reactor inoculated with *S. aureus* can be seen. Here, there was only a significant reduction in total biofilm biomass for the PVC coated coupons.
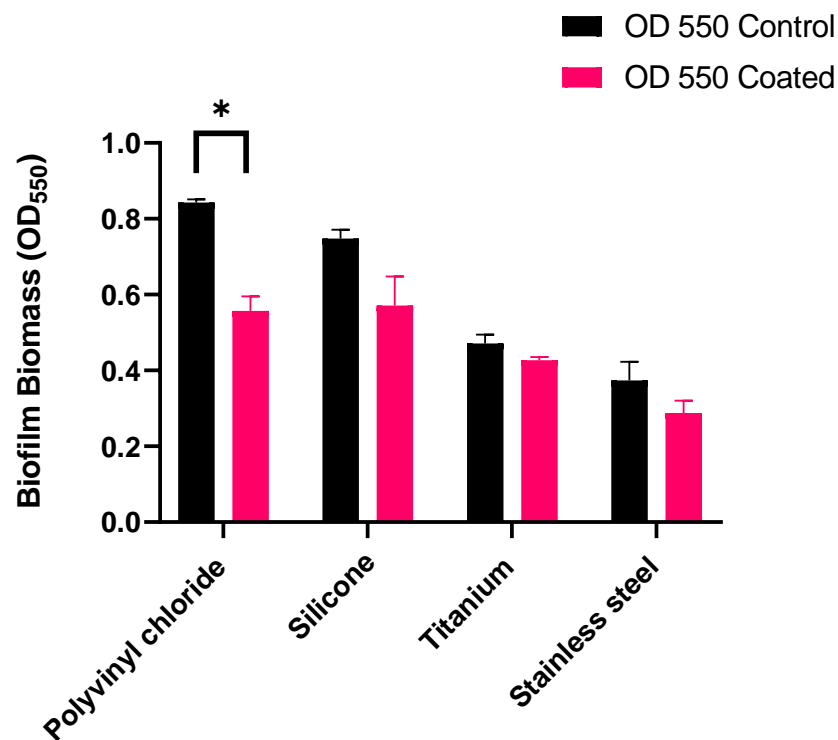
Figure 3.15 *The change in biofilm formation between untreated and treated coupons of the different materials. The difference between the untreated and treated Centre for Disease and Control coupons of different medical grade materials. Each coupon was entered into the CDC reactor, which was performed in batch mode with plasma like medium inoculated with S. aureus. This bioreactor was incubated at 37 °C for 24 hours where the coupons, and*

subsequently adhered biofilm, was carefully removed from the coupons and measured using crystal violet staining.

Viable cell counts from biofilms formed on the coupons were also determined. Investigation into the viable cells in the MBEC experiment showed that there was a higher significance in the reduction of viable cells compared to the total biofilm biomass. Below (Figure 3.16), a similar trend observed with biofilms formed on the coupons as that in the MBEC assay; a greater reduction in viable count compared to the reduction in total biofilm biomass formed on the coupons. This suggests that fewer cells were increasing the expression of biofilm related genes under these conditions, but this does still reflect a reduction in bacterial load.
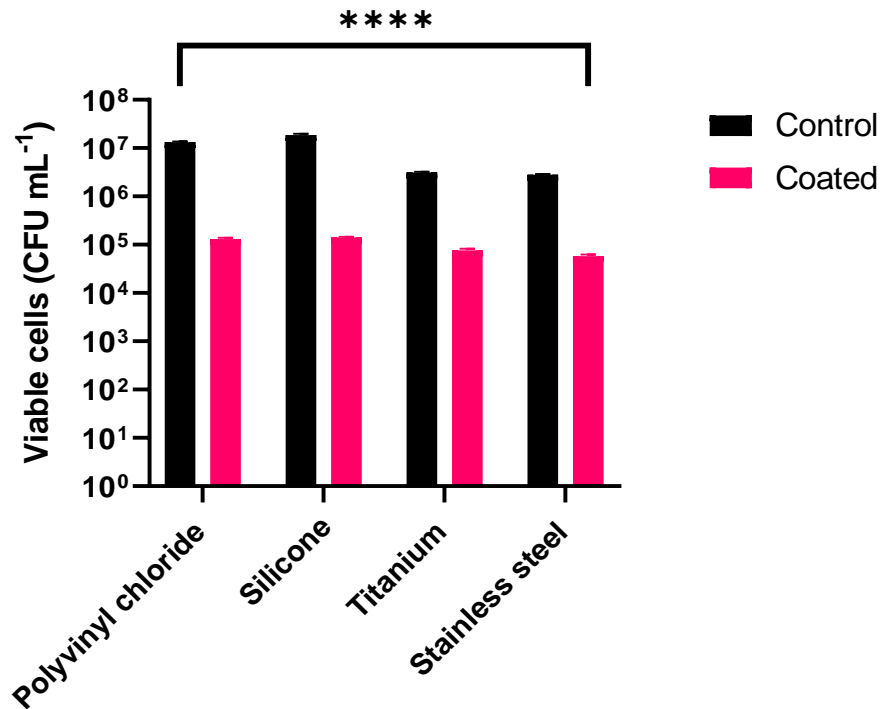
Figure 3.16 *The reduction in viable counts measured between uncoated and Glu-CuO nanoparticle coated CDC coupons. The difference between the untreated and treated Centre for Disease and Control coupons of different medical grade materials. Each coupon was entered into the CDC reactor, which was performed in batch mode with plasma like medium inoculated with S. aureus. This bioreactor was incubated at 37 °C for 24 hours where the biofilm was carefully removed from the coupons and measured using crystal violet staining.*

3.3.15 Incorporation of the Pharm2Farm Ltd. Lys-CuO nanoparticles into porous medical materials

As conventional antibiotics have shown to be ineffective against various bacterial pathogens (Figure 3.2 and Table 3.4), using copper nanoparticles to coat other medical materials beyond non-porous materials provides an opportunity to further establish the broad range of application of these antimicrobial nanoparticles.

Establishing the effect of lysine-coated copper oxide nanoparticles (Lys-CuO) provided by Pharm2farm Ltd, on different porous coated materials, of various airborne species was performed. Pharm2farm Ltd are a Small Medium Enterprise that focuses on the production of various nanoparticles for different applications, such as hydroponics for agricultural purposes, to medical equipment, such as face masks used during the COVID-19 pandemic. As part of their medical equipment during COVID-19, Pharm2farm Ltd produced Lys-CuO nanoparticle coated face masks, which whilst antiviral, were not assessed for their antibacterial properties. Lys-CuO nanoparticles were therefore assessed to understand whether these antiviral face masks have further marketable value by offering antibacterial protection.

Lysine coated copper oxide nanoparticles were coated and evaluated on porous materials. Using Pharm2farm Ltd.'s polypropylene filtration media used in their face masks and their polyester filtration material used for ventilation, the Lys-CuO nanoparticles were evaluated against various airborne pathogens. These materials were spray coated with the Lys-CuO nanoparticles. SEM images were taken for both the polypropene and polyester materials with EDS to confirm the materials were coated in the copper oxide nanoparticles.

3.2.14.1 Evaluation of the face mask material

The face masks assessed are made from polypropylene fibres that have no discernible orientation and have a thread count of 300 threads per square inch and were imaged using SEM to image the copper oxide spray coating performed by Pharm2farm Ltd. The Lys-CuO coated, and uncoated fibres can be seen below (Figure 3.17 A and B) where

particulates are seen on the uncoated fibres (A), and the Lys-CuO nanoparticles are seen on the two parallel fibres (B)
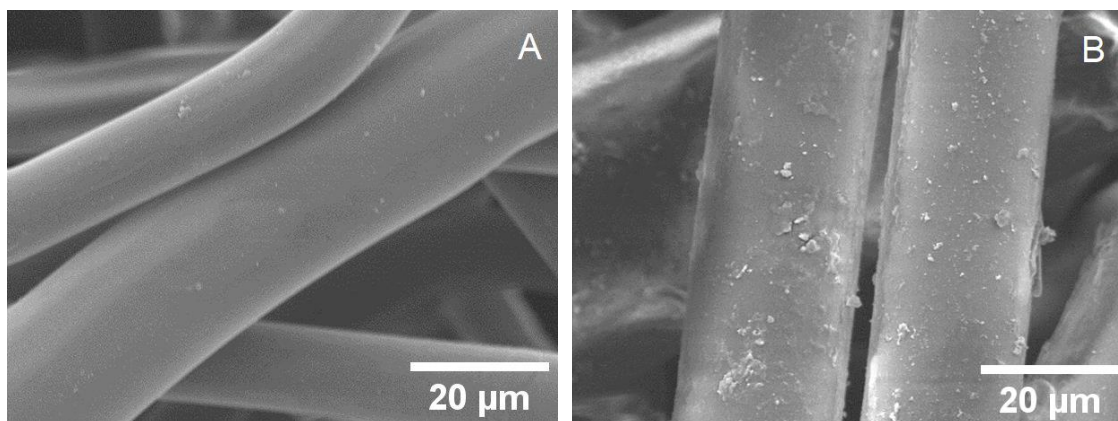
Figure 3.17 *SEM images of uncoated polypropylene fibres of the face mask material. Evaluation of the coated and uncoated polypropylene face masks was performed. Using SEM imaging, a textural difference can be seen between the coated and uncoated fibres. A) Two strands of polypropylene fibres with particulates of debris on the material from handling and transporting the material. B) Two strands of coated polypropylene fibres, coated in Lys-CuO nanoparticles.*

SEM-EDS was performed to analyse the coating to ensure it was Lys-CuO nanoparticles the material and that their was coverage across the entire mask. Copper was added as a separate figure to highlight the coating seen in the EDS analysis (Figure 4.18 A and B) as they were not part of the polyester material but are commonly observed during EDS. Due to the damage of the material which was sustained by the focused electron beam, different regions of the same sample were used to perform EDS, particularly as EDS requires an electron beam voltage of greater than 10 kV to cause electrons to eject at both emission energies.
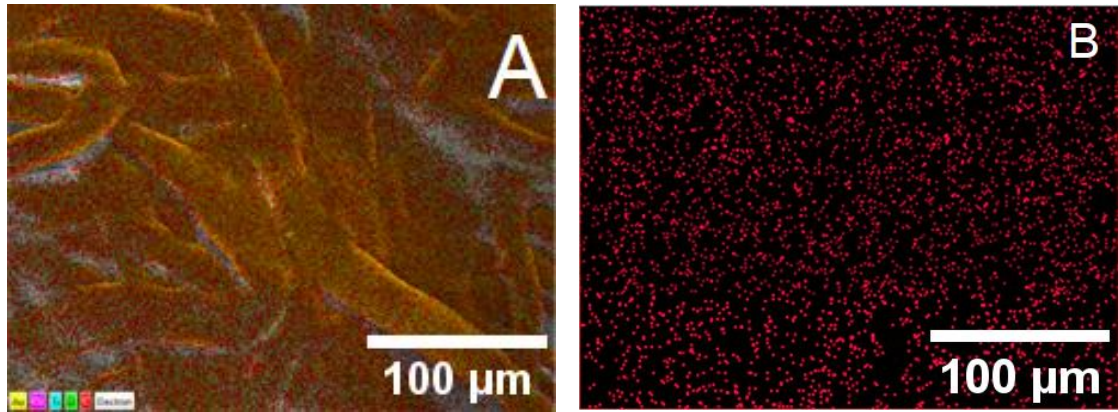
Figure 3.18 *SEM-EDS images taken of the polypropylene face mask material after it was coated in the Lys-CuO nanoparticles. EDS performed on Lys-CuO coated polypropylene face mask material showed that copper was spread evenly across the fibres, which was separated from the rest of the elemental analysis. A) Carbon, oxygen, silicon, aluminium, and copper are shown where they cannot be differentiated. B) Copper is separated from the other elemental analysis to highlight its coverage on the fibres.*

3.2.14.2 Evaluation of the filter material

Uncoated polyester fibres used in the filter material were also imaged using SEM and SEM-EDS to examine the coating and the fibres when uncoated. Below (Figure 3.19 A) torn polyester fibres can be seen with traces of debris in them but are otherwise uncoated and have no copper on them. Additionally, two fibres can be seen of the filter material after it has been spray-coated with the copper lysine nanoparticles (Figure 3.19 B). The coating is once again not homogeneous but visually has coated more of the fibres so could be described as isotropic in appearance.
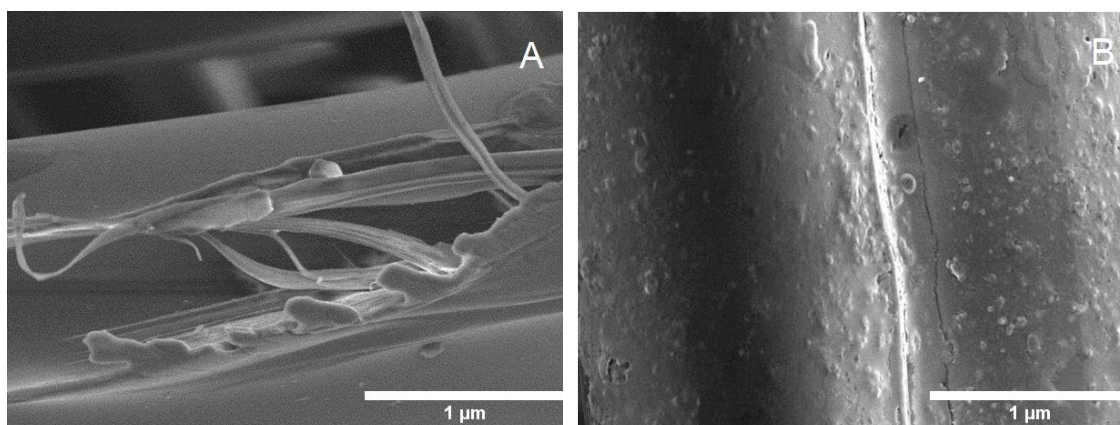
Figure 3.19 SEM imaging of torn uncoated and Lys-CuO nanoparticle coated polyester filter material fibres. SEM images of polyester filtration material fibres, quantitatively evaluating the Lys-CuO nanoparticle coating. A) Torn, uncoated fibres of polyester fibres are seen in the filtration material, showing a smooth texture up to the tear. B) Lys-CuO coated polyester fibres coated with a rough texture.

Like the EDS of the polypropylene fibres (Figure 3.18), EDS was performed of another region of the coated polyester material as extended exposure of a single region caused topological damage at the high 10 KeV required to perform EDS. Below (Figure 3.20), the Lys-CuO nanoparticles can be seen adhered to the surface of the polyester material.
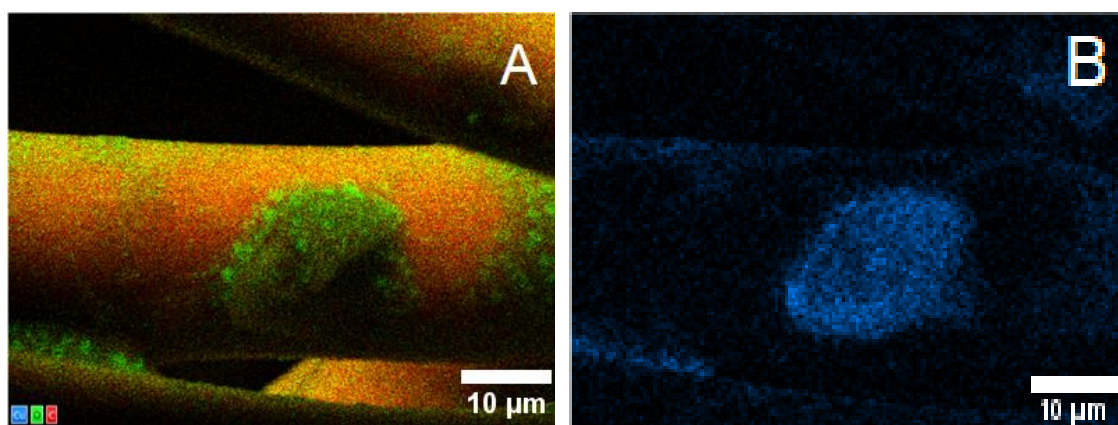
Figure 3.20 SEM-EDS images taken of the polyester filter material after it was coated in the Lys-CuO nanoparticles. Carbon and oxygen, red and green, are shown for structure whilst the copper, blue, is shown to highlight the copper deposition. Lysine coated Copper oxide nanoparticles are well dispersed on the material as seen in the blue image.

3.3.16 Antimicrobial testing of the Lys-CuO coated face mask materials

Antimicrobial testing these materials was achieved following ISO 20743:2021 with modifications[402]. The experiments performed showed a reduced number of viable cells recovered on the Lys-CuO coated materials compared to the uncoated materials. This is due to the antimicrobial activity caused by the Lys-CuO nanoparticle, causing the recovered viable cells to be lower than on uncoated material. At the baseline, the Lys-CuO coated polypropene showed an immediate touch killing effect against *A. baumannii E. coli* and P*. aeruginosa* (Figure 3.21), indicating that the copper coating added a clear the antimicrobial effect of the face mask. After 18 hours, there were no recovered live bacterial cells from the treated material showing that the Lys-CuO nanoparticletreatment completely eradicated any viable bacterial cells.
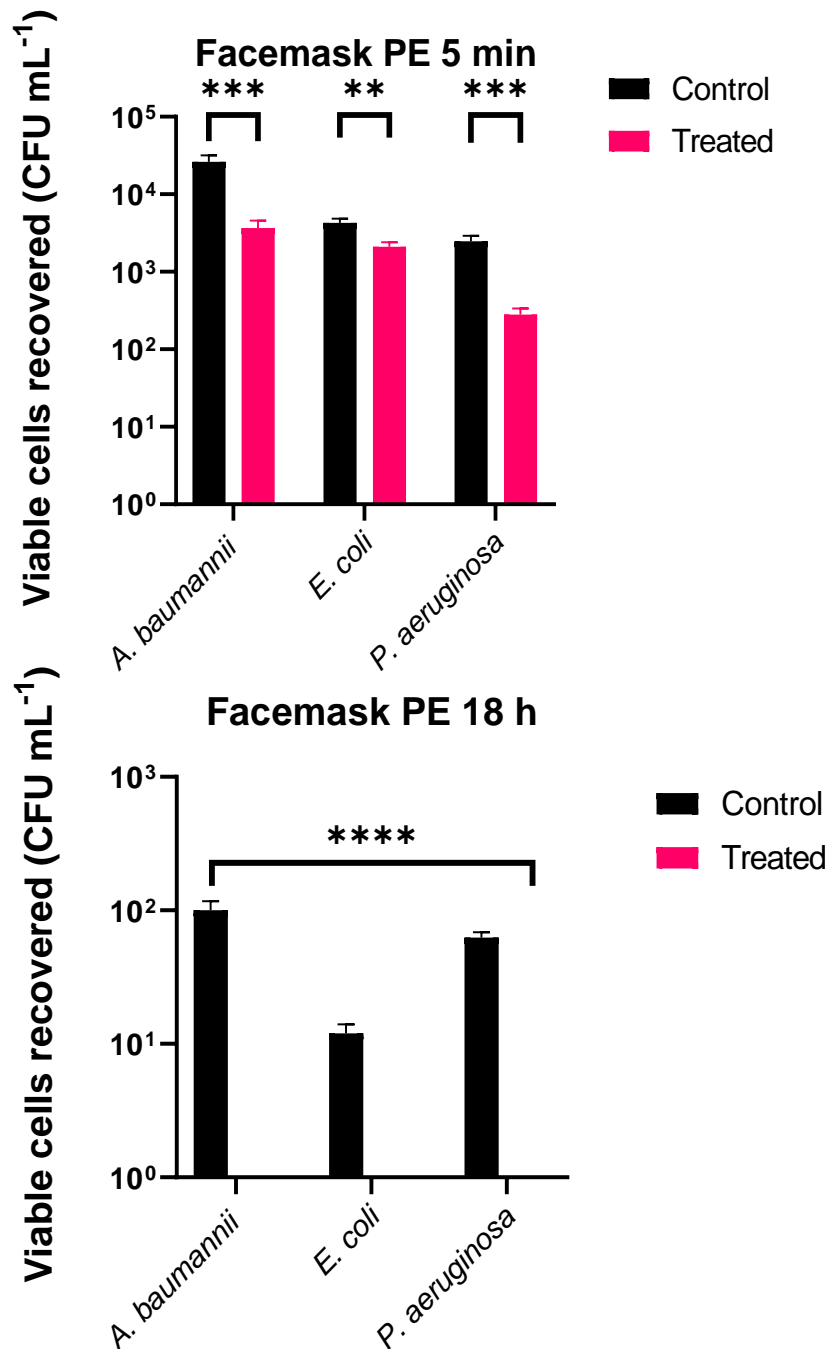
Figure 3.21 *Bacterial viability enumerated after 5 minute and 18 hour exposure to the Lys-CuO coated polypropylene filtration media. Each bacterial species applied and enumerated from the Lys-CuO nanoparticle coated polypropylene. Each sample of coated or uncoated polypropylene was inoculated at 10^5 CFU mL^{-1} following ISO 20743:2021. Viable cells were enumerated after 18 hours of incubation at 37 °C*

3.3.16 Testing airborne pathogens and *Salmonella enterica* on filter material for commercial value

Using the polyester filtration media, a clinical isolate of *Salmonella enterica* was investigated for potential application in the various food manufacturing industries such as the poultry industry. A comparison of the viable cells recovered can be seen below (Figure 3.22), which shows a five minute exposure time and an 18 hour exposure time. A significant reduction in the *S. enterica* and *A. baumannii* clinical isolates was observed after five minutes of exposure. After 18 hours complete eradication is seen in the *A. baumannii, E. coli* and *S. enterica* species with significant reduction in the *P. aeruginosa* viable counts.
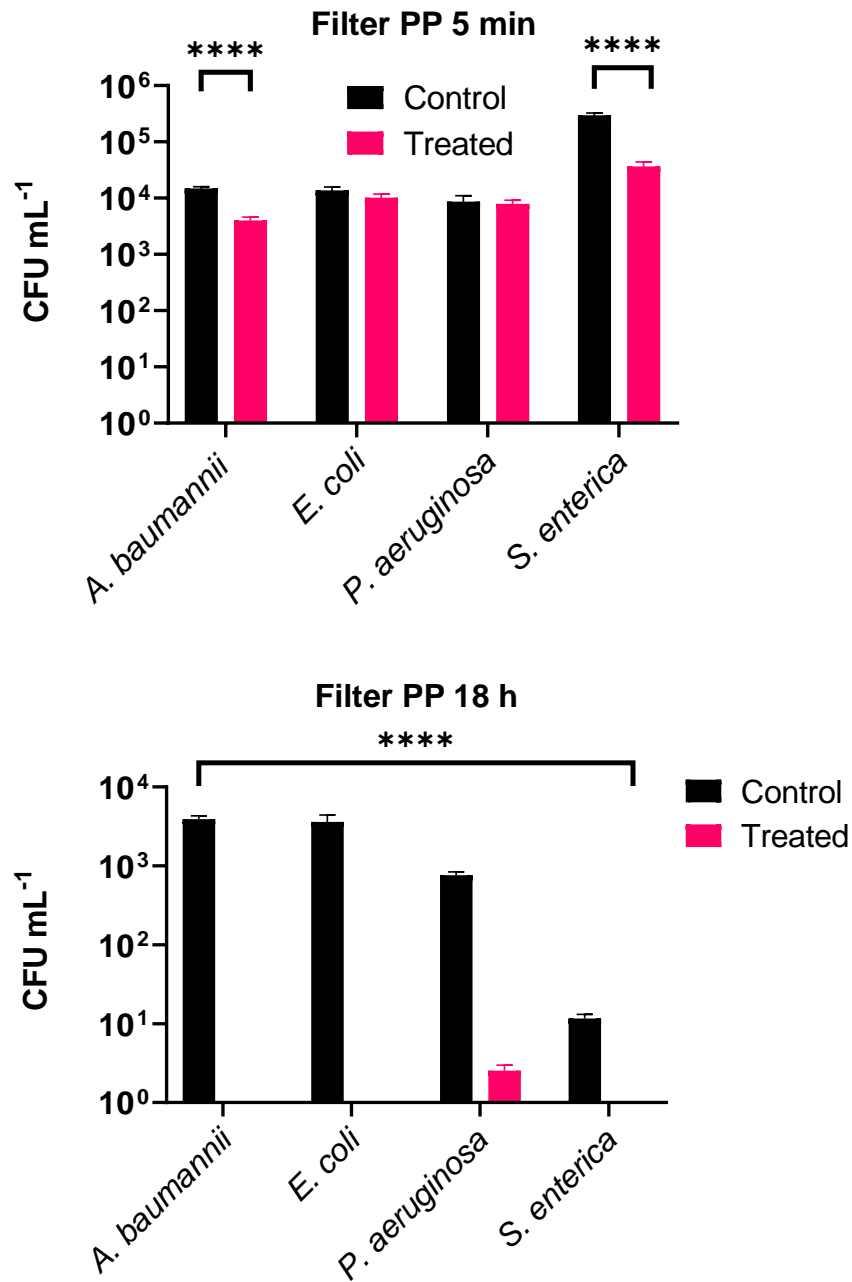
Figure 3.22 *Exposure of Salmonella enterica and airborne pathogens to filter material after 5 minutes and after 18 hours. S. enterica, A. baumannii, E. coli, and P. aeruginosa were all used to inoculate the polyester filtration media and examine whether the Lys-CuO Nanoparticle coating had an antimicrobial effect that may hold potential commercial value. Each species was evaluated using ISO20743:2021, where each species was inoculated at 10^5 CFU mL^{-1} for 18 hours at 37 °C.*

3.4 Discussion

Each of the bacterial species investigated in this chapter either forms part of the ESKAPE family of pathogens, or possesses a significant financial burden on various industries, including medical or food manufacturing[407,408,409]. The variety of these species show that it would not be appropriate to test a new antimicrobial against just a single bacterium, as evaluation of the species in this chapter highlight the different levels of antibiotic resistance and resistance to many of the different classes of antibiotics (Table 3.2 and 3.4). This varied level of resistance between species is further observed between different strains within the species[410,411]. Evaluation of the genotypic data showed that there was marginal concordance between the genotypic and phenotypic data, however, this concordance was not as significant as hoped (Figure 3.3). This is due to the limited antibiotic testing each species was evaluated against, with further antibiotic testing possibly changing the measured concordance or discordance. The lack of agreement, however, is not uncommon as other extensive studies suggest that the concordance is also lower than initially hoped[412]. This indicates that genotypic evaluation of the antibiotic resistance profile of a strain may not indicate the entire resistance profile of that strain and that phenotypic data is more reliable than genotypic for antibiotic susceptibility determination. However, genotypic analyses also provide analysis of other aspects of the bacterial strains evaluated, including data such as the bacteriophage found within the genome and other virulence factors, which contribute to the virulence of the species and may contribute to antimicrobial resistances (Table 3.5 and Figures 3.4 to 3.7). The *S. aureus* strain used here, possesses a copper exporter, which may have predicted an increase in concentration of copper exposure, where examples of copper exporter genes directly increase the resistance of copper-based antimicrobials[413]. However, no significant difference in sensitivity to the copper nanoparticles was observed for this species here, suggesting that the potential resistance mechanism is possibly ineffective against the Glu-CuO nanoparticles.

As bacteria grow differently in different media, selecting the correct medium, to emulate the correct growth environment, was important to appropriately emulate various medical devices and the conditions they would be found in[414]. Comparison of the different media as measured through different starting inoculation concentrations in

different media. As many of the assays that determine bacteriostatic or bactericidal effects of antimicrobials rely on starting inoculation of 10^5 or 10^6 CFU mL^{-1}, varying starting inoculation concentrations were tested to determine whether there was any relevance using one of these assays[415,416]. Between each medium and each starting inoculation, no significant difference was seen between each starting inoculation and overall biofilm formation

 (Figure 3.8). Using the classical minimum inhibitory concentration and minimum bactericidal concentration assays, the glutamic acid coated copper oxide nanoparticles and copper chloride salt, the precursor to making the nanoparticles, were evaluated (Table 3.6). The salt showed a considerably higher concentration required to cause both an inhibitory and bactericidal effect on each of the species, when compared to the nanoparticles they produced in Chapter 3. Evaluating the Glu-CuO nanoparticles showed that their bactericidal concentration for each of the tested species was 325 mg L^{-1}, which varied from some of the literature results of 100 mg L^{-1} to 250 mg L^{-1} [417,418]. The variation is caused by the size of the nanoparticle with smaller nanoparticles expressing a greater antimicrobial effect as nanoparticles at 10 nm have a greater antimicrobial effect than nanoparticles at 100 nm[264].

Testing the effect of the Glu-CuO nanoparticle coating was performed using a modified minimum biofilm eradication concentration assay, altering a conventional biofilm assay that is used for its reproducibility of biofilms[419]. This assay uses pegs on a 96-well plate and is excellent at reproducing biofilms, however, the biofilm formed only occurs on an external surface of the peg, which does not emulate the conditions of endotracheal tube. Contamination of endotracheal tubes rapidly forms on its internal diameter and progressively spreads to the end of the tube, which sits at the carina, exposing the outer diameter and the nutrient rich mucous to the bacteria, encouraging biofilm formation[420]. The assay was, therefore, modified by changing the pegs to one cm silicone tube cuttings and adhering them to a 24-well plate (Figure 3.9). This modification allowed evaluation of the novel Glu-CuO coating, at the MBC concentration determined in 3.2.9 using the dip coating technique developed in Chapter 2. This novel coating showed some reduction in the biofilm biomass measured from the bacterial species tested (Figure 3.10) but a significant reduction in all species when evaluation of the viable cells

recovered from treatment. To be considered antimicrobial however, a minimum of log-2 to log-3 reduction in viable cells is required, where coating at MBC concentration lead to only a log-1 to log-2 reduction (Figure 3.12)[421]. As the toxicity of the Glu-CuO nanoparticles was determined to be caused by free nanoparticles, the bonded coating was increased assuming a linear increase in leaching, to a linear increase in coated Glu-CuO nanoparticle concentration. At 20 times the MBC, and assuming linear leaching, the potential leaching of the coating is predicted to be 160 mg L^{-1}, still well below the measured toxic level and was used to coat a new set of mMBEC assays. Evaluation of the biofilm biomass showed that less biofilm formed on the silicone tube at 20 times MBC compared to one times MBC (Figure 3.13). Furthermore, examining the viable cells at 20 times MBC concentration showed that all species had a viable cell count that was reduced between log-2 and log-4, depending on species, indicating that there is a therapeutic window where the antimicrobial criteria were met[421].

Examining the spray coating of Chapter 3 was performed by coating bioreactor coupons, of different medical grade materials. As a common site of infection includes orthopaedic implants that are intraoperatively modified, stainless steel 316, titanium, silicone rubber and PVC coupons were selected to cover a variety of these orthopaedic implants[422,423,424]. Current antimicrobial treatments of these *ad hoc* modified materials involve dipping the modified material into a bath of antibiotics or other antimicrobial, such as iodine, before implantation, which drives antibiotics resistance[425]. This spray coating offers a novel coating that can be rapidly cured using UV curing, with the bonus of sterilizing the material post modification and before the coating has fully cured. This coating can be a cured within 30 minutes of application, offering a different type of antimicrobial coating, that leaches minimally and is non-toxic. The spray coating showed similar results to the dip coating, where biofilm reduction was observed to varying levels of significance depending on the material, with more porous materials seeing a larger change in biofilm biomass (Figure 3.15). Similarly, the viable cell count was observed (Figure 3.16) with log-1 to log-2 reductions, depending on the medical material. While this does not meet the criteria to call this coating antimicrobial, it leads towards increasing the Glu-CuO nanoparticle concentration to have that antimicrobial effect. Further study with increased Glu-CuO concentrations is required to draw firm conclusions from this work.

Finally, evaluation of lysine coated copper oxide nanoparticles incorporated into facemasks produced by Pharm2Farm Ltd. during the COVID-19 pandemic for their antiviral properties was performed. These nanoparticles were also used on a polyester filtration material, and this material may hold potential commercial avenues in various manufacturing industries, such as the food industry[426]. Various airborne pathogens were tested against these two materials to evaluate their antimicrobial behaviour, with three species that have the capability of causing ventilator associated pneumonia, and one additional species against the ventilator material which causes salmonellosis [427,428]. The material coated with Lys-CuO nanoparticles showed a significant touch killing effect, with near complete eradication of viable cells after 18 hours of contact. This antiviral product therefore has applications as both PPE where sterility is critical, such as during surgery, or during any industry where sterility is crucial.

Chapter 4. Non-invasive imaging of biofilms on implanted medical devices

4.1 Introduction

Implanted medical devices are the ideal breeding ground for pathogenic bacteria due to their presence within the body. Currently, the primary method of detecting an infected medical device is through direct patient observation, where symptoms will occur. Once these symptoms have been observed, a localised biopsy should be performed to confirm the result and determine whether a course of antibiotics is sufficient, in most cases it is not, or to remove the infected device. For catheters, a common source of infection, the procedure to remove this device is simple, but causes great discomfort to the patient. In the case where the device needs to be removed, further complications arise from the need for sterile removal to prevent further spread of infection. This all occurs after the patient has undergone surgery to implant the device and symptoms can take anywhere between a few days and a few years to manifest depending on the severity of the infection[429]. Non-invasive imaging modalities such as magnetic resonance imaging (MRI) are crucial in studying and understanding how biofilms adhere and propagate on implanted medical devices. Current work allows MRI to reveal the structure and composition of biofilms using a variety of different sequence types, also allowing for the visualization of changes to biofilm structure as it matures over time[430]. Many implanted medical devices are safe for MRI, however there are implants that are not suitable such as cochlear implants or previous iterations of pacemakers. Similarly, certain medical devices such as titanium plates, pins and screws are safe for MRI but induce artefacts when imaging in the region of the implant. These artefacts will make detecting biofilm formation difficult, however for devices that are not made from these materials, often metals, MRI can offer a non-invasive way to detect infection.

Measurements of biofilms using MRI can be broken down into two different categories, firstly, the bulk fluid in the material, which includes the media the biofilm grow in, which is predominantly water. Secondly, the biofilm itself can be imaged and measurements made if appropriate resolution is achieved.

Typical MRI focuses on ^{1}H nuclei, so water molecules within tissues provide the signal and contrast received within the image. The contrast is dependent on the spin-lattice relaxation, T_1 or the spin-spin relaxation, T_2^{eff} and these are dependent on the local chemical composition the water molecule is found in[431]. Understanding the differences in the T_1 and T_2^{eff} relaxation of biofilms and that of human tissues, may lead to a better understanding of how to non-invasively detect the formation of biofilms *in situ*. This detection would aid in preventing patients from becoming symptomatic by detecting possible biofilms early.

In this chapter a low-field nuclear magnetic resonance (NMR) system investigates the T_1 and T_2 relaxation of bulk biofilm media. After promising results, a blind trial were performed on ten random bacterial species to determine if there was a characteristic difference between Gram positive and Gram negative species, and their corresponding relaxation values, similar to alternative studies in literatures[432]. These experiments were repeated using a clinical 1.5T MRI scanner and investigated over a week to evaluate the change in relaxation. At the same time, the change in biofilm biomass is evaluated to compare the change in relaxation properties of the bulk biofilm media to the change in biofilm. Furthermore, the apparent diffusion coefficient and self-diffusion coefficient is measured for each species over time to examine the nutrients in the media and how they become depleted from the media[433]. Finally, this chapter shows that it is possible to image biofilm on an endotracheal tube *in vivo* of a porcine pluck trachea, with clinically relevant sequences and times[434].

4.2 methods

T_1 weighted, T_2 weighted, diffusion weighted, proton density and spin echo images were taken using a 1.5T siemens Avanto MRI scanner. Samples were places onto the gantry and imaged using one of the different sequences described in these methods sections.

4.2.1 T$_1$ measurements using inversion recovery

T_1 measurements of bulk biofilm solutions of *Escherichia coli*, *Pseudomonas aeuriginosa*, *Staphylococcus epidermidis*, *Staphylococcus aureus Klebsiella pneumoniae*, *Acinetobacter baumannii* and *Acinetobacter pittii*, were made using an inversion recovery sequence with the settings below (Table 4.1). This scan sequence was repeated multiple times using varying measurement times, which are defined as the inversion time (T_I) . Measurements were taken at room temperature (20°C)To observe the excitation, and the relaxation back into the low energy state, aligned with the B$_0$ field signal at variable inversion times. These values were chosen to cover the recovery time of both the medium and the biofilm, where the medium is water based and would have a recovery time less than pure water at 4000 ms. Further higher values were measured to ensure full relaxation of the material.

Settings	Value
T_r	12000 ms
T_e	72 ms
T_I	25, 50, 100, 150, 200, 300, 400, 600, 800, 1200, 1600, 2400, 3200, 4800, 6400, 8000, 10000 ms
FoV	207 mm
Slice thickness	8.0 mm
FoV phase	84%
Phase oversampling	0%
Averages	1
Concatenations	1

Table 4.1 *Sequence settings for the T_1 inversion recovery scans. The MRI sequence used to measure the T_1 value of each bulk biofilm. The T_I corresponds to the variable inversion recovery times that signal was measured at to estimate the T_1 value of the bulk biofilms using the MRI scanner.*

4.2.2 T$_2$^{eff} effective or measurements using Gradient echo sampling

T$_2$^{eff} measurements can be made using gradient echo sampling, a technique which uses echo sequencing to capture a series of images that can estimate the T$_2$^{eff} of the imaged sample. This sequence uses increasing echo times to measure the relaxation of the spin-spin system and determine when the measured protons return to phase. Using this gradient echo sampling sequence, the echo time was increased incrementally in 50ms steps until 1600 ms, which is the limit of the MRI scanner. Each measurement was taken at room temperature (20°C)

Settings	Value
T_r	4583 ms
T_e	50 ms
FoV	500 mm
Slice thickness	8.0 mm
FoV phase	32.0 %
Phase oversampling	54%
Averages	1
Concatenations	5

Table 4.2 *Sequence settings for the T$_2$^{eff} gradient echo sampling sequence. The T_e values are varied over the duration of the sequence to evaluate the T$_2$^{eff} effective value of each bacterial species. The relaxation time changes based on sample, samples with longer T$_2$^{eff} times would range from 50 ms to 1600 ms in increments of 50ms to account for the full length of the possible relaxation.*

4.2.3 T$_1$ weighted imaging

After positioning the bulk biofilm samples grown with *Escherichia coli*, *Pseudomonas aeuriginosa, Staphylococcus epidermidis, Staphylococcus aureus Klebsiella pneumoniae, Acinetobacter baumannii* and *Acinetobacter pittii* bacterial species, into the centre of the magnetic bore, where the field is most homogenous, T$_1$ weighted imaging was performed. This captured structural images to examine the regions of biofilms in the sagittal plane using a spin echo sequence, the settings are shown in Table 4.3. Contrast in this these images showed lipids in biofilm as a brighter region of interest compared to that of media. T$_1$ weighted imaging of porcine pluck was performed using the

following sequence with a reduced field of view and one additional average. These settings were taken from the inversion time sequencing and were captured at room temperature (20°C).

Settings	Value
T_r	550 ms
T_e	9.4 ms
FoV	220 x 220 mm
Slices	5
Slice thickness	3.0 mm
FoV phase	100 %
Phase oversampling	13 %
Averages	2 *
Concatenations	1

Table 4.3 The T_1 Spin echo sequence used for structural imaging. The spin echo sequence used for T_1 weighted imaging used the settings above. These settings were selected and modified aiding in accurate region selection during Inversion sequencing to determine the true T_1 value of the biofilms. T_r was chosen based upon the inversion recovery results and T_1 value measured and T_e was chosen as the shortest possible value the software would allow.

4.2.4 T_2 weighted Imaging

T_2 weighted imaging was performed to examine the biofilm and media content together to determine when the biofilm has formed significantly on the surface of the material, the settings used are shown in table 4.4. Each image was captured withing the MRI scanner at room temperature (20°C). T_2 weighted imaging showed the media brighter than the biofilm, consisting of extracellular polysaccharides and cells, providing additional contrast and secondary confirmation of the T_1 results.

Settings	Value
T_r	7000 ms
T_e	15 ms
FoV	73 x 73 mm
Slices	5
Slice thickness	1.0 mm
FoV phase	100 %
Phase oversampling	100%
Averages	2
Concatenations	1

Table 4.4 *The T_2^{eff} turbo spin echo sequence used for determination of biofilm formation. The T_2^{eff} settings above were used to image the biofilm using MRI, allowing for clear definition between media and biofilm. These parameters were the default settings found within the Siemens preprogrammed sequences on the 1.5T Siemens Avanto MRI scanner*

4.2.5 Proton density imaging

Proton density imaging was used to confirm the results of both T_1 and T_2^{eff} weighted imaging by providing a second image showing the contrast between the water dominant media and the low levels of lipids produced in biofilm formation.

Settings	Value
T_r	7140 ms
T_e	11 ms
FoV	247 x 247 mm
Slice thickness	2.0 mm
FoV phase	17 %
Phase oversampling	30%
Averages	3
Concatenations	1

Table 4.5 *The Proton density sequence used to confirm the imaging results of T_1 and T_2^{eff} weighted imaging. The Proton density settings used to validate the T_1 and T_2^{eff} imaging confirming the regions of biofilm and media. The settings chosen were the default proton density sequence provided by Siemens, with modification to the field of view and slice thickness.*

4.2.6 Diffusion measurements in biofilms using spin echo sequences

Diffusion was measured using a spin echo sequence and varying the echo time (T_e), then comparing the signal between the shortest echo time and each measured echo time thereafter. 12 different echo times were used to cover the range allowed by the default spin echo sequence.

Settings	Value
T_r	3000 ms
T_e	11, 50, 100, 200, 300, 400, 500, 600, 700, 800, 900 and 1000 ms
FoV	500 mm
Slice thickness	20 mm
FoV phase	100 %
Phase oversampling	0%
Averages	1
Concatenations	1

Table 4.6 Sequence settings for the spin echo sequence used to measure diffusion via the Stejskal-tanner equation. A spin echo sequence was used with varying echo times to satisfy the Stejskal-Tanner equation. The varying echo times selected covered the range of minimum to maximum allowed echo times, with equal spacing between these two values. This produced a set of data that had a linear fit that would provide a gradient to estimate the diffusion over the range of echo times.

4.2.7 Diffusion Weighted Imaging MRI

Diffusion weighted images were used to analyse the diffusion of a sample by varying the b values of the DWI sequence. The settings used covered the range of b values allowed by the scanner using the default DWI sequence preprogrammed by Siemens.

Settings	Value
T_r	3500 ms
T_e	109* ms
Fov	230 x 230 mm
Slice thickness	5 mm
FoV phase	100 %
Phase oversampling	0%
Averages	3
Concatenations	1
Diffusion weightings	12
b value	0, 50, 100. 200, 300, 400, 500, 600, 700, 800, 900, 1000 mm $^{-2}$

Table 4.7 *Sequence settings for the diffusion-weighted sequence. Diffusion measurements were taken at increasing b values to satisfy the b factor described by Le Bihan as a modification of the Stejskal-tanner equation. This ensured a linear plot that could accurately fit apparent diffusion coefficient (ADC).*

4.2.8 Nuclear magnetic resonance

Measuring the T_1 or T_2^{eff} of any given sample was performed using a Halbach array with a bore size of 25mm connected to a Kea^2 spectrometer, Magritek, Germany. The software Prospa, also written by Magritek was used to run sequences which would measure and fit T_1 inversion recovery and T_2^{eff} estimations. The Halbach system, created at Nottingham Trent University, possessed an internal field strength of 0.186T, which was achieved by multiple 0.5T permeant magnets and arranging them in a cylindrical array called a Halbach cylinder. The Halbach system receiver coil was tuned to receive signal in the correct B$_0$ frequency range, using a network analyser to alter the capacitance of the circuits variable capacitors and tuning to the correct frequency which ranged between 7.89 and 7.91 MHz, corresponding to a magnetic field strength of 0.1853T to 0.1857T.

4.2.9 Frequency sweeping and coil tuning

Prior to using the Halbach arrack, the frequency coil used to transmit and receive radio frequency signals required tuning to optimize sensitivity and receive maximum signal. A coil connected to two variable capacitors was tuned using a network analyser (Agilent

8712ET RF network analyser, USA) to ensure the capacitance was adjusted to the optimal frequency i.e. the frequency measured using a frequency sweep in the Halbach array. A frequency sweep was performed with the Halbach array and a kea^2 spectrophotometer between 7.85 and 7.95 MHz in equally spaced increments to determine the resonant frequency.

4.2.10 T_1 inversion recovery using inhomogeneous low field

An inversion recovery sequence was used to determine the T_1 relaxation time of the biofilms with the inversion recovery time values measured at increasing inversion recovery times. This was performed using the Halbach array and Kea^2 spectrophotometer Each sample was then plotted using the T_1 plot function built into Prospa to determine the measured T_1 value. After Prospa determined the value of T_1, the raw data was passed through MRI data processor software written in MATLAB to confirm the results from Prospa by performing the same non-negative least squares (NNLS) regression analysis, as well as perform exponential fitting with a 95% confidence to evaluate the T_1 measured from the raw data. Non-negative least square analysis was performed as each measurement should show an increase to the net magnetic moment and therefor has no negative component. Least squares regression allows an analytical approach to determining the best fit for a set of data points. The settings used to estimate T_1 in the inhomogeneous Halbach array can be seen in table 4.8.

Settings	Value
B1 Frequency	7.92 MHz
Repetition time	18000 ms
T_I	25, 50, 60, 75, 90, 100, 125, 150, 200, 300, 400, 800, 1000, 1500, 2000, 3000, 6000, 10000 ms
Amplitude	-12 dB
Amplitude	-6 dB
Pulse length	12 µs
Echo time	150 µs
Number of echoes	2
Echo shift	0 µs

Table 4.8 *Sequence settings for the T_1 inversion recovery sequence. T_1 was estimated by measuring the signal after increasing the inversion recovery time. The inversion recovery time was altered between 25 and 10000ms to measure up to three times the suspected relaxation time of pure water, which would have a longer relaxation time than biofilm forming in Mueller Hinton Broth.*

4.2.11 T_2^{eff} CPMG sequencing

A Carr-Purcell-Meiboom-Gill sequence (CPMG) sequence was used to measure the T_2^{eff} value in all the bacterial samples. The sequence was used to refocus the echoes in the lowfield Halbach system, whilst also accounting for any inhomogeneity within the magnetic field by refocusing the magnetization with a 180° pulse.

Settings	Value
B1 Frequency	7.92 MHz
Repetition time	12000 ms
Amplitude	-12 Db
Amplitude	-6 dB
Pulse length	8 μs
Echo time	150 μs
Number of echoes	2048 μs
Echo shift	0.8 μs
Dummy echo's	0

Table 4.9 *CPMG sequence settings to predict the measurement of planktonic cells and biofilms. The settings used in the CPMG sequence to measure the T_2^{eff} value of planktonic cells and biofilm in a 0.5T Halbach NMR system.*

4.3 Results

Results were gathered from both a low-field inhomogeneous Halbach array produced at Nottingham Trent University and a 1.5T Siemens Avanto scanner. This section looks at the measurements of T_1 inversion recovery and T_2^{eff} to determine optimal relaxation and echo times to Image biofilms within an intubated porcine pluck.

4.3.1 Spin-lattice relaxation of biofilms bulk using NMR

T_1 relaxation was measured and recorded for each strain, oil, media, sodium alginate, and water, showing the raw T_1 value, and the T_1 value accounting for noise, which can be seen in table 4.1. The values recorded for *Pseudomonas aeruginosa*, fitting the data as an exponential, is 2802 ms. Performing NNLS regression is measured to be 2688 ms. Between the values of predicted T_1 using an exponential fit compared to a non-negative least squares regression fit, two trends occur, Gram negatives have their a longer T_1 relaxation time, while Gram positives have a shorter T_1 relaxation time. The difference between the two trends can be seen below (Table 4.1), which shows a difference in the

bulk measurement when analysing the received signal using the two different fitting techniques.

	Exponential fitting		NNLS regression fitting	
Sample	T_1 (ms)	SEM (ms)	T_1 (ms) NNLS	SEM (ms) NNLS
Water	2170	30	1630	23
Mueller Hinton broth	1940	38	2050	43
Sodium alginate	2100	72	1650	72
Escherichia coli	2850	37	2700	27
Staphylococcus aureus	2220	4	1830	34
Pseudomonas aeruginosa	2800	11	2690	42
Klebsiella pneumoniae	2860	46	2580	75
Staphylococcus epidermidis	2280	39	1660	29
Acinetobacter pittii	2650	49	2120	48
Acinetobacter baumannii	2700	80	1820	36

Table 4.10 *The values of T_1 measured for 10 different samples, 7 bacterial samples including Escherichia coli, Staphylococcus aureus, Pseudomonas aeruginosa, Klebsiella pneumoniae, Staphylococcus epidermidis, Acinetobacter pittii and Acinetobacter baumannii. Other samples include sodium alginate, a polysaccharide matrix, Mueller Hinton broth (MHB) a rich lab medium for growing bacteria and water.. The measured samples of Water, media, sodium alginate and seven different species of bacteria that produce biofilm. Exponential fitting was compared to NNLS regression to determine the optimal fitting technique for data. Each sample was measured in triplicate and plotted against the fitting to determine the error in the average of the measurements.*

4.3.2 Spin-spin relaxation of biofilm bulk media using NMR

Measurement of the T_2^{eff} can also be made using NMR, using a CPMG sequence with the settings described in 2.9.2. The measurements of T_2^{eff} vary between 50 to 60 ms, as seen below (Table 5.2), for each of the species and this is considerably shorter than expected. This is due to the inhomogeneity of the magnetic field induced by the 0.5T neodymium magnets, causing the measured T_2^{eff} effective to be substantially shorter.

Sample	T_2^{eff} (ms)	SEM (ms)	T_2^{eff} (ms) NNLS	SEM (ms)
Water	79	1.4	74	0.8
Media	65	2.5	63	3.6
Sodium Alginate	74	7.2	58	0.9
Escherichia coli	58	0.4	62	0.3
Staphylococcus aureus	59	2.8	62	2.5
Pseudomonas aeruginosa	53	0.2	67	0.7
Klebsiella pneumoniae	50	1.2	39	5.4
Staphylococcus epidermidis	55	1.5	54	4.1
Acinetobacter pittii	59	1.8	59	0.6
Acinetobacter baumannii	67	0.9	73	3.0

Table 4.11 *The T_2^{eff} effective measurements using a Halbach magnet array to create a 0.187 T system. T_2^{eff} effective measurements using the halfback array. These values are lower than would be found in a MRI or other expensive homogenous field, however*

4.3.3 Blind trial to determine whether a trend in T_1 value of biofilm bulk can determine Gram positive v Gram negative species.

As the observed properties of T_1 appear to correlate to the Gram classification of the species tested, a blind trial was conducted. Ten unknown bacterial species were provided with the initial aim of measuring the T_1 value of each species to assign them a Gram positive and a Gram negative classification based upon the trend seen prior. As the T_1 changed after the second day and fluctuated rather than keeping constant like 5.2.2. However, all the T_1 values are between 2700 ms and 3000 ms which is significantly longer than most human tissues as seen below (Figure 5.1).
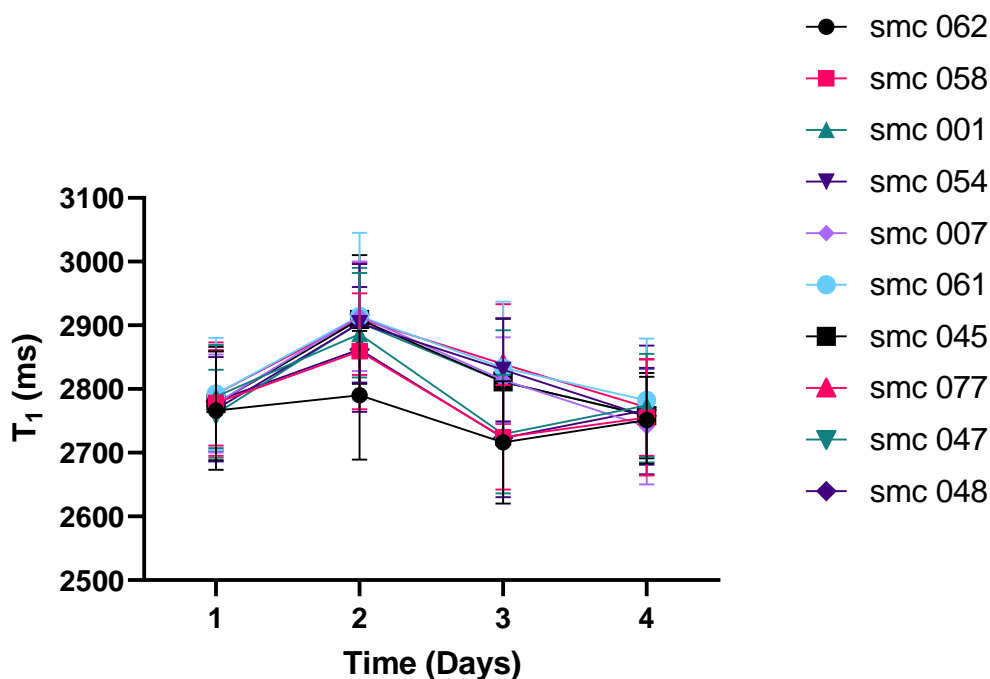
Figure 4.1 *A blind trial of 10 random strains provided to determine whether there was a correlation between T_1 and the gram classification of the species. T_1 measurements made over four days on 10 random strains provided. Based on the results seen in Figure determination of the species characteristics is not possible from the bulk measurements. The strains used in order of legend are E. coli smc 062, K. pneumoniae smc 058, E. coli smc 001, MR S. aureus smc 054 , S. aureus smc 007, E. cloacae smc 061, S. aureus smc 045, S. marcescens smc 077, S. aureus smc 047, S. aureus smc 048. These measurements were taken with the Halbach array, showing the fluctuation in T_1 relaxation time in the species with no discernible way to determine the classification of each species using T_1 relaxation.*

4.3.4 Spin-lattice relaxation of biofilm bulk using Magnetic Resonance Imaging

T_1 measurements were made using a 1.5T clinical scanner on a *Pseudomonas Aeruginosa* strain over the course of a week to determine whether there was any change in T_1 measurement vs biofilm formation. Below (Figure 5.6), the T_1 values of *Pseudomonas aeruginosa* change significantly after two days of growth, starting with a similar value as sterile Mueller Hinton broth and increasing to a value around 2800ms after two days and remaining at this value for the remainder of the measurements taken. The change in T_1 value was also measured alongside the optical density of the biofilm, providing

change in T_1 against time and a change in biomass against time, which can be seen below (Figure 4.2-Figure 4.3).
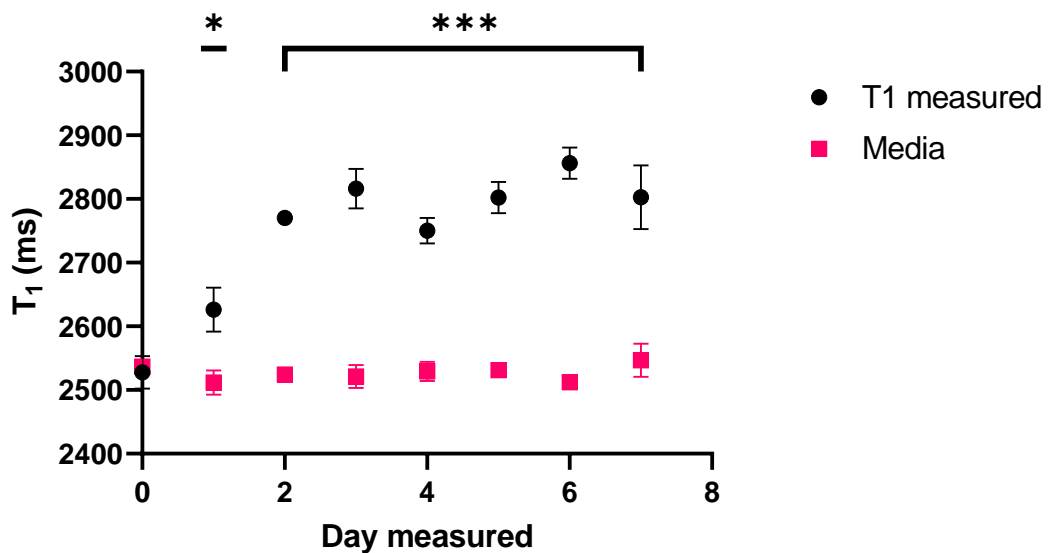
Figure 4.2 *The T_1 value of Pseudomonas aeurginosa measured over seven days compared to Mueller Hinton broth. The measured T_1 value as biofilm forms on a glass slide within a 50mL falcon (Fisher Scientific, uk) tube and compared to MHB. Samples were performed in triplicate and the SEM is the error bars, where * P >0.05, *** P > 0.005 using a multiple t-tests*

The optical density of the biofilm was measured by crystal violet staining glass slides in a fresh falcon tube and washing with ethanol to remove the biofilm from glass slide, staining the ethanol with the crystal violet in the process. The ethanol was then pipetted into a 96 well plate and the turbidity at 550 nm was measured using a BioTek Cytation 3 plate reader, (Agilent, USA), to measure the amount of crystal violet stained biofilm. The results were compared with the T_1 value to determine if there was a corelation between the biofilm biomass formed and the T_1 value of the bulk sample of the strain seen below (Figure 5.3).
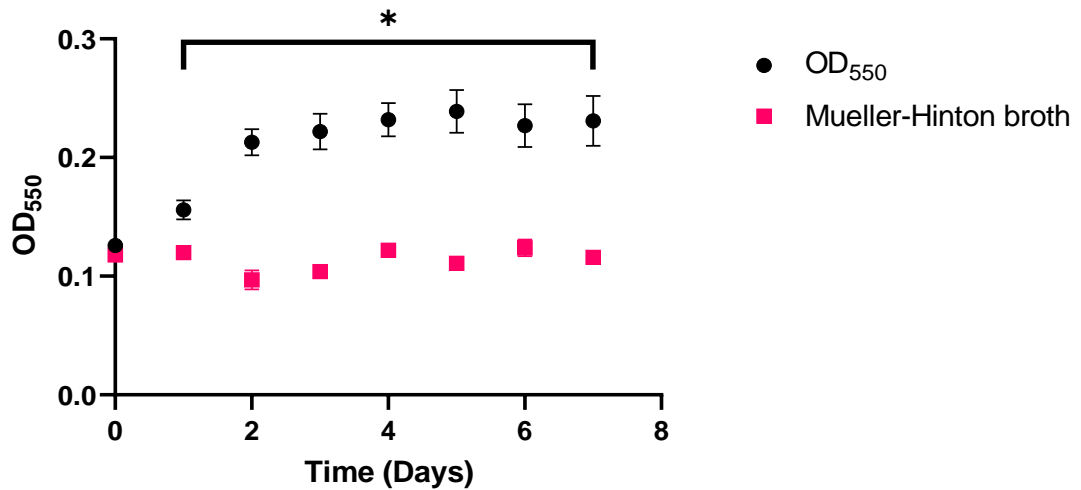
Figure 4.3 *The optical density measured of crystal violet-stained biofilm over seven days. The optical density was measured by staining the biofilm that had formed on glass slides. Glass slides in sterile media were also stained as a control. N = 3 * P > 0.05 using multiple t tests*

To measure the T_1, T_2^{eff}, spin echo diffusion and obtain diffusion weighted imaging to measure different properties of the bulk biofilm, a sample holder was cut out of acrylic, and adhered using Extrufix. Samples were loaded into 15mL falcon tubes and placed in the holder and imaged using various techniques to measure the properties of the bulk biofilm. Below (Figure 4.4), the different samples can be seen using an offset of one sample to ensure the orientation between measurements was kept.
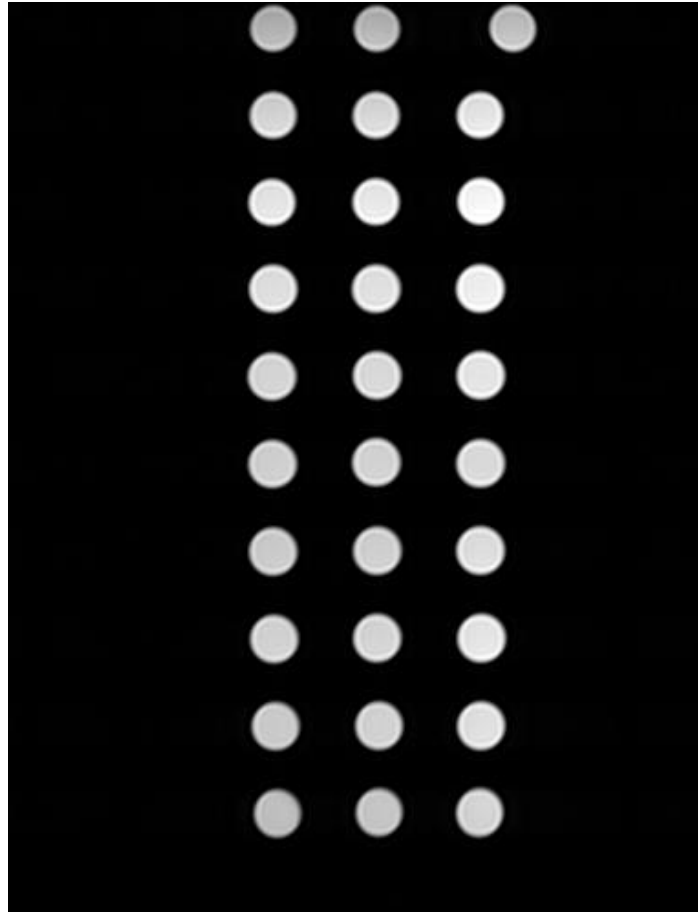
Figure 4.4 *every sample imaged, with water, sodium alginate, Mueller Hinton broth and the seven bacterial species in collection order after the third day of bacterial growth. Each sample had its T_1, T_2^{eff}, self-diffusion coefficient and apparent diffusion coefficient measured. The offset sample is water, and samples in the same row were the same allowing for measurements to be made in triplicate. Samples were placed in descending order, starting with water, sodium alginate, Mueller Hinton broth, Escherichia coli, Staphylococcus aureus, Pseudomonas aeruginosa, Klebsiella pneumoniae, Staphylococcus epidermidis, Acinetobacter pittii and Acinetobacter baumannii on the bottom row.*

All species were examined using the same sequences using the siemens 1.5T scanner over a week as seen below (Figure 4.5). The results show that there is a change in the bulk measurements of the media, leading to longer T_1 measurements. This could imply that the salts and other minerals found within the media and water used are being taken out of the bulk water by the bacterial cells, essentially purifying the media and turning it to water.
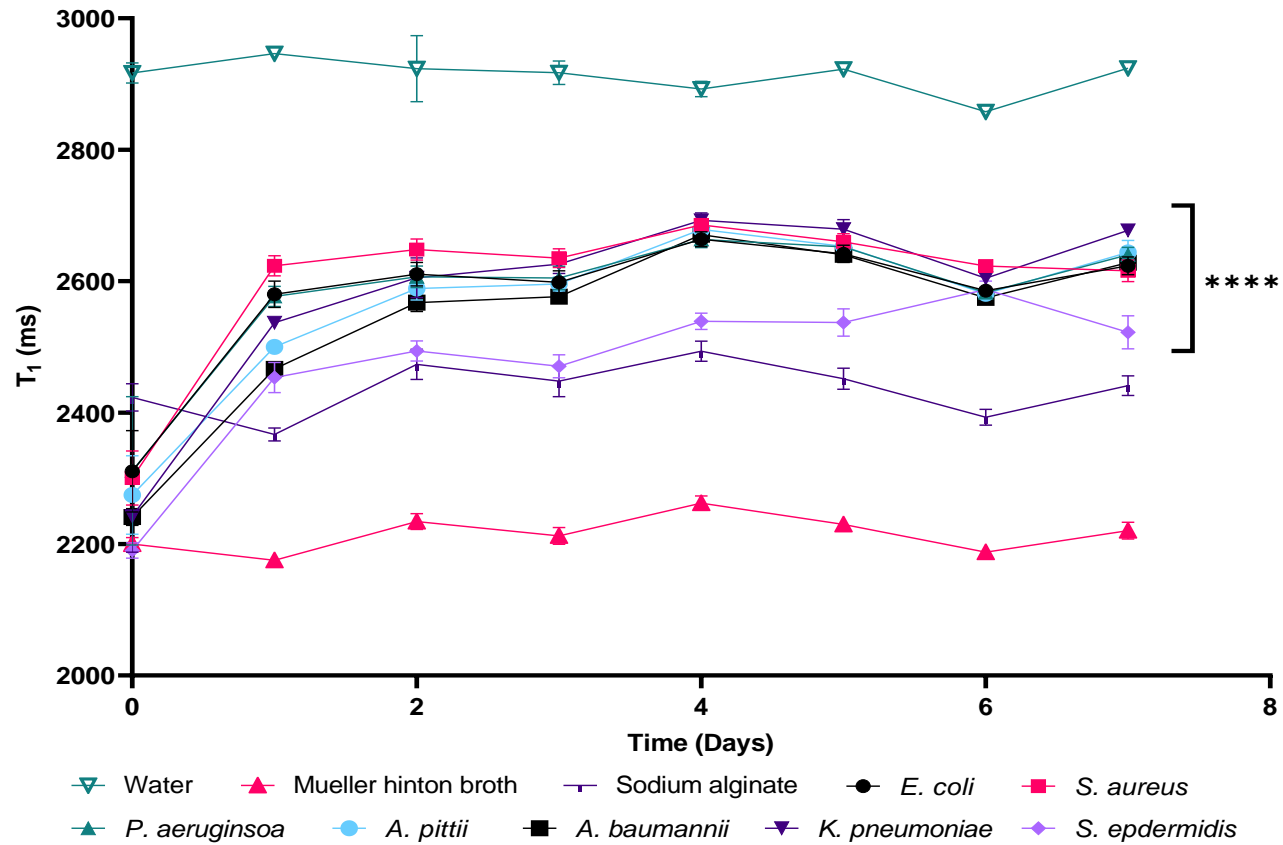
Figure 4.5 *one week of T₁ measurements across all species and Mueller Hinton broth. Gram positive and negative species with spin-relaxation measurements taken over the course of a week. A general trend of the measurements indicates Gram negative species have a longer relaxation time than that of gram negatives. Water and Sodium alginate are also included to show perspective on similar organic compounds. N = 3 ****P > 0.0001 for all bacterial species compared to sodium alginate using a one way ANOVA test. Lines are added to aid in distinguishing the species.*

4.3.5 Spin-spin relaxation of biofilm bulk using MRI

Measuring the T_2^{eff} effective using the 1.5T siemens Avanto scanner was performed using a gradient echo sampling (GRE) sequence with settings described in 2.8.5. The echo time was performed using 32 measurements ranging from 50ms to 1600ms changing in increments of 50ms. Some of the bulk media containing bacterial species had shorter relaxation times that were observable after two days, as seen below (Figure 4.6).
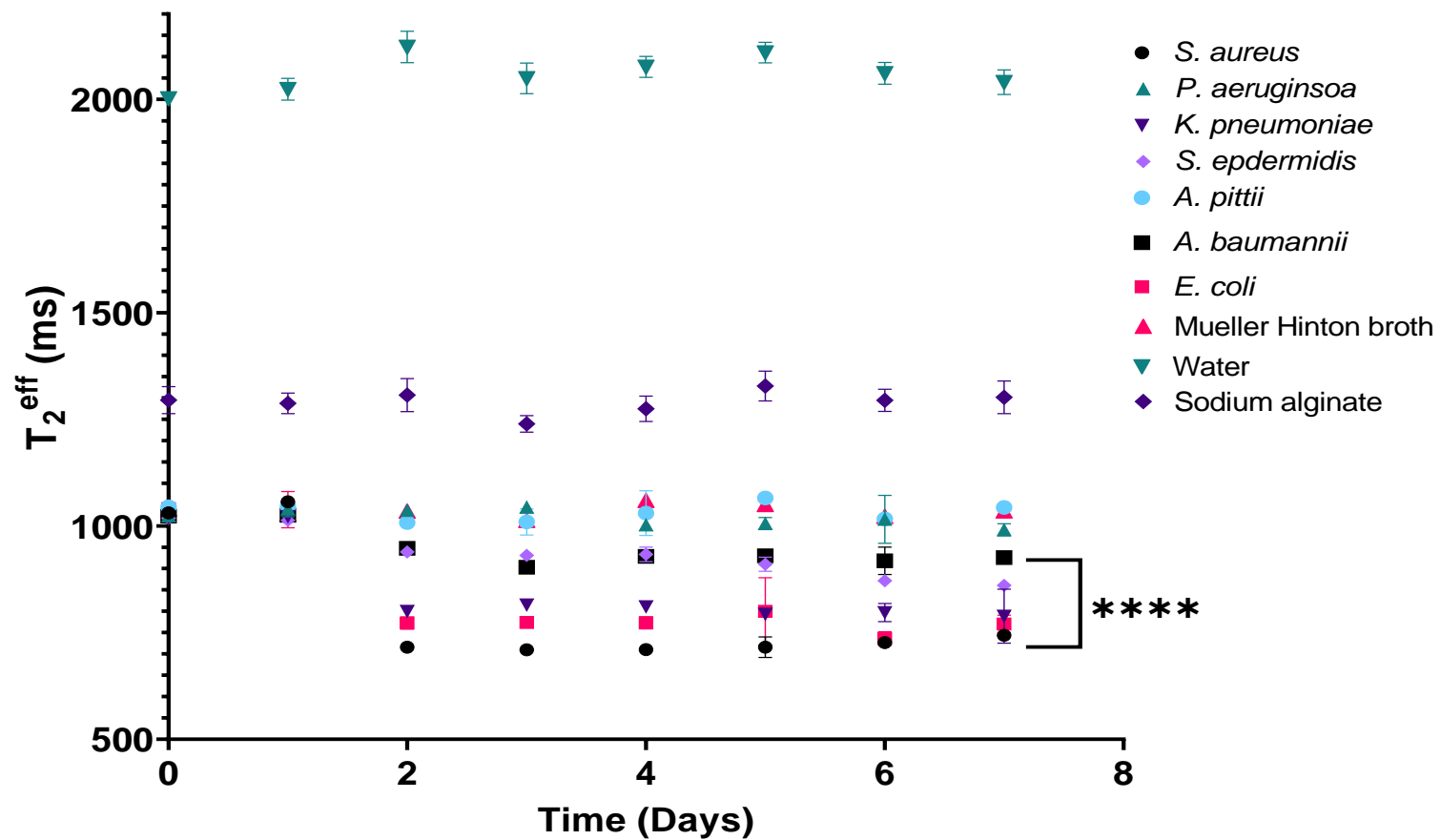
Figure 4.6 T_2^{eff} *effective relaxation of the bulk measured using a 1.5T Siemens Avanto scanner. The T_2^{eff} measurements made over the course of seven days of growth as well as the day of inoculation. Each species was measured and the change in T_2^{eff} was seen between day one and day two, where the Each species was performed in replicate and were imaged at 18°C.*

4.3.6 Spin echo diffusion of bulk media

Spin echo diffusion is measurable using a spin echo sequence at an appropriate relaxation time (T_R) and varying the echo time (T_e). The change in signal between two images and the two echo times can be plotted against each other to calculate the self-diffusion coefficient of the material using the Stejskal-Tanner equation. In total, 12 measurements were taken to improve accuracy and provide error in diffusion caused by slight inhomogeneity in the MRI scanner. Below (Figure 4.7) the diffusion coefficient of a sample is measured over the course of a week including the inoculation day for each of the bacterial species (Figure 4.8). Figure 4.7 shows the constant diffusion of water, sodium alginate made to a 1% w/w concentration and Mueller Hinton broth. These samples retained a constant diffusion coefficient during the seven days of growth in the bacterial species with water having a value tending at $1.991 \times 10^{-9} \pm 9.595 \times 10^{-11}\ m^2 s^{-1}$ which is within tolerance of the literature value for water at $1.916 \times 10^{-9}\ m^2 s^{-1}$ at 18°C. Sodium alginate was also measured to examine a static natural polysaccharide matrix and the diffusion coefficient was measured to be $8.053 \times 10^{-10} \pm 2.955 \times 10^{-11}\ m^2 s^{-1}$. Mueller Hinton broth was measured to see how diffusion in the media compared to that of water, with the diffusion being measured as $6.638 \times 10^{-10} \pm 2.455 \times 10^{-11}\ m^2 s^{-1}$ which is significantly slower than water and is attributed to the sugars, beef infusion solids and starch added to water. The level of precision for these measurements is usually given as $cm^2\ s^{-1}$, however, literature measurements are given as $m^2 s^{-1}$ with the only variables in the Stesjkal-Tanner equation being T_e given as milliseconds, signal measured in arbitrary units and the field gradient with homogeneity of 1 part per million.
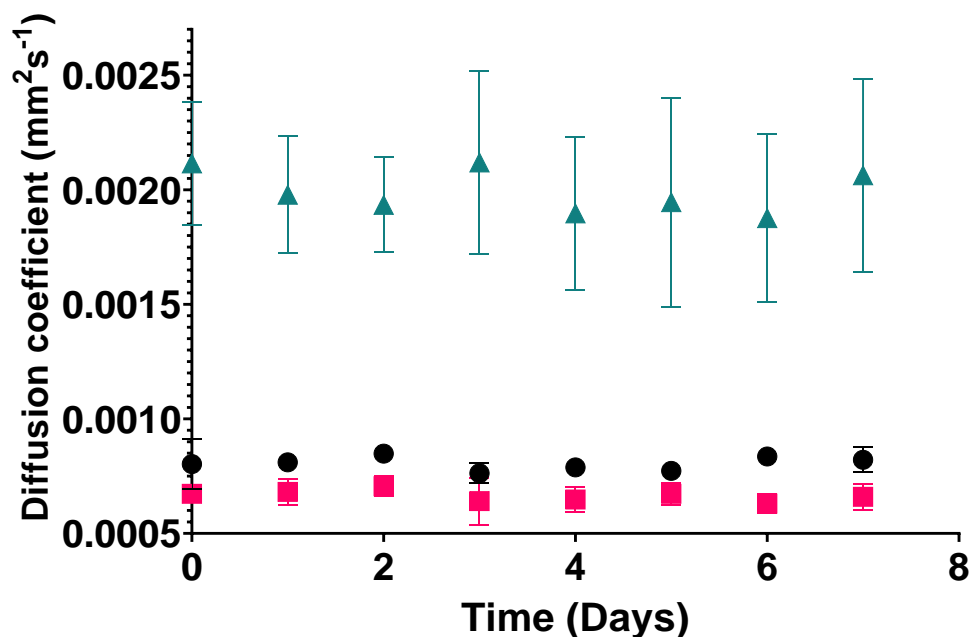
Figure 4.7 *Diffusion measured using a spin echo sequence and using the Stejskal-Tanner equation to calculate the diffusion coefficient of each sample. Samples were measured including water, Mueller Hinton broth and sodium alginate to compare to bacterial cultures in Mueller Hinton broth. Samples were measured at 18°C but were kept with the bacterial cultures overnight in an incubator at 37°C between measurements. Each sample was measured in triplicate and at the same time using a 1.5T siemens Avanto scanner.*

The change in diffusion coefficients of the bacterial species grown for a week following inoculation are seen in figure 4.8. The initial diffusion coefficients after inoculation start at values close to that of pure Mueller Hinton broth and progressively decrease due to the cell growth over the course of two days. This suggests that the increase in cell content causes diffusion through the sample to decrease while the nutrients of the media are also decreased. Afterwards, the diffusion increases which is caused by bacterial cell death and lysis, as a consequence of a lack of new nutrients in the broth.
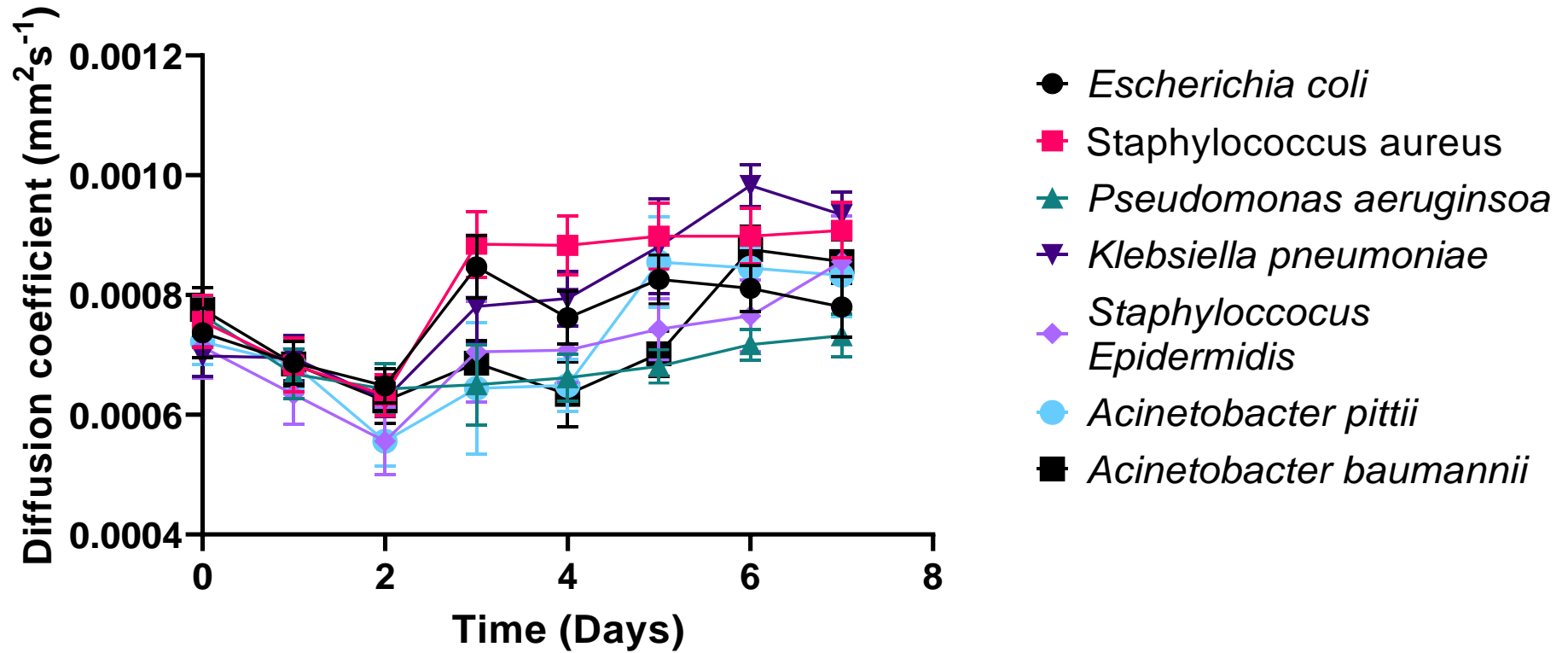
Figure 4.8 *The diffusion coefficient measured over one week, of different bacterial species in Mueller Hinton Broth. Seven bacterial species were measured over a week to determine the change in the diffusion coefficient of each species. Initially, the diffusion of bulk decreases until the second day of measurements, which is likely due to the increased cell count, however, the diffusion then increases due to dead cells and remaining cells being bound to the limited biofilm, causing bulk to be mostly water. Lines are left to aid in following the change in diffusion over time*

4.3.7 Diffusion Weighted Imaging of bulk media

These samples were measured using the acrylic stand produced previously. The three constant samples of sodium alginate, water, and Mueller Hinton broth are seen in Figure 4.9. The diffusion of the bacterial species can be seen with diffusion starting at a similar value as media and gradually increasing over to a value like sodium alginate as seen in Figure 4.10.
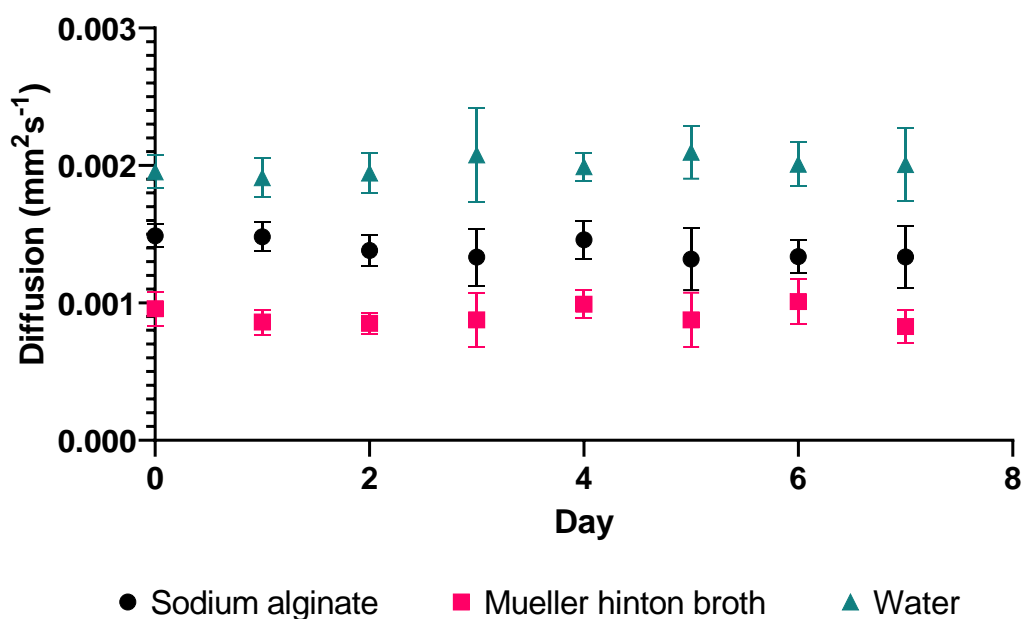
Figure 4.9 *The measured apparent diffusion coefficient of water, sodium alginate and Mueller Hinton broth measured over the course of one week including the date of inoculation. Using a diffusion weighted imaging sequence, the diffusion of the samples was measured to compare the values measured by the spin echo sequence. The samples remain constant throughout the seven days including the day of inoculation. Samples were measured in triplicate.*
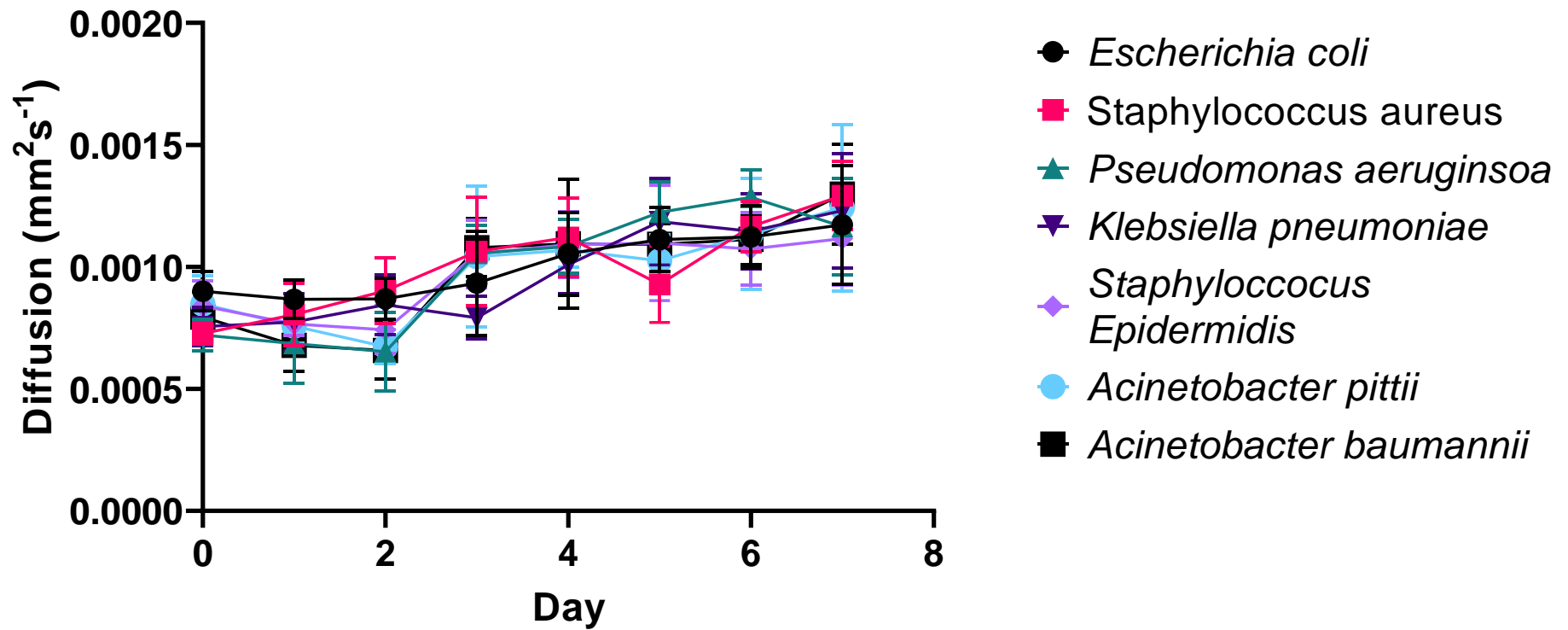
Figure 4.10 *The apparent diffusion coefficient measured using diffusion weighted sequencing. The apparent diffusion coefficient measured using a diffusion weighted sequence ranging from a b value of 0 to a b value of 1000 s mm^{-2}. Lines are left into further aid in visualisation of the species*

The self-diffusion coefficient and apparent diffusion coefficient were compared to determine whether there was a significant difference between the diffusion of water in the substance. This was performed to evaluate the difference between the low field system and MRI as they should be identical, where only water exhibited similar values between the two different diffusion techniques as seen in figure 5.11.
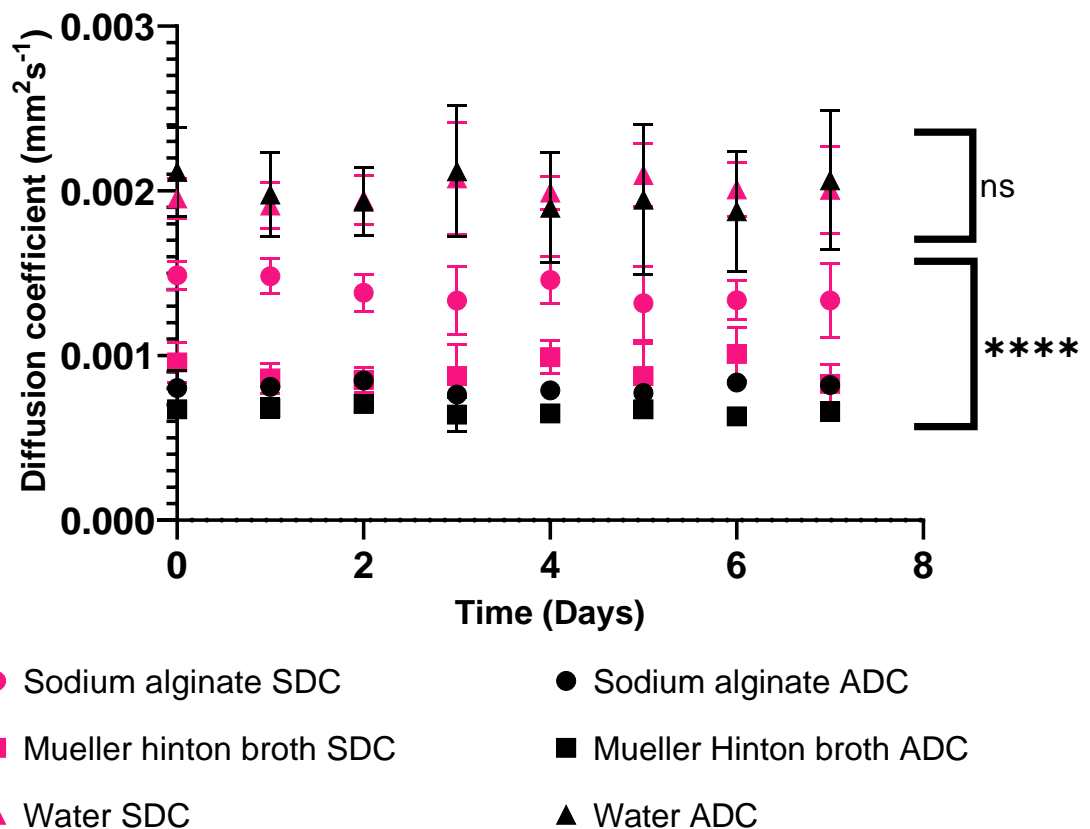
Figure 4.11 *Comparison of the self-diffusion coefficient and the apparent diffusion coefficient of the three unchanging samples. The measured SDC and ADC of the three samples no significance is seen in water whilst the sodium alginate and Mueller Hinton broth have significantly different values compared*

Five species: *Escherichia coli, Pseudomonas aeruginosa, Staphylococcus epidermidis, Acinetobacter pittii* and *Acinetobacter baumannii*, were seen with a significant difference between measured SDC and ADC of the bacterial species can be seen below (Figure 4.12 and Figure 4.13). The SDC of these species increased by a significantly larger amount after the second day of growth of the bacteria than when the ADC was measured. Figure 4.12 shows three species, *Escherichia coli, Pseudomonas aeruginosa* and *Staphylococcus epidermidis* had a greater level of difference between the two

measured coefficients of diffusion. Below (Figure 4.14), *Staphylococcus aureus* and *Klebsiella pneumonias* show no significant difference between the two different diffusion coefficients. The different graphs are presented below to show the varying level of significance between each species measured apparent and self-diffusion coefficients, where significance is seen in five species and not in two species, and to aid in clarifying how diffusion changes over time.
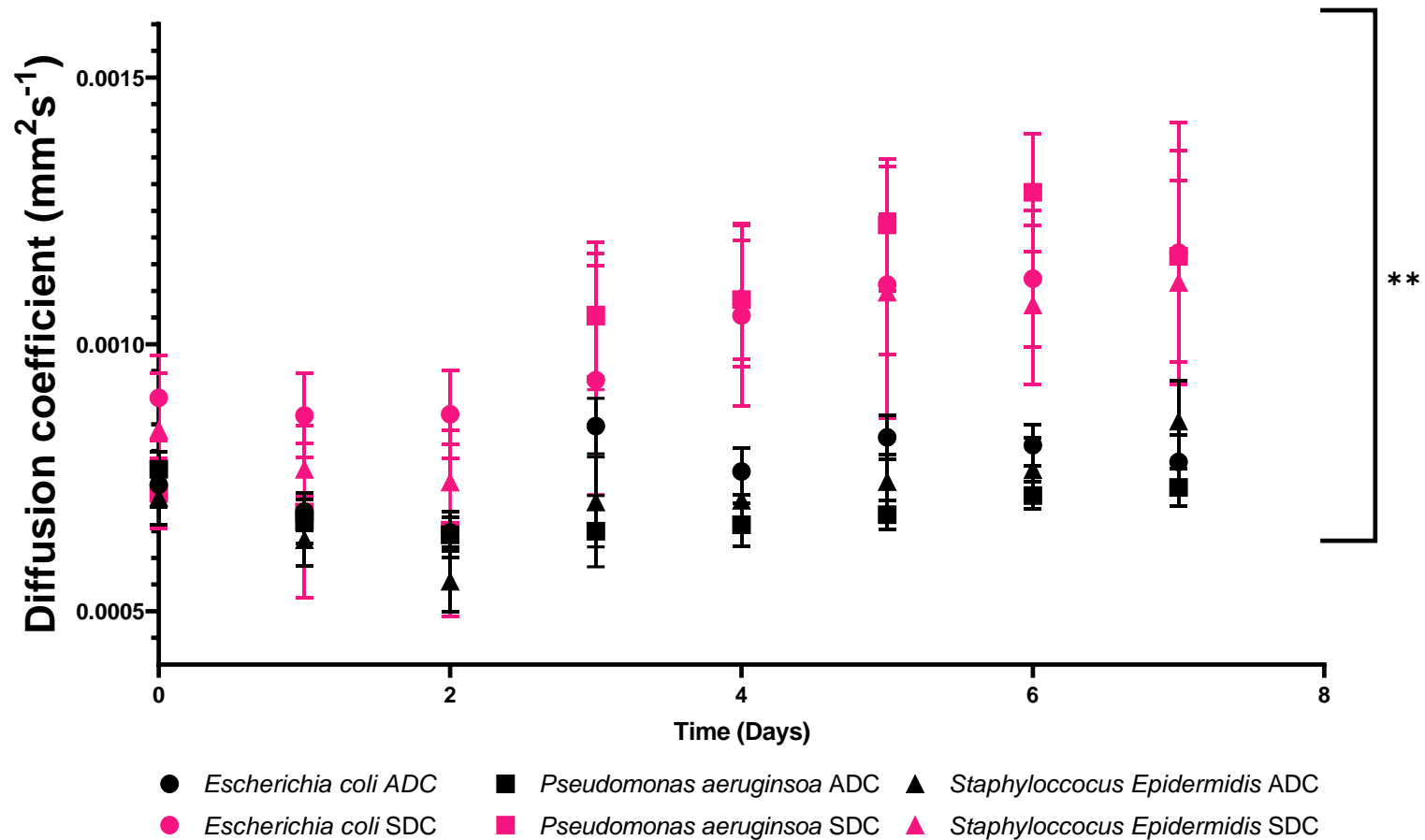
Figure 4.12 *Comparison of three bacterial species with a significant difference between the measured SDC and ADC. Three species with a significant difference between the measured SDC and ADC. ** P > 0 .01 using a one way ANOVA test comparing SDC to ADC for the same species.*
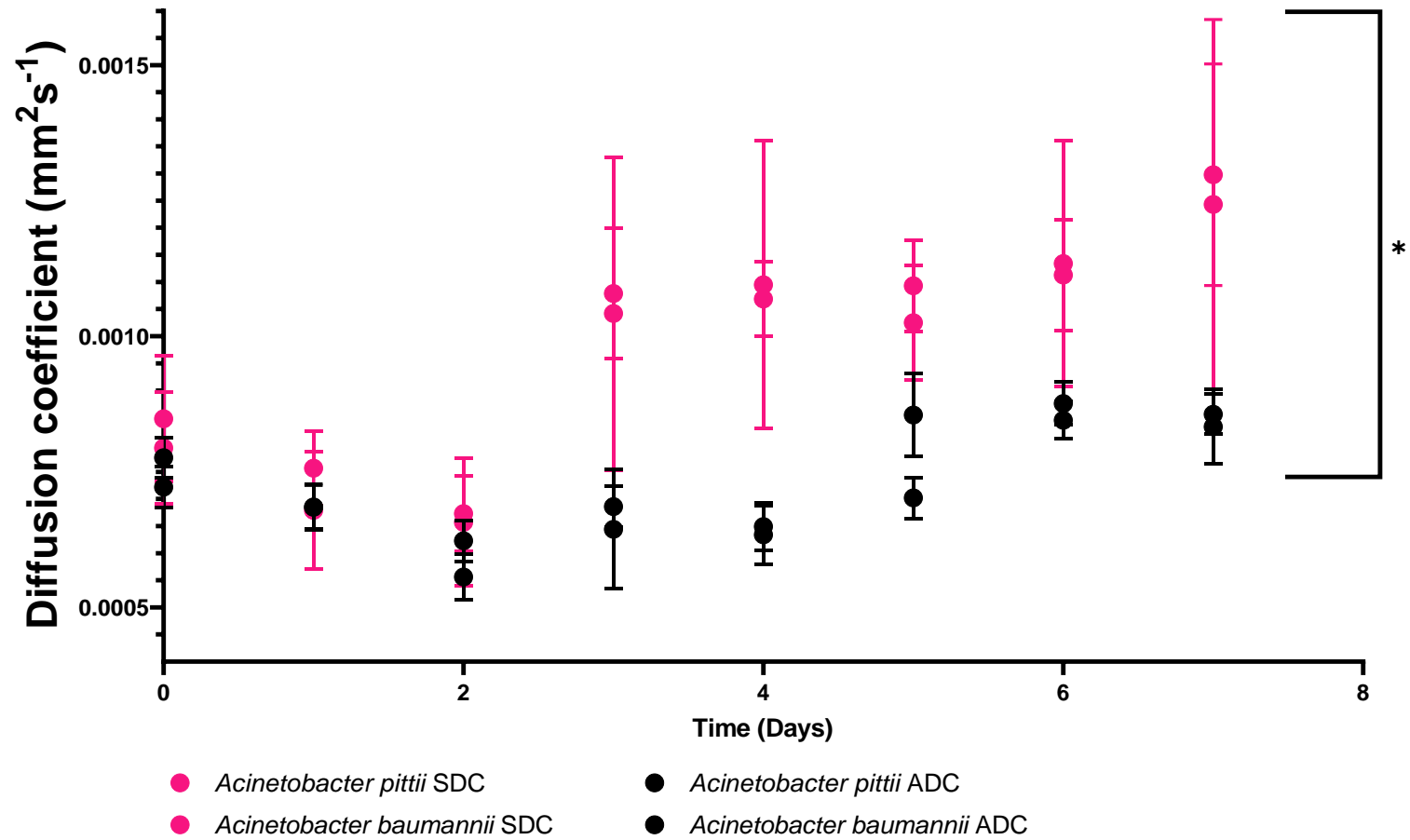
Figure 4.13 *Comparison between the Acinetobacter spp. which have a significant difference between the SDC and ADC. Two different Acinetobacter species that have different measured SDC and ADC using a spin echo sequence and a diffusion tensor imaging sequence.*
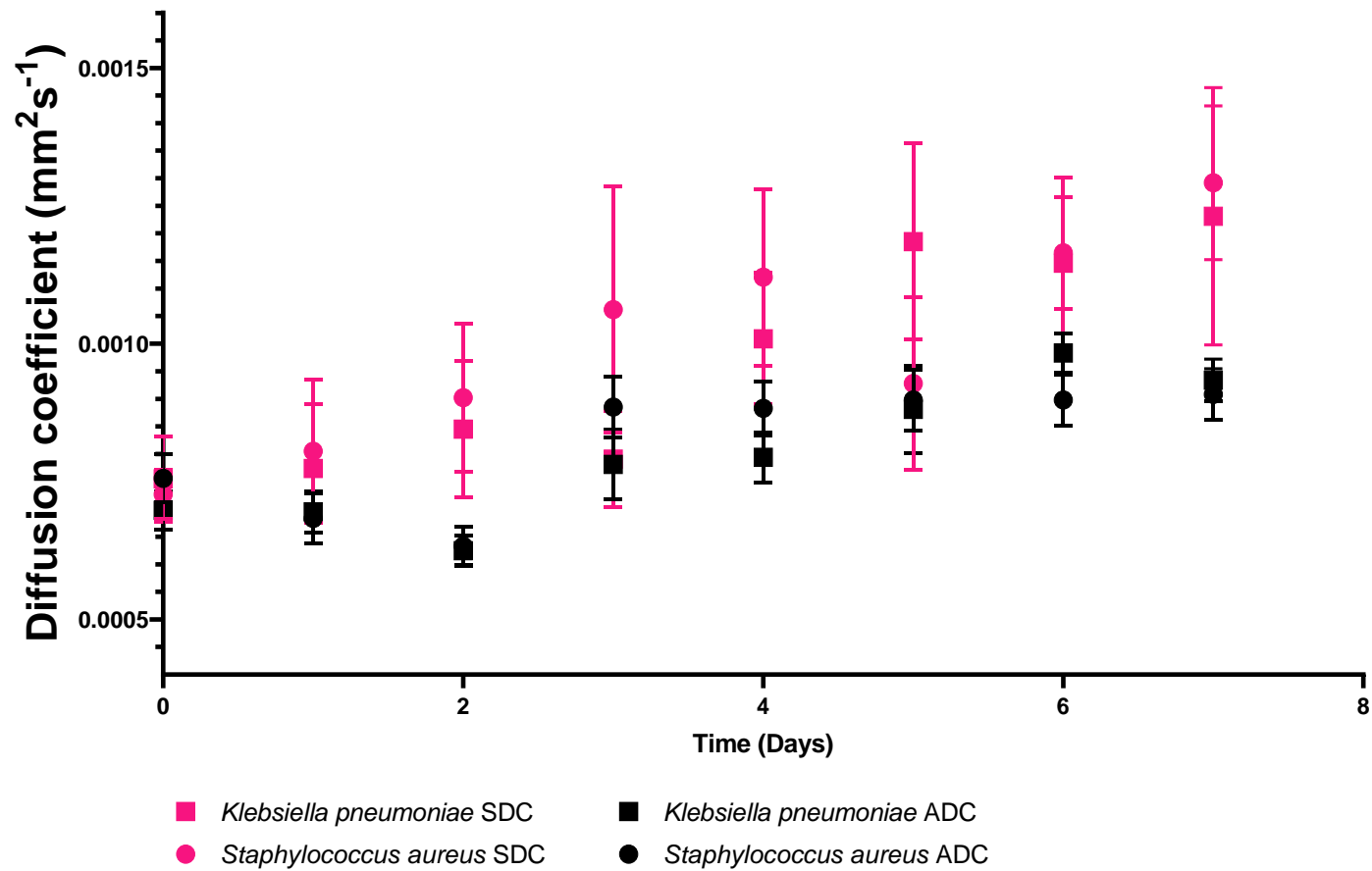
Figure 4.14 *comparison between two species where the difference between measured ADC and SDC was not significant. Klebsiella pneumoniae and Staphylococcus aureus species with measured SDC and ADC where the difference between the two was determined to be not significant.*

4.3.8 T_1 and T_2 effective measurements of porcine respiratory tract

A porcine pluck, the larynx, trachea, lung, heart, and liver, was acquired and scanned to determine the T_1 and T_2^{eff} effective *in vivo* to measure a system like a human respiratory system, whilst causing no actual harm to a living animal or person. Furthermore, imaging the porcine track would determine if the T_1 and T_2^{eff} of the tracheal have different relaxation times to the biofilms, allowing a contrast difference between the two. An example of a porcine pluck is seen in figure 4.15 to show the various organs[435].
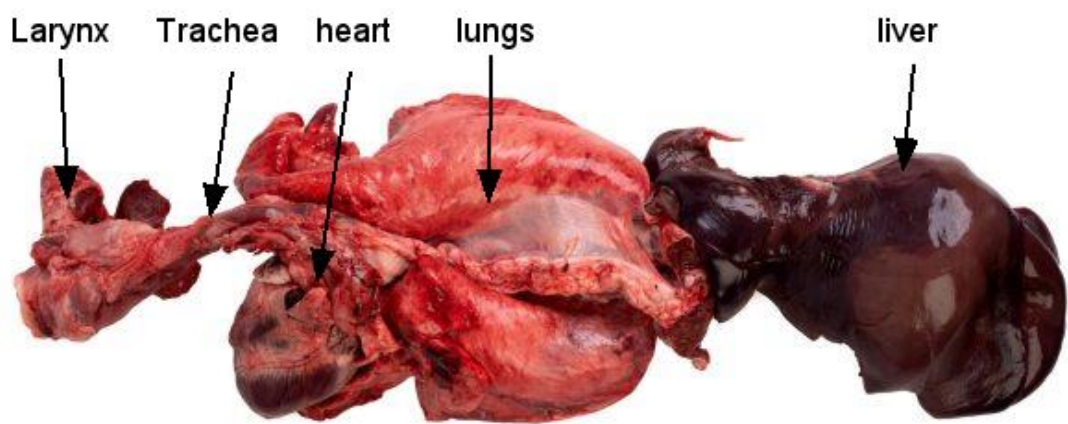
Figure 4.15 A porcine pluck showing the larynx, trachea, heart, lungs, and liver. The relaxation properties were investigated on the tracheal wall, to determine if there were sufficient relaxation differences between the wall and biofilms[435]. Copyright permission achieved from author of image

The measurements were made with sequences described in 4.2.3 and 4.2.4 and were performed on a singular pluck, with measurements made at various locations along the tract, ensuring measurements were only taken along the trachea and not of the bronchi. T_1 inversion recovery was performed, with T_1 values measured from 24ms to 3000 ms and 10 measurements were taken along the tracheal wall. The average value for the T_1 of the tracheal wall was measured, using MATLAB seen in Figure 4.16 and measured to be 594 ± 10 ms.
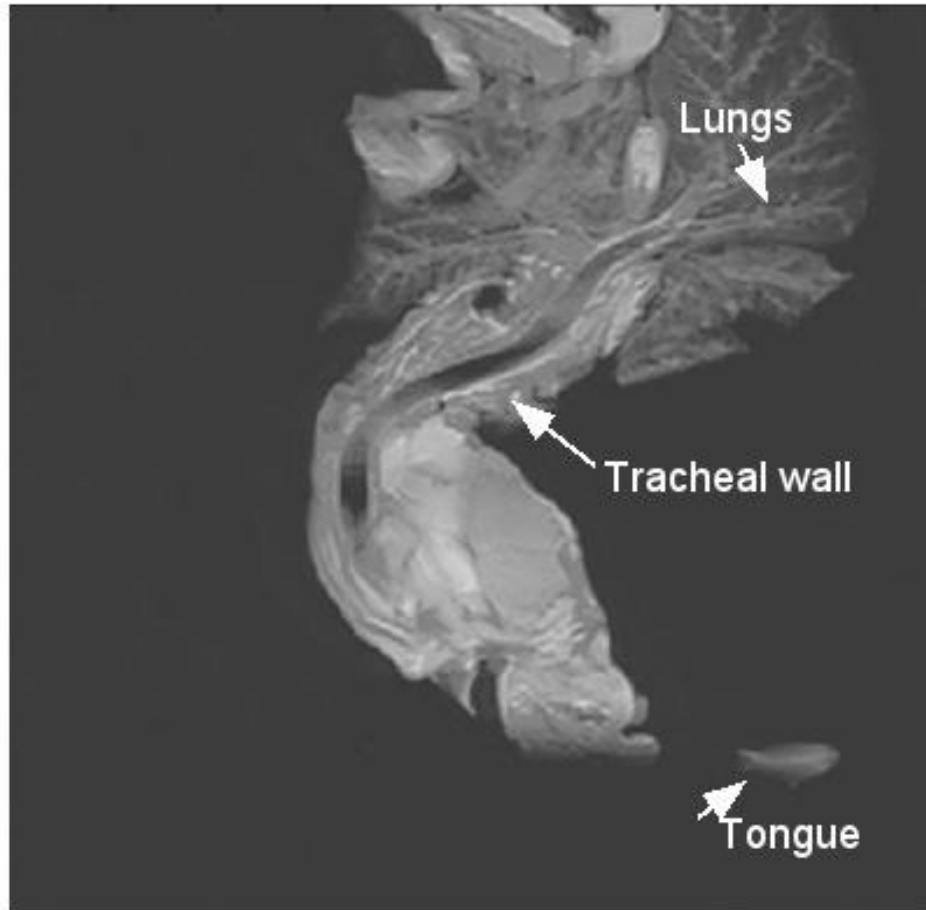
Figure 4.16 *an image in MATLAB used to load map the spin-lattice relaxation (T_1) of the tracheal wall. An inversion recovery sequence image was used to measure the T_1 relaxation values of the tracheal wall. The trachea can be seen along the pathways and into the lungs.*

T_2^{eff} was measured using a gradient echo pulse sequence with echo times varying from 13.8 ms to 220.8 ms, incrementally increasing by 13.8 ms, to ensure the full range of the T_2^{eff} effective decay was measured. The T_2^{eff} effective relaxation was measured along the endotracheal wall at ten locations and the measured result was recorded as 73 ± 3 ms as seen in Figure 4.17.
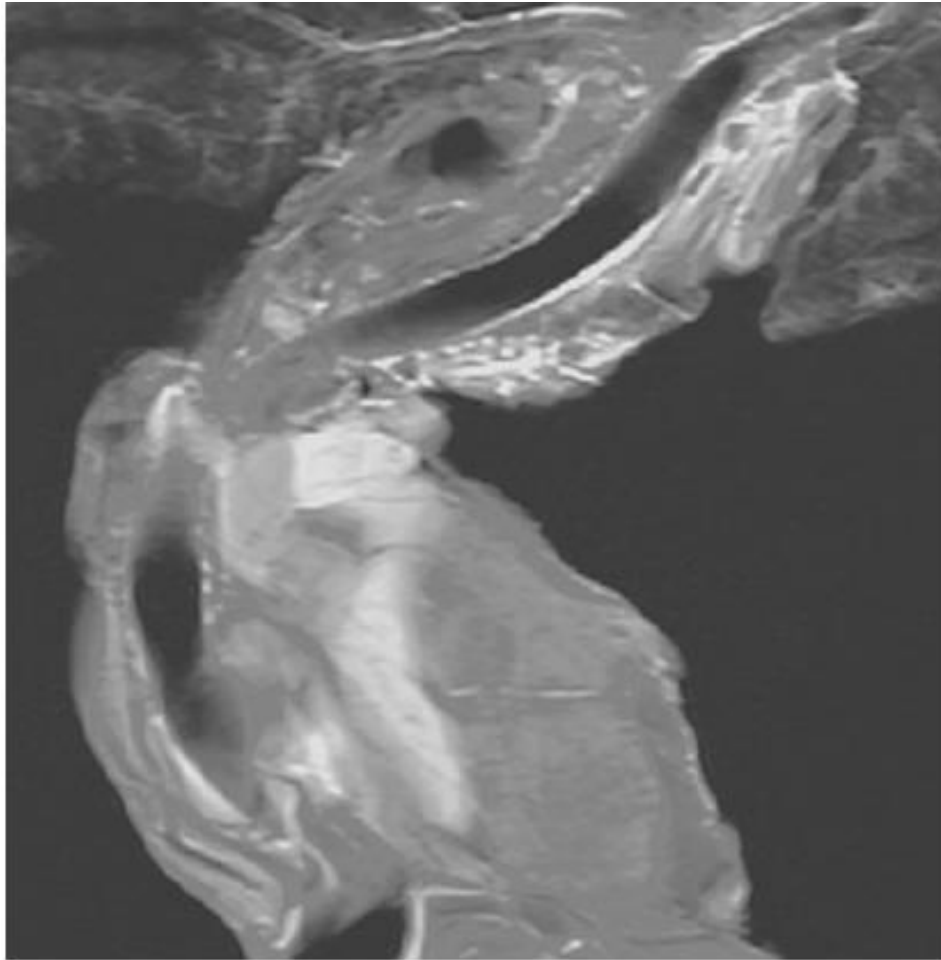
Figure 4.17 *The T_2^{eff} gradient pulse echo sequence location used to determine the T_2^{eff} effective measurements along the tracheal wall. A gradient pulse echo sequence image used to determine the T_2^{eff} of the porcine plucks tracheal wall.*

The T_1 and T_2^{eff} effective relaxation was also measured when the respiratory system of the pluck was filled with water. This would aid in reducing any signal dropout caused by different magnetic susceptibilities at the air-tissue interface . By filling the pluck with water, more nuclei are present for imaging, causing higher contrast, Measurements were made in MATLAB, by plotting a T_1 map, with images acquired from the T_1 inversion recovery sequence used for the pluck without water saturation. An example of this can be seen in Figure 4.18 where the bright signal water can be seen between the tracheal wall along the bottom of the image. Measurements of the T_1 value were taken at ten locations along the endotracheal wall and the measured value of T_1 of the tissue surrounded by water was estimated as 670 ± 30 ms.

Figure 4.18 A T_1 *inversion recovery image of the porcine pluck saturated with water. The tracheal wall can be seen at the bottom of the image where the tubular structure can be seen at the bottom of the Figure.*

The T_2^{eff} effective relaxation was also measured with the pluck saturated with water as seen in Figure 4.19. The trachea can be seen filled with water at the bottom of the Figure where the voxel intensity is higher than the surrounding tissues. The measured value of spin-spin relaxation of the tracheal wall was measured to be 80 ± 10ms. This value is longer than the value measured when the pluck was not filled with water but improves signal acquisition due to more measurable sample.
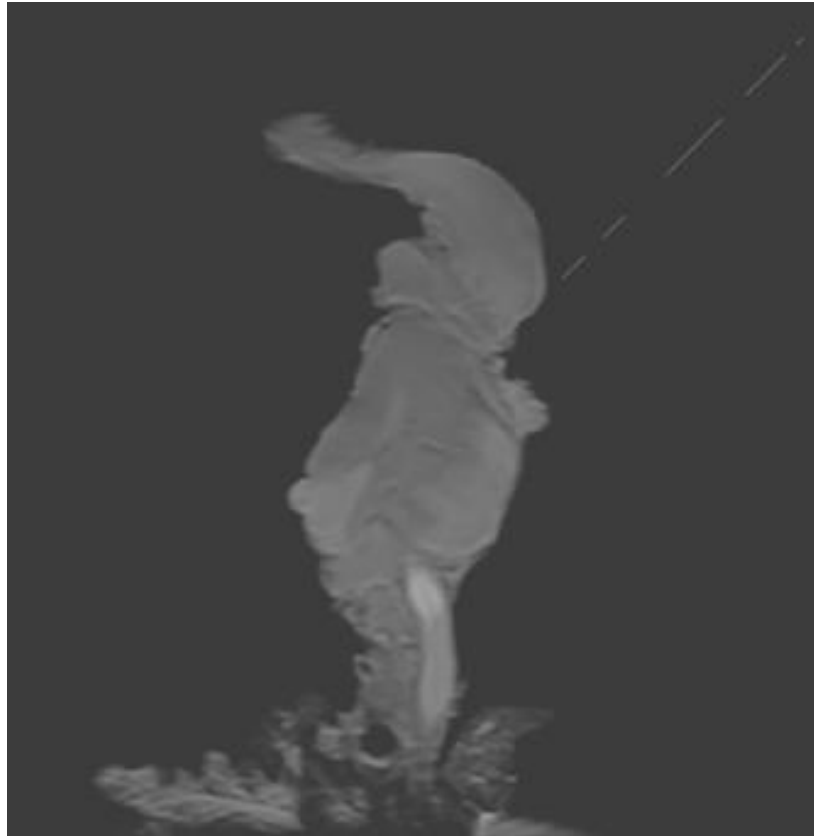
Figure 4.19 *A slice from the CPMG sequence used to measure the T_2^{eff} effective relaxation of the tracheal wall. The porcine pluck filled with water to reduce possible artefacts caused by a lack of signal, where the bright region at the bottom is the water inside the trachea.*

4.3.9 T_1 and T_2 weighted imaging of a biofouled, intubated porcine pluck to determine if non-invasive imaging is possible

In Figure 4.20, we can see a T_1 weighted image of the porcine pluck, showing the lungs at the top of the image, the porcine tongue, and the pharynx at the bottom of the image. Between the lungs and the tongue is the trachea, which can be seen as the dark tube structure running to the lungs.

Figure 4.20 *A T_1 weighted image of the porcine pluck, imaging its respiratory system with particular focus on the porcine trachea. The porcine pluck was imaged using a T_1 weighted image as described in 4.2.3 to acquire this image. The airways are clear without fluid and the trachea can be seen clearly compared to the surrounding tissue.*

The porcine pluck was intubated with silicone tube, fed to the lungs. The silicone tube spent 18 hours in an Erlenmeyer flask filled with artificial saliva media and inoculated with *Acinetobacter baumannii* strain to best emulate the conditions of an intubated patient in intensive care. Figure 4.21 shows the porcine pluck filled with water, the brighter region of the pluck to reduce potential artefacts and improve signal to noise ratio.

Figure 4.21 *The porcine pluck filled with water, showing the trachea from the tongue to the lungs. A T_1 weighted image of the porcine pluck after it was filled with water. The brighter region is the trachea filled with water and can be seen most of the way down to the lungs at the bottom of the image*

For the intubated tube a higher resolution was used for the image, taking the scan time to 32 minutes. This was done to try and acquire the highest resolution possible, to determine if the biofilm was differentiable from the surrounding tissue. Due to the increase in resolution, each voxel size was reduced by a factor of 16, resulting in less signal per voxel, causing a lower signal to noise ratio and a grainer image. To achieve a SNR of 1, the scan would still require 2 hours and 40 minutes to complete which is not an appropriate scanning length. While a higher SNR leads to a higher quality image, it is often not achievable in a clinically relevant length of time, and so long as enough contrast is visible, lower SNR's are accepted.
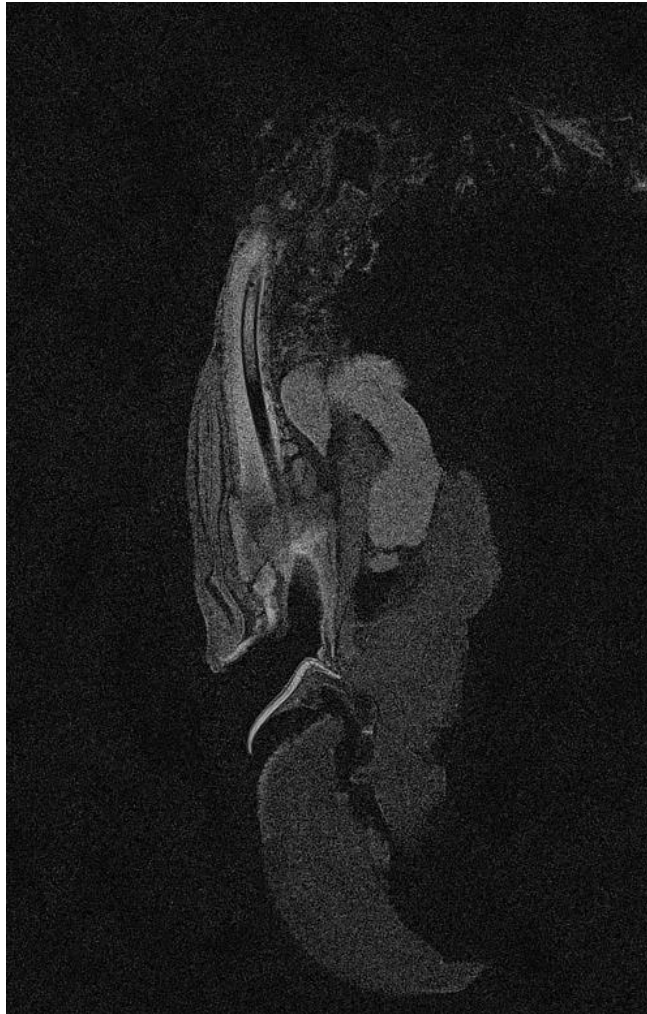
Figure 4.22 *A high-resolution image of an intubated tube in the porcine pluck. A high-resolution image of the porcine pluck that has been intubated along the respiratory tract. The silicone tube used to intubate the pluck can be seen along the trachea on the left of the image as a secondary structure within the trachea. The resolution of this image was increased causing a grainy appearance due to lower signal to noise ratio. The increased resolution also caused the scan to take four times as long, leading to a scan time of 32 minutes.*

Lowering the resolution with the same sequence led to an 8 minute scan time and an increased SNR which can be seen in Figure 4.23. The lower resolution still clearly shows the intubated tube within the pluck.

Figure 4.23 *A lower resolution image showing the silicone tube within (Highlighted in red oval) the trachea. A T_1 weighted image of the intubated porcine pluck with base resolution of 256 voxels showing that the contrast between the water and the silicone tube*

The endotracheal tube is clearly visible with an internal fluid and an external fluid; however, the image makes decerning the biofilm nearly impossible without measuring the signal intensity. Figure 4.24 shows the change in signal intensity across the length of the tube, where the endotracheal tube can be seen as having a lower intensity taken from Figure 5.23. However, the signal intensity does not show a significant change between the fluid on the inside of the endotracheal tube and the outside fluid.
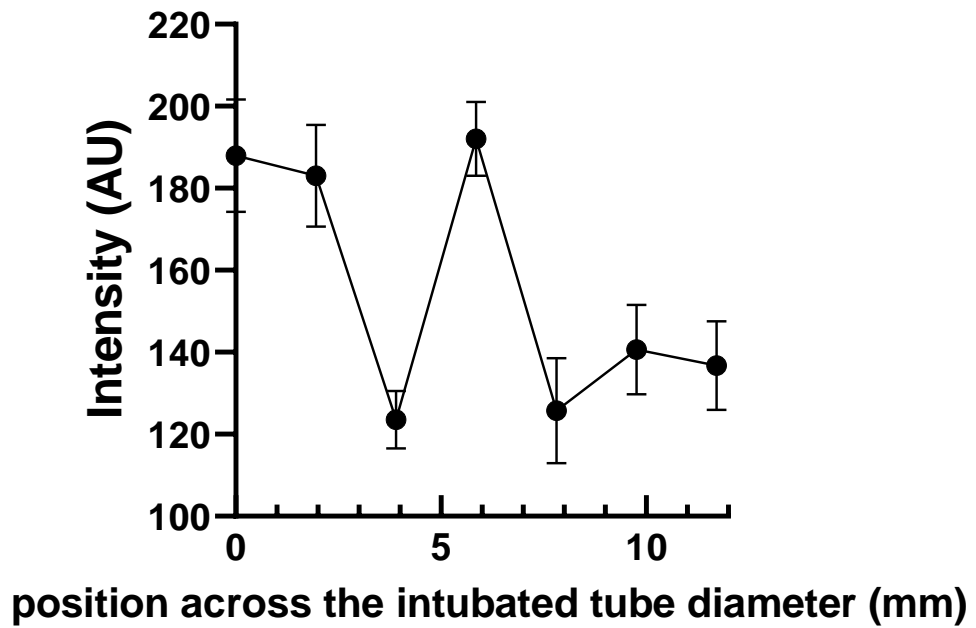
Figure 4.24 *By plotting the intensity of signal along the diameter of the silicone tube and porcine pluck in Figure 4.23, it is possible to determine if there is a significant difference . The effect of the biofilm on the signal intensity measured inside the endotracheal tube compared to the fluid on the outside. No significance was determined using a Grubbs outlier test with an alpha = 0.05*

A T_2^{eff} weighted imaging sequence was also performed on the porcine pluck to determine if using T_2^{eff} weighted imaging could show measure the difference a biofilm has on bulk media *in situ.* A T_2^{eff} weighted sequence with a Tr of 3000ms and a T_e of 100ms was performed as seen in Figure 4.25 with the increased resolution.

Figure 4.25 *A High resolution T_2^{eff} weighted image showing the intubated porcine pluck where the silicone tube can be seen on the left of the image. The silicone tube can be seen on the left of the pluck inside the trachea. The silicone provides no signal and makes it clear the location of the endotracheal tube inside the trachea.*

Due to the SNR being as low as it is, a lower resolution scan was employed, again reducing the time of the scan to that of a relevant clinical time. Figure 4.26 shows the reduced resolution image where the endotracheal tube that has been intubated can still be seen.

Figure 4.26 A lower resolution T_2^{eff} weighted image which still shows the endotracheal tube that can be seen on the left side of the pluck. The intubated silicone tube can be seen on the left side of the pluck using a T_2^{eff} weighted sequence. The silicone provides no measurable signal and so appears black within the trachea and the fluid within.

Using the lower resolution sequence, measurements of the signal intensity can be performed to see if the change in signal caused by the biofilm can be measured and detect whether biofilm formation has occurred earlier on the device. Figure 4.27 shows the change in intensity with the silicone tube being clearly visible in the change in intensity, however there is no discernible different between the fluid seen on the inside of the silicone tube or the fluid outside of the silicone tube with no statistical difference measured by a Grubbs test with an Alpha = 0.05.
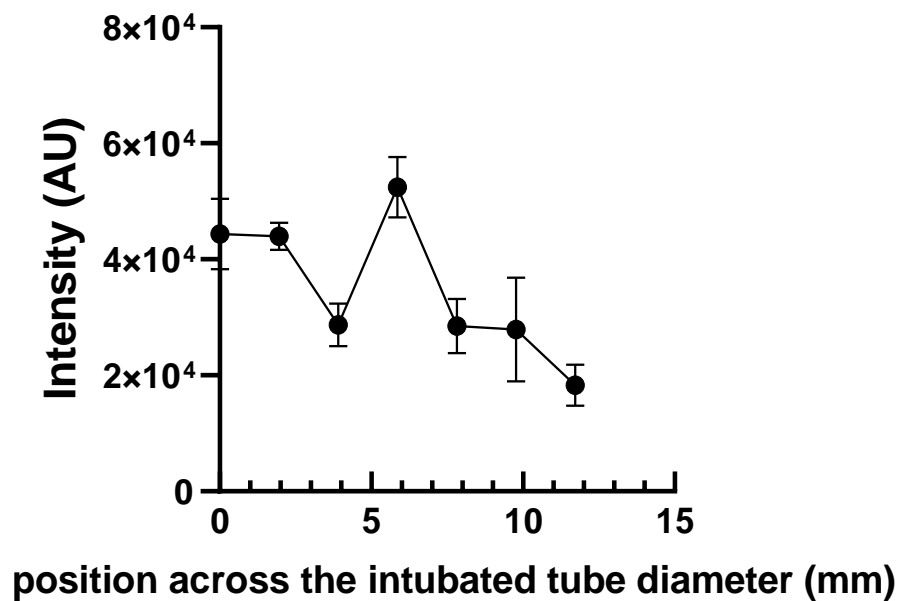
Figure 4.27 *The measured intensity across the silicone tube inside the trachea. The intensity along the diameter of the silicone tube at 7 points, to determine whether the biofilm has discernible. No significance was determined using a Grubbs outlier test with an alpha = 0.05*

Figure 4.28 shows a T_2 weighted image of a porcine pluck, intubated with a biofilm that has grown for eight days. The biofilm is clearly visible along the diameter of the intubated endotracheal tube inside the trachea of the pluck, as well as briefly on the tracheal tube outside of the pluck. To confirm the biofilm is visible to the MRI scanner, a selection of the Endotracheal tube was left outside of the pluck and imaged using the same sequence. This can be seen the red highlighted region where the biofilm coated tube is visible. The brightness of the image has been increased to show the biofilm clearly, as compared to the pluck the signal it produces is substantially lower and is difficult to see without changing the brightness.

Figure 4.28 *The red highlighted biofilm coating the inside and outside of a silicone endotracheal tube. The biofilm is visible on the endotracheal tube outside of the porcine pluck, with the brightness of the image increased to better show the biofilm imaged in the red oval region.*

4.4 Discussion

Using NMR, it is found that there are consistent changes in both spin lattice and spin-spin relaxation when investigating media that has been contaminated. These measurements indicate that biocontamination of media increase T_1 and decrease T_2^{eff} This has been previously seen in other literature studies[436]. However, little work in examining medium inoculated with bacteria is available, in part due to the high volume of water, and a lot of literature evaluating bacteria, investigates the metabolomics[437]. Biofilms in the literature exhibit a shorter T_1 and T_2 value as the biofilm matures and develops, however, by the time they are mature enough to visualise, they are four weeks matured and are likely causing a septic infection[438,439]. This change in relaxation indicates an infection and within mucous rich environments, a measurable change in T_1 relaxation may indicate the presence of a developing bacterial infection. As the Halbach array is custom made, the homogeneity of the magnetic field is anisotropic, and the results of this experiment were confirmed using a 1.5T Siemens Avanto MRI scanner using an inversion recovery sequence. The results confirmed that the Halbach array using NMR sequences and MRI can be used as an early warning system for contaminated media. This phenomenon has been documented previously in the literature but has been applied to the storage of food and may present possible medical applications[440].

The different T_1 values between the Gram positive and Gram negative bacteria were interesting as if NMR could determine the difference between a bacterial infection that was non-destructive and rapidly measurable, treatment against the infection could begin sooner. As bacterial infections are treated through conventional antibiotics, giving the correct antibiotic that works against that Gram class, can aid in preventing long term illness, sepsis and overall reduce the cost of treatment[441]. A blind trial was conducted with ten strains selected at random, and these strains were tested over four consecutive days, with predictions of what the species was, based on the relaxation time. This unfortunately did not provide the results expected and showed that classification through the T_1 relaxation using a low cost system is not viable (Figure 5.5).

The measured value of the Spin-spin relaxation, for all fluids and inoculated media were measured and determined to be marginally different as seen in table 4.2. These results show that T_2^{eff} measurements could be used to detect bacterial contamination, however

measuring T_1 is more effective as every species exhibited significant difference, whereas only five species exhibited different T_2^{eff} after two days of growth.

Diffusion can be used to evaluate the growth of a bacterial culture in a media. The decreasing self and apparent diffusion coefficient after two days of growth clearly indicates a growth in bacteria and biofilm. After which, an increase in the diffusion corresponds to the cell death caused by the bacterial cultures not receiving new nutrients from fresh medium, where biofilm had adhered to the edges of the falcon tubes used to contain the samples, pulling out nutrients from the surrounding media. These bacteria had effectively cleaned the medium they resided in and had turned the medium to water, an effect that is seen in marshland[442]. This result was also observed when the bacteria-inoculated medium, the sodium alginate, water, and sterile medium were all evaluated using diffusion weighted imaging (DWI).

While these early detection techniques for bacterial infections are achievable, development of further non-invasive detection is also important. Currently, a bacterial infection is confirmed via invasive techniques or examination of symptoms expressed in an infected individual[443,444]. Initial experiments were performed on a porcine pluck to determine the T_1 and T_2^{eff} values of the tracheal wall in a porcine pluck, and comparing these values to that of the bacteria measured previously to determine whether there was significant contrast difference between the two measured values. The difference was determined to be significant with both an unfilled porcine pluck and a water filled porcine pluck. With significantly shorter relaxation times, both T_1 and T_2 weighted imaging were performed, where in both imaging modalities, the biofilm can be seen and measured. This shows that it is possible to non-invasively image biofilms forming on endotracheal tubes and that it is possible to image these biofilms around the time symptoms start to appear within an infected patient[445].

Chapter 5. Discussion and conclusion

The work set out in this thesis has consisted of work that has pushed three different scientific fields with the singular focus of detecting and preventing bacterial infections on medical materials, with a particular focus on endotracheal tubes. The use of copper oxide nanoparticles that are functionalised with an amino acid, with glutamic acid being underutilised in literature as an apparent preference for lysine is observed, is well known to improve various properties of nanoparticles such as their stability in solution and their biocompatibility[235, 368]. These nanoparticles were then adhered to medical grade silicone, using a known nanoparticle immobiliser that is also used in manufacturing and water purification[446,447]. Using this process, these functionalised nanoparticles can be adhered to medical grade silicone using a dip coating process, creating a new antimicrobial coating. Furthermore, this coating is evaluated to be non-toxic using conventional, ISO accredited techniques, with the leaching of the material also evaluated to be below the measured toxic limit of the Glu-CuO nanoparticles as well as the mercaptopropyltrimethoxysilane. This coating was further improved upon by incorporating a spray coating into the technique, with the coating applied to other medical-grade materials including stainless steel and titanium[306].

Evaluation of various species, some of which are causing experts to expect an imminent global health crisis, were selected to test against these antimicrobial nanoparticle coatings[90]. These ESKAPE pathogens were characterised and confirmed to possess many of the resistances that have earned them a place on the World Health Organisations list of critical pathogens for the research into new antibiotics to combat them, with two extensively drug resistant *Acinetobacter* species highlighting the concerns of experts[129]. With current techniques such as gDNA sequencing being available, evaluation of the concordance between genotypic and phenotypic data was evaluated, highlighting the marginal concordance between the two different data sets. The marginal concordance showed that genotypic data can be used as an insite to new therapeutic windows, as by having agreeing data between the two different techniques may predict new therapeutic targets[448]. This may not always be the case however, as within the genotypic data, the S. *aureus* strain possessed a copper exporter virulence factor, that may have predicted a higher level of copper resistance than phenotypic data suggested. This data

collected using a minimum inhibitory concentration and minimum bactericidal concentration assays showed that in fact, genotypic data may not predict new therapeutics nor reliably predict antibiotic sensitivity with current methods[449]. The Glu-CuO nanoparticles were evaluated against these species and the MBC was determined to be greater than seen in literature values, however it is also established that the MBC value changes substantially with particle size, with smaller nanoparticles having a higher antimicrobial effect, but an increased cytotoxic effect too[264]. Evaluation of both biofilm biomass formation and viable cell counts showed that the Glu-CuO nanoparticle coating possessed some level of antimicrobial properties, however the standard definition of antimicrobial requires a change in concentration of greater than Log-2 reduction[421]. The measured reduction was between log-1 and log-2, still a significant reduction in viable cells, especially as a real infection does not occur due to a sudden influx of 10^6 viable cells but may occur from a contamination source contain a few tens of thousands of cells[311]. Increasing this concentration showed a significant increase in the log reduction, achieving between a log-2 and log-4 reduction and meeting the proposed criteria for what can be considered antimicrobial. Finally, this coating was applied to other medical grade materials and rapidly cured using ultraviolet irradiation, providing a novel, rapidly curing coating to replace current intraoperative antimicrobial coatings[311]. This chapter achieved the goals to characterise various pathogens including high priority and critical priority species. This was achieved with the modification of currently existing assays that fall short in emulating real world scenarios where infection occurs. Further experimentation showed that copper oxide nanoparticles can be functionalised with lysine and coated on porous fabric materials, further diversifying their coating ability, and providing a material that has diverse applications.

These two chapters show that CuO nanoparticles can be synthesised using a precipitation technique and can be scaled up to industrial quantities. This technique is frequently used in literature as it is a simple technique that is considered green[450]. These nanoparticles do not stay in suspension and enhancing them by coating in glutamic acid improves there zeta potential. Literature has a preference towards lysine coatings, as opposed to a glutamic acid coating of copper oxide nanoparticles, however, research into Glu-CuO nanoparticles is emerging and shows promising results[239]. Analysis of these

nanoparticles after coating showed a substantial increase in the size of the nanoparticles which is often not reported in literature as the coating of the nanoparticles occurs during their synthesis[451]. The coating of CuO nanoparticles in this thesis was done by hand rather than by using a milling machine, so pressure, temperature and speed were not consistent and may have detrimentally affected the coating process. This should be done using an appropriate milling machine and re-evaluate the synthesised and coated nanoparticles to determine size and the quantity of glutamic acid on the coated copper oxide nanoparticles. This work builds on the use of amino acid coatings, by enhancing copper oxide nanoparticles that were otherwise impossible to measure via ISO accredited standards and showing they still retain their antimicrobial properties.

Measurements of the cytotoxicity of the nanoparticle coating were made using a keratinocyte cell line which closely resembles skin cells. The measured toxicity is close to the toxicity measured of copper oxide nanoparticles measured in literature, with a different size and no coating, indicating that the glutamic acid does not increase toxicity[371]. However, the cells of the trachea are consistent with ciliated pseudostratified epithelial cells and will have a different effect when exposed to the Glu-CuO nanoparticles[452]. These cells should be tested to understand the potential cytotoxic effect of a coating on an endotracheal tube. Further cell lines should also be evaluated in future work to ensure that the concentration used on implanted devices are sufficient to prevent biofilm formation of species that are likely to infect that device. These Glu-CuO nanoparticles can be used at concentrations higher than their uncoated counterpart as literature shows they behave with acute toxicity for larger particles, which are considered to have a lower toxic effect[453].

Each bacterial species behaves differently in terms of its growth and its antibiotic resistance profile, and this should be evaluated for each species tested. The work performed here showed slight concordance between the genotypic and phenotypic data, as literature suggests and further work evaluating different species should aim to characterise them both phenotypically and genotypically to predict resistance[454, 455]. Evaluating each species in any antimicrobial test should be performed using a relevant growing medium to that species. Classical MIC tests should be performed with Mueller Hinton Broth or Mueller Hinton agar to conform to EUCAST standards, but when testing

these species against an antimicrobial like a nanoparticle, the growth medium is relevant to real models[456]. Different implants are found in different environments, so using artificial saliva medium and plasma-like medium, is only suitable for environments that are mimicked by that media. Future work should look at each implant's location and use media to mimic that, repeating these experiments and determining what change in biofilm formation or inhibitory concentrations occur.

The touch killing effect seen in literature of copper oxide nanoparticles is observed with the lysine-coated copper oxide nanoparticles in both the polyethylene and polypropylene materials[457, 458]. The results found that within 45 seconds, a touch-killing effect of 99.9% of ten thousand CFU was observed, research here reports a similar value of 90% of one million CFU within five minutes, against different strains and species of bacteria. Further work should investigate the repeated exposure of bacteria to the same samples, to explore and evaluate the robust coating and its persistence.

Finally, NMR and MRI can be used to pre-emptively investigate bacterial contamination through the evaluation of relaxation times in sterile medium compared to inoculated medium. The T_1 relaxation changes significantly after inoculation, increasing the relaxation time to its maximum after two days, with changes being observed after a single day. Evaluating this change can be performed rapidly with both NMR, using a CPMG sequence with varying echo time and MRI with an inversion recovery sequence[459, 460]. While the application of these sequences is not new, the purpose of evaluating contaminated medium provides insight into how bacteria may grow in infected mucoid regions of the tracheal system. A blind trial failed to bring the desired results of identification of Gram classification of a bacterial species, however, it furthered the work that showed a changed spin-lattice relaxation time indicated a bacterial contamination. Evaluation of this effect into the spin-spin relaxation showed that the change in T_1 was not seen in every species in the T_2^{eff} measurements, particularly in the Halbach system due to the inhomogeneity of the magnetic field. MRI was used to evaluate the diffusion of inoculated medium and comparison of the apparent diffusion coefficient and the self-diffusion coefficient presented insight into the changing state of the inoculated medium, with the diffusion coefficients declining as bacterial cell count

increased. After the second day of growth, an increase in the diffusion coefficients indicated that the bacteria had consumed many of the nutrients present in the medium and confirming results previously found within the literature[442].

Investigation into imaging bacteria non-invasively was performed on a porcine pluck. These plucks were first evaluated to measure the T_1 and T_2^{eff} values of the tracheal wall, as pigs are frequently used as substitute for human studies[461]. These values were measured and were significantly different to the relaxation values measured in bulk medium and should provide significant contrast between biofilm coated tubing and trachea. In both T_1 and T_2^{eff} weighted imaging, biofilm was observed on both the inside of the porcine pluck, and in the case of the T_2 weighted image, could be seen outside of the porcine pluck, showing that MRI can be used to non-invasively image and detect the presence of biofilms on certain medical devices such as endotracheal tubes, completing the final objective set out in this thesis.

The values measured for T_1 and T_2 relaxation are different to those compared in literature for biofilms as typical values range from tens to hundred of milliseconds, compared to the seconds measured in this study[436]. This is attributed to the measurement of bulk media, which includes water, media and biofilm and future work should investigate biofilms grown in quantities where they dominate as opposed to bulk media. The blind trial initially showed promising results as NMR relaxation has previously not been used to quantify bacterial cell structure i.e. Gram negative vs Gram-positive species. NMR has been used to investigate the metabolomics of bacterial species and can be combined with chemometric analysis to detect differences between wild-type and mutants of the same species[462]. Metabolomic analysis using NMR could provide these answers and would be important to investigate in the future as a faster, non-destructive technique of bacterial culture identification, in addition to evaluating changes in a population through chemometric analysis.

Measuring the diffusion properties of a biofilm provides information about its lifecycle and the environment the biofilm is found. Similar work evaluating the diffusion around biofilms over time to give insight into biofilm growth have been conducted and show changes over time corresponding to growth[463, 464]. Future work should include measuring the changes in diffusion and both T_1 and T_2 relaxation more frequently, to cover more

of the growth phase of the biofilm, where changes to these properties would be greatest. Finally, while biofilm imaging has been performed in animal models, future work should be to investigate infection in human clinical trials to determine whether MRI can be used in vivo, and reduces the number of medical implants removed erroneously[465, 466]

6. References

1. Roszak, D. B. & Colwell, R. Survival strategies of bacteria in the natural environment. *Microbiol. Rev.* **51**, 365–379 (1987).

2. Vaishampayan, A. & Grohmann, E. Multi-resistant biofilm-forming pathogens on the International Space Station. *J. Biosci.* **44**, 1–5 (2019).

3. Rohmer, L., Hocquet, D. & Miller, S. I. Are pathogenic bacteria just looking for food? Metabolism and microbial pathogenesis. *Trends Microbiol.* **19**, 341–348 (2011).

4. Woese, C. R., Kandler, O. & Wheelis, M. L. Towards a natural system of organisms: proposal for the domains Archaea, Bacteria, and Eucarya. *Proceedings of the National Academy of Sciences* **87**, 4576–4579 (1990).

5. Forterre, P., Benachenhou-Lafha, N. & Labedan, B. Universal tree of life. *Nature* **362**, 795 (1993).

6. Yarza, P. *et al*. Uniting the classification of cultured and uncultured bacteria and archaea using 16S rRNA gene sequences. *Nature Reviews Microbiology* **12**, 635–645 (2014).

7. Trüper, H. G. How to name a prokaryote?: Etymological considerations, proposals and practical advice in prokaryote nomenclature. *FEMS Microbiol. Rev.* **23**, 231–249 (1999).

8. Liu, J., Dazzo, F. B., Glagoleva, O., Yu, B. & Jain, A. K. CMEIAS: a computer-aided system for the image analysis of bacterial morphotypes in microbial communities. *Microb. Ecol.*, 173–194 (2001).

9. Bowden, G. A., Paredes, A. M. & Georgiou, G. Structure and morphology of protein inclusion bodies in Escherichia coli. *Bio/technology* **9**, 725–730 (1991).

10. https://microbeonline.com/characteristics-shape-of-pathogenic-bacteria/.

11. Beveridge, T. J. Use of the Gram stain in microbiology. *Biotechnic & Histochemistry* **76**, 111–118 (2001).

12. Rohde, M. The Gram-positive bacterial cell wall. *Microbiology Spectrum* **7**, 10.1128/microbiolspec. gpp3–2018 (2019).

13. Salem, I., Ramser, A., Isham, N. & Ghannoum, M. A. The gut microbiome as a major regulator of the gut-skin axis. *Frontiers in microbiology* **9**, 1459 (2018).

14. Mayr, F. B., Yende, S. & Angus, D. C. Epidemiology of severe sepsis. *Virulence* **5**, 4–11 (2014).

15. Ramachandran, G. Gram-positive and gram-negative bacterial toxins in sepsis: a brief review. *Virulence* **5**, 213–218 (2014).

16. Monack, D. M., Mueller, A. & Falkow, S. Persistent bacterial infections: the interface of the pathogen and the host immune system. *Nature Reviews Microbiology* **2**, 747–765 (2004).

17. Wu, H., Wang, A. H. & Jennings, M. P. Discovery of virulence factors of pathogenic bacteria. *Curr. Opin. Chem. Biol.* **12**, 93–101 (2008).

18. Fleming, A. On the antibacterial action of cultures of a penicillium, with special reference to their use in the isolation of B. influenzae. *Br. J. Exp. Pathol.* **10**, 226 (1929).

19. Aminov, R. History of antimicrobial drug discovery: Major classes and health impact. *Biochem. Pharmacol.* **133**, 4–19 (2017).

20. Lewis, K. The science of antibiotic discovery. *Cell* **181**, 29–45 (2020).

21. Walsh. Introduction: antibiotic resistance. *Chem. Rev.* **105**, 391–394 (2005).

22. Etebu, E. & Arikekpar, I. Antibiotics: Classification and mechanisms of action with emphasis on molecular perspectives. *Int.J.Appl.Microbiol.Biotechnol.Res* **4**, 90–101 (2016).

23. Leive, L. The barrier function of the Gram-negative envelope. *Ann. N. Y. Acad. Sci.* **235**, 109–129 (1974).

24. Courvalin, P. Vancomycin resistance in gram-positive cocci. *Clinical infectious diseases* **42**, S25–S34 (2006).

25. Toyofuku, M. *et al*. Environmental factors that shape biofilm formation. *Biosci. Biotechnol. Biochem.* **80**, 7–12 (2016).

26. Kapoor, G., Saigal, S. & Elongavan, A. Action and resistance mechanisms of antibiotics: A guide for clinicians. *Journal of anaesthesiology, clinical pharmacology* **33**, 300 (2017).

27. Höltje, J. Growth of the stress-bearing and shape-maintaining murein sacculus of Escherichia coli. *Microbiology and molecular biology reviews* **62**, 181–203 (1998).

28. Bush, K. & Bradford, P. A. β-Lactams and β-lactamase inhibitors: an overview. *Cold Spring Harbor perspectives in medicine* **6**, a025247 (2016).

29. Knowles, J. R. Penicillin resistance: the chemistry of. beta.-lactamase inhibition. *Acc. Chem. Res.* **18**, 97–104 (1985).

30. Wolkenberg, S. E. & Boger, D. L. Mechanisms of in situ activation for DNA-targeting antitumor agents. *Chem. Rev.* **102**, 2477–2496 (2002).

31. Warner, K. D., Hajdin, C. E. & Weeks, K. M. Principles for targeting RNA with drug-like small molecules. *Nature reviews Drug discovery* **17**, 547–558 (2018).

32. Blondeau, J. M. Fluoroquinolones: mechanism of action, classification, and development of resistance. *Surv. Ophthalmol.* **49**, S73–S78 (2004).

33. Reece, R. J. & Maxwell, A. DNA gyrase: structure and function. *Crit. Rev. Biochem. Mol. Biol.* **26**, 335–375 (1991).

34. Liu, L. F. & Wang, J. C. Supercoiling of the DNA template during transcription. *Proceedings of the National Academy of Sciences* **84**, 7024–7027 (1987).

35. Dougherty, T. J. & Saukkonen, J. J. Membrane permeability changes associated with DNA gyrase inhibitors in Escherichia coli. *Antimicrob. Agents Chemother.* **28**, 200–206 (1985).

36. Bourgeois, C. F., Mortreux, F. & Auboeuf, D. The multiple functions of RNA helicases as drivers and regulators of gene expression. *Nature reviews Molecular cell biology* **17**, 426–438 (2016).

37. Hong, W., Zeng, J. & Xie, J. Antibiotic drugs targeting bacterial RNAs. *Acta Pharmaceutica Sinica B* **4**, 258–265 (2014).

38. Davies, J. & Davies, D. Origins and evolution of antibiotic resistance. *Microbiology and molecular biology reviews* **74**, 417–433 (2010).

39. Watkins, R. R., Smith, T. C. & Bonomo, R. A. On the path to untreatable infections: colistin use in agriculture and the end of 'last resort'antibiotics. *Expert Review of Anti-infective Therapy* **14**, 785–788 (2016).

40. Zhao, X., Yu, Z. & Ding, T. Quorum-sensing regulation of antimicrobial resistance in bacteria. *Microorganisms* **8**, 425 (2020).

41. Harms, A., Maisonneuve, E. & Gerdes, K. Mechanisms of bacterial persistence during stress and antibiotic exposure. *Science* **354**, aaf4268 (2016).

42. Baym, M. *et al*. Spatiotemporal microbial evolution on antibiotic landscapes. *Science* **353**, 1147–1151 (2016).

43. Pokharel, S., Raut, S. & Adhikari, B. Tackling antimicrobial resistance in low-income and middle-income countries. *BMJ global health* **4**, e002104 (2019).

44. Bashaar, M., Thawani, V., Hassali, M. A. & Saleem, F. Disposal practices of unused and expired pharmaceuticals among general public in Kabul. *BMC Public Health* **17**, 1–8 (2017).

45. Manzetti, S. & Ghisi, R. The environmental release and fate of antibiotics. *Mar. Pollut. Bull.* **79**, 7–15 (2014).

46. Chang, Q., Wang, W., Regev-Yochay, G., Lipsitch, M. & Hanage, W. P. Antibiotics in agriculture and the risk to human health: how worried should we be? *Evolutionary applications* **8**, 240–247 (2015).

47. Kumar, K., Gupta, S. C., Chander, Y. & Singh, A. K. Antibiotic use in agriculture and its impact on the terrestrial environment. *Adv. Agron.* **87**, 1–54 (2005).

48. Paterson, D. L. & Harris, P. N. Colistin resistance: a major breach in our last line of defence. *The Lancet Infectious Diseases* **16**, 132–133 (2016).

49. Xie, W., Shen, Q. & Zhao, F. J. Antibiotics and antibiotic resistance from animal manures to soil: a review. *Eur. J. Soil Sci.* **69**, 181–195 (2018).

50. Gogarten, J. P. & Townsend, J. P. Horizontal gene transfer, genome innovation and evolution. *Nature Reviews Microbiology* **3**, 679–687 (2005).

51. Virolle, C., Goldlust, K., Djermoun, S., Bigot, S. & Lesterlin, C. Plasmid transfer by conjugation in Gram-negative bacteria: from the cellular to the community level. *Genes* **11**, 1239 (2020).

52. Lorenz, M. G. & Wackernagel, W. Bacterial gene transfer by natural genetic transformation in the environment. *Microbiol. Rev.* **58**, 563–602 (1994).

53. Brito, I. L. Examining horizontal gene transfer in microbial communities. *Nature Reviews Microbiology* **19**, 442–453 (2021).

54. Kulp, A. & Kuehn, M. J. Biological functions and biogenesis of secreted bacterial outer membrane vesicles. *Annu. Rev. Microbiol.* **64**, 163–184 (2010).

55. Schwechheimer, C. & Kuehn, M. J. Outer-membrane vesicles from Gram-negative bacteria: biogenesis and functions. *Nature reviews microbiology* **13**, 605–619 (2015).

56. Jan, A. T. Outer membrane vesicles (OMVs) of gram-negative bacteria: a perspective update. *Frontiers in microbiology* **8**, 1053 (2017).

57. Llosa, M., Gomis-Rüth, F. X., Coll, M. & Cruz, F. d. l. Bacterial conjugation: a two-step mechanism for DNA transport. *Mol. Microbiol.* **45**, 1–8 (2002).

58. Shu, A. *et al*. Evidence of DNA transfer through F-pilus channels during Escherichia coli conjugation. *Langmuir* **24**, 6796–6802 (2008).

59. Stock, J. B., Stock, A. M. & Mottonen, J. M. Signal transduction in bacteria. *Nature* **344**, 395–400 (1990).

60. Ozeki, H. & Ikeda, H. Transduction mechanisms. *Annu. Rev. Genet.* **2**, 245–278 (1968).

61. Chiang, Y. N., Penadés, J. R. & Chen, J. Genetic transduction by phages and chromosomal islands: The new and noncanonical. *PLoS Pathogens* **15**, e1007878 (2019).

62. Vu, B., Chen, M., Crawford, R. J. & Ivanova, E. P. Bacterial extracellular polysaccharides involved in biofilm formation. *Molecules* **14**, 2535–2554 (2009).

63. Sauer, K. *et al*. The biofilm life cycle: expanding the conceptual model of biofilm formation. *Nature Reviews Microbiology* **20**, 608–620 (2022).

64. Vickery, K., Pajkos, A. & Cossart, Y. Removal of biofilm from endoscopes: evaluation of detergent efficiency. *Am. J. Infect. Control* **32**, 170–176 (2004).

65. Høiby, N., Bjarnsholt, T., Givskov, M., Molin, S. & Ciofu, O. Antibiotic resistance of bacterial biofilms. *Int. J. Antimicrob. Agents* **35**, 322–332 (2010).

66. Makabenta, J. M. V. *et al*. Nanomaterial-based therapeutics for antibiotic-resistant bacterial infections. *Nature Reviews Microbiology* **19**, 23–36 (2021).

67. Crabbé, A., Jensen, P. Ø, Bjarnsholt, T. & Coenye, T. Antimicrobial tolerance and metabolic adaptations in microbial biofilms. *Trends Microbiol.* **27**, 850–863 (2019).

68. Roszak, D. B. & Colwell, R. Survival strategies of bacteria in the natural environment. *Microbiol. Rev.* **51**, 365–379 (1987).

69. Blair, J. M., Webber, M. A., Baylay, A. J., Ogbolu, D. O. & Piddock, L. J. Molecular mechanisms of antibiotic resistance. *Nature reviews microbiology* **13**, 42–51 (2015).

70. Reygaert, W. Methicillin-resistant Staphylococcus aureus (MRSA): molecular aspects of antimicrobial resistance and virulence. *Clinical Laboratory Science* **22**, 115 (2009).

71. HULSMANN, A. R. Peptidases: structure, function and modulation of peptide-mediated effects in the human lung. *Clinical and Experimental Allergy* **29**, 445 (1999).

72. Srisuknimit, V., Qiao, Y., Schaefer, K., Kahne, D. & Walker, S. Peptidoglycan cross-linking preferences of Staphylococcus aureus penicillin-binding proteins have implications for treating MRSA infections. *J. Am. Chem. Soc.* **139**, 9791–9794 (2017).

73. Lambert, P. A. Bacterial resistance to antibiotics: modified target sites. *Adv. Drug Deliv. Rev.* **57**, 1471–1485 (2005).

74. Kouzarides, T. Acetylation: a regulatory modification to rival phosphorylation? *EMBO J.* **19**, 1176–1179 (2000).

75. Wright, G. D. Bacterial resistance to antibiotics: enzymatic degradation and modification. *Adv. Drug Deliv. Rev.* **57**, 1451–1470 (2005).

76. Massova, I. & Mobashery, S. Kinship and diversification of bacterial penicillin-binding proteins and β-lactamases. *Antimicrob. Agents Chemother.* **42**, 1–17 (1998).

77. He, Y., Lei, J., Pan, X., Huang, X. & Zhao, Y. The hydrolytic water molecule of Class A β-lactamase relies on the acyl-enzyme intermediate ES* for proper coordination and catalysis. *Scientific reports* **10**, 10205 (2020).

78. Ounissi, H. & Courvalin, P. Nucleotide sequence of the gene ereA encoding the erythromycin esterase in Escherichia coli. *Gene* **35**, 271–278 (1985).

79. Allen, N. E. Macrolide resistance in Staphylococcus aureus: inducers of macrolide resistance. *Antimicrob. Agents Chemother.* **11**, 669–674 (1977).

80. Davidson, A. L. & Chen, J. ATP-binding cassette transporters in bacteria. *Annu. Rev. Biochem.* **73**, 241–268 (2004).

81. Venter, H., Mowla, R., Ohene-Agyei, T. & Ma, S. RND-type drug efflux pumps from Gram-negative bacteria: molecular mechanism and inhibition. *Frontiers in microbiology* **6**, 377 (2015).

82. Tenover, F. C. Mechanisms of antimicrobial resistance in bacteria. *Am. J. Med.* **119**, S3–S10 (2006).

83. Delcour, A. H. Outer membrane permeability and antibiotic resistance. *Biochimica et Biophysica Acta (BBA)-Proteins and Proteomics* **1794**, 808–816 (2009).

84. Zhang, G., Meredith, T. C. & Kahne, D. On the essentiality of lipopolysaccharide to Gram-negative bacteria. *Curr. Opin. Microbiol.* **16**, 779–785 (2013).

85. Matsuura, M. Structural modifications of bacterial lipopolysaccharide that facilitate gram-negative bacteria evasion of host innate immunity. *Frontiers in immunology* **4**, 109 (2013).

86. O'Neill, J. Tackling drug-resistant infections globally: final report and recommendations. (2016).

87. Naylor, N. R. *et al*. Estimating the burden of antimicrobial resistance: a systematic literature review. *Antimicrobial Resistance & Infection Control* **7**, 1–17 (2018).

88. Mancuso, G., Midiri, A., Gerace, E. & Biondo, C. Bacterial antibiotic resistance: The most critical pathogens. *Pathogens* **10**, 1310 (2021).

89. World Health Organization. WHO strategic priorities on antimicrobial resistance: preserving antimicrobials for today and tomorrow. (2021).

90. Zhang, Z. *et al*. Assessment of global health risk of antibiotic resistance genes. *Nature communications* **13**, 1553 (2022).

91. Hacker, J. & Blum-Oehler, G. In appreciation of Theodor Escherich. *Nature Reviews Microbiology* **5**, 902 (2007).

92. Kaper, J. B., Nataro, J. P. & Mobley, H. L. Pathogenic escherichia coli. *Nature reviews microbiology* **2**, 123–140 (2004).

93. Martinson, J. N. & Walk, S. T. Escherichia coli residency in the gut of healthy human adults. *EcoSal Plus* **9** (2020).

94. Pandit, R. *et al*. Extended-spectrum β-lactamase (ESBL) genotypes among multidrug-resistant uropathogenic Escherichia coli clinical isolates from a teaching hospital of Nepal. *Interdisciplinary perspectives on infectious diseases* **2020** (2020).

95. Asokan, G. V., Ramadhan, T., Ahmed, E. & Sanad, H. WHO global priority pathogens list: a bibliometric analysis of Medline-PubMed for knowledge mobilization to infection prevention and control practices in Bahrain. *Oman medical journal* **34**, 184 (2019).

96. Griffin, P. M. & Tauxe, R. V. The epidemiology of infections caused by Escherichia coli O157: H7, other enterohemorrhagic E. coli, and the associated hemolytic uremic syndrome. *Epidemiol. Rev.* **13**, 60–98 (1991).

97. Smith, D. *et al*. Ecological relationships between the prevalence of cattle shedding Escherichia coli O157: H7 and characteristics of the cattle or conditions of the feedlot pen. *J. Food Prot.* **64**, 1899–1903 (2001).

98. Barkocy-Gallagher, G. A. *et al*. Seasonal prevalence of Shiga toxin–producing Escherichia coli, including O157: H7 and non-O157 serotypes, and Salmonella in commercial beef processing plants. *J. Food Prot.* **66**, 1978–1986 (2003).

99. Mead, P. S. & Griffin, P. M. Escherichia coli O157: H7. *The Lancet* **352**, 1207–1212 (1998).

100. Miryala, S. K. & Ramaiah, S. Exploring the multi-drug resistance in Escherichia coli O157: H7 by gene interaction network: a systems biology approach. *Genomics* **111**, 958–965 (2019).

101. Odugbemia, T. Multidrug resistance in E. coli 0157 strains and the public health implication. *Science* **3**, 22–33 (2007).

102. Licitra, G. Etymologia: Staphylococcus. *Emerging infectious diseases* **19**, 1553 (2013).

103. Cheng, A. G., DeDent, A. C., Schneewind, O. & Missiakas, D. A play in four acts: Staphylococcus aureus abscess formation. *Trends Microbiol.* **19**, 225–232 (2011).

104. Washer, P. & Joffe, H. The "hospital superbug": social representations of MRSA. *Soc. Sci. Med.* **63**, 2141–2152 (2006).

105. Deurenberg, R. H. & Stobberingh, E. E. The evolution of Staphylococcus aureus. *Infection, genetics and evolution* **8**, 747–763 (2008).

106. Chambers, H. F. The changing epidemiology of Staphylococcus aureus? *Emerging infectious diseases* **7**, 178 (2001).

107. Boswihi, S. S. & Udo, E. E. Methicillin-resistant Staphylococcus aureus: An update on the epidemiology, treatment options and infection control. *Current Medicine Research and Practice* **8**, 18–24 (2018).

108. Dennis, L. S. *et al*. Linezolid versus vancomycin for the treatment of methicillin-resistant Staphylococcus aureus infections. *Clinical Infectious Diseases* **34**, 1481–1490 (2002).

109. Allison, D. G. & Matthews, M. J. Effect of polysaccharide interactions on antibiotic susceptibility of Pseudomonas aeruginosa. *J. Appl. Bacteriol.* **73**, 484–488 (1992).

110. Poole, K. Pseudomonas aeruginosa: resistance to the max. *Frontiers in microbiology* **2**, 65 (2011).

111. Friedländer, C. Ueber die Schizomyceten bei der acuten fibrösen Pneumonie. *Archiv für pathologische Anatomie und Physiologie und für klinische Medicin* **87**, 319–324 (1882).

112. Yan, K. *et al*. Synergistic effect of low-frequency ultrasound and antibiotics on the treatment of Klebsiella pneumoniae pneumonia in mice. *Microbial Biotechnology* **15**, 2819–2830 (2022).

113. Singla, S., Harjai, K. & Chhibber, S. Susceptibility of different phases of biofilm of Klebsiella pneumoniae to three different antibiotics. *J. Antibiot.* **66**, 61–66 (2013).

114. Vuotto, C. *et al*. Biofilm formation and antibiotic resistance in Klebsiella pneumoniae urinary strains. *J. Appl. Microbiol.* **123**, 1003–1018 (2017).

115. Authority, E. F. S. The European Union summary report on trends and sources of zoonoses, zoonotic agents and food-borne outbreaks in 2017. *EFSa Journal* **16** (2018).

116. Brenner, F. W., Villar, R. G., Angulo, F. J., Tauxe, R. & Swaminathan, B. Salmonella nomenclature. *J. Clin. Microbiol.* **38**, 2465–2467 (2000).

117. Antunes, P., Réu, C., Sousa, J. C., Peixe, L. & Pestana, N. Incidence of Salmonella from poultry products and their susceptibility to antimicrobial agents. *Int. J. Food Microbiol.* **82**, 97–103 (2003).

118. Eng, S. *et al*. Salmonella: a review on pathogenesis, epidemiology and antibiotic resistance. *Frontiers in Life Science* **8**, 284–293 (2015).

119. Joo, H. & Otto, M. Molecular basis of in vivo biofilm formation by bacterial pathogens. *Chem. Biol.* **19**, 1503–1513 (2012).

120. Otto, M. *Molecular basis of Staphylococcus epidermidis infections* (Seminars in immunopathology Ser. 34, Springer, 2012).

121. O'GARA, J. P. & Humphreys, H. Staphylococcus epidermidis biofilms: importance and implications. *J. Med. Microbiol.* **50**, 582–587 (2001).

122. Gad, G. F. M. *et al*. Detection of icaA, icaD genes and biofilm production by Staphylococcus aureus and Staphylococcus epidermidis isolated from urinary tract catheterized patients. *The Journal of Infection in Developing Countries* **3**, 342–351 (2009).

123. Gerner-Smidt, P., Tjernberg, I. & Ursing, J. Reliability of phenotypic tests for identification of Acinetobacter species. *J. Clin. Microbiol.* **29**, 277–282 (1991).

124. Chan, J. Z., Halachev, M. R., Loman, N. J., Constantinidou, C. & Pallen, M. J. Defining bacterial species in the genomic era: insights from the genus Acinetobacter. *BMC microbiology* **12**, 1–11 (2012).

125. Vijayakumar, S., Biswas, I. & Veeraraghavan, B. Accurate identification of clinically important Acinetobacter spp.: an update. *Future science OA* **5**, FSO395 (2019).

126. Baumann, P. Isolation of Acinetobacter from soil and water. *J. Bacteriol.* **96**, 39–42 (1968).

127. Almasaudi, S. B. Acinetobacter spp. as nosocomial pathogens: Epidemiology and resistance features. *Saudi journal of biological sciences* **25**, 586–596 (2018).

128. Peleg, A. Y., Seifert, H. & Paterson, D. L. Acinetobacter baumannii: emergence of a successful pathogen. *Clin. Microbiol. Rev.* **21**, 538–582 (2008).

129. Bouvet, P. J. & Grimont, P. A. Taxonomy of the genus Acinetobacter with the recognition of Acinetobacter baumannii sp. nov., Acinetobacter haemolyticus sp. nov., Acinetobacter johnsonii sp. nov., and Acinetobacter junii sp. nov. and emended descriptions of Acinetobacter calcoaceticus and Acinetobacter lwoffii. *Int. J. Syst. Evol. Microbiol.* **36**, 228–240 (1986).

130. Boucher, H. W. *et al*. Bad bugs, no drugs: no ESKAPE! An update from the Infectious Diseases Society of America. *Clinical infectious diseases* **48**, 1–12 (2009).

131. Pendleton, J. N., Gorman, S. P. & Gilmore, B. F. Clinical relevance of the ESKAPE pathogens. *Expert review of anti-infective therapy* **11**, 297–308 (2013).

132. De Oliveira, D. M. *et al*. Antimicrobial resistance in ESKAPE pathogens. *Clin. Microbiol. Rev.* **33**, 181 (2020).

133. Magiorakos, A. *et al*. Multidrug-resistant, extensively drug-resistant and pandrug-resistant bacteria: an international expert proposal for interim standard definitions for acquired resistance. *Clinical microbiology and infection* **18**, 268–281 (2012).

134. Abbo, A. *et al*. Multidrug-resistant Acinetobacter baumannii. (2005).

135. Antunes, L. C., Visca, P. & Towner, K. J. Acinetobacter baumannii: evolution of a global pathogen. *Pathogens and disease* **71**, 292–301 (2014).

136. Chusri, S. *et al*. Clinical outcomes of hospital-acquired infection with Acinetobacter nosocomialis and Acinetobacter pittii. *Antimicrob. Agents Chemother.* **58**, 4172–4179 (2014).

137. Tierney, B. T. *et al*. Multidrug-resistant Acinetobacter pittii is adapting to and exhibiting potential succession aboard the International Space Station. *Microbiome* **10**, 1–14 (2022).

138. Yang, L., Dong, N., Xu, C., Ye, L. & Chen, S. Emergence of ST63 pandrug-resistant Acinetobacter pittii isolated from an AECOPD patient in China. *Frontiers in cellular and infection microbiology* **11**, 1009 (2021).

139. Bravo, Z., Chapartegui-Gonzalez, I., Lazaro-Diez, M. & Ramos-Vivas, J. Acinetobacter pittii biofilm formation on inanimate surfaces after long-term desiccation. *J. Hosp. Infect.* **98**, 74–82 (2018).

140. Grass, G., Rensing, C. & Solioz, M. Metallic copper as an antimicrobial surface. *Appl. Environ. Microbiol.* **77**, 1541–1547 (2011).

141. Politano, A. D., Campbell, K. T., Rosenberger, L. H. & Sawyer, R. G. Use of silver in the prevention and treatment of infections: silver review. *Surgical infections* **14**, 8–20 (2013).

142. Jolliffe, D. A history of the use of arsenicals in man. *J. R. Soc. Med.* **86**, 287–289 (1993).

143. Bazaka, K., Jacob, M. V., Crawford, R. J. & Ivanova, E. P. Efficient surface modification of biomaterial to prevent biofilm formation and the attachment of microorganisms. *Appl. Microbiol. Biotechnol.* **95**, 299–311 (2012).

144. Mikolay, A. *et al*. Survival of bacteria on metallic copper surfaces in a hospital trial. *Appl. Microbiol. Biotechnol.* **87**, 1875–1879 (2010).

145. Fricker, S. P. Metal based drugs: from serendipity to design. *Dalton transactions*, 4903–4917 (2007).

146. Frei, A. Metal complexes, an untapped source of antibiotic potential? *Antibiotics* **9**, 90 (2020).

147. Lemire, J. A., Harrison, J. J. & Turner, R. J. Antimicrobial activity of metals: mechanisms, molecular targets and applications. *Nature Reviews Microbiology* **11**, 371–384 (2013).

148. Dizaj, S. M., Lotfipour, F., Barzegar-Jalali, M., Zarrintan, M. H. & Adibkia, K. Antimicrobial activity of the metals and metal oxide nanoparticles. *Materials Science and Engineering: C* **44**, 278–284 (2014).

149. https://www.fda.gov/drugs/historical-status-otc-rulemakings/rulemaking-history-otc-colloidal-silver-drug-products.

150. Yakabe, Y., Sano, T., Ushio, H. & Yasunaga, T. Kinetic studies of the interaction between silver ion and deoxyribonucleic acid. *Chem. Lett.* **9**, 373–376 (1980).

151. Mijnendonckx, K., Leys, N., Mahillon, J., Silver, S. & Van Houdt, R. Antimicrobial silver: uses, toxicity and potential for resistance. *Biometals* **26**, 609–621 (2013).

152. Clement, J. L. & Jarrett, P. S. Antibacterial silver. *Metal-based drugs* **1**, 467–482 (1994).

153. Li, X., Nikaido, H. & Williams, K. E. Silver-resistant mutants of Escherichia coli display active efflux of Ag and are deficient in porins. *J. Bacteriol.* **179**, 6127–6132 (1997).

154. Blair, C. & Blair, J. Copper alloys. *English Medieval Industries: Craftsmen, Techniques, Products*, 81–106 (1991).

155. Michels, H., Moran, W. & Michel, J. Antimicrobial properties of copper alloy surfaces, with a focus on hospital-acquired infections. *International Journal of Metalcasting* **2**, 47–56 (2008).

156. Tetaz, T. J. & Luke, R. K. Plasmid-controlled resistance to copper in Escherichia coli. *J. Bacteriol.* **154**, 1263–1268 (1983).

157. Cooksey, D. A. Molecular mechanisms of copper resistance and accumulation in bacteria. *FEMS Microbiol. Rev.* **14**, 381–386 (1994).

158. Borkow, G. & Gabbay, J. Copper as a biocidal tool. *Curr. Med. Chem.* **12**, 2163–2175 (2005).

159. Letelier, M. E. *et al*. Possible mechanisms underlying copper-induced damage in biological membranes leading to cellular toxicity. *Chem. Biol. Interact.* **151**, 71–82 (2005).

160. Rivero-Müller, A., De Vizcaya-Ruiz, A., Plant, N., Ruiz, L. & Dobrota, M. Mixed chelate copper complex, Casiopeina IIgly®, binds and degrades nucleic acids: A mechanism of cytotoxicity. *Chem. Biol. Interact.* **165**, 189–199 (2007).

161. Tambosi, R. *et al*. Silver and copper acute effects on membrane proteins and impact on photosynthetic and respiratory complexes in bacteria. *MBio* **9**, 10.1128/mbio. 01535–18 (2018).

162. Honjo, G. Electron diffraction studies on oxide films formed on metals and alloys part 1. Oxidation of pure copper. *Journal of the Physical Society of Japan* **4**, 330–333 (1949).

163. Christy, A. J., Nehru, L. C. & Umadevi, M. A novel combustion method to prepare CuO nanorods and its antimicrobial and photocatalytic activities. *Powder Technol* **235**, 783–786 (2013).

164. Meghana, S., Kabra, P., Chakraborty, S. & Padmavathy, N. Understanding the pathway of antibacterial activity of copper oxide nanoparticles. *RSC advances* **5**, 12293–12299 (2015).

165. Lemire, J. A., Harrison, J. J. & Turner, R. J. Antimicrobial activity of metals: mechanisms, molecular targets and applications. *Nature Reviews Microbiology* **11**, 371–384 (2013).

166. Festa, R. A. & Thiele, D. J. Copper: an essential metal in biology. *Current Biology* **21**, R877–R883 (2011).

167. Argüello, J. M., Raimunda, D. & Padilla-Benavides, T. Mechanisms of copper homeostasis in bacteria. *Frontiers in cellular and infection microbiology* **3**, 73 (2013).

168. Godoy-Gallardo, M. *et al.* Antibacterial approaches in tissue engineering using metal ions and nanoparticles: From mechanisms to applications. *Bioactive Materials* **6**, 4470–4490 (2021).

169. Raghunath, A. & Perumal, E. Metal oxide nanoparticles as antimicrobial agents: a promise for the future. *Int. J. Antimicrob. Agents* **49**, 137–152 (2017).

170. Muzammil, S. *et al.* Nanoantibiotics: Future nanotechnologies to combat antibiotic resistance. *Front. Biosci.* **10**, 352–374 (2018).

171. Tamás, M. J., Sharma, S. K., Ibstedt, S., Jacobson, T. & Christen, P. Heavy metals and metalloids as a cause for protein misfolding and aggregation. *Biomolecules* **4**, 252–267 (2014).

172. Dharmaraja, A. T. Role of reactive oxygen species (ROS) in therapeutics and drug resistance in cancer and bacteria. *J. Med. Chem.* **60**, 3221–3240 (2017).

173. Barzilai, A. & Yamamoto, K. DNA damage responses to oxidative stress. *DNA repair* **3**, 1109–1115 (2004).

174. Imlay, J. A. Diagnosing oxidative stress in bacteria: not as easy as you might think. *Curr. Opin. Microbiol.* **24**, 124–131 (2015).

175. Pereira, Y. *et al.* Chromate causes sulfur starvation in yeast. *Toxicological Sciences* **106**, 400–412 (2008).

176. Gold, K., Slay, B., Knackstedt, M. & Gaharwar, A. K. Antimicrobial activity of metal and metal-oxide based nanoparticles. *Advanced Therapeutics* **1**, 1700033 (2018).

177. Iavicoli, I., Fontana, L., Leso, V. & Bergamaschi, A. The effects of nanomaterials as endocrine disruptors. *International journal of molecular sciences* **14**, 16732–16801 (2013).

178. Slavin, Y. N., Asnis, J., Hńfeli, U. O. & Bach, H. Metal nanoparticles: understanding the mechanisms behind antibacterial activity. *Journal of nanobiotechnology* **15**, 1–20 (2017).

179. Chen, Z. *et al.* Acute toxicological effects of copper nanoparticles in vivo. *Toxicol. Lett.* **163**, 109–120 (2006).

180. Amro, N. A. *et al.* High-resolution atomic force microscopy studies of the Escherichia coli outer membrane: structural basis for permeability. *Langmuir* **16**, 2789–2796 (2000).

181. Delmar, J. A., Su, C. & Yu, E. W. Bacterial multidrug efflux transporters. *Annual review of biophysics* **43**, 93–117 (2014).

182. Pal, C. *et al*. Metal resistance and its association with antibiotic resistance. *Adv. Microb. Physiol.* **70**, 261–313 (2017).

183. Nies, D. H. Efflux-mediated heavy metal resistance in prokaryotes. *FEMS Microbiol. Rev.* **27**, 313–339 (2003).

184. Schalk, I. J. & Guillon, L. Pyoverdine biosynthesis and secretion in P seudomonas aeruginosa: implications for metal homeostasis. *Environ. Microbiol.* **15**, 1661–1673 (2013).

185. Vijver, M. G., Van Gestel, C. A., Lanno, R. P., Van Straalen, N. M. & Peijnenburg, W. J. Internal metal sequestration and its ecotoxicological relevance: a review. *Environ. Sci. Technol.* **38**, 4705–4712 (2004).

186. Chandrangsu, P., Rensing, C. & Helmann, J. D. Metal homeostasis and resistance in bacteria. *Nature Reviews Microbiology* **15**, 338–350 (2017).

187. Jiao, Y., Tay, F. R., Niu, L. & Chen, J. Advancing antimicrobial strategies for managing oral biofilm infections. *International journal of oral science* **11**, 28 (2019).

188. Colquhoun, J. M. & Rather, P. N. Insights into mechanisms of biofilm formation in Acinetobacter baumannii and implications for uropathogenesis. *Frontiers in cellular and infection microbiology* **10**, 253 (2020).

189. Khatoon, Z., McTiernan, C. D., Suuronen, E. J., Mah, T. & Alarcon, E. I. Bacterial biofilm formation on implantable devices and approaches to its treatment and prevention. *Heliyon* **4** (2018).

190. Harrison, J. J., Ceri, H. & Turner, R. J. Multimetal resistance and tolerance in microbial biofilms. *Nature Reviews Microbiology* **5**, 928–938 (2007).

191. https://www.nano.gov.

192. Feynman, R. P. There's plenty of room at the bottom [data storage]. *J Microelectromech Syst* **1**, 60–66 (1992).

193. Mahdavi, M. *et al*. Synthesis, surface modification and characterisation of biocompatible magnetic iron oxide nanoparticles for biomedical applications. *Molecules* **18**, 7533–7548 (2013).

194. Blanco, E., Shen, H. & Ferrari, M. Principles of nanoparticle design for overcoming biological barriers to drug delivery. *Nat. Biotechnol.* **33**, 941–951 (2015).

195. Jones, N., Ray, B., Ranjit, K. T. & Manna, A. C. Antibacterial activity of ZnO nanoparticle suspensions on a broad spectrum of microorganisms. *FEMS Microbiol. Lett.* **279**, 71–76 (2008).

196. Pandey, P., Merwyn, S., Agarwal, G. S., Tripathi, B. K. & Pant, S. C. Electrochemical synthesis of multi-armed CuO nanoparticles and their remarkable bactericidal potential against waterborne bacteria. *Journal of Nanoparticle Research* **14**, 1–13 (2012).

197. Dodoo-Arhin, D., Leoni, M. & Scardi, P. Microemulsion synthesis of copper oxide nanorod-like structures. *Molecular Crystals and Liquid Crystals* **555**, 17–31 (2012).

198. Lassoued, A., Dkhil, B., Gadri, A. & Ammar, S. Control of the shape and size of iron oxide (α-Fe2O3) nanoparticles synthesized through the chemical precipitation method. *Results in physics* **7**, 3007–3015 (2017).

199. Therese, G. H. A. & Kamath, P. V. Electrochemical synthesis of metal oxides and hydroxides. *Chemistry of materials* **12**, 1195–1204 (2000).

200. Tomé, L. I., Baião, V., da Silva, W. & Brett, C. M. Deep eutectic solvents for the production and application of new materials. *Applied Materials Today* **10**, 30–50 (2018).

201. Wagle, D. V., Zhao, H. & Baker, G. A. Deep eutectic solvents: sustainable media for nanoscale and functional materials. *Acc. Chem. Res.* **47**, 2299–2308 (2014).

202. Zhang, W., Qiao, X. & Chen, J. Synthesis of silver nanoparticles—effects of concerned parameters in water/oil microemulsion. *Materials Science and Engineering: B* **142**, 1–15 (2007).

203. Poolakkandy, R. R. & Menamparambath, M. M. Soft-template-assisted synthesis: a promising approach for the fabrication of transition metal oxides. *Nanoscale Advances* **2**, 5015–5045 (2020).

204. Chairam, S., Poolperm, C. & Somsook, E. Starch vermicelli template-assisted synthesis of size/shape-controlled nanoparticles. *Carbohydr. Polym.* **75**, 694–704 (2009).

205. Verma, N. & Kumar, N. Synthesis and biomedical applications of copper oxide nanoparticles: an expanding horizon. *ACS biomaterials science & engineering* **5**, 1170–1188 (2019).

206. Siddiqui, H., Qureshi, M. S. & Haque, F. Z. Effect of copper precursor salts: facile and sustainable synthesis of controlled shaped copper oxide nanoparticles. *Optik* **127**, 4726–4730 (2016).

207. Alam, M. A. *et al*. The effect of precursor concentration on the crystallinity synchronization of synthesized copper nanoparticles. *J. Cryst. Growth* **621**, 127386 (2023).

208. Sagadevan, S. *et al*. Synthesis and evaluation of the structural, optical, and antibacterial properties of copper oxide nanoparticles. *Applied Physics A* **125**, 1–9 (2019).

209. Chang, M., Liu, H. & Tai, C. Y. Preparation of copper oxide nanoparticles and its application in nanofluid. *Powder Technol* **207**, 378–386 (2011).

210. Khashan, K. S., Jabir, M. S. & Abdulameer, F. A. *Preparation and characterization of copper oxide nanoparticles decorated carbon nanoparticles using laser ablation in liquid* (Journal of Physics: Conference Series Ser. 1003, IOP Publishing, 2018).

211. Katwal, R., Kaur, H., Sharma, G., Naushad, M. & Pathania, D. Electrochemical synthesized copper oxide nanoparticles for enhanced photocatalytic and antimicrobial activity. *Journal of Industrial and Engineering Chemistry* **31**, 173–184 (2015).

212. Yuan, G., Jiang, H., Lin, C. & Liao, S. Shape-and size-controlled electrochemical synthesis of cupric oxide nanocrystals. *J. Cryst. Growth* **303**, 400–406 (2007).

213. Mott, D., Galkowski, J., Wang, L., Luo, J. & Zhong, C. Synthesis of size-controlled and shaped copper nanoparticles. *Langmuir* **23**, 5740–5745 (2007).

214. Li, D. & Kaner, R. B. Shape and aggregation control of nanoparticles: not shaken, not stirred. *J. Am. Chem. Soc.* **128**, 968–975 (2006).

215. Ingham, B. X-ray scattering characterisation of nanoparticles. *Crystallography Reviews* **21**, 229–303 (2015).

216. Ealia, S. A. M. &Saravanakumar, M. P. *A review on the classification, characterisation, synthesis of nanoparticles and their application* (IOP conference series: materials science and engineering Ser. 263, IOP Publishing, 2017).

217. Ren, G. *et al*. Characterisation of copper oxide nanoparticles for antimicrobial applications. *Int. J. Antimicrob. Agents* **33**, 587–590 (2009).

218. Goldstein, J. I. *et al*. in *Scanning electron microscopy and X-ray microanalysis* (springer, 2017).

219. Zhou, W., Apkarian, R., Wang, Z. L. & Joy, D. Fundamentals of scanning electron microscopy (SEM). *Scanning Microscopy for Nanotechnology: Techniques and Applications*, 1–40 (2007).

220. Seiler, H. Secondary electron emission in the scanning electron microscope. *J. Appl. Phys.* **54**, R1–R18 (1983).

221. Vernon-Parry, K. D. Scanning electron microscopy: an introduction. *III-Vs review* **13**, 40–44 (2000).

222. Siegbahn, K. in *Alpha-, beta-and gamma-ray spectroscopy* (Elsevier, 2012).

223. Inkson, B. J. in *Materials characterization using nondestructive evaluation (NDE) methods* 17–43 (Elsevier, 2016).

224. Shatila, F., Yaşa, İ & Yalçın, H. T. Biofilm formation by Salmonella enterica strains. *Curr. Microbiol.* **78**, 1150–1158 (2021).

225. Williams, D. L. & Bloebaum, R. D. Observing the biofilm matrix of Staphylococcus epidermidis ATCC 35984 grown using the CDC biofilm reactor. *Microscopy and Microanalysis* **16**, 143–152 (2010).

226. Abdullah, S. Z., Bérubé, P. R. & Horne, D. J. SEM imaging of membranes: Importance of sample preparation and imaging parameters. *J. Membr. Sci.* **463**, 113–125 (2014).

227. Kruk, T., Szczepanowicz, K., Stefańska, J., Socha, R. P. & Warszyński, P. Synthesis and antimicrobial activity of monodisperse copper nanoparticles. *Colloids and surfaces B: Biointerfaces* **128**, 17–22 (2015).

228. Williams, D. B., Carter, C. B., Williams, D. B. & Carter, C. B. in *The transmission electron microscope* (Springer, 1996).

229. Kimoto, K. *et al*. Local crystal structure analysis with several picometer precision using scanning transmission electron microscopy. *Ultramicroscopy* **110**, 778–782 (2010).

230. Karlsson, H. L., Cronholm, P., Gustafsson, J. & Moller, L. Copper oxide nanoparticles are highly toxic: a comparison between metal oxide nanoparticles and carbon nanotubes. *Chem. Res. Toxicol.* **21**, 1726–1732 (2008).

231. Egerton, R. F., Li, P. & Malac, M. Radiation damage in the TEM and SEM. *Micron* **35**, 399–409 (2004).

232. Wang, S. *et al*. Synthesis, growth mechanism and thermal stability of copper nanoparticles encapsulated by multi-layer graphene. *Carbon* **50**, 2119–2125 (2012).

233. Coats, A. W. & Redfern, J. P. Thermogravimetric analysis. A review. *Analyst* **88**, 906–924 (1963).

234. Karimzadeh, I. *et al*. Amino acid coated superparamagnetic iron oxide nanoparticles for biomedical applications through a novel efficient preparation method. *Journal of Cluster Science* **28**, 1259–1271 (2017).

235. Selvakannan, P. R., Mandal, S., Phadtare, S., Pasricha, R. & Sastry, M. Capping of gold nanoparticles by the amino acid lysine renders them water-dispersible. *Langmuir* **19**, 3545–3549 (2003).

236. Mansfield, E., Tyner, K. M., Poling, C. M. & Blacklock, J. L. Determination of nanoparticle surface coatings and nanoparticle purity using microscale thermogravimetric analysis. *Anal. Chem.* **86**, 1478–1484 (2014).

237. Dongargaonkar, A. A. & Clogston, J. D. Quantitation of surface coating on nanoparticles using thermogravimetric analysis. *Characterization of Nanoparticles Intended for Drug Delivery*, 57–63 (2018).

238. Badetti, E. *et al*. Interaction between copper oxide nanoparticles and amino acids: influence on the antibacterial activity. *Nanomaterials* **9**, 792 (2019).

239. Goldburg, W. I. Dynamic light scattering. *American Journal of Physics* **67**, 1152–1160 (1999).

240. Chu, B. & Liu, T. Characterization of nanoparticles by scattering techniques. *Journal of Nanoparticle Research* **2**, 29–41 (2000).

241. Ragheb, R. & Nobbmann, U. Multiple scattering effects on intercept, size, polydispersity index, and intensity for parallel (VV) and perpendicular (VH) polarization detection in photon correlation spectroscopy. *Scientific Reports* **10**, 21768 (2020).

242. Lawaczeck, R., Menzel, M. & Pietsch, H. Superparamagnetic iron oxide particles: contrast media for magnetic resonance imaging. *Applied organometallic chemistry* **18**, 506–513 (2004).

243. Bhattacharjee, S. DLS and zeta potential–what they are and what they are not? *J. Controlled Release* **235**, 337–351 (2016).

244. Ahamed, M., Alhadlaq, H. A., Khan, M. M., Karuppiah, P. & Al-Dhabi, N. A. Synthesis, characterization, and antimicrobial activity of copper oxide nanoparticles. *Journal of Nanomaterials* **2014**, 637858 (2014).

245. Mekapothula, S. *et al*. Antipathogenic Applications of Copper Nanoparticles in Air Filtration Systems. *Materials* **17**, 2664 (2024).

246. Badetti, E. *et al*. Interaction between copper oxide nanoparticles and amino acids: influence on the antibacterial activity. *Nanomaterials* **9**, 792 (2019).

247. Bai, B. *et al*. Biosynthesized copper oxide nanoparticles (CuO NPs) enhances the anti-biofilm efficacy against K. pneumoniae and S. aureus. *Journal of King Saud University-Science* **34**, 102120 (2022).

248. Nithiyavathi, R. *et al*. Gum mediated synthesis and characterization of CuO nanoparticles towards infectious disease-causing antimicrobial resistance microbial pathogens. *Journal of Infection and Public Health* **14**, 1893–1902 (2021).

249. Ren, G. *et al*. Characterisation of copper oxide nanoparticles for antimicrobial applications. *Int. J. Antimicrob. Agents* **33**, 587–590 (2009).

250. Naz, S., Gul, A. & Zia, M. Toxicity of copper oxide nanoparticles: a review study. *IET nanobiotechnology* **14**, 1–13 (2020).

251. Meghana, S., Kabra, P., Chakraborty, S. & Padmavathy, N. Understanding the pathway of antibacterial activity of copper oxide nanoparticles. *RSC advances* **5**, 12293–12299 (2015).

252. Chatterjee, A. K., Chakraborty, R. & Basu, T. Mechanism of antibacterial activity of copper nanoparticles. *Nanotechnology* **25**, 135101 (2014).

253. Behzadinasab, S., Williams, M. D., Falkinham III, J. O. & Ducker, W. A. Antimicrobial mechanism of cuprous oxide (Cu2O) coatings. *J. Colloid Interface Sci.* **652**, 1867–1877 (2023).

254. Veal, E. A., Day, A. M. & Morgan, B. A. Hydrogen peroxide sensing and signaling. *Mol. Cell* **26**, 1–14 (2007).

255. Afonso, V., Champy, R., Mitrovic, D., Collin, P. & Lomri, A. Reactive oxygen species and superoxide dismutases: role in joint diseases. *Joint Bone Spine* **74**, 324–329 (2007).

256. Hans, M. *et al*. Role of copper oxides in contact killing of bacteria. *Langmuir* **29**, 16160–16166 (2013).

257. Macomber, L. & Imlay, J. A. The iron-sulfur clusters of dehydratases are primary intracellular targets of copper toxicity. *Proceedings of the National Academy of Sciences* **106**, 8344–8349 (2009).

258. Laha, D. *et al*. Shape-dependent bactericidal activity of copper oxide nanoparticle mediated by DNA and membrane damage. *Mater. Res. Bull.* **59**, 185–191 (2014).

259. Bezza, F. A., Tichapondwa, S. M. & Chirwa, E. M. Fabrication of monodispersed copper oxide nanoparticles with potential application as antimicrobial agents. *Scientific Reports* **10**, 16680 (2020).

260. ShamsiJazeyi, H., Miller, C. A., Wong, M. S., Tour, J. M. & Verduzco, R. Polymer-coated nanoparticles for enhanced oil recovery. *J Appl Polym Sci* **131** (2014).

261. Chen, N. *et al*. Investigation of the characteristics and antibacterial activity of polymer-modified copper oxide nanoparticles. *International Journal of Molecular Sciences* **22**, 12913 (2021).

262. Kruk, T., Szczepanowicz, K., Stefańska, J., Socha, R. P. & Warszyński, P. Synthesis and antimicrobial activity of monodisperse copper nanoparticles. *Colloids and surfaces B: Biointerfaces* **128**, 17–22 (2015).

263. Jeong, Y., Lim, D. W. & Choi, J. Assessment of size-dependent antimicrobial and cytotoxic properties of silver nanoparticles. *Advances in Materials Science and Engineering* **2014** (2014).

264. Saunders, S. R., Eden, M. R. & Roberts, C. B. Modeling the precipitation of polydisperse nanoparticles using a total interaction energy model. *The Journal of Physical Chemistry C* **115**, 4603–4610 (2011).

265. Karabulut, G., Üllen, N. B., Karakuş, S. & Toruntay, C. Enhancing antibacterial and anticorrosive properties of 316L stainless steel with nanocoating of copper oxide nanoparticles. *Mater. Chem. Phys.* **308**, 128265 (2023).

266. Anita, S., Ramachandran, T., Rajendran, R., Koushik, C. V. & Mahalakshmi, M. A study of the antimicrobial property of encapsulated copper oxide nanoparticles on cotton fabric. *Text. Res. J.* **81**, 1081–1088 (2011).

267. Merkl, P., Long, S., McInerney, G. M. & Sotiriou, G. A. Antiviral activity of silver, copper oxide and zinc oxide nanoparticle coatings against SARS-CoV-2. *Nanomaterials* **11**, 1312 (2021).

268. Cioffi, N. *et al*. Copper nanoparticle/polymer composites with antifungal and bacteriostatic properties. *Chemistry of Materials* **17**, 5255–5262 (2005).

269. Guan, N. & Liu, L. Microbial response to acid stress: mechanisms and applications. *Appl. Microbiol. Biotechnol.* **104**, 51–65 (2020).

270. Zhao, X. *et al*. Glutamine promotes antibiotic uptake to kill multidrug-resistant uropathogenic bacteria. *Science Translational Medicine* **13**, eabj0716 (2021).

271. Lewis, K. Multidrug tolerance of biofilms and persister cells. *Bacterial biofilms*, 107–131 (2008).

272. Hall, C. W. & Mah, T. Molecular mechanisms of biofilm-based antibiotic resistance and tolerance in pathogenic bacteria. *FEMS Microbiol. Rev.* **41**, 276–301 (2017).

273. Mah, T. C. & O'Toole, G. A. Mechanisms of biofilm resistance to antimicrobial agents. *Trends Microbiol.* **9**, 34–39 (2001).

274. Khardori, N. & Yassien, M. Biofilms in device-related infections. *Journal of industrial microbiology and biotechnology* **15**, 141–147 (1995).

275. Zimlichman, E. *et al*. Health care–associated infections: a meta-analysis of costs and financial impact on the US health care system. *JAMA internal medicine* **173**, 2039–2046 (2013).

276. Percival, S. L., Suleman, L., Vuotto, C. & Donelli, G. Healthcare-associated infections, medical devices and biofilms: risk, tolerance and control. *J. Med. Microbiol.* **64**, 323–334 (2015).

277. Josephs-Spaulding, J. & Singh, O. V. Medical device sterilization and reprocessing in the era of Multidrug-Resistant (MDR) bacteria: issues and regulatory concepts. *Frontiers in medical technology* **2**, 587352 (2021).

278. Luft, D. *et al*. Central venous catheter-associated bloodstream infection and colonisation of insertion site and catheter tip. What are the rates and risk factors in haematology patients? *Ann. Hematol.* **89**, 1265–1275 (2010).

279. Pneumatikos, I. A., Dragoumanis, C. K., Bouros, D. E., Warner, D. S. & Warner, M. A. Ventilator-associated pneumonia or endotracheal tube-associated pneumonia? An approach to the pathogenesis and preventive strategies emphasizing the importance of endotracheal tube. *The Journal of the American Society of Anesthesiologists* **110**, 673–680 (2009).

280. Baran, G. *et al*. Risk factors for nosocomial imipenem-resistant Acinetobacter baumannii infections. *International Journal of Infectious Diseases* **12**, 16–21 (2008).

281. Bauer, T. T. *et al*. Biofilm formation in endotracheal tubes. Association between pneumonia and the persistence of pathogens. *Monaldi archives for chest disease* **57**, 84–87 (2002).

282. Montefour, K. *et al*. Acinetobacter baumannii: an emerging multidrug-resistant pathogen in critical care. *Crit. Care Nurse* **28**, 15–25 (2008).

283. Watson, W. F. Development of the PVC endotracheal tube. *Biomaterials* **1**, 41–46 (1980).

284. Gunatillake, P. A. & Adhikari, R. in *Biosynthetic Polymers for Medical Applications* 33–62 (Elsevier, 2016).

285. Ahmed, R. A. & Boyer, T. J. Endotracheal tube. (2019).

286. Mort, T. C. Emergency tracheal intubation: complications associated with repeated laryngoscopic attempts. *Anesthesia & Analgesia* **99**, 607–613 (2004).

287. Jougon, J., Cantini, O., Delcambre, F., Minniti, A. & Velly, J. F. Esophageal perforation: life threatening complication of endotracheal intubation. *European journal of cardio-thoracic surgery* **20**, 7–11 (2001).

288. Miller, K. A., Kimia, A., Monuteaux, M. C. & Nagler, J. Factors associated with misplaced endotracheal tubes during intubation in pediatric patients. *J. Emerg. Med.* **51**, 9–18 (2016).

289. Bauer, T. T. *et al*. Biofilm formation in endotracheal tubes. Association between pneumonia and the persistence of pathogens. *Monaldi archives for chest disease* **57**, 84–87 (2002).

290. Hotterbeekx, A. *et al*. The endotracheal tube microbiome associated with Pseudomonas aeruginosa or Staphylococcus epidermidis. *Scientific reports* **6**, 36507 (2016).

291. Berra, L. *et al*. Endotracheal tubes coated with antiseptics decrease bacterial colonization of the ventilator circuits, lungs, and endotracheal tube. *The Journal of the American Society of Anesthesiologists* **100**, 1446–1456 (2004).

292. Adair, C. *et al*. Eradication of endotracheal tube biofilm by nebulised gentamicin. *Intensive Care Med.* **28**, 426–431 (2002).

293. Dsouza, R. *et al*. In vivo detection of endotracheal tube biofilms in intubated critical care patients using catheter-based optical coherence tomography. *Journal of biophotonics* **12**, e201800307 (2019).

294. Gravenstein, N. & Blackshear, R. H. In vitro evaluation of relative perforating potential of central venous catheters: comparison of materials, selected models, number of lumens, and angles of incidence to simulated membrane. *J. Clin. Monit.* **7**, 1–6 (1991).

295. Mermel, L. A. Prevention of intravascular catheter–related infections. *Ann. Intern. Med.* **132**, 391–402 (2000).

296. Bouza, E., Burillo, A. & Munoz, P. Catheter-related infections: diagnosis and intravascular treatment. *Clinical Microbiology and Infection* **8**, 265–274 (2002).

297. Al-Hazmi, H. Role of duration of catheterization and length of hospital stay on the rate of catheter-related hospital-acquired urinary tract infections. *Research and reports in urology*, 41–47 (2015).

298. Foxman, B. The epidemiology of urinary tract infection. *Nature Reviews Urology* **7**, 653–660 (2010).

299. Crump, J. A. & Collignon, P. J. Intravascular catheter-associated infections. *European Journal of Clinical Microbiology and Infectious Diseases* **19**, 1–8 (2000).

300. Gominet, M., Compain, F., Beloin, C. & Lebeaux, D. Central venous catheters and biofilms: where do we stand in 2017? *APMIS* **125**, 365–375 (2017).

301. Lai, N. M. *et al*. Catheter impregnation, coating or bonding for reducing central venous catheter-related infections in adults. *Cochrane Database of Systematic Reviews* (2016).

302. Samuel, U. & Guggenbichler, J. P. Prevention of catheter-related infections: the potential of a new nano-silver impregnated catheter. *Int. J. Antimicrob. Agents* **23**, 75–78 (2004).

303. Osada, D., Viegas, S. F., Shah, M. A., Morris, R. P. & Patterson, R. M. Comparison of different distal radius dorsal and volar fracture fixation plates: a biomechanical study. *J. Hand Surg.* **28**, 94–104 (2003).

304. Bagby, G. W. Arthrodesis by the distraction-compression method using a stainless steel implant. *Orthopedics* **11**, 931–934 (1988).

305. Hayes, J. S. & Richards, R. G. The use of titanium and stainless steel in fracture fixation. *Expert review of medical devices* **7**, 843–853 (2010).

306. ISO, D. 5832-12: 2019-02 Implants for Surgery—Metallic Materials—Part 12: Wrought Cobalt-Chromium-Molybdenum Alloy. (2019).

307. Al-Mulhim, F. A., Baragbah, M. A., Sadat-Ali, M., Alomran, A. S. & Azam, M. Q. Prevalence of surgical site infection in orthopedic surgery: a 5-year analysis. *Int. Surg.* **99**, 264–268 (2014).

308. Rodríguez-Merchán, E. C., Davidson, D. J. & Liddle, A. D. Recent strategies to combat infections from biofilm-forming bacteria on orthopaedic implants. *International Journal of Molecular Sciences* **22**, 10243 (2021).

309. Zhang, E. *et al.* Antibacterial metals and alloys for potential biomedical implants. *Bioactive materials* **6**, 2569–2612 (2021).

310. Knobben, B. A. S., Van Horn, J. R., Van der Mei, H. C. & Busscher, H. J. Evaluation of measures to decrease intra-operative bacterial contamination in orthopaedic implant surgery. *J. Hosp. Infect.* **62**, 174–180 (2006).

311. Blawert, C., Dietzel, W., Ghali, E. & Song, G. Anodizing treatments for magnesium alloys and their effect on corrosion resistance in various environments. *Advanced Engineering Materials* **8**, 511–533 (2006).

312. Sahir Arıkan, M. A. & Balkan, T. Process modeling, simulation, and paint thickness measurement for robotic spray painting. *J. Robot. Syst.* **17**, 479–494 (2000).

313. Hadavand, B. S., Ataeefard, M. & Bafghi, H. F. Preparation of modified nano ZnO/polyester/TGIC powder coating nanocomposite and evaluation of its antibacterial activity. *Composites Part B: Engineering* **82**, 190–195 (2015).

314. Devaraj, S., Anand, B., Gibbons, M., McDonald, A. & Chandra, S. Thermal spray deposition of aluminum and zinc coatings on thermoplastics. *Surface and Coatings Technology* **399**, 126114 (2020).

315. Grosso, D. How to exploit the full potential of the dip-coating process to better control film formation. *Journal of Materials Chemistry* **21**, 17033–17038 (2011).

316. Yow, H. N., Goikoetxea, M., Goehring, L. & Routh, A. F. Effect of film thickness and particle size on cracking stresses in drying latex films. *J. Colloid Interface Sci.* **352**, 542–548 (2010).

317. McHugh, T. H. & Krochta, J. M. Sorbitol-vs glycerol-plasticized whey protein edible films: integrated oxygen permeability and tensile property evaluation. *J. Agric. Food Chem.* **42**, 841–845 (1994).

318. Meermann, B. & Nischwitz, V. ICP-MS for the analysis at the nanoscale–a tutorial review. *J. Anal. At. Spectrom.* **33**, 1432–1468 (2018).

319. Guinée, J. Handbook on life cycle assessment—operational guide to the ISO standards. *The international journal of life cycle assessment* **6**, 255 (2001).

320. Rodloff, A., Bauer, T., Ewig, S., Kujath, P. & Müller, E. Susceptible, intermediate, and resistant–the intensity of antibiotic action. *Deutsches Ärzteblatt International* **105**, 657 (2008).

321. Singh, G., Joyce, E. M., Beddow, J. & Mason, T. J. Evaluation of antibacterial activity of ZnO nanoparticles coated sonochemically onto textile fabrics. *Journal of microbiology, biotechnology and food sciences* **2**, 106–120 (2012).

322. Plewes, D. B. & Kucharczyk, W. Physics of MRI: a primer. *Journal of magnetic resonance imaging* **35**, 1038–1054 (2012).

323. Knispel, R. R., Thompson, R. T. & Pintar, M. M. Dispersion of proton spin-lattice relaxation in tissues. *Journal of Magnetic Resonance (1969)* **14**, 44–51 (1974).

324. Chavhan, G. B., Babyn, P. S., Thomas, B., Shroff, M. M. & Haacke, E. M. Principles, techniques, and applications of T2*-based MR imaging and its special applications. *Radiographics* **29**, 1433–1449 (2009).

325. Brix, G., Schad, L. R., Deimling, M. & Lorenz, W. J. Fast and precise T1 imaging using a TOMROP sequence. *Magn. Reson. Imaging* **8**, 351–356 (1990).

326. Tanenbaum, L. N. *et al*. Synthetic MRI for clinical neuroimaging: results of the magnetic resonance image compilation (MAGiC) prospective, multicenter, multireader trial. *Am. J. Neuroradiol.* **38**, 1103–1110 (2017).

327. Lauterbur, P. C. Image formation by induced local interactions: examples employing nuclear magnetic resonance. *Nature* **242**, 190–191 (1973).

328. Mansfield, P. & Grannell, P. K. NMR'diffraction'in solids? *Journal of Physics C: solid state physics* **6**, L422 (1973).

329. Stehling, M. K., Turner, R. & Mansfield, P. Echo-planar imaging: magnetic resonance imaging in a fraction of a second. *Science* **254**, 43–50 (1991).

330. Lancaster, J. L. *et al*. Measurement of abdominal fat with T1-weighted MR images. *Journal of Magnetic Resonance Imaging* **1**, 363–369 (1991).

331. Doty, F. D., Entzminger, G., Kulkarni, J., Pamarthy, K. & Staab, J. P. Radio frequency coil technology for small-animal MRI. *NMR in Biomedicine: An International Journal Devoted to the Development and Application of Magnetic Resonance In vivo* **20**, 304–325 (2007).

332. Sundaram, M., McGuire, M. H. & Schajowicz, F. Soft-tissue masses: histologic basis for decreased signal (short T2) on T2-weighted MR images. *Am. J. Roentgenol.* **148**, 1247–1250 (1987).

333. Modic, M. T., Pflanze, W., Feiglin, D. H. & Belhobek, G. Magnetic resonance imaging of musculoskeletal infections. *Radiol. Clin. North Am.* **24**, 247–258 (1986).

334. Palestro, C. J., Love, C. & Miller, T. T. Diagnostic imaging tests and microbial infections. *Cell. Microbiol.* **9**, 2323–2333 (2007).

335. McAlindon, T. E., Watt, I., McCrae, F., Goddard, P. & Dieppe, P. A. Magnetic resonance imaging in osteoarthritis of the knee: correlation with radiographic and scintigraphic findings. *Ann. Rheum. Dis.* **50**, 14–19 (1991).

336. Conturo, T. E., McKinstry, R. C., Aronovitz, J. A. & Neil, J. J. Diffusion MRI: precision, accuracy and flow effects. *NMR Biomed.* **8**, 307–332 (1995).

337. Bammer, R. Basic principles of diffusion-weighted imaging. *Eur. J. Radiol.* **45**, 169–184 (2003).

338. Merboldt, K., Hanicke, W. & Frahm, J. Self-diffusion NMR imaging using stimulated echoes. *Journal of Magnetic Resonance (1969)* **64**, 479–486 (1985).

339. Phoenix, V. R. & Holmes, W. M. Magnetic resonance imaging of structure, diffusivity, and copper immobilization in a phototrophic biofilm. *Appl. Environ. Microbiol.* **74**, 4934–4943 (2008).

340. Manz, B., Volke, F., Goll, D. & Horn, H. Investigation of biofilm structure, flow patterns and detachment with magnetic resonance imaging. *Water science and technology* **52**, 1–6 (2005).

341. Manz, B., Volke, F., Goll, D. & Horn, H. Measuring local flow velocities and biofilm structure in biofilm systems with magnetic resonance imaging (MRI). *Biotechnol. Bioeng.* **84**, 424–432 (2003).

342. Hoskins, B. C., Fevang, L., Majors, P. D., Sharma, M. M. & Georgiou, G. Selective imaging of biofilms in porous media by NMR relaxation. *Journal of Magnetic Resonance* **139**, 67–73 (1999).

343. Chirwa, E. M. & Wang, Y. Hexavalent chromium reduction by Bacillus sp. in a packed-bed bioreactor. *Environ. Sci. Technol.* **31**, 1446–1451 (1997).

344. Gargouri, B., Karray, F., Mhiri, N., Aloui, F. & Sayadi, S. Application of a continuously stirred tank bioreactor (CSTR) for bioremediation of hydrocarbon-rich industrial wastewater effluents. *J. Hazard. Mater.* **189**, 427–434 (2011).

345. Nicolella, C., Van Loosdrecht, M. & Heijnen, J. J. Wastewater treatment with particulate biofilm reactors. *J. Biotechnol.* **80**, 1–33 (2000).

346. Shieh, W. K. & Keenan, J. D. in *Bioproducts* 131–169 (Springer, 2005).

347. Metzger, U., Lankes, U., Hardy, E. H., Gordalla, B. C. & Frimmel, F. H. Monitoring the formation of an Aureobasidium pullulans biofilm in a bead-packed reactor via flow-weighted magnetic resonance imaging. *Biotechnol. Lett.* **28**, 1305–1311 (2006).

348. Nott, K. P., Heese, F. P., Hall, L. D., Macaskie, L. E. & Paterson-Beedle, M. Measurement of flow field in biofilm reactors by 3-D magnetic resonance imaging. *AIChE J.* **51**, 3072–3079 (2005).

349. Li, A. E. *et al*. Total knee arthroplasty: diagnostic accuracy of patterns of synovitis at MR imaging. *Radiology* **281**, 499–506 (2016).

350. Heidari, A. E. *et al*. Visualizing biofilm formation in endotracheal tubes using endoscopic three-dimensional optical coherence tomography. *J. Biomed. Opt.* **20**, 126010 (2015).

351. Aumann, S., Donner, S., Fischer, J. & Müller, F. Optical coherence tomography (OCT): principle and technical realization. *High resolution imaging in microscopy and ophthalmology: new frontiers in biomedical optics*, 59–85 (2019).

352. Fortunato, L. & Leiknes, T. In-situ biofouling assessment in spacer filled channels using optical coherence tomography (OCT): 3D biofilm thickness mapping. *Bioresour. Technol.* **229**, 231–235 (2017).

353. Rasmussen, K., Reilly, C., Li, Y. & Jones, R. S. Real-time imaging of anti-biofilm effects using CP-OCT. *Biotechnol. Bioeng.* **113**, 198–205 (2016).

354. Daddi Oubekka, S., Briandet, R., Fontaine-Aupart, M. & Steenkeste, K. Correlative time-resolved fluorescence microscopy to assess antibiotic diffusion-reaction in biofilms. *Antimicrob. Agents Chemother.* **56**, 3349–3358 (2012).

355. Schlafer, S. & Meyer, R. L. Confocal microscopy imaging of the biofilm matrix. *J. Microbiol. Methods* **138**, 50–59 (2017).

356. Netuschil, L., Auschill, T. M., Sculean, A. & Arweiler, N. B. Confusion over live/dead stainings for the detection of vital microorganisms in oral biofilms-which stain is suitable? *BMC oral health* **14**, 1–12 (2014).

357. Niehaus, W. L. *et al*. Development of X-ray micro-focus computed tomography to image and quantify biofilms in central venous catheter models in vitro. *Microbiology* **162**, 1629–1640 (2016).

358. Dao, A. *et al*. Murine models of orthopedic infection featuring Staphylococcus aureus biofilm. *Journal of Bone and Joint Infection* **8**, 81–89 (2023).

359. Gangi, S. *et al*. Time interval between abnormalities seen on CT and the clinical diagnosis of pancreatic cancer: retrospective review of CT scans obtained before diagnosis. *Am. J. Roentgenol.* **182**, 897–903 (2004).

360. Duncan, C. F., Youngstein, T., Kirrane, M. D. & Lonsdale, D. O. Diagnostic challenges in sepsis. *Curr. Infect. Dis. Rep.* **23**, 1–14 (2021).

361. Lusic, H. & Grinstaff, M. W. X-ray-computed tomography contrast agents. *Chem. Rev.* **113**, 1641–1666 (2013).

362. Kurmoo, Y. *et al*. Real time monitoring of biofilm formation on coated medical devices for the reduction and interception of bacterial infections. *Biomaterials science* **8**, 1464–1477 (2020).

363. Lemire, J. A., Harrison, J. J. & Turner, R. J. Antimicrobial activity of metals: mechanisms, molecular targets and applications. *Nature Reviews Microbiology* **11**, 371–384 (2013).

364. Cave, G. Spinning disc reactor with concave reactor bed. *Reactor* (2021).

365. Ceri, H. *et al*. The Calgary Biofilm Device: new technology for rapid determination of antibiotic susceptibilities of bacterial biofilms. *J. Clin. Microbiol.* **37**, 1771–1776 (1999).

366. Schneider, C. A., Rasband, W. S. & Eliceiri, K. W. NIH Image to ImageJ: 25 years of image analysis. *Nature methods* **9**, 671–675 (2012).

367. Liu, Y., Kuo, H., Lai, C. & Chou, C. Single amino acid utilization for bacterial categorization. *Scientific Reports* **10**, 12686 (2020).

368. Halliwell, C. M. & Cass, A. E. A factorial analysis of silanization conditions for the immobilization of oligonucleotides on glass surfaces. *Anal. Chem.* **73**, 2476–2483 (2001).

369. Attarilar, S. *et al*. The toxicity phenomenon and the related occurrence in metal and metal oxide nanoparticles: a brief review from the biomedical perspective. *Frontiers in bioengineering and biotechnology* **8**, 822 (2020).

370. Hejazy, M., Koohi, M. K., Bassiri Mohamad Pour, A. & Najafi, D. Toxicity of manufactured copper nanoparticles-A review. *Nanomedicine Research Journal* **3**, 1–9 (2018).

371. Standard, I. Biological evaluation of medical devices—Part 5: Tests for in vitro cytotoxicity. *Geneve, Switzerland: International Organization for Standardization* (2009).

372. https://eur-lex.europa.eu/legal-content/EN/TXT/PDF/?uri=CELEX:32011H0696.

373. Einstein, A. in *Investigations on the Theory of the Brownian Movement* (Courier Corporation, 1956).

374. Chakraborty, A., Boer, J. C., Selomulya, C. & Plebanski, M. Amino acid functionalized inorganic nanoparticles as cutting-edge therapeutic and diagnostic agents. *Bioconjug. Chem.* **29**, 657–671 (2017).

375. Ebrahiminezhad, A., Ghasemi, Y., Rasoul-Amini, S., Barar, J. & Davaran, S. Impact of amino-acid coating on the synthesis and characteristics of iron-oxide nanoparticles (IONs). *Bulletin of the Korean Chemical Society* **33**, 3957–3962 (2012).

376. Inbaraj, B. S. *et al*. The synthesis and characterization of poly (γ-glutamic acid)-coated magnetite nanoparticles and their effects on antibacterial activity and cytotoxicity. *Nanotechnology* **22**, 075101 (2011).

377. Kumar, R., Inbaraj, B. S. & Chen, B. H. Surface modification of superparamagnetic iron nanoparticles with calcium salt of poly (γ-glutamic acid) as coating material. *Mater. Res. Bull.* **45**, 1603–1607 (2010).

378. Parekh, Z. R. *et al*. CuO nanoparticles–synthesis by wet precipitation technique and its characterization. *Physica B: Condensed Matter* **610**, 412950 (2021).

379. Sagadevan, S., Pal, K. & Chowdhury, Z. Z. Fabrication of CuO nanoparticles for structural, optical and dielectric analysis using chemical precipitation method. *J. Mater. Sci. : Mater. Electron.* **28**, 12591–12597 (2017).

380. Ananth, A., Dharaneedharan, S., Heo, M. & Mok, Y. S. Copper oxide nanomaterials: Synthesis, characterization and structure-specific antibacterial performance. *Chem. Eng. J.* **262**, 179–188 (2015).

381. Chang, M., Liu, H. & Tai, C. Y. Preparation of copper oxide nanoparticles and its application in nanofluid. *Powder Technol* **207**, 378–386 (2011).

382. Lanje, A. S., Sharma, S. J., Pode, R. B. & Ningthoujam, R. S. Synthesis and optical characterization of copper oxide nanoparticles. *Adv Appl Sci Res* **1**, 36–40 (2010).

383. Wu, J. *et al*. Inkjet-printed microelectrodes on PDMS as biosensors for functionalized microfluidic systems. *Lab on a Chip* **15**, 690–695 (2015).

384. Melnyk, I. V. *et al*. Protection of thiol groups on the surface of magnetic adsorbents and their application for wastewater treatment. *Scientific Reports* **8**, 8592 (2018).

385. Scriven, L. E. Physics and applications of dip coating and spin coating. *MRS Online Proceedings Library (OPL)* **121**, 717 (1988).

386. Gurav, A. B. *et al*. Superhydrophobic coatings prepared from methyl-modified silica particles using simple dip-coating method. *Ceram. Int.* **41**, 3017–3023 (2015).

387. Laurent, S. & Mahmoudi, M. Superparamagnetic iron oxide nanoparticles: promises for diagnosis and treatment of cancer. *International journal of molecular epidemiology and genetics* **2**, 367 (2011).

388. Shalev, T., Gopin, A., Bauer, M., Stark, R. W. & Rahimipour, S. Non-leaching antimicrobial surfaces through polydopamine bio-inspired coating of quaternary ammonium salts or an ultrashort antimicrobial lipopeptide. *Journal of Materials Chemistry* **22**, 2026–2032 (2012).

389. Egbuna, C. *et al*. Toxicity of nanoparticles in biomedical application: nanotoxicology. *Journal of Toxicology* **2021**, 1–21 (2021).

390. He, F. *et al*. Rapid removal of Hg (II) from aqueous solutions using thiol-functionalized Zn-doped biomagnetite particles. *ACS applied materials & interfaces* **4**, 4373–4379 (2012).

391. Košak, A., Lobnik, A. & Bauman, M. Adsorption of mercury (II), lead (II), cadmium (II) and zinc (II) from aqueous solutions using mercapto-modified silica particles. *International Journal of Applied Ceramic Technology* **12**, 461–472 (2015).

392. Gaetke, L. M. & Chow, C. K. Copper toxicity, oxidative stress, and antioxidant nutrients. *Toxicology* **189**, 147–163 (2003).

393. Uriu-Adams, J. Y. & Keen, C. L. Copper, oxidative stress, and human health. *Mol. Aspects Med.* **26**, 268–298 (2005).

394. https://www.gelest.com/wp-content/uploads/product_msds/SIM6476.0-msds.pdf.

395. Melnyk, I. V. *et al*. Protection of thiol groups on the surface of magnetic adsorbents and their application for wastewater treatment. *Scientific Reports* **8**, 8592 (2018).

396. Luo, X. *et al*. Preparation and physical properties of functionalized graphene/waterborne polyurethane UV-curing composites by click chemistry. *Polym. Int.* **65**, 415–422 (2016).

397. Darouiche, R. O. Antimicrobial approaches for preventing infections associated with surgical implants. *Clinical infectious diseases* **36**, 1284–1289 (2003).

398. Sunderland, I. R., Edwards, G., Mainprize, J. & Antonyshyn, O. A technique for intraoperative creation of patient-specific titanium mesh implants. *Plastic Surgery* **23**, 95–99 (2015).

399. Murray, C. J. *et al*. Global burden of bacterial antimicrobial resistance in 2019: a systematic analysis. *The Lancet* **399**, 629–655 (2022).

400. Béahdy, J. Recent developments of antibiotic research and classification of antibiotics according to chemical structure. *Adv. Appl. Microbiol.* **18**, 309–406 (1974).

401. Rabiei, H., Torshabi, M., Montazer, M., Khaloo, S. S. & Dehghan, S. F. Antimicrobial activity and cytotoxicity of cotton-polyester fabric coated with a metal–organic framework and metal oxide nanoparticle. *Applied Nanoscience*, 1–12 (2023).

402. Towe, M. *et al*. Impact of antimicrobial dipping solutions on postoperative infection rates in patients with diabetes undergoing primary insertion of a coloplast titan inflatable penile prosthesis. *The Journal of Sexual Medicine* **17**, 2077–2083 (2020).

403. Wong, L. & Sissions, C. H. A comparison of human dental plaque microcosm biofilms grown in an undefined medium and a chemically defined artificial saliva. *Arch. Oral Biol.* **46**, 477–486 (2001).

404. Ackermann, T. & Tardito, S. Cell culture medium formulation and its implications in cancer metabolism. *Trends in cancer* **5**, 329–332 (2019).

405. Vande Voorde, J. *et al*. Improving the metabolic fidelity of cancer models with a physiological cell culture medium. *Science advances* **5**, eaau7314 (2019).

406. Pendleton, J. N., Gorman, S. P. & Gilmore, B. F. Clinical relevance of the ESKAPE pathogens. *Expert review of anti-infective therapy* **11**, 297–308 (2013).

407. Otto, M. Staphylococcus epidermidis—the'accidental'pathogen. *Nature reviews microbiology* **7**, 555–567 (2009).

408. Carrasco, E., Morales-Rueda, A. & García-Gimeno, R. M. Cross-contamination and recontamination by Salmonella in foods: A review. *Food Res. Int.* **45**, 545–556 (2012).

409. Larsson, D. G. & Flach, C. Antibiotic resistance in the environment. *Nature Reviews Microbiology* **20**, 257–269 (2022).

410. Appelbaum, P. C. Microbiology of antibiotic resistance in Staphylococcus aureus. *Clinical infectious diseases* **45**, S165–S170 (2007).

411. Davies, T. J. *et al*. Reconciling the potentially irreconcilable? Genotypic and phenotypic amoxicillin-clavulanate resistance in Escherichia coli. *Antimicrob. Agents Chemother.* **64**, 10.1128/aac. 02026–19 (2020).

412. Poole, K. At the nexus of antibiotics and metals: the impact of Cu and Zn on antibiotic activity and resistance. *Trends Microbiol.* **25**, 820–832 (2017).

413. Bonnet, M., Lagier, J. C., Raoult, D. & Khelaifia, S. Bacterial culture through selective and non-selective conditions: the evolution of culture media in clinical microbiology. *New microbes and new infections* **34**, 100622 (2020).

414. Campbell, J. High-throughput assessment of bacterial growth inhibition by optical density measurements. *Current protocols in chemical biology* **2**, 195–208 (2010).

415. Wiegand, I., Hilpert, K. & Hancock, R. E. Agar and broth dilution methods to determine the minimal inhibitory concentration (MIC) of antimicrobial substances. *Nature protocols* **3**, 163–175 (2008).

416. Rajivgandhi, G. *et al*. Biologically synthesized copper oxide nanoparticles enhanced intracellular damage in ciprofloxacin resistant ESBL producing bacteria. *Microb. Pathog.* **127**, 267–276 (2019).

417. Jadhav, S., Gaikwad, S., Nimse, M. & Rajbhoj, A. Copper oxide nanoparticles: synthesis, characterization and their antibacterial activity. *Journal of cluster science* **22**, 121–129 (2011).

418. Ceri, H. *et al*. in *Methods in enzymology* 377–385 (Elsevier, 2001).

419. Berra, L. *et al*. Endotracheal tubes coated with antiseptics decrease bacterial colonization of the ventilator circuits, lungs, and endotracheal tube. *The Journal of the American Society of Anesthesiologists* **100**, 1446–1456 (2004).

420. Cunliffe, A. J. *et al*. How do we determine the efficacy of an antibacterial surface? A review of standardised antibacterial material testing methods. *Antibiotics* **10**, 1069 (2021).

421. Geetha, M., Singh, A. K., Asokamani, R. & Gogia, A. K. Ti based biomaterials, the ultimate choice for orthopaedic implants–A review. *Progress in materials science* **54**, 397–425 (2009).

422. Zhuang, Y., Zhang, S., Yang, K., Ren, L. & Dai, K. Antibacterial activity of copper-bearing 316L stainless steel for the prevention of implant-related infection. *Journal of Biomedical Materials Research Part B: Applied Biomaterials* **108**, 484–495 (2020).

423. Seil, J. T. & Webster, T. J. Reduced Staphylococcus aureus proliferation and biofilm formation on zinc oxide nanoparticle PVC composite surfaces. *Acta Biomaterialia* **7**, 2579–2584 (2011).

424. Xi, W. *et al*. Point-of-care antimicrobial coating protects orthopaedic implants from bacterial challenge. *Nature communications* **12**, 5473 (2021).

425. Ehuwa, O., Jaiswal, A. K. & Jaiswal, S. Salmonella, food safety and food handling practices. *Foods* **10**, 907 (2021).

426. Jones, R. N. Microbial etiologies of hospital-acquired bacterial pneumonia and ventilator-associated bacterial pneumonia. *Clinical infectious diseases* **51**, S81–S87 (2010).

427. Acheson, D. & Hohmann, E. L. Nontyphoidal salmonellosis. *Clinical infectious diseases* **32**, 263–269 (2001).

428. Kojic, E. M. & Darouiche, R. O. Candida infections of medical devices. *Clin. Microbiol. Rev.* **17**, 255–267 (2004).

429. Caizán-Juanarena, L. *et al*. 3D biofilm visualization and quantification on granular bioanodes with magnetic resonance imaging. *Water Res.* **167**, 115059 (2019).

430. Buxton, R. B., Edelman, R. R., Rosen, B. R., Wismer, G. L. & Brady, T. J. Contrast in rapid MR imaging: T1-and T2-weighted imaging. *J. Comput. Assist. Tomogr.* **11**, 7–16 (1987).

431. Palama, T. L. *et al*. Identification of bacterial species by untargeted NMR spectroscopy of the exo-metabolome. *Analyst* **141**, 4558–4561 (2016).

432. Herrling, M. P., Lackner, S., Nirschl, H., Horn, H. & Guthausen, G. Recent NMR/MRI studies of biofilm structures and dynamics. *Annual Reports on NMR Spectroscopy* **97**, 163–213 (2019).

433. Prakkamakul, S. *et al*. Ultrafast brain MRI: clinical deployment and comparison to conventional brain MRI at 3T. *Journal of Neuroimaging* **26**, 503–510 (2016).

434. https://samples-for-schools.co.uk/product/pig-pluck/.

435. Codd, S. L. *et al*. NMR relaxation measurements of biofouling in model and geological porous media. *Org. Geochem.* **42**, 965–971 (2011).

436. Gupta, A., Dwivedi, M., Mahdi, A. A., Khetrapal, C. L. & Bhandari, M. Broad identification of bacterial type in urinary tract infection using 1H NMR spectroscopy. *Journal of proteome research* **11**, 1844–1854 (2012).

437. Manz, B., Volke, F., Goll, D. & Horn, H. Measuring local flow velocities and biofilm structure in biofilm systems with magnetic resonance imaging (MRI). *Biotechnol. Bioeng.* **84**, 424–432 (2003).

438. Hotchkiss, R. S. *et al*. Sepsis and septic shock. *Nature reviews Disease primers* **2**, 1–21 (2016).

439. Pinter, M. D., Harter, T., McCarthy, M. J. & Augustine, M. P. Towards using NMR to screen for spoiled tomatoes stored in 1,000 L, aseptically sealed, metal-lined totes. *Sensors* **14**, 4167–4176 (2014).

440. Arnold, S. R. & Straus, S. E. Interventions to improve antibiotic prescribing practices in ambulatory care. *Cochrane database of systematic reviews* (2005).

441. Morris, R. H. et al. *Long term monitoring of constructed wetlands using an NMR sensor* (SENSORS, 2009 IEEE, IEEE, 2009).

442. Kurmoo, Y. *et al*. Real time monitoring of biofilm formation on coated medical devices for the reduction and interception of bacterial infections. *Biomaterials science* **8**, 1464–1477 (2020).

443. Neut, D., van Horn, J. R., van Kooten, T. G., van der Mei, H. C. & Busscher, H. J. Detection of biomaterial-associated infections in orthopaedic joint implants. *Clinical Orthopaedics and Related Research®* **413**, 261–268 (2003).

444. Safdar, N., Crnich, C. J. & Maki, D. G. The pathogenesis of ventilator-associated pneumonia: its relevance to developing effective strategies for prevention. *Respir. Care* **50**, 725–741 (2005).

445. Byun, I., Coleman, A. W. & Kim, B. Transfer of thin Au films to polydimethylsiloxane (PDMS) with reliable bonding using (3-mercaptopropyl) trimethoxysilane (MPTMS) as a molecular adhesive. *J Micromech Microengineering* **23**, 085016 (2013).

446. Stawicka, K., Gierada, M., Gajewska, J., Tielens, F. & Ziolek, M. The importance of residual water for the reactivity of MPTMS with silica on the example of SBA-15. *Appl. Surf. Sci.* **513**, 145802 (2020).

447. Varney, A. M., Mannix-Fisher, E., Thomas, J. C. & McLean, S. Evaluation of phenotypic and genotypic methods for the identification and characterisation of bacterial isolates recovered from catheter-associated urinary tract infections. *bioRxiv*, 2023.12. 11.571106 (2023).

448. Bondarczuk, K. & Piotrowska-Seget, Z. Molecular basis of active copper resistance mechanisms in Gram-negative bacteria. *Cell Biol. Toxicol.* **29**, 397–405 (2013).

449. Luna, I. Z. *et al*. Preparation and characterization of copper oxide nanoparticles synthesized via chemical precipitation method. *Open Access Library Journal* **2**, 1–8 (2015).

450. Petcharoen, K. & Sirivat, A. Synthesis and characterization of magnetite nanoparticles via the chemical co-precipitation method. *Materials Science and Engineering: B* **177**, 421–427 (2012).

451. Rock, J. R., Randell, S. H. & Hogan, B. L. Airway basal stem cells: a perspective on their roles in epithelial homeostasis and remodeling. *Disease models & mechanisms* **3**, 545–556 (2010).

452. Alarifi, S., Ali, D., Verma, A., Alakhtani, S. & Ali, B. A. Cytotoxicity and genotoxicity of copper oxide nanoparticles in human skin keratinocytes cells. *Int. J. Toxicol.* **32**, 296–307 (2013).

453. Baunoch, D. *et al*. Concordance between antibiotic resistance genes and susceptibility in symptomatic urinary tract infections. *Infection and drug resistance*, 3275–3286 (2021).

454. Viñes, J. *et al*. Concordance between antimicrobial resistance phenotype and genotype of Staphylococcus pseudintermedius from healthy dogs. *Antibiotics* **11**, 1625 (2022).

455. Hammond, A. A. *et al*. An in vitro biofilm model to examine the effect of antibiotic ointments on biofilms produced by burn wound bacterial isolates. *Burns* **37**, 312–321 (2011).

456. Arendsen, L. P., Thakar, R. & Sultan, A. H. The use of copper as an antimicrobial agent in health care, including obstetrics and gynecology. *Clin. Microbiol. Rev.* **32**, 10.1128/cmr. 00125–18 (2019).

457. Gonçalves, R. A. *et al.* Copper-nanoparticle-coated fabrics for rapid and sustained antibacterial activity applications. *ACS Applied Nano Materials* **5**, 12876–12886 (2022).

458. Greenman, R. L. &Mulkern, R. V. *Fast T1 Mapping Using a CPMG Sequence* (Proc. Intl. Soc. Mag. Reson. Med Ser. 17, 2009).

459. Bydder, G. M., Hajnal, J. V. & Young, I. R. MRI: use of the inversion recovery pulse sequence. *Clin. Radiol.* **53**, 159–176 (1998).

460. Lunney, J. K. *et al.* Importance of the pig as a human biomedical model. *Science translational medicine* **13**, eabd5758 (2021).

461. Zhang, B. & Powers, R. Analysis of bacterial biofilms using NMR-based metabolomics. *Future medicinal chemistry* **4**, 1273–1306 (2012).

462. Ranzinger, F., Schröter, K., Horn, H. & Wagner, M. Investigation of Biofilm Growth within a Monodisperse Porous Medium under Fluctuating Water Level Assessed by Means of MRI. *Water* **13**, 2456 (2021).

463. Liu, S. *et al.* Understanding, monitoring, and controlling biofilm growth in drinking water distribution systems. *Environ. Sci. Technol.* **50**, 8954–8976 (2016).

464. Van de Vyver, H. *et al.* A novel mouse model of Staphylococcus aureus vascular graft infection: noninvasive imaging of biofilm development in vivo. *The American Journal of Pathology* **187**, 268–279 (2017).

465. Grainger, D. W. *et al.* Critical factors in the translation of improved antimicrobial strategies for medical implants and devices. *Biomaterials* **34**, 9237–9243 (2013).

7. Appendix

Antipathogenic applications of copper nanoparticles in air filtration systems

Subbareddy Mekapothula [1], **Elvina Chrysanthou** [1], **James Hall** [1], **Phani Durga Nekkalapudi** [1], **Samantha McLean** [1], **and Gareth W. V. Cave** [1,*]

[1] School of Science and Technology, Nottingham Trent University, Clifton Lane, Nottingham NG11 8NS, UK

[*] Correspondence: gareth.cave@ntu.ac.uk; Tel.: +44 115 848 3242

Abstract:

The COVID-19 pandemic has underscored the critical need for effective air filtration systems in healthcare environments to mitigate the spread of viral and bacterial pathogens. This study explores the utilization of copper nanoparticle-coated materials for air filtration, offering both antiviral and antimicrobial properties. Highly uniform spherical copper oxide nanoparticles (~10 nm) were synthesized via a spinning disc reactor, and subsequently functionalized with carboxylated ligands, to ensure colloidal stability in aqueous solutions. The functionalized copper oxide nanoparticles were applied as antipathogenic coatings on extruded polyethylene and melt-blown polypropylene fibers to assess their efficacy in air filtration applications. Notably, Type IIR medical facemasks, incorporating the copper nanoparticle-coated polyethylene fibers, demonstrated a >90% reduction in influenza virus and SARS-CoV-2 within 2 hours of exposure. Similarly, heating, ventilation, and air conditioning (HVAC) filtration pre (polyester) and post (polypropylene) filtration media, were fictionalised with the copper nanoparticles and exhibited a 99% reduction in various viral and bacterial strains, including SARS-CoV-2, *Pseudomonas aeruginosa*, *Acinetobacter baumannii*, *Salmonella enterica*, and *Escherichia coli*. In both cases this mitigates not only the immediate threat from these pathogens but also the risk of biofouling and secondary risk factors. Assessment of leaching properties confirmed that the copper nanoparticle coatings remained intact on the polymeric fiber surfaces without releasing nanoparticles into solution or airflow. These findings highlight the potential of nanoparticle-coated materials in developing biocompatible and environmentally friendly air filtration systems for healthcare settings, crucial in combating current and future pandemic threats.

Keywords: Copper oxide nanoparticles; nanoparticle coated polymeric fibers; SARS-CoV-2; antiviral activity; antibacterial activity.

Introduction

Airborne pathogen transmission traditionally occurs due to the transmission of droplets, in the respirable size range of ≤ 5 μm, from the respiratory tract of one individual to another individual's mucosal surface or conjunctivae *i.e.* airborne transmission of infectious influenza, *via* breathing, coughing, sneezing, talking, and laughing. Bacterial pathogens present a distinct hazard to patients within healthcare environments, especially those already debilitated by pre-existing conditions, illnesses, or surgical procedures [1]. Utilizing barrier protection methods, such as face masks, can significantly mitigate the transmission of bacterial pathogens. These masks serve a dual purpose: firstly, by impeding the dissemination of pathogens from an infected patient into the surrounding environment, and secondly, by safeguarding vulnerable individuals, such as those afflicted with cystic fibrosis, from exposure to potential pathogens. The transformation of respiratory airborne particles to droplets has significant practical implications for infection control measures in hospital and primary care [2-4].

Human health has been challenged by microbial threats globally, especially in epidemics and pandemics, since the beginning of human existence. Once effective medicines and vaccines increasingly fail due to microbial evolution, the development of personal protective equipment (PPE) as a rapid response to reduce the transmission of infectious diseases is a cornerstone of modern medicine [5-7]. Airborne pathogens present a particular risk, exemplified in recent years by the COVID-19 pandemic. The widespread use of single-use polymeric filtration materials to reduce transmission of infective particles through the air was a major factor in preventing the spread of the pathogen [8-10]. However, significant waste is created with single-use PPE, particularly when used on the scale of a pandemic [11-12]. Moreover, the UK government has estimated the healthcare cost measures of the COVID-19 pandemic at between £310-410 billion in the UK.

Barrier protection with standard air filtration systems (such as face masks, respirators and HVAC) may reduce transmission; however, any filtration that traps the pathogen without killing/inactivating it, only nets the threat and therefore presents a clear risk to anyone in contact with the materials as the virus and bacteria still remains infectious promoting biofouling [13-16]. Biofouling is restricting the efficacy and performance of air filtration membranes *via* self-replicating bacterial growth on filter layers, resulting in biofilm formation, which eventually mechanically blocks the filtration surfaces. Therefore, several applications have been reported to mitigate biofouling and provide antipathogenic properties *via* incorporation and immobilization of naturally occurring metals and their oxides, such as silver, copper and zinc oxides, on polymeric air filter membranes [17-226, 7].

 The medicinal properties of copper are well established and have been demonstrated since the ancient Egyptians [23-26]. Current applications of copper include touch surfaces such as bed frames and door handles due to copper oxide having unique electrical properties, allowing biomedical and antipathogenic properties [27-31]. Copper and both its oxides were investigated during both Swine flu (H1N1) and Bird flu (H5N1) outbreaks and have more

recently been used to combat the SARS-CoV-2 pandemic [32,33]. Generally, copper oxides hold a beneficial price/performance ratio, making it the principal antifoulant oxide against both Gram-positive and Gram-negative bacteria. Also, the insoluble and high hydrophobic nature of copper ions allows it to easily precipitate and accumulate on filtering materials. These oxide nanoparticles also provide high surface areas, improving the antifouling efficacy, while minimizing the environmental influence due to exposing higher contact sites and lower copper ions release [34].

The functionalization of CuO NPs on the surface of polymeric fibers has demonstrated remarkable outcomes in inhibiting the growth of a wide range of microorganisms and significant applications in areas like food packaging, medical instruments, and water treatment. Copper/polymer fibers exhibit bactericidal properties, primarily due to their capacity to release metal ions in an aqueous environment. These ions facilitate electrostatic interactions with the negatively charged bacterial cell walls, leading to their disruption and eventual rupture. Consequently, intracellular material leaks out, resulting in cell death. The process of metal ion release from the composites begins with water diffusing into the composite bulk. Subsequently, the reaction between metallic particles and water molecules generates metal ions. Finally, the migration of these ions to the composite's external surface enables interaction with bacteria [35].

The characteristics of the polymeric matrix, such as crystallinity and hydrophobic behavior, can affect the composite's ability to release metal ions. Damm et al. suggested that water molecule and metal ion diffusion primarily occur in the amorphous regions of the polymer matrix. Therefore, enhancing the hydrophilicity and reducing the crystallinity of the polymer matrix could enhance ion release [36].

However, a common issue encountered in composite materials produced via melt mixing is the inadequate dispersion of nanoparticles (NPs) within the polymeric matrix. NP aggregation in the matrix is linked to its high surface energy. Typically, the formation of large NP aggregates leads to a decline in the mechanical, thermal, and antimicrobial properties of the composite [37].

Herein, we report the synthesis of highly uniform copper oxide nanoparticles (~10 nm) by a chemical precipitation method using a high throughput continuous flow spinning disc reactor, functionalized *via* carboxylated ligands in the form of an amino acids, resulting in colloidally stable aqueous suspensions. Subsequently, the solution was applied as a surface-bound nanoparticle coating to polyethylene and polypropylene air filtration media to evaluate their applied antiviral and antibacterial applications.

Materials and Methods

All chemicals and solvents purchased as a reagent grade, ICP-MS grade and used without further purification. Spinning Disc Reactor used for synthesis of copper oxide nano particles. Inductive Coupled Plasma-Mass Spectrometry (ICP-MS) was used to elemental analysis of copper oxide nano particles. Emission Scanning Electron Microscope (SEM) for structural morphology of copper oxide nano particles and SEM-EDX used to determine the loading of copper on filter media. Transmission Electron Microscope (TEM) for size of copper oxide nano particles. Cell Culture. Bacterial stocks of *Pseudomonas aeruginosa*, strain identifier: 21Y000035 and *Escherichia coli* Strain identifier 21Y000039 were purchased from QMC pathogen bank. Strain PS_Acine9, *Acinetobacter baumannii* was used with the permission of Lesley Hoyles, Nottingham Trent University. The study of this anonymized isolate for use in non-commercial research beyond the diagnostic requirement was approved by an NHS research ethics committee (number 06/Q0406/20).

Aqueous solutions of copper (II) chloride (0.1 M, 2.5 L) and sodium hydroxide (0.1 M, 2.5 L) were prepared. The solutions were subsequently pumped (60 mL/min) into the center of a spinning disc reactor (1500 RPM, 60 °C) where they reacted on the rotating disc (15 cm dimeter) to spontaneously form CuO nanoparticles (9.1 ± 1.9 nm dimeter). The product was collected and filtered against gravity using a sintered glass funnel (porosity grade 3). The filter cake was then dried in an oven (*ca*. 3 h, 120 °C) after washing with deionized water (3x250 mL). Copper oxide nanoparticles (50 g, 1 eq.) and *L*-lysine monohydrochloride (50 g, 1 eq.) were ground using a mechanochemical extruder and stored in an airtight container under nitrogen until further use [38,41]. Subsequently, lysine-coated copper oxide nanoparticles were characterized by scanning electron microscopy (SEM, JEOL, JSM-7100f, Tokyo, Japan), transmission electron microscopy (TEM, JEM-2100, Joel, Japan), powder X-ray diffraction (XRD, Rigaku Co. Ltd., Tokyo, Japan), dynamic light scattering (DLS, Malvern, UK), thermogravimetric analysis (TGA, PerkinElmer, TGA 4000) and Fourier transform infrared spectroscopy (FTIR, PerkinElmer Spectrum Two IR, UK). The 4-Ply CNC-PE masks are composed of an inner hypoallergic layer combined with a melt-blown filter (MEDIsyntex media, Volz Luftfilter GmbH & Co), the CNC-PE anti-viral fiber layer and the fluid-repellent outer layer (Texsus material, Shalag Industries Ltd). Furthermore, a lysine-coated copper oxide nanoparticle (10% w/v) solution was used to prepare copper nanoparticle-coated polypropylene fibers (CNC-PP fibers) using spray *via* nebulization while polyethylene fibers (CNC-PE fibers) were synthesized *via* dip coating or extracted *via* a print drum roller. Subsequently, the polymeric filtration media were cured using UV (355 nm) and dried *via* an IR heating lamp (750 nm - 1000 μm). Later, these polymeric air filtration fibers (CNC-PP and CNC-PE) were characterized by scanning electron microscopy - energy dispersive X-ray spectroscopy (SEM-EDS).

The leaching properties of copper from the polymeric fibers were determined according to the modified ISO 17294-2:2023. The leaching properties of copper from the filter textiles were investigated both in solution and airflow *via* inductive-coupled plasma mass spectrometry (PerkinElmer NexION 1000, Waltham, MA, USA). Both CNC-PE and CPC-PP filter fabrics (5cm*5cm) were tested under water (2 mL, 8 mL, and 10 mL separately) over 24 h. to test the copper leaching. Subsequently, airflow leaching studies were performed on both sides of the filter fabrics under constant air flow (10 L min-1 over 7 h) for copper leaching.

Subsequently, the water samples (1 mL) from both solution and airblown fabric fibers were digested with HN03 (70%, 10 mL) for 4 hours and diluted further prior to the ICP-MS elemental analysis using standard calibration (0-1000 ppb) from Certipur® ICP Single-Element standards of Copper and Indium (20 ppb) as internal standard.

All virucidal activity assessments of the CNC-PP and CNC-PE textiles, including dust-treated CNC-PP textile material were investigated against Influenza A/WSN/33 (H1N1) and SARS-CoV-2 viruses relative to non-treated reference controls under standard ISO18184:2019 protocol. African Green Monkey Kidney Epithelial (Vero) cells were used as viral host cells when assessing SARS-CoV-2 and Madin-Darby Canine Kidney (MDCK) cells for Influenza virus assessments. Supplementary material on virus titres and test conditions are provided in Table S3. If not otherwise stated all experimental conditions were performed in triplicate.

Textile squares (20 x 20 mm and 0.4 g) were used for the assessment procedures. The antiviral tests were performed with 200 µL viral inoculum, to completely soak up the assessed test (copper-treated) and reference (non-treated) textiles while these were placed in individual test tubes. The assessed virus was left to incubate at room temperature with the textile for a period of time (2 h or 7 h) as detailed in Table 1 and Table S3 and this time is referred to as contact time. Upon the completion of the incubation time the textiles were thoroughly washed with media several times to recover the virus. TCID50 was then used to calculate the amount of the recovered virus in each of the tested materials.

To determine this, the isolated virus-containing wash media was incubated and assessed using a seven-point, ten-fold serial dilution of the media on host cells in quadruplicate for each sample as mentioned in Table 1 and Table S3. TCID50 was calculated using the Reed and Muench method to quantify the dilution (TCID50), where 50% of the cells are infected/killed using regression analysis. An additional, non-treated reference control (virus recovery control) was obtained by viral incubation on non-treated textiles (ISO18184:2019) with immediate recovery to assess the starting viral concentration and used for Mv calculation.

The antiviral activity (Mv) was calculated using the following formula while an Mv value of $\geqslant 1$ indicates antiviral activity:

$$Mv = Log(Va)-Log(Vc) \tag{1}$$

where Log(Va) is the average of the common logarithm of the number of infectious units recovered from the reference specimens immediately after inoculation and Log(Vc) is the average of the common logarithm of the number of infectious units recovered from the treated test specimens at the end of the incubation time.

For the virucidal activity assessments to be valid, the materials tested should not have any cytotoxic activity on assessed host cells nor affect cell sensitivity to infection. For cytotoxicity controls, media with no textile contact, media with 5 min contact to treated textile, and reference control textile were incubated with host cells for a period of time (Table S3) followed by crystal violet staining to determine cell viability. For sensitivity control tests, media with no textile contact, media with 5 min contact to treated textile, and reference control textile were incubated with the virus, and following incubation time the amount of infectious virus infecting test cells was quantified with TCID50 assay.

Bacterial strains were human clinical isolates from UK hospitals (see Table S4 for details). All bacteriological media and buffers were prepared as per manufacturer's instructions. The touch-killing antibacterial properties of the CNC-PE fibers and CNC-PP fibers were investigated against *Acinetobacter baumannii*, *Pseudomonas aeruginosa*, *Escherichia coli,* and *Salmonella enterica* following ISO20743:2021 with modification. Phosphate buffer saline (PBS, Merch, UK:P4417) was used instead of Polysorbate 80 due to its high viscosity when spun. Stocks of the strains were streaked and incubated (37 °C for 24 h) onto Tryptic soy agar (TSA) plates (Merck, UK: 70191). Tryptic soy broth (TSB, Merck, UK: 70192, 20 mL) was added to an Erlenmeyer flask (100 mL), and one colony from the incubated agar plate was added to the broth and incubated (37 °C for 18 h at 110 RPM). Another Erlenmeyer flask was prepared with TSB (20 mL) and inoculum (0.4 mL) was added from the first flask, which was measured at 1 x 10^8 CFU mL^{-1} and incubated (37 °C for 3 h) at 110 RPM. The inoculum was adjusted to 1 x 10^5 CFU mL^{-1}, preserved on ice and used within 4 h of adjustment (as per ISO20743:2021). Six test samples, three treated and three untreated, were prepared with a mass of (0.4 g) and were sent for autoclave sterilization. Inoculum (200 µL) was pipetted directly to the fabric samples and placed in an incubator (37 °C for 18 h). After incubation, PBS (20 mL) was added to each sample and vortexed (2 min at 1500 RPM) to recover any viable cells after contact with the treated and untreated samples. The recovered inoculum was then spotted out onto agar plates *via* serial dilution to enumerate the viable cells.

3. Results and discussion

3.1 Synthesis and characterization of lysine-copper oxide-coated polymeric air filtration media fibers.

Synthesis of various nanoparticles *via* spinning disc reactors (SDRs) is a well-established technique over co-precipitation methods by allowing control over the reaction time to achieve monodisperse nanoparticles [3913]. SDRs generally consist of a flat spinning reaction surface where reaction materials are applied. Subsequently, the reaction materials travel to the surface to react, and reacted liquid colloids are ejected from the disc's surface. Several methods of nanoparticle fabrication have been reported while aiming to create and control substantially monodisperse materials, such as a uniform and controlled particle size. Even though SDRs are controlled by varying the disc rotation and temperature of the disc, the drawback with these SDRs is limited control over the reaction time. Subsequently, it hinders SDR application when bulk production of nanoparticles is required [38].

To overcome these difficulties, we reported a patented continuous flow process spinning disc reactor that consists of a concave spinning disc along the rotating axis, allowing reactants' residence time over the flat reaction surface. This allows more control of reaction time to achieve monodisperse nanoparticles by choosing the optimal degree of concavity of the surface. These SDRs have scaled up the production of nanoparticles to 2 kg hr^{-1} per disc[40]. Upon scaling up the production of copper oxide nanoparticles *via* SDRs, the nanoparticles were characterized *via* electron microscopy (SEM, TEM), X-ray diffraction, and FTIR techniques. The copper oxide nanoparticles were qualitatively spherical in shape as observed *via* scanning electron microscopy (Figure 1a). Transmission electron microscopy quantified the size of the nanoparticles with an average particle size of ~10 (± 1.9 SD) nm (Figure 1b and c).
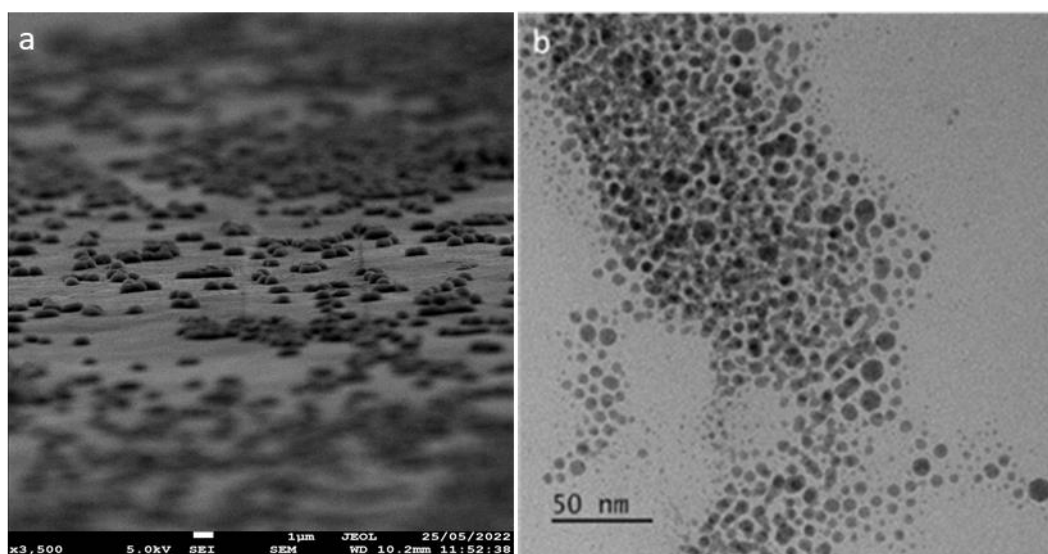
Figure 1. (a) Scanning electron microscopy and (b) transmission electron microscopy characterization of copper oxide nanoparticles.

Powdered XRD analysis determined the phase composition and crystalline structure of copper oxide (CuO) nanoparticles synthesized using a spinning disc reactor. As shown in Figure 2, the XRD 2θ values ranged from 30° to 75°. The large peaks for 2θ values between 35° to 40° correspond to the planes of (002), (-110), (111), and (200), which are in line with the JCPDS card no 00–041-0254. The XRD patterns demonstrated that the nanoparticles were polycrystalline with a monoclinic CuO crystal structure. The other crystal planes (-202), (020), (202), (-113), (022), (-311), (113), (220), and (311) correspond to other important Bragg's reflection peaks. The Zeta potential characterization of copper oxide nanoparticles produced from the spinning disk reactor was found to have a positive surface charge. The hydrodynamic size of the copper oxide nanoparticles was measured to be 78.8 ± 6.4 nm with a polydispersity index of 0.24 (Figure S3).
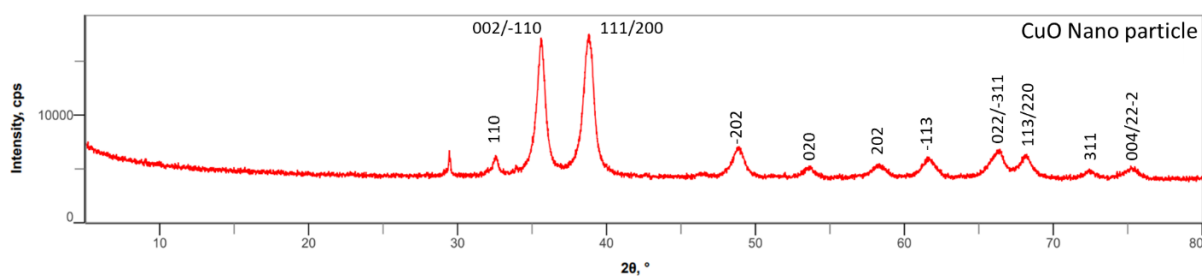
Figure 2. Powder XRD analysis of copper oxide nanoparticles synthesized using SDRs.

The mechanical process facilitates high levels of shear to dry the copper oxide mixture, which subsequently distributes the *L*-lysine-hydrochloride around and among the copper oxide nanoparticles. Copper oxide nanoparticles were coated with amino acid to improve stability and retain a hydrodynamic surface to keep the ions active.

Subsequently, powder XRD analysis confirmed the phase composition of CuO-lysine-coated nanoparticles, as shown in Figure S2, consisting of all planes in line with the 2θ values of lysine and CuO. The planes for L-lysine (020), (011), (021), (-121), (210), (-121), (230), and (151) correspond to the 2θ values in the range of 9° to 75° along with CuO planes. Thermogravimetric analysis (TGA) analysis confirmed that L-lysine-hydrochloride (1:1) w/w was loaded on copper oxide nanoparticles as shown in Figures S4 and S5. The functional group characterization of copper oxide-coated L-lysine nanoparticles was performed *via* FTIR spectroscopy (Agilent, Cary 630 FTIR Spectrometer), as shown in Figure S6. The absorption band at 532 cm^{-1} corresponds to the vibrations of the Cu-O bond, confirming the CuO nanoparticles as shown in Figure S6 (a). In Figure S6 (b), NH$_2$ vibrational stretching frequencies are observed at 3400 cm^{-1}, while characteristic asymmetric and symmetric frequencies of carboxylate are at 1598 cm^{-1} (C=O) and 1418 cm^{-1} (C-O), respectively. This spectroscopic analysis confirms the synthesis of copper oxide nanoparticles and their successful chemosorption of the amino acid *via* electrostatic interactions

Subsequently, these polymeric air filtration fibers (CNC-PP and CNC-PE) were characterized by scanning electron microscopy - energy dispersive X-ray spectroscopy (SEM-EDS) as shown in Figure 3.
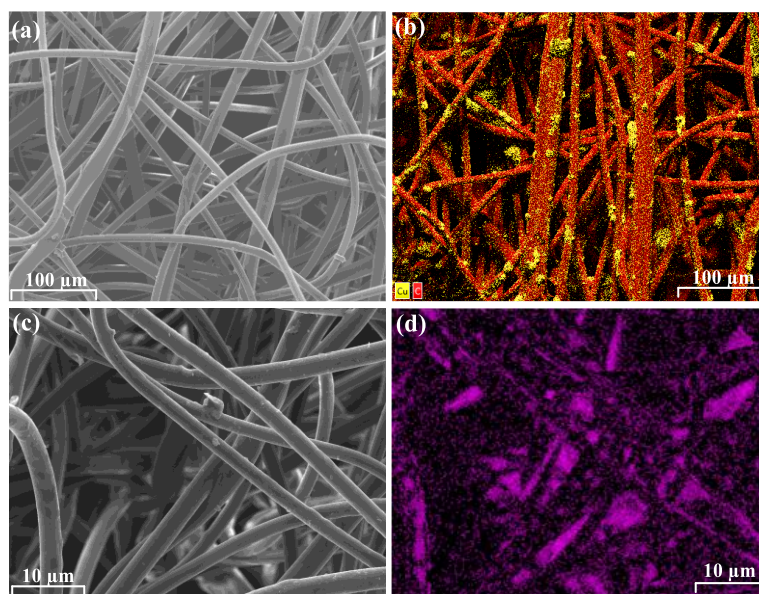

Figure 3. SEM-EDX characterization of CNC-PE fibers (a,b) and CPC-PP fibers (c,d). Copper coating represented in yellow (b) and purple (d) while fibers are represented in red and black respectively.

3.2 Evaluation of copper leaching from polymeric fibers

The leaching properties of copper from the polymeric fibers were performed according to the modified ISO 17294-2:2023 method [42]. The leaching properties of copper from the filter textiles were investigated both in solution and airflow. Both CNC-PE and CPC-PP filter fabrics were tested under water over 24 h to test the copper leaching. ICP-MS (PerkinElmer NexION 1000, Waltham, MA, USA) elemental analysis confirmed that there was no leaching from either of the resultant filter fabrics. Subsequently, airflow leaching studies were performed on both sides of the filter fabrics under constant air flow (10 L min^{-1} over 7 h) for copper leaching. The results of the ICP-MS analysis showed that there was evidence of copper leaching from the CNC-PP filter within the environmental limits while there was no leaching of copper from the CNC-PE filter within the limits of detection.

3.3 Virucidal activity assessments of polymeric fibers

In contrast to the standard antiviral masks, the 4-Ply CNC-PE masks are composed of an inner hypoallergic layer combined with a melt-blown filter (MEDIsyntex media, Volz Luftfilter GmbH & Co), the CNC-PE antiviral fiber layer and the fluid-repellent outer layer (Texsus material, Shalag Industries Ltd), as shown in Figure 4. The external compartment of the mask confers a hydrophobic environment to prevent airborne pathogens/bioaerosol contamination from bodily fluids. The antipathogenic fiber layer consisting copper oxide nanoparticle coated with amino acids improves stability and also retain a hydrodynamic surface to ensure that the ions remain active on the surface. Subsequently, "wet" metallic structure (CuO) interact with the cells and kill the virus or bacteria *via* the emission of ions that travel through the aqueous media. The melt blown filter that been used, prevents over 95% of bacteria and other airborne particulate matter passing the layer, as shown in Figure 4(3). A soft hypoallergenic inner layer incorporated in order to be breathable, removing moisture from the face for extended periods of wearing the masks without causing discomfort and rashes around the face.

The 4-Ply CNC-PE antiviral masks passed all standard test reports for bacterial filtration efficiency (BFE) under EN 14683:2019+AC:2019 Annex B, microbial cleanliness (bioburden) under EN ISO 11737-1:2018, breathability (differential pressure) under EN 14683:2019+AC2019 Annex C, resistance to synthetic blood splashes under ISO 22609:2004 and biocompatibility analytical under EN ISO 10993-10:2013/ ISO 10993-5:2009 tests.

Figure 4. Different layers within the 4-Ply CNC-PE antiviral mask, (1) fluid repellent outer layer, (2) CNC-PE fiber layer, (3) melt blown filter, and (4) soft hypoallergic inner layer.

In validation control tests, the CNC-PP and CNC-PE textile filters showed no interference with the host cells' sensitivity to both of the assessed viruses as per ISO18184:2019 test requirements [43]. When excluding the undiluted recovered media, the treated and non-treated textiles showed no cytotoxicity toward the host cells, allowing the completion of the antiviral activity tests.

Table 1. The average infectious units mL^{-1} recovered from the test and reference control materials in air vent and face masks at a contact time of 2 h or 7 h with the assessed viruses

Virus type	Filter use	Test condition	Virus recovery control (TCID50/sample)	Antiviral test (TCID50/sample)	Contact time	TCID50 (log10)	Mv
Influenza	HVAC	CNC-PP	N/A	$(9.25 \pm 7.91) \times 10^4$	7h	4.97	2.68
		Untreated control	$(4.38 \pm 2.06) \times 10^7$	$(1.71 \pm 1.37) \times 10^7$	7h	7.64	
SARS-CoV-2		CNC-PP	N/A	$(9.84 \pm 4.22) \times 10^3$	2h	3.99	2.60
		Untreated control	$(3.94 \pm 2.01) \times 10^6$	$(4.59 \pm 1.88) \times 10^6$	2h	6.60	
Influenza	Face mask	CNC-PE	N/A	$(1.40 \pm 0.715) \times 10^4$	7h	4.15	1.19
		Untreated control	$(2.17 \pm 0.64) \times 10^5$	$(3.30 \pm 2.80) \times 10^5$	7h	5.34	
SARS-CoV-2		CNC-PE	N/A	$(2.01 \pm 1.22) \times 10^4$	2h	4.30	1.61
		Untreated control	$(8.15 \pm 3.34) \times 10^5$	$(2.01 \pm 1.22) \times 10^5$	2h	5.91	

CNC-PP textile with an Mv value of 2.60, demonstrated a clear 99.8% viral reduction compared to its reference control textile following 2 h contact time with SARS-CoV-2 and a 99.5% (Mv 2.68) viral reduction following 7 h contact time with Influenza virus (Table 1). With an average recovered viral titer of 4.59 x10^4 TCID50/sample, CNC-PP/dust textile appeared with 99%

antiviral activity when compared to 5.59 x10^6 TCID50/sample in reference/dust textile. The resulting Mv of 1.93 still verified the CNC-PP filters' antiviral action against SARS-CoV-2 irrespective of deposited dust particles proving its long-term activity (Table S3, supplementary). Virucidal activity results on CNC-PP dust-treated textiles, indicated no antiviral activity against Influenza A/WSN/33 (H1N1) compared to their reference controls with an Mv value of 0.18. The CNC-PE textile displays virucidal activity following 7 h contact time and 95.8% reduction of the Influenza virus (Mv 1.19) while for SARS-CoV-2 it was greater than 90 % (Mv 1.61) reduced following 2 h contact time compared to its reference controls. The average recovered titers from treated and non-treated textiles are shown in Table 1.

3.4 Antibacterial activity assessment of polymeric fibers

The use of filtration materials in personal protective equipment such as face masks and within filters that control airflow will reduce the transmission of bacterial pathogens, however the organisms still present an infection risk as the pathogens are not killed, making such materials a significant infection risk (44). We therefore tested both filtration media using ISO 20743:2021 methodology [45] for their touch-killing properties to determine whether the copper-lysine nanoparticles were effective antibacterials against clinical pathogens associated with these materials. The bacterial species tested included *P. aeruginosa*, *A. baumannii*, *S. enterica,* and *E. coli* due to their impact on human health.
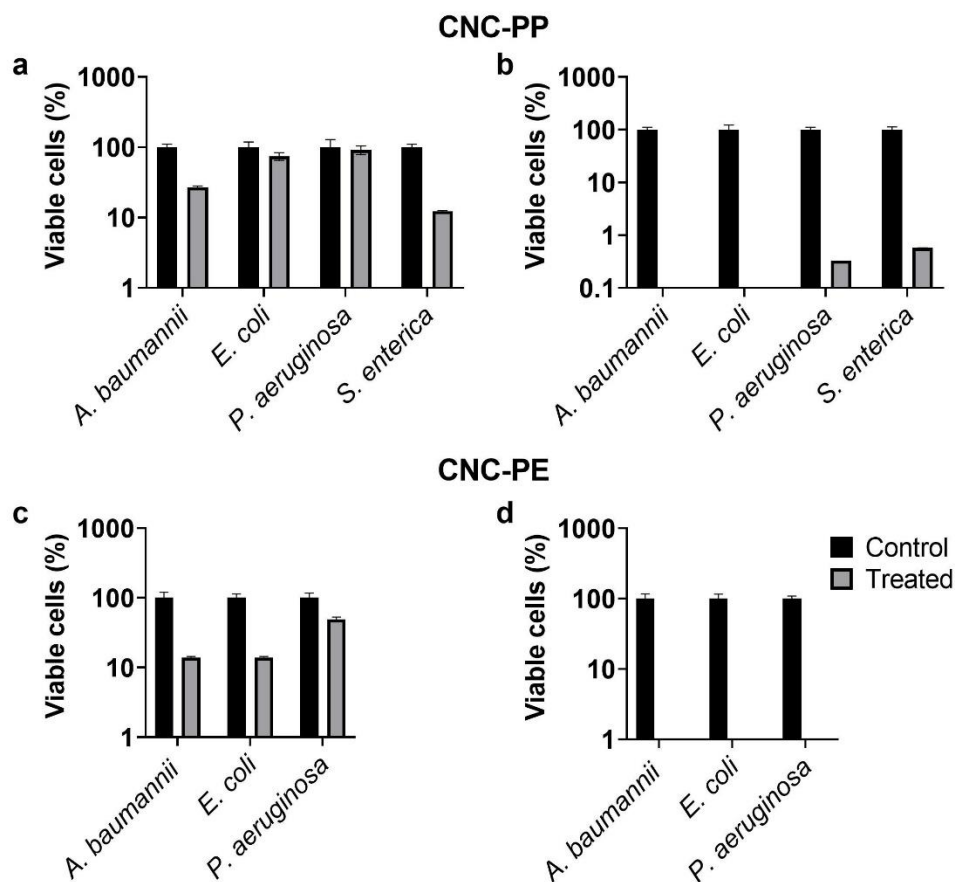
Figure 5. Bacterial cells were exposed to CNC – polypropylene (a and b) or CNC – polyethylene (c and d) at a final concentration of 10^5 CFU mL^{-1} and incubated for 5 min (a and c) or 18 h (b and d) at 37°C. Bacterial cell viability was determined after recovery into PBS. N=9 ±SEM.

A significant touch-killing effect was established on CNC-PP textile against all bacterial pathogens after 18 h contact with treated material, with *A. baumannii* and *E. coli* exhibiting the greatest decrease in viable cells compared to control media (Figure 5a+b). A significant touch-killing effect was also observed after contact with treated CNC-PE, with recovery of viable bacterial cells below the threshold for detection for all pathogens after 18 h contact (Figure 5c+d).

4. Conclusions

A potential scalable route to copper oxide nanoparticles synthesis and functionalization was established for the formulation of a antipathogenic functionalized ink that was successfully applied, *via* there commercially viable processes, to polyethylene (and polypropylene filtration media. The resulting fabrics did not demonstrate any significant leaching of the active coating in both solution and air flow, thereby demonstrating the processes environmental safety. Both polypropylene and polyethylene filters demonstrated significant antibacterial effects, with over 99.9% reduction in bacterial species. The polypropylene filters exhibited sustained virucidal activity against SARS-CoV-2 and Influenza virus over at least 7 h and showing activity during accelerated aging worth of 1 years' filtration. The antipathogenic properties against SARS-CoV-2 remained even after prolonged dust exposure demonstrating the potential effectiveness in commercial HVAC filtration systems and PPE.

References

Yousefimashouf, M.; Yousefimashouf, R.; Alikhani, M.S.; Hashemi, H.; Karami, P.; Rahimi, Z.; Hosseini, S.M. Evaluation of the Bacterial Contamination of Face Masks Worn by Personnel in a

Center of COVID 19 Hospitalized Patients: A Cross-Sectional Study. New Microbes and New Infections **2023**, *52*, 101090.

Jiang, X.; Wang, C.; Guo, J.; Hou, J.; Guo, X.; Zhang, H.; Tan, J.; Li, M.; Li, X.; Zhu, H. Global Meta-Analysis of Airborne Bacterial Communities and Associations with Anthropogenic Activities. *Environmental Science & Technology* **2022**, *56*, 9891-9902.

Fennelly, K.P. Particle Sizes of Infectious Aerosols: Implications for Infection Control. *The Lancet Respiratory Medicine* **2020**, *8*, 914-924.

Hasan, J.; Xu, Y.; Yarlagadda, T.; Schuetz, M.; Spann, K.; Yarlagadda, P. Antiviral and Antibacterial Nanostructured Surfaces with Excellent Mechanical Properties for Hospital Applications. ACS Biomaterials Science & Engineering **2020**, 6, 3608-3618.

2Li, B.; Wang, D.; Lee, M.M.S.; Wei, W.; Tan, Q.; Zhao, Z.; Huang, X. Fabrics Attached with Highly Efficient Aggregation-Induced Emission Photosensitizer: Toward Self-Antiviral Personal Protective Equipment. *ACS Nano* **2021**, *15*, 13857-13870.

Keum, H.; Kim, D.; Whang, C.; Kang, A.; Lee, S.; Na, W.; Jon, S. Impeding the Medical Protective Clothing Contamination by a Spray Coating of Trifunctional Polymers. *ACS Omega* **2022**, *7*, 10526-10538.

Karim, N.; Afroj, S.; Lloyd, K.; Oaten, L.C.; Andreeva, D.V.; Carr, C.; Farmery, A.D.; Kim, I.; Novoselov, K.S. Sustainable Personal Protective Clothing for Healthcare Applications: A Review. *ACS Nano* **2020**, *14*, 12313-12340.

Armentano, I.; Barbanera, M.; Carota, E.; Crognale, S.; Marconi, M.; Rossi, S.; Rubino, G.; Scungio, M.; Taborri, J.; Calabrò, G. Polymer Materials for Respiratory Protection: Processing, End Use, and Testing Methods. *ACS Applied Polymer Materials* **2021**, *3*, 531-548.

Shi, S.; Si, Y.; Li, Z.; Meng, S.; Zhang, S.; Wu, H.; Zhi, C.; Io, W.F.; Ming, Y.; Wang, D.; et al. An Intelligent Wearable Filtration System for Health Management. *ACS Nano* **2023**, *17*, 7035-7046.

Kuo, L.; Luijten, B.J.; Li, S.; De Moraes, A.C.M.; Silvaroli, A.J.; Wallace, S.G.; Hui, J.; Downing, J.R.; Shull, K.R.; Hersam, M.C. Sterilizable and Reusable UV-Resistant Graphene–Polyurethane Elastomer Composites. *ACS Applied Materials & Interfaces.* **2022**, *14*, 53241–53249.

Prata, J.C.; Silva, A.L.P.; Walker, T.R.; Duarte, A.C.; Rocha-Santos, T. COVID-19 Pandemic Repercussions on the Use and Management of Plastics. *Environmental Science & Technology* **2020**, *54*, 7760-7765.

Liu, R.; Mabury, S.A. Single-Use Face Masks as a Potential Source of Synthetic Antioxidants to the Environment. *Environmental Science and Technology Letters.* **2021**, *8*, 651-655.

Teo, J.C.M.; Kng, J.; Periaswamy, B.; Liu, S.; Lim, P.C.; Lee, C.E.; Tan, B.H.; Loh, X.J.; Ni, X.; Tiang, D.; et al. Exploring Reusability of Disposable Face Masks: Effects of Disinfection Methods on Filtration Efficiency, Breathability, and Fluid Resistance. *Global Challenges* **2021**, *5*, 2100030.

Zacharias, N.; Haag, A.; Brang-Lamprecht, R.; Gebel, J.; Essert, S.M.; Kistemann, T.; Exner, M.; Mutters, N.T.; Engelhart, S. Air Filtration as a Tool for the Reduction of Viral Aerosols. *Science of the Total Environment* **2021**, *772*, 144956.

Shen, H.; Zhu, Z.; Wang, H.; Chen, J.; Zhang, M.; Han, M.; Shen, Y.; Shuai, D. Photosensitized Electrospun Nanofibrous Filters for Capturing and Killing Airborne Coronaviruses under Visible Light Irradiation. *Environmental Science & Technology* **2022**, *56*, 4295-4304.

Jin, X.; Gao, F.; Qin, M.; Yu, Y.; Zhao, Y.; Shao, T.; Cai, C.; Zhang, W.; Xie, B.; Xiong, Y.; et al. How to Make Personal Protective Equipment Spontaneously and Continuously Antimicrobial (Incorporating Oxidase-like Catalysts). *ACS Nano* **2022**, *16*, 7755-7771.

Tamboli, D.P.; Lee, D.H. Mechanistic Antimicrobial Approach of Extracellularly Synthesized Silver Nanoparticles against Gram Positive and Gram Negative Bacteria. *Journal of Hazardous Materials* **2013**, *260*, 878–884.

Sadrhaghighi, A.; Sarvari, R.; Fakhri, E.; Poortahmasebi, V.; Sedighnia, N.; Torabi, M.; Mohammadzadeh, M.; Azhiri, A.H.; Eskandarinezhad, M.; Moharamzadeh, K.; et al. Copper-Nanoparticle-Coated Melt-Blown Facemask Filter with Antibacterial and SARS-CoV-2 Antiviral Ability. *ACS Applied Nano Materials* **2023**, *6*, 12849–12861.

 Ammendolia, M.G.; De Berardis, B. Nanoparticle Impact on the Bacterial Adaptation: Focus on Nano-Titania. *Nanomaterials* **2022**, *12*, 3616.

Kim, J.-H.; Lee, G.-H.; Ma, J.; Lee, S.; Kim, C.-S. Facile Nanostructured Zinc Oxide Coating Technique for Antibacterial and Antifouling Air Filters with Low Pressure Drop. *Journal of Colloid and Interface Science* **2022**, *612*, 496-503.

Habib, Z.; Khan, S.J.; Ahmad, N.M.; Shahzad, H.M.A.; Jamal, Y.; Hashmi, I. Antibacterial Behaviour of Surface Modified Composite Polyamide Nanofiltration (NF) Membrane by Immobilizing Ag-Doped TiO2 Nanoparticles. *Environmental Technology* **2019**, *41*, 3657-3669.

Waheed, A.; Baig, U.; Ansari, M.A. Fabrication of CuO Nanoparticles Immobilized Nanofiltration Composite Membrane for Dye/Salt Fractionation: Performance and Antibiofouling. *Journal of Environmental Chemical Engineering* (Print) **2022**, *10*, 106960.

Gonçalves, R.A.; Ku, J.W.K.; Zhang, H.; Salim, T.; Oo, G.; Zinn, A.A.; Boothroyd, C.; Tang, R.M.Y.; Gan, C.L.; Gan, Y.; et al. Copper-Nanoparticle-Coated Fabrics for Rapid and Sustained Antibacterial Activity Applications. *ACS Applied Nano Materials* **2022,** *5*, 12876-12886.

Goel, S.; Chen, F.; Cai, W. Synthesis and Biomedical Applications of Copper Sulfide Nanoparticles: From Sensors to Theranostics. *Small* **2013**, *10*, 631-645.

Laha, D.; Pramanik, A.; Chattopadhyay, S.; Dash, S.K.; Roy, S.; Pramanik, P.; Karmakar, P. Folic Acid Modified Copper Oxide Nanoparticles for Targeted Delivery in in Vitro and in Vivo Systems. *RSC Advances* **2015**, *5*, 68169-68178.

Ammara, S.; Shamaila, S.; Zafar, N.; Bokhari, A.; Sabah, A. Nonenzymatic Glucose Sensor with High Performance Electrodeposited Nickel/Copper/Carbon Nanotubes Nanocomposite Electrode. *Journal of Physics and Chemistry of Solids* **2018**, *120*, 12-19.

Behzadinasab, S.; Chin, A.W.H.; Hosseini, M.H.; Poon, L.L.M.; Ducker, W.A. A Surface Coating That Rapidly Inactivates SARS-CoV-2. *ACS Applied Materials & Interfaces* **2020**, *12*, 34723–34727

Jana, I.D.; Kumbhakar, P.; Banerjee, S.; Gowda, C.C.; Kedia, N.; Kuila, S.K.; Banerjee, S.; Das, N.C.; Das, A.K.; Manna, I.; et al. Copper Nanoparticle–Graphene Composite-Based Transparent

Surface Coating with Antiviral Activity against Influenza Virus. *ACS Applied Nano Materials* **2020**, *4*, 352–362.

Hosseini, M.H.; Chin, A.W.H.; Behzadinasab, S.; Poon, L.L.M.; Ducker, W.A. Cupric Oxide Coating That Rapidly Reduces Infection by SARS-COV-2 via Solids. *ACS Applied Materials & Interfaces* **2021**, *13*, 5919–5928.

Behzadinasab, S.; Chin, A.W.H.; Hosseini, M.H.; Poon, L.L.M.; Ducker, W.A. A Surface Coating That Rapidly Inactivates SARS-CoV-2. *ACS Applied Materials & Interfaces* **2020**, *12*, 34723-34727.

Liu, M.; Bauman, L.; Nogueira, C.L.; Aucoin, M.G.; Anderson, W.A.; Zhao, B. Antimicrobial Polymeric Composites for High-Touch Surfaces in Healthcare Applications. *Current Opinion in Biomedical Engineering* **2022**, *22*, 100395.

Merkl, P.; Long, S.; McInerney, G.M.; Sotiriou, G.A. Antiviral Activity of Silver, Copper Oxide and Zinc Oxide Nanoparticle Coatings against SARS-CoV-2. *Nanomaterials* **2021**, *11*, 1312.

Fujimori, Y.; Sato, T.; Hayata, T.; Nagao, T.; Nakayama, M.; Nakayama, T.; Sugamata, R.; Suzuki, K. Novel Antiviral Characteristics of Nanosized Copper(I) Iodide Particles Showing Inactivation Activity against 2009 Pandemic H1N1 Influenza Virus. *Applied and Environmental Microbiology* **2012**, *78*, 951-955.

Zhang, X.; Feng, Y.; Gao, D.; Ma, W.; Cheng-Zhu, J.; Jiang, X.; Lin, J.; Yang, F. Functionalization of Cellulosic Hydrogels with Cu2O@CuO Nanospheres: Toward Antifouling Applications. *Carbohydrate Polymers* **2022**, *282*, 119136.

Jardón-Maximino, N.; Cadenas‑Pliego, G.; Ávila‑Orta, C.A.; Comparán-Padilla, V.E.; Uribe, L.E.L.; Pérez-Álvarez, M.; Fernández, S.; De Jesús Sosa Santillán, G. Antimicrobial Property of Polypropylene Composites and Functionalized Copper Nanoparticles. *Polymers* **2021**, *13*, 1694.

Damm, C.; Münstedt, H.; Rösch, A. The Antimicrobial Efficacy of Polyamide 6/Silver-Nano- and Microcomposites. *Materials Chemistry and Physics* **2008**, *108*, 61-66.

Sierra-Ávila, R.; Pérez-Alvarez, M.; Valdez-Garza, J.; Avila-Orta, C.A.; Jiménez-Regalado, E.J.; Mata-Padilla, J.M.; Soto-Castruita, E.; Cadenas-Pliego, G. Synthesis and Thermomechanical Characterization of Nylon 6/Cu Nanocomposites Produced by an Ultrasound-Assisted Extrusion Method. *Adv. Mat. Sci. Eng*. **2018,** 1-10.

N. Smith, C. L. Raston, M. Saunders and R. Woodward, NSTI-Nanotech, **2006**.

Massart, R., Magnetic Fluids and Process For Obtaining Them, USP: 4329241, **1982**

Cave, G.W.V. **2021**. Reactor. US10926236B2, September 24.

Cave, G.W.V and Mundell V. J. **2013**. Coating metal oxide particles. EP2825515A2, March 15.

ISO 17294-2:2023 Available online: https://www.iso.org/standard/82245.html.

ISO 18184:2019 Available online: https://www.iso.org/standard/71292.html.

Yousefimashouf, M.; Yousefimashouf, R.; Alikhani, M.S.; Hashemi, H.; Karami, P.; Rahimi, Z.; Hosseini, S.M. Evaluation of the Bacterial Contamination of Face Masks Worn by Personnel in a Center of COVID 19 Hospitalized Patients: A Cross-Sectional Study. *New Microbes and New Infections* **2023**, *52*, 101090.

ISO 20743:2021 Available online: https://www.iso.org/standard/79819.html.

Bio-compatible antimicrobial coatings for medical devices

James Hall [1], Subbareddy Mekapothula [1], Becky Coxhill [1], Gareth W. V. Cave [1], and Samantha McLean [1], *

[1]   School of Science and Technology, Nottingham Trent University, Clifton Lane, Nottingham NG11 8NS, UK

*   Correspondence: Samantha.McLean@ntu.ac.uk; Tel.: +44 115 84 83324

Abstract:

Copper oxide nanoparticles have been synthesised and investigated for their antimicrobial action on medical grade silicone tubing to reduce the dependence on antibiotics and the subsequent development of further antibiotic resistance amongst clinical pathogens. We Demonstrate that copper oxide nanoparticles can be coated onto medical grade tubing using an oxysilane as a bonding agent and that these mamoparticles and the coating are applied at non-toxic concentrations. The coating can induce up two log reduction in viable cells at MIC concentrations and up to a four-log reduction when increased to 20 times MIC, compared to uncoated tubing in multi-drug resistant pathogens at concentrations substantially below the LD_{50} value. We also show that this coating is robust and can be applied by both a dip coating and a spray coating, allowing coating at a manufacturing level and reapplication during *ad hoc* material modification in orthopedic implants.

Keywords: Copper oxide nanoparticles; ESKAPE pathogens; 3-Mercaptopropyltrimethoxysilane; MPTMS; antimicrobial activity; multi-drug resistance; Glutamic acid; Glu-CuO nanoparticles; Tissue culture; CDC reactor.

Introduction

Antibiotics have been widely exploited since the discovery of penicillin to treat bacterial infections; however, their exploitation has resulted in significant increases in antibiotic resistance, including within the highly virulent pathogens *Escherichia coli* and *Staphylococcus aureus*; that represent a major threat to human health [1]. Alternatives to antibiotics such as metals have been used as early as in the Ancient Egyptian era, where silver and copper were used to treat burn wounds, which ultimately led to modern day metallic therapeutics and treatments [2]. Silver nanomaterials are now commonly utilised for their antipathogenic properties, from food storage to wound dressings [3]. However, there are a growing number of reports of silver resistance amongst bacterial pathogens [4]. In addition, silver is susceptible to oxidation, and subsequent reduction in antipathogenic properties, it is also reported to have elevated cytotoxic effects in mammals, including reduced cell viability, lactate dehydrogenase leakage and the generation of reactive oxygen species [5]

A viable and emerging alternative to silver as an antimicrobial is copper, which was utilised during the SARS-CoV-2 pandemic for its antiviral properties and was officially classified by the Environmental Protection Agency in 2008 as an antimicrobial metal [6,7] Copper and its alloys are widely used, both commercially and domestically, as touch surfaces to reduce the spread and build-up of pathogens. Nanoparticles, offer excellent surface area to volume ratios as well as having excellent interaction rates with bacterial cells [8]. Therefore, the development of copper nanoparticles as antimicrobial agents, harnesses the antimicrobial potential of copper whilst also utilising the advantageous properties of nanoparticle technologies presents a promising avenue of investigation. Further improvement to the nanoparticles, to improve their bioavailability and ingestion by pathogenic bacteria by funcionalisation in an amino acid is also possible [9].

Advancements in modern medicine mean that implanted medical devices are utilising to support and improve quality of life more than at any time in our history. However, this development is a double-edged sword with implanted materials within the body providing an excellent scaffold for microbial contamination and subsequent host infection. Herein, we report for the first time the antipathogenic surface modification of medical grade silicone tubing with copper oxide nanoparticles, which caused a significant reduction in the number of viable bacterial cells able to adhere to tubing of bacterial pathogens.

Materials and Methods

2.1 Reagents and instruments

All chemicals and solvents were purchased as reagent grade or LC-MS grade and used without further purification. Copper (II) chloride anhydrous (Glentham Life Sciences), Sodium Hydroxide (Glentham Life Sciences), L-Glutamate (Merck, Germany). Other consumable labware like 24 well and 96 well polystyrene plates were acquired (Merck, Germany), 10, 200 and 1000 µl tips and filtertips were acquired (Starlab, UK). Mueller Hinton Broth (Merck, Germany), Mueller Hinton Agar (Merck, Germany), Magnesium Chloride (Merck, Germany), Calcium Chloride (Merck, Germany), Potassium Thiocyanate (Merck, Germany), Sodium Chloride (Merck, Germany), Potassium Chloride (Merck, Germany), Porcine mucin (Merck, Germany), Potassium Dihydrogen Phosphate (Merck, Germany), Dipotassium Phosphate (Merck, Germany), Urea (Merck, Germany), Ammonium Chloride (Merck, Germany). DMEM (Thermo Fischer Scientific, USA), Dulbecco PBS (Thermo Fischer Scientific, USA), FBS (Thermo Fischer Scientific, USA) DMSO (Thermo Fischer Scientific, USA), Penicillin-Streptomycin solution (Thermo Fischer Scientific, USA)

Strain PS_Acine9 and PS_Acine7 were used with the permission of Prof Lesley Hoyles, Nottingham Trent University. The study of this anonymized isolate for use in non-commercial research beyond the diagnostic requirement was approved by an NHS research ethics committee (number 06/Q0406/20). *Staphylococcus aureus* USA 300 LEC2 and *Escherichia coli* O157:H7 were a kind gift from the Poole group at the University of Sheffield, UK. *Staphylococcus epidermidis* ATCC 12228 was obtained from the American Type Culture Collection. A clinical isolate of *Klebsiella pneumoniae* and *Pseudomonas aeuriginosa* that were acquired from Nottingham University Hospitals (NUH) Trust Pathogen Bank, under MTA with

permission granted for publication. An immortal HaCaT cell line was acquired from Elvina Chrysanthou at Nottingham Trent University and used for tissue culture work.

Centre for disease and control (CDC) reactor coupons were acquired in Stainless steel 316, Titanium, PVC, and Silicone rubber (BioSurface technologies, USA)

Synthesis of copper oxide nanoparticles via aqeuous precipitation

Copper oxide nanoparticles were synthesized using an aqueous precipitation, following a modified literature procedure.(Br. pat., GB202304579A, March 2012) Copper (II) chloride (100 mL, 0.1 M) was added with sodium hydroxide (100 mL, 0.2 M) via a peristaltic pump onto the centre of a rotating concave disk, (10.5 cm diameter, 18 3x3 mm stepped ridges, 1000 RPM) yielding copper oxide nanoparticles (6.42 g, 80.9 %). The resultant solution was filtered and washed with deionized water then was placed in a vacuum rotary pump at 60°C until a fine powder had formed, and excess water content was removed.

The nanoparticles were coated with glutamic acid (1:1 w/w) to improve dispersion as glutamic acid is an essential amino acid that introduces biocompatible functionalities to the copper nanoparticles to improve biological interactions. Glutamic acid coating was achieved by mechanochemistry using excess glutamic acid to coat the surface of the copper oxide. The copper oxide nanoparticle, glutamic acid mixture was ground together until no free glutamic acid was observed, where the glutamic acid coated copper oxide nanoparticles were then washed in deionized water, filtered and placed into a rotary pump at 60 °C until a fine powder had formed and excess water content was removed

2.3 Characterization of Glutamic acid-coated copper oxide nanoparticles

The glutamic acid coated copper oxide nanoparticles (Glu-CuO nanoparticles) were analysed using a Transmission electron microscope (TEM) and Dynamic light scattering (DLS) to determine the size of the nanoparticles. A Zetasizer DLS was used to measure the zeta potential of the uncoated and coated nanoparticles.

2.3.1Transmission electron microscopy (TEM)

Transmission electron microscopy was performed using a JEOL 2100 Transmission Electron Microscope. 10 µl of suspended CuO and Glu-CuO nanoparticles were loaded onto Holey carbon TEM grids (TAAB, UK) and were allowed to dry for 30 minutes. Excess suspension was removed by carefully absorbing the remaining fluid before placing the holey carbon grid into the TEM sample holder before imaging. Approximately 50 nanoparticles were analyzed to measure the particle size and the distribution of the nanoparticle size using ImageJ (NIH, USA).

2.3.2 Dynamic Light Scattering and Zeta potential measurements

Dynamic light scattering and Zeta potential measurements were made using a Zetasizer nano series (Malvern, UK) to measure the hydrodynamic size and the zeta potential of both the uncoated and glutamic acid coated copper oxide nanoparticles. Copper oxide nanoparticles in water solution at a concentration of 1 mg mL^{-1} were loaded into a cuvette and measured for for 100 repeats at room temperature (20 °C). This was performed on glutamic acid coated copper oxide nanoparticles following the same procedure. Zeta potential was measured by filling a folded capillary zeta cell (Malvern, UK) with the copper oxide nanoparticles in water solution at room temperature (20 °C) at a concentration of 1 mg mL^{-1}. This procedure was also performed on the glutamic acid coated copper oxide nanoparticles.

2.3.3 Thermogravimetric analysis (TGA)

Thermogravimetric analysis (TGA) was performed using a TGA 4000 (Perkin Elmer, USA) to analyse the weight of the glutamic acid coating on the copper oxide nanoparticles and the Glu-CuO nanoparticles on the silicone material. 50 mg of Glu-CuO nanoparticles was added into a ceramic crucible at room temperature and placed into the TGA 4000. The temperature of the TGA 4000 was then increased in increments of 5 °C until a temperature of 900 °C was achieved, where this temperature was held for 30 minutes and subsequently brought back to room temperature. 50 mg of Glu-CuO nanoparticle coated silicone was added and the same procedure was applied.

2.3.4 Inductive coupled Plasma-Mass spectrometry

Inductively Coupled Plasma-Mass Spectrometry (ICP-MS) was performed on the copper oxide nanoparticles for elemental analysis and on various media to determine additionally leached copper from the various material coatings. A 10 cm length of coated silicone tube was placed in line of a peristaltic pump with a flow rate of 0.75 mL min^{-1} for 22 hours to allow one litre of artificial saliva media to pass through the coated tube. After the media had completely passed through, the media was homogenized and 1ml was taken to digest at a 1:10 ratio in 70% nitric acid. The digested sample was then further diluted in 2% nitric acid until a one part per billion dilution was achieved.

The spray coated CDC coupons were placed, in 24 well plates (Merck, Germany) into 2 mL of plasma like media and oscillated on a bench top shaker bed at 150 rpm for 24 hours. The coupons were removed, and 1 mL of media was taken for digestion and dilution to a one part per billion (ppb) concentration. A copper standard was also diluted to concentrations of 1 ppb, 100 ppb, 250 ppb, 500ppb, 750ppb, and 1000 ppb to generate a calibration of the system.

2.5 Adhesion of Glu-CuO nanoparticles to material surfaces

Adhesion of the Glu-CuO nanoparticles on silicone tube was performed by a dip coating procedure with three steps. The first step was a one-minute submersion of the silicone tube into 3-mercaptopropyltrimethoxysilane, at a concentration of 0.1 Molar, under minor agitation. Then, the silicone tube was placed into a 0.1 w/w mixture of glycerol to water, for an additional minute with minor agitation. Finally, the silicone tube was submerged in Glu-CuO nanoparticles suspended in water, for 1 minute under minor agitation, either at MIC

concentration or twenty times MIC concentration. The coating was then UV sterilized for 30 minutes prior to testing. Spray coating CDC coupons was performed with two spray coatings. The first was a 0.1 Molar concentration of 3-mercaptopropyltrimethoxysilane and the second coating was Glu-CuO nanoparticles suspended in water at MIC concentration. The spray coating was then UV cured for 30 minutes prior to testing ensuring the coating had cured and was sterile.

2.6 Leaching of the Material coatings

Leaching was performed using a 300 series cased peristaltic pump (Watson-Marlow, UK) set to a flow rate of 0.75 mL min^{-1} equivalent to 1.08 litre in 24 hours. Freshly produced artificial saliva media was produced and used as the leaching media passing the coated silicone tube. After 24 hours, the media was taken for ICP-MS and analysed. The coated CDC coupons (BioSurface technologies, USA) were placed into 2 mL of freshly prepared plasma like media and shaken for 24 hours at 150 rpm, where the media was then taken for ICP-MS and leached copper was evaluated.

2.7 Characterization of nanoparticle coated materials

The Glu-CuO nanoparticle coated silicone tube and CDC coupons were examined under a JEOL JSM-7100F Scanning Electron Microscope (SEM) (JEOL, Japan). Samples were adhered using conductive copper tape on aluminium stubs (TAAB, UK) and placed into an eights piece sample holder. Samples were then coated in a 5nm goal coating via a rotary pumped sputter coater (Quorom Q150R ES, UK). A high accelerating voltage of 15 KeV were used to image copper and allow further analysis using Energy dispersive spectroscopy.

2.7.1 SEM coupled with energy dispersive X-ray spectroscopy (SEM-EDS)

With the samples placed into the SEM and a high accelerating voltage used, elemental analysis of the coated materials was performed using the same electron microscope. Only brief exposure to the surface of the silicone tube was allowed to reduce surface damage and ensure appropriate elemental analysis of the coating.

2.8 Minimum inhibition and bacterialcidal concentration assays

Minimum inhibition concentration (MIC) and minimum bacterialcidal concentration (MBC) assays were performed as per the EUCAST standards to ensure the Glu-CuO nanoparticles were antibacterial. Each species was tested using a 96-well plate with 90 µL of fresh Mueller Hinton Broth (MHB) in nine wells, leaving the first well for growth inoculum, the last well as a control for media and an empty well in the eleventh column. Each well then had a further 90 µL of MHB mixed with concentrations of Glu-CuO nanoparticles ranging from 4.02 mg mL^{-1} to 1.92 mg mL^{-1}. 200 µL of the broth culture, diluted to 0.1 OD was added to the first well, and used to serial dilute at a 1:10 ratio, along the plate in triplicate. The plate was incubated for 18 hours at 37 °C and retrieved, with the first well showing no signs of growth marked as the inhibition concentration. Three wells from either side of the MIC value were spotted onto

Mueller Hinton Agar (MHA) to determine if any viable cells remained, with the first dilution showing no bacterial growth on the agar indicating the bacterialcidal concentration of the Glu-CuO nanoparticles.

2.9 Toxicity assays of Glu-CuO nanoparticles and MPTMS

MTT assays were used to measure the toxicity of Glu-CuO nanoparticles and MPTMS of the material coating. HaCaT epethelial cells were split until the seventh passage was achieved and all experiments were performed on this passage. The cells were grown in Dulbecco's Modified eagle medium to confluency and spun at 300 RPM to reduce the cells to a pellet, where the spent media was removed, and fresh media was added and diluted to a concentration of $2*10^5$ cells mL^{-1} and 100 µL of the diluted solution was added to each well and incubated for 24 hours allowing the cells to adhere to the well. The media of the wells was carefully removed and the Glu-CuO nanoparticles were added in Dulbecco's Modified eagle medium at concentrations ranging from 500 µg mL^{-1} to 275 µg mL^{-1} and tested.

3-Mercraptopropyltrimethoxysilane (MPTMS) was tested by adding 100 µL at concentrations ranging from 1 Molar to 0.05 Molar concentration, however this chemical is known to be toxic, and an alternative testing technique was used instead. ISO 10993-5:2009 was followed where 3mm by 3mm silicone tube surface was coated with MPTMS and cured. These surfaces were added to a plate with an additional control well with sterile untreated silicone to observe the effect of the material on the cells.

2.10 Antibacterial assessments

The material coatings were examined by using a modified Minimum Biofilm Eradication Concentration (mMBEC) assay and the Center for Disease and Control (CDC) bioreactor. The mMBEC assay was performed using 24-well plates adhered with 1 cm silicone tube cuttings which were subsequently dip coated and tested against each bacterial species to determine the change in biofilm formation and the change in viable cells recovered from the material. Each well was filled with 1800 µL of MHB and inoculated with 200 µL of each species grown in MHB and diluted to a concentration of 10^6 Colony Forming units per mililiter (CFU mL^{-1}). Measuring the biofilm formation was performed by submerging the silicone tubes in Crystal violet at a 0.1% concentration for two hours, gently washing the excess with sterile Phosphate Buffer Solution (PBS) and submerging the detached silicone tubes in ethanol to recover the Crystal violet dye. Optical density measurements were made of the biofilm, with increased optical density corresponding to an increase in biofilm production. Viable cell measurements were made by gently washing the silicone tubes with sterile PBS and placing tubes into 7 mL bijous with 2 mL of sterile PBS and vortexing for 1 minute to recover the viable cells. The recovered cells were then serial diluted in PBS and plated on MHA to count the viable cells recovered.

The CDC bioreactor was used to measure the adhesion of bacteria through the spray coating on various orthopedic materials. CDC coupons were coated, sterilised, and placed into a sterile CDC bioreactor, with 500 mL of plasma like media and inoculated with 1 mL of 10^8 CFU mL^{-1} of Staphylococcus aureus. The reactor was ran overnight for 24 hours at 125 RPM where the coupons were removed aseptically and taken for biofilm and viable cell measurements.

Results and discussion

3.1. Synthesis of copper oxide nanoparticles and coating in glutamic acid

Synthesis of Copper oxide nanoparticles is well studied, and co-precipitation allows excellent control of the size and shape of the nanoparticle, which can be achieved by temperature changes, reaction time and mixing rate controlable via a Spinning Disc Reactor (SDR) or magnetic flea [13]. By altering the temperature and rate of rotation of the SDR or magnetic flea, the size of the nanoparticle can increase or decrease, with increasing temperatures correlating to an increase in nanoparticle size and slower rotational speeds correlationg to an increase nanoparticle size.

Using an aqueous precipitation technique on a spinning disc reactor, with concave geometry, copper (II) chloride (100 mL, 0.1 M) and sodium hydroxide (100 mL, 0.2 M) were fed into the reactor using peristaltic pumps, onto the centre of the reactor. The SDR (1000 RPM) yielded a black coloured slurry, assumed to be copper oxide nanoparticles in salt water, which was collected and centrifuged, removing the surfactant, and washed again in deionized water, repeating three times. The resulting solution was then added to a rotary vacuum pump at 60 °C until a fine powder was achieved. These nanoparticles were first characterized using Dynamic light scattering, Transmission Electron microscopy and Zeta potential measurements.

The fine powder was added into a mortar and pestle and mixed with glutamic acid (1:1 w/w) to improve dispersion biocompatibility and bioavailability [14]. The two powders were grinded together to coat the copper oxide nanoparticles until no observable glutamic acid powder was left in the mix. The mixed powder was washed in deionized water and once again placed into a rotary vacuum pump at 60 °C until a fine powder was achieved. These coated nanoparticles were also subject to analysis using DLS, TEM and Zeta potential measurements, additionally, Thermogravimetric Analysis was also performed to determine the weight-by-weight ratio of the copper oxide nanoparticles to glutamic acid.

3.2 Characterization of copper oxide nanoparticles and glutamic acid coated copper oxide nanoparticles

Having synthesized nanoparticles via aqueous precipitation and washed them sufficiently, characterization of the shape and morphology of the nanoparticles using TEM and evaluating the dispersity of the produced nanoparticles was performed. TEM imaging showed that the produce nanoparticles varied in size but were spherical shaped (Fig.1).
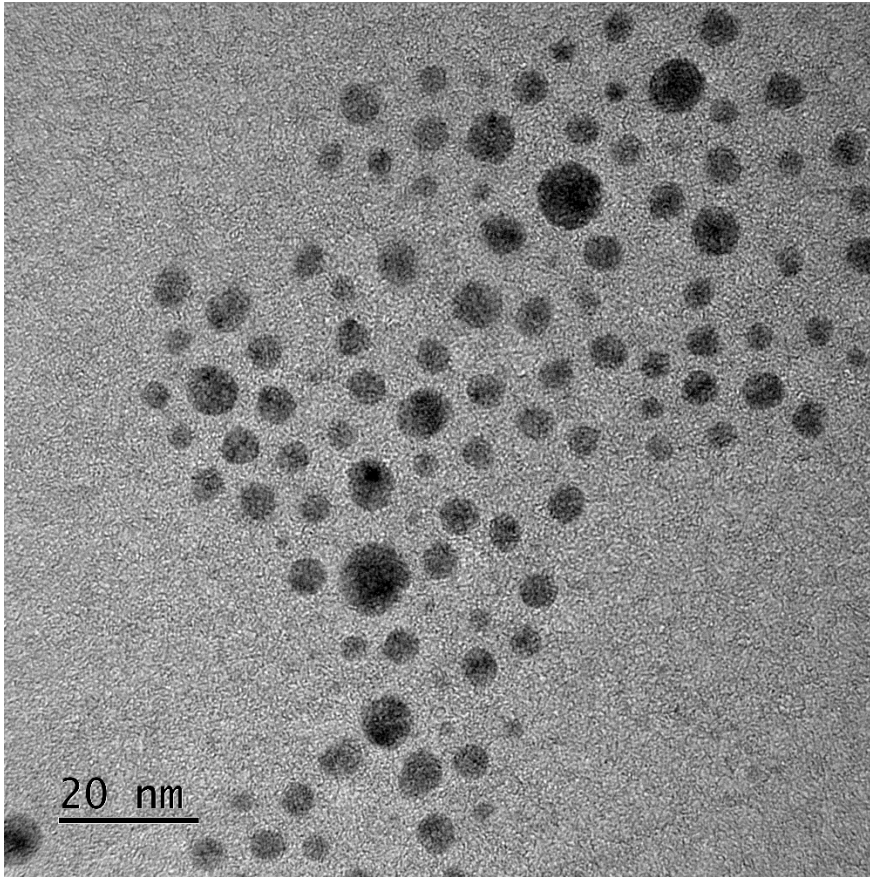
Figure 3 TEM image of copper oxide nanoparticles with spherical shape produced using aqueous precipitation

ImageJ analysis to measure the size was conducted with a histogram produced of the distrubution of the synthesised nanoparticles with an average size of 5.8 ± 1.8 nm (Fig.2). Agglomorates were also present, increasing the average size and deviation from that size.
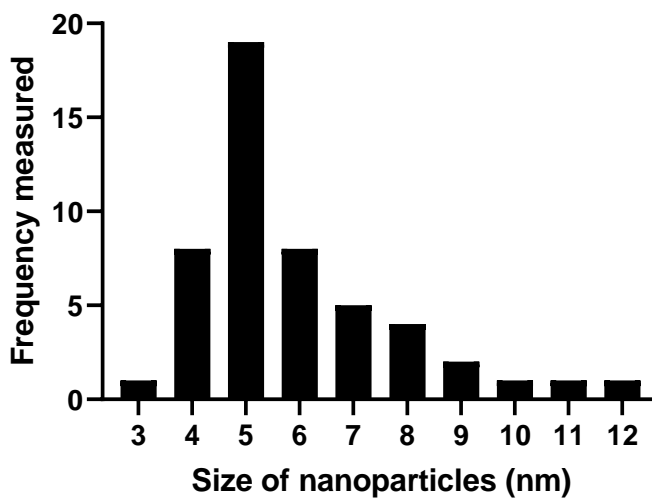

Figure 4 ImageJ analysis of the measured nanoparticle sizes to determine the average size and deviation of 50 measured nanoparticles.

With the size of the nanoparticle characterised, the hydrodynamic size, polydispersity and zeta potential were also measured to determine the nanoparticles stability in aqueous solution. A concentration of 1mg mL^{-1} of copper oxide nanoparticles in water were placed into a cuvette and analysed using a zetasizer nano series. The hydrodynamic size of the nanoparticles was measured to be 74.93 ± 5.170 nm with a polydispersity index of 0.35 (Fig.3).
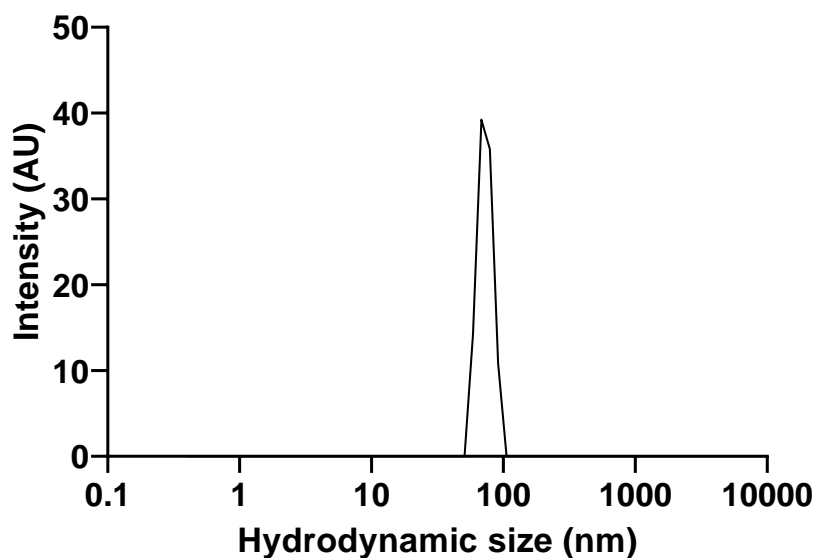
Figure 5 The measured hydrodynamic size of the copper oxide nanoparticles imaged using TEM

The zeta potential of these nanoparticles was also measured using the same zetasizer nano series, with a measured potential of -0.4 ± 6.2 mV, indicating that these nanoparticles would not be stable in aqeuous solution as values of stable particles typically require ± 30 mV [15]. As the nanoparticles were coated in glutamic acid, these analytical techniques were also performed on the Glu-CuO nanoparticles, with TEM analysis showing spherical shaped nanoparticles. Due to the organic coating, imaging of the nanoparticles showed significant organic content around the nanoparticles (Fig.4).
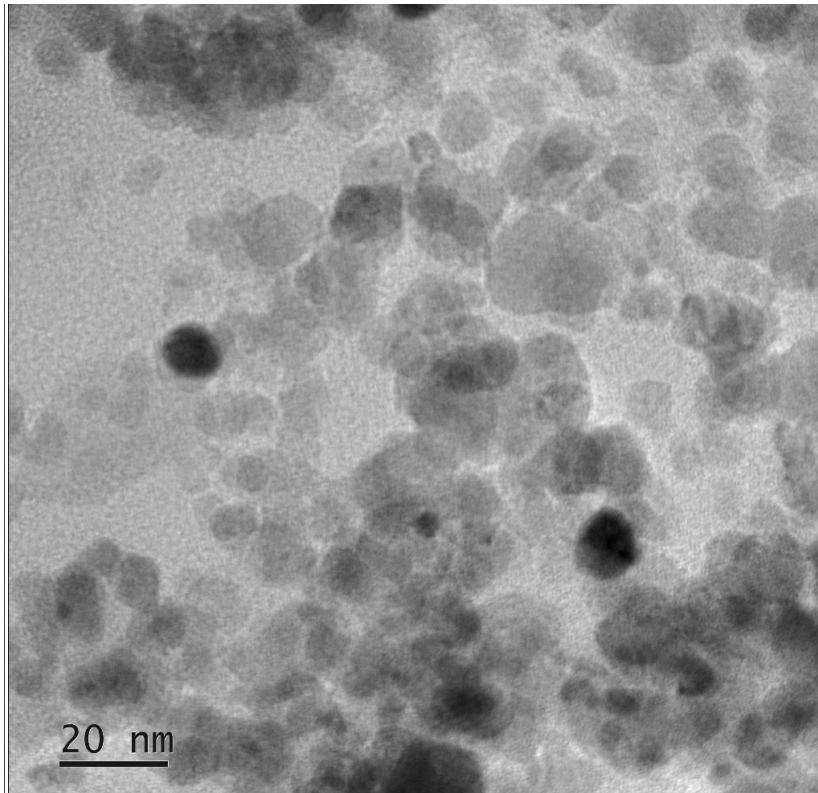
Figure 6 The glutamic acid coated copper oxide nanoparticles, with darker regions showing the nanoparticle core and the grey areas indicating glutamic acid

ImageJ analysis of the TEM images of Glu-CuO nanoparticles showed an increase in nanoparticle size, with a new siize of 21.3 ± 5.5 nm across 50 measured nanoparticles (Fig.5)
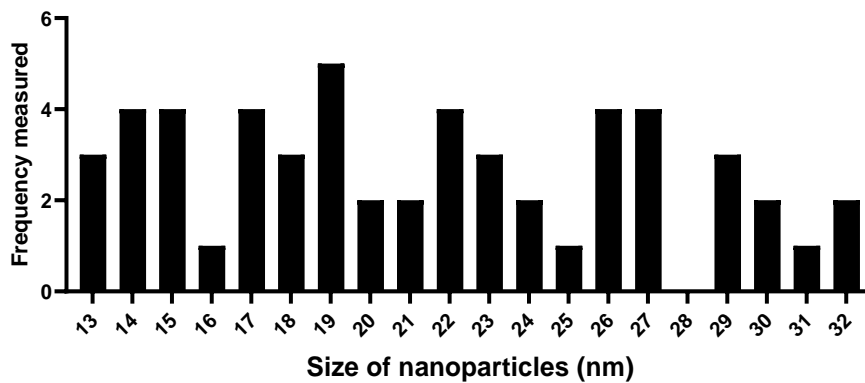

Figure 7 Histogram of the measured Glu-CuO nanoparticle sizes imaged using TEM

The DLS measurements of these nanoparticles showed that they had become polydisperse and that the hydrodynamic size of these nanoparticles had also increased, measuring 123.1 ± 12.7 nm (Fig.6). The zeta potential of these coated nanoparticles was also measured as -42.0 ± 3.2 mV indicating stable particles in aqeuous solutions.
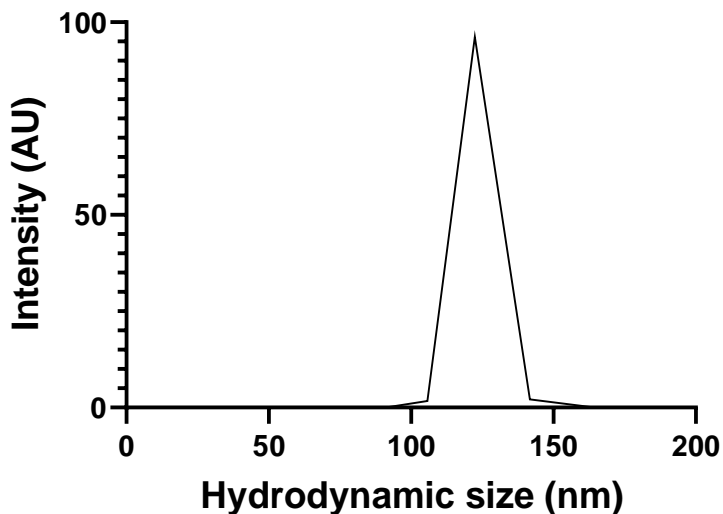
Figure 8 The measured hydrodynamic size of the Glu-CuO nanoparticles

Thermogravimetric analysis was also performed on the coated nanoparticles to measure the weight ratio between the glutamic acid and the copper oxide nanoparticle. TGA analysis the weight of the copper oxide nanoparticles to glutamic acid coating (1:1.19 w/w) (Fig.7)
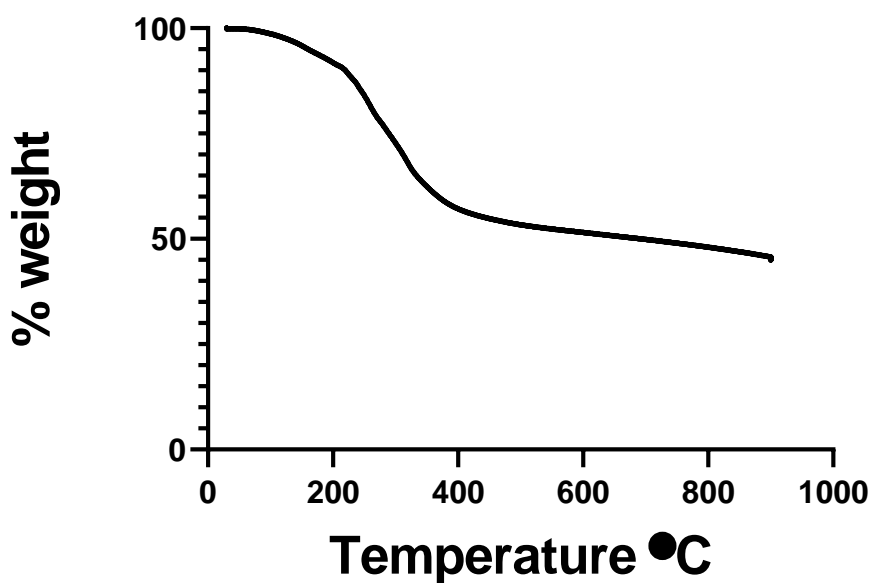
Figure 9 The measured weight of the Glu-CuO nanoparticles as temperature increases

3.3 Antimicrobial evaluation of the Glu-CuO nanoparticles

The Glu-CuO nanoparticles were tested using Minimum inhibition concentration and Minimum Bacterialcidal concentration assays after they had been determined to be stable in solution. The MIC and MBC values varied against Gram positive and Gram negative species with no discernable preference between *Gram* classifications.

Species	MIC (mg L^{-1})	MBC (mg L^{-1})
Escherichia coli	258	325
Staphylococcus aureus	258	325
Pseudomonas aeruginosa	325	325
Klebsiella pneumoniae	325	325
Staphylococcus epidermidis	258	325
Acinetobacter pittii	258	325
Acinetobacter baumannii	258	325

Table 1 The MIC and MBC results of the Glu-CuO nanoparticles against clinical isolates of both Gram positve and Gram negative species

3.4 Adhesion of Glu-CuO nanoparticles to medical grade materials

The Glu-CuO nanoparticles were adhered using 3-Mercaptopropyltrimethoxysilane to stainless steel, titanium, PolyVinyl Chloride (PVC), silicone rubber and silicone tube. Silicone tube was coated using a dip coating while the orthopedic materials were spray coated. The dip coating procedure was performed by prepreparing 24 well plates as modified Minimum Biofilm Eradication Concentration (mMBEC) assays and filling the plates with the appropriate agent. MPTMS (0.1 M) was used as the bonding agent between the silicone, glycerol-water solution (0.1% w/w) and final Glu-CuO nanoparticle concentration. Spray coating was performed using MPTMS (0.1 M) and the final Glu-CuO nanoparticle concentration, not requiring the glycerol solution due to the rigidness of the CDC coupons. SEM-EDS was performed to quantify the coating on the material surfaces to evaluate coverage (Fig. 8).
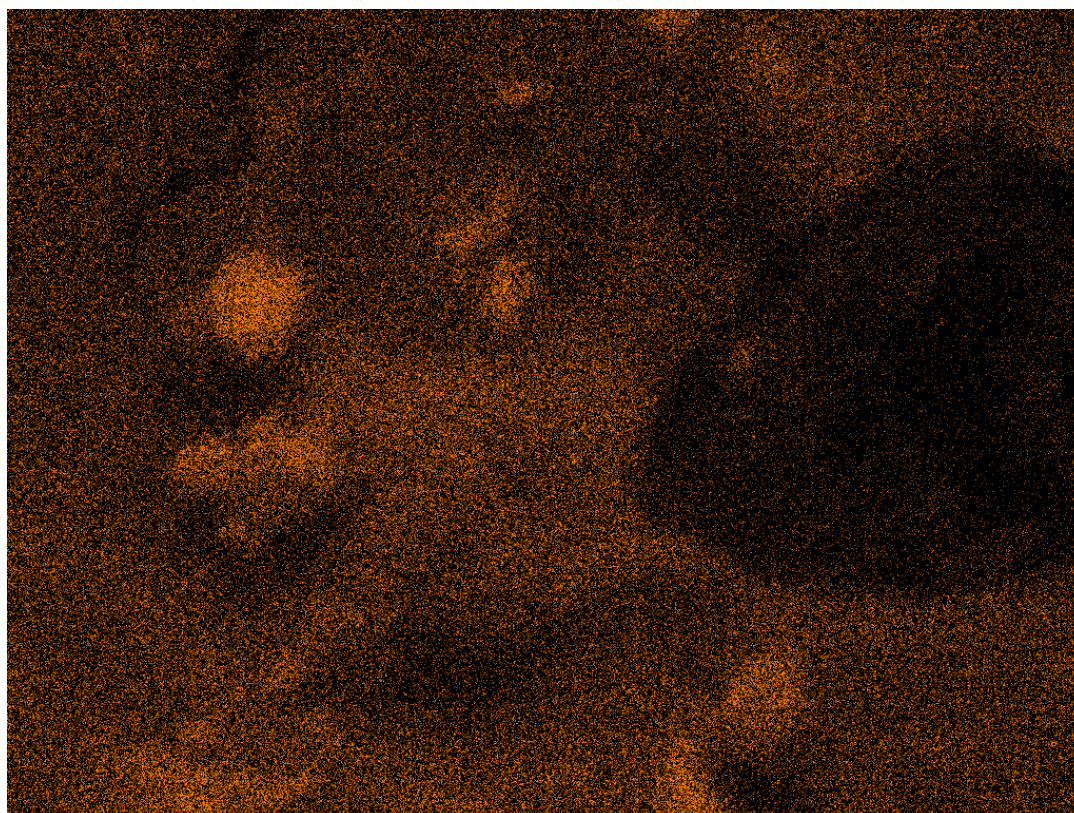

Figure 10 EDS analysis of the copper present on a stainless steel CDC coupon

3.4 Toxicity assay on coating components

An MTT assay was performed on both parts of the material to analyse the toxic effect of both components of the coating. The Glu-CuO nanoparticles were examined, and significant toxic effects were shown to occour at 350 μg mL^{-1} where a near linear increase in toxicity is seen with increasing concentration (Fig. 9). These nanoparticles were added freely in a suspension Dublecos modified eagle medium (DMEM) and removed after 24 hours, with the MTT solution added and solulised using DMSO.
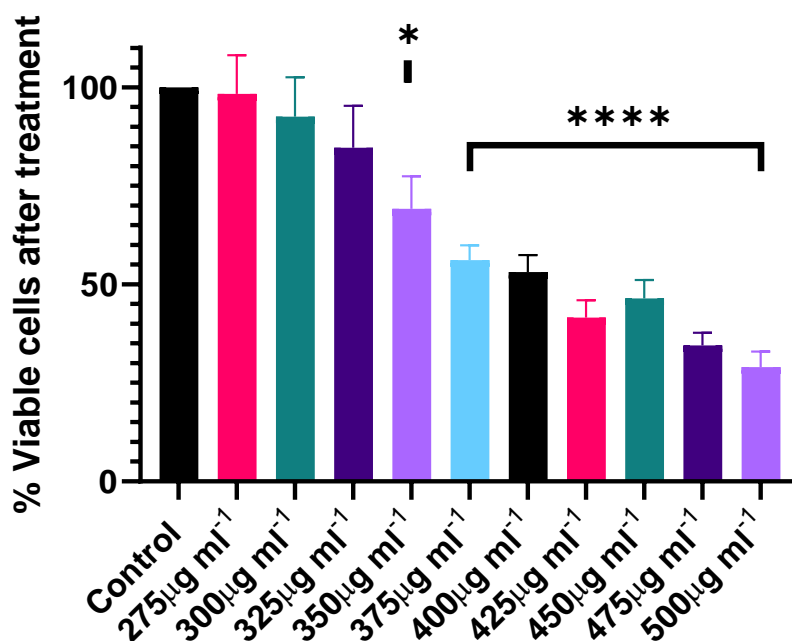

Figure 11 The measureable viable cells percentage compared to a control with no nanoparticles. Significance * P > 0.05 **** P > 0.001

The MPTMS was also measured as oxysilanes are known to be excellent adhesives of oxides to other substrates, such as silicone wafers, metals and PDMS [16] MPTMS was added in liquid form where significant toxicity at all concentrations was observed (Fig. 10).
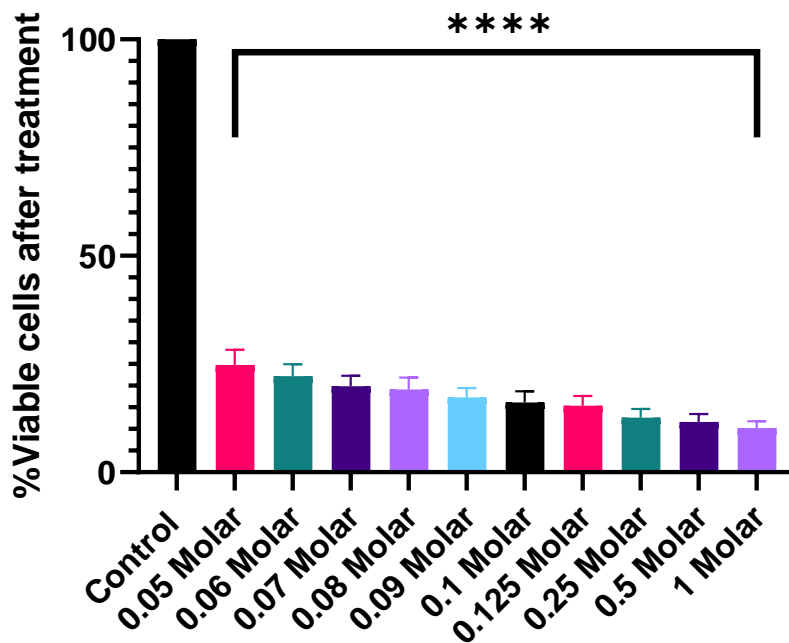
Figure 12 The measureable viable cell percentage compared to a control with no MPTMS. Significance **** P > 0.001

Due to the application of MPTMS in anticancer drug delivery systems, evaluation of the toxicity was performed after the MPTMS had cured, using ISO 10993-5:2009, where significant toxicity was presented in high concentrations of MPTMS greater than 0.1 Molar concentrations (Fig. 11).
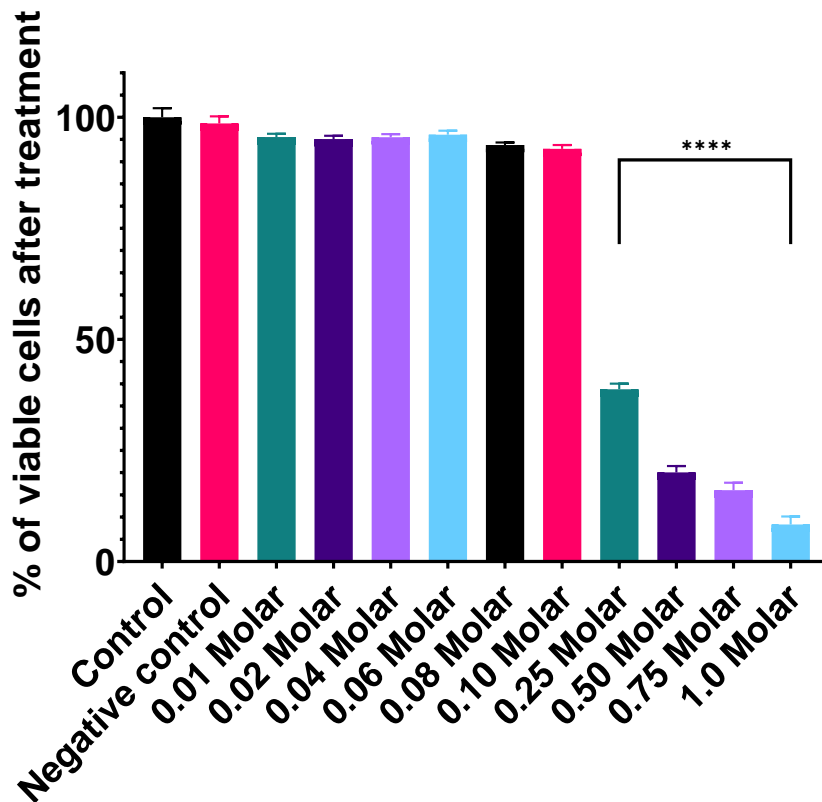
Figure 13 Viable cells measured from a control and negative control with silicone tube following ISO 10993-5:2009

3.3 Modified Minimum Biofilm Eradication Concentration assay

A modification to the Minimum Biofilm Eradication Concentration (MBEC) assay, or Calgary device, was performed to allow an inner and outer diameter of biofilm adhesion to better represent the endotracheal tube environment. This modified MBEC (mMBEC) was used to evaluate the effect of the antimicroibial coating on both biofilm formation and viable cell adhesion at MBC concentration and 20 times MBC concentration. At MBC concentration, biofilm reduction was significant in five of the seven tested species (Fig. 11) whereas significant reduction was seen in all seven of the tested species (Fig. 12). The viable cell reduction measured indicated promising results but was deemed to not be antimicrobial due to only two species presenting a greater than log 2 reduction in viable cells.
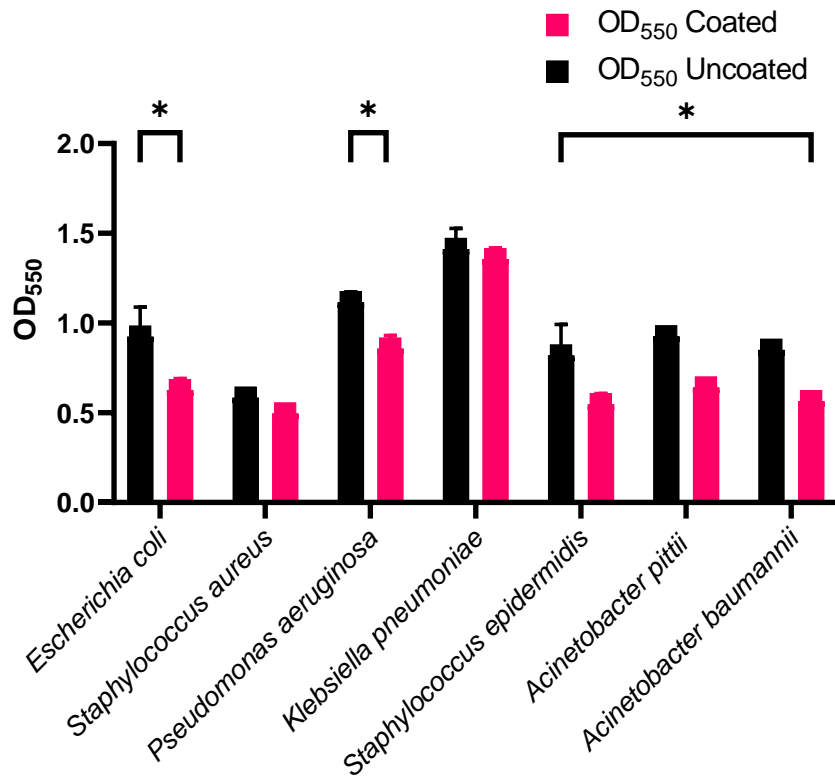
Figure 14 The biofilm reduction measured in seven clinical species, between coated and uncoated mMBEC assay plates
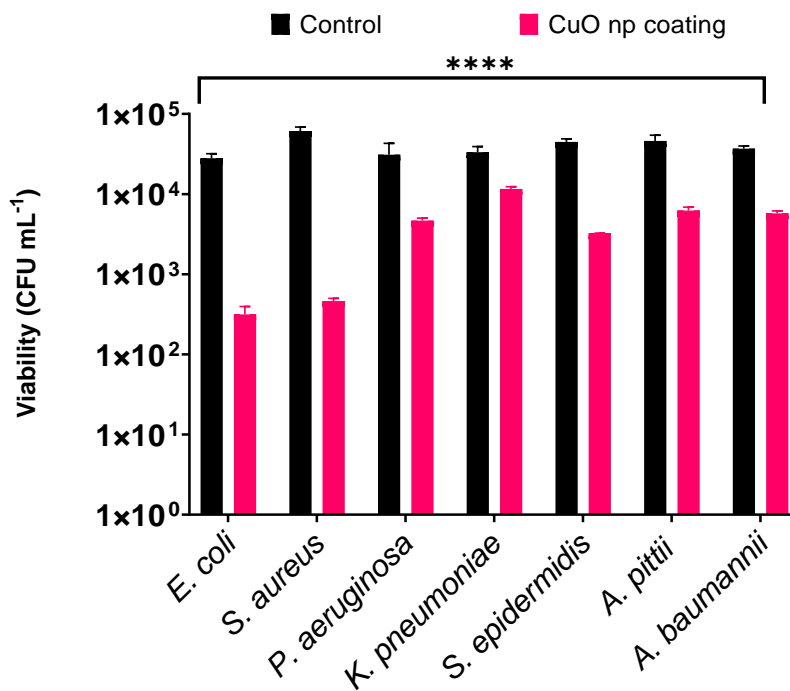

Figure 15 The viable cell reduction measured between treated and untreated mMBEC assay plates

At 20 timesthe MBC concentration, the assays were performed again with a greater effect on biofilm formation in three species and all species showing some decrease in biofilm formation due to the coating (Fig. 13). Similarly, all species exhibited an increase in reduction of viable cells with the *Acinetobacter pittii* species exhibiting a log 4 reduction in viable cells (Fig. 14).
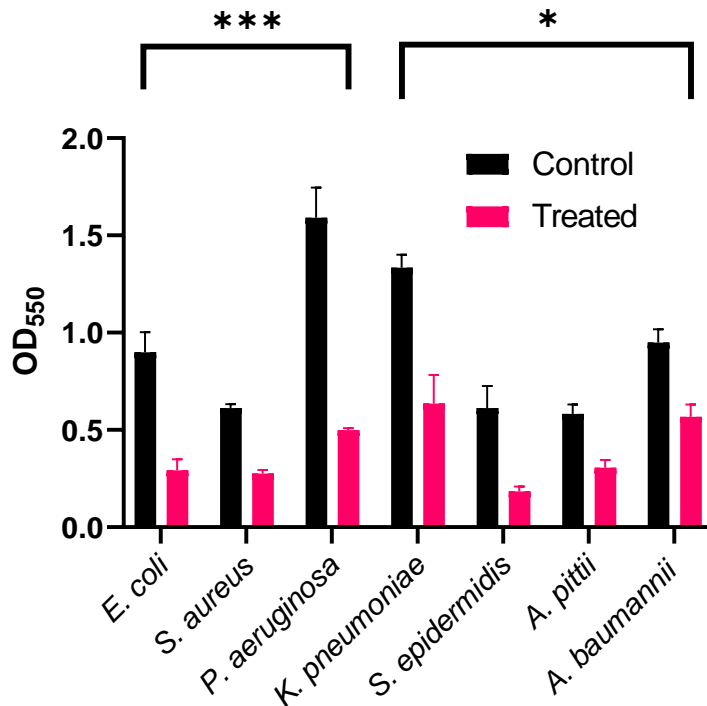
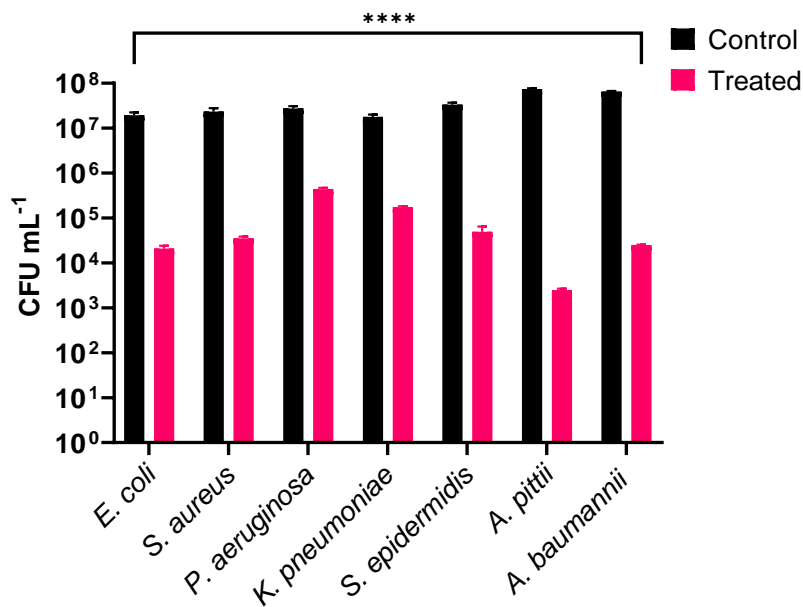Figure 16 The reduction in biofilm formation measured at 20 times MBC concentration compared to untreated mMBEC pegs

Figure 17 The reduction in viable cells recovered at 20 times MBC concentration compared to untreated mMBEC pegs

3.4 Centre for disease and control bioreactor assay

To test other materials, and the efficacy of the spray coating, a Centre for Disease and Control (CDC) bioreactor was used with stainless steel, titanium, PVC, and Silicone rubber coupons. The coupons were recovered from a batch run and evaluated for both the biofilm formation (Fig. 16) and the viable cells (Fig. 17). Reduction in biofilm formation on the coupons was only significant for the PVC coupons while the reduction in viable cells adhered to the coupons is observed for all tested materials.
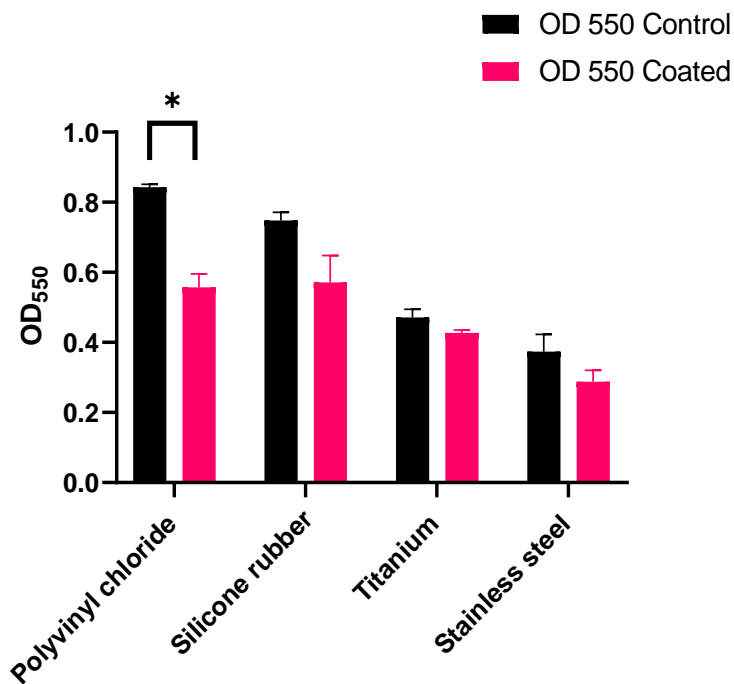

Figure 18 The reduction of biofilm recovered from each of the materials treated with a spray coating at MBC concentration
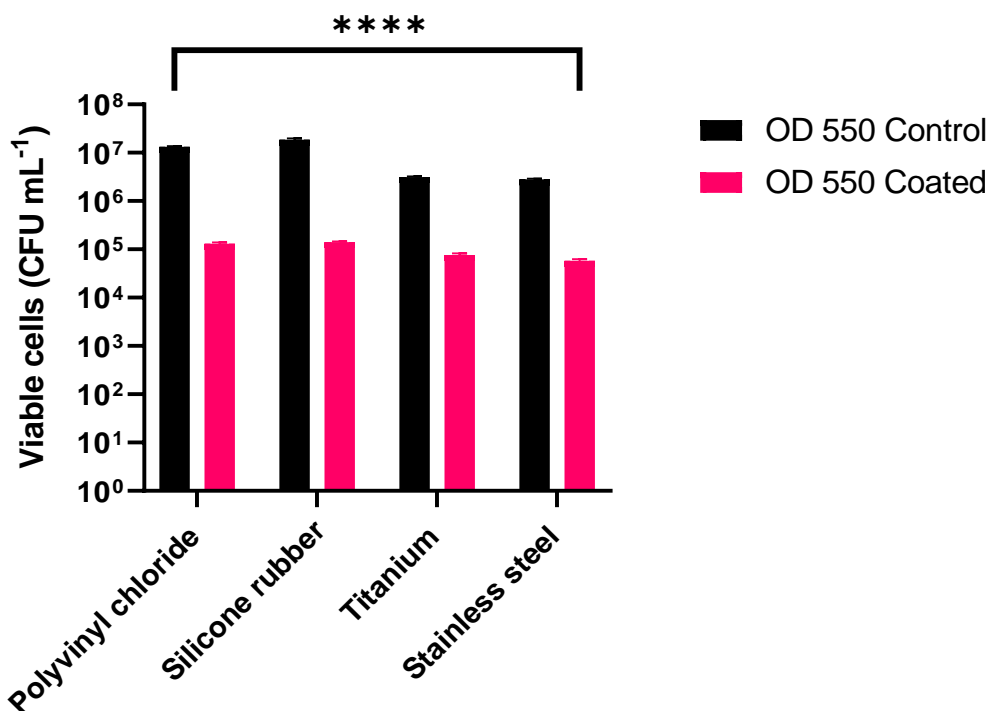
Figure 19 Reduction in recovered viable cells from treated and untreated CDC coupons, of various materials, at MBC concentration.

Conclusions

Here we show that CuO nanoparticles can be functionalized with glutamic acid, to improve the stability of the particle in solution, whilst retaining their antimicrobial properties. These Glu-CuO nanoparticles can then be adhered to a variety of medical grade materials, using MPTMS as an adhesive, such as silicone, stainless steel, titanium, and PVC. The MPTMS shows toxicity at concentrations exceeding 0.1 M, and the Glu-CuO nanoparticles showing toxicity at concentrations exceeding 325 μg mL^{-1}, but offer a therapeutic window before toxicity is present. The coating can be applied using a dip coating procedure, allowing malleable materials to be coated as well as a spray coating that can be rapidly cured using UV radiation on *ad hoc* modified materials. These coatings don't differ between the two coating techniques and can provide up to log 4 reduction, depending on species.

5. Patents

US Pat., 10926236B2, 2021, US Pat., 10154628B2, 2018

Supplementary Materials: The following supporting information can be downloaded at

Author Contributions:

References

1 M. S. Mulani, E. E. Kamble, S. N. Kumkar, M. S. Tawre and K. R. Pardesi, *Frontiers in microbiology,* 2019, **10**, 539.

2 B. Halioua and B. Ziskind, *Medicine in the Days of the Pharaohs*, Harvard University Press, 2005.

3 F. Zivic, N. Grujovic, S. Mitrovic, I. U. Ahad and D. Brabazon, *Commercialization of nanotechnologies–a case study approach,* 2018, , 227-273.

4 S. Franke, G. Grass and D. H. Nies, *Microbiology,* 2001, **147**, 965-972.

5 A. Kędziora, M. Speruda, E. Krzyżewska, J. Rybka, A. Łukowiak and G. Bugla-Płoskońska, *International journal of molecular sciences,* 2018, **19**, 444.

6 N. Lin, D. Verma, N. Saini, R. Arbi, M. Munir, M. Jovic and A. Turak, *Nano Today,* 2021, **40**, 101267.

7 https://www3.epa.gov/pesticides/chem_search/ppls/082012-00005-20080229.pdf, (accessed 5th June 2023).

8 E. Weir, A. Lawlor, A. Whelan and F. Regan, *Analyst,* 2008, **133**, 835-845.

9 M. Khan, M. R. Shaik, S. T. Khan, S. F. Adil, M. Kuniyil, M. Khan, A. A. Al-Warthan, M. R. H. Siddiqui and M. Nawaz Tahir, *ACS omega,* 2020, **5**, 1987-1996.

10 J. J. Harrison, C. A. Stremick, R. J. Turner, N. D. Allan, M. E. Olson and H. Ceri, *Nature protocols,* 2010, **5**, 1236-1254.

11 C. A. Schneider, W. S. Rasband and K. W. Eliceiri, *Nature methods,* 2012, **9**, 671-675.

12 A. J. Cunliffe, P. D. Askew, I. Stephan, G. Iredale, P. Cosemans, L. M. Simmons, J. Verran and J. Redfern, *Antibiotics,* 2021, **10**, 1069.

13 S. Sagadevan, K. Pal and Z. Z. Chowdhury, *J. Mater. Sci. : Mater. Electron.,* 2017, **28**, 12591-12597

14 A. Chakraborty, J. C. Boer, C. Selomulya and M. Plebanski, *Bioconjug. Chem.,* 2017, **29**, 657-671.

15. D. J. Pochapski, C. Carvalho dos Santos, G. W. Leite, S. H. Pulcinelli and C. V. Santilli, *Langmuir,* 2021, **37**, 13379-13389.

16 I. Byun, A. W. Coleman and B. Kim, *J Micromech Microengineering,* 2013, **23**, 085016.